Aix*Marseille université
Socialement engagée

NNT/NL : 2024AIXM0053/006ED353

THÈSE DE DOCTORAT

Soutenue à Aix-Marseille Université
le 12 mars 2024 par

Gabriel GUILLET

Concept of Restaurants Optimised for Solar Cooking

Discipline
Sciences pour l'ingénieur

Spécialité
Énergétique

École doctorale
ED 353 Sciences pour l'ingénieur : mécanique, physique, micro et nanoélectronique

Laboratoire/Partenaires de recherche
IUSTI UMR CNRS 7343
Région Sud Provence-Alpes-Côtes d'Azur
Société CANOPÉE Le Présage SAS

Composition du jury

Celestino RUIVO Prof., Universidade do Algarve	Rapporteur
Régis OLIVÈS Prof., Université de Perpignan Via Domitia	Rapporteur
Nolwenn LE PIERRES Prof., Université Savoie-Mont-Blanc	Examinatrice
Yasmine LALAU MCF, IMT Mines Albi	Examinatrice
Benoît ROUSSEAU DR CNRS, LTEN	Président du jury
Benjamin KADOCH MCF, Aix-Marseille Université	Directeur de thèse
Thomas FASQUELLE MCF, Aix-Marseille Université	Co-encadrant de thèse
Séverine BARBOSA MCF, Aix-Marseille Université	Co-encadrante de thèse
Pierre-Andrée AUBERT Ingé., CANOPÉE Le Présage	Membre invité
Benjamin LEROY Ingé., CANOPÉE Le Présage	Membre invité

IUSTI LABORATOIRE AIX MARSEILLE UNIVERSITÉ CNRS

RÉGION SUD PROVENCE ALPES CÔTE D'AZUR

LE PRÉSAGE

Affidavit

I, undersigned, Gabriel Guillet, hereby declare that the work presented in this manuscript is my own work, carried out under the scientific direction of Benjamin Kadoch, in accordance with the principles of honesty, integrity and responsibility inherent to the research mission. The research work and the writing of this manuscript have been carried out in compliance with both the french national charter for Research Integrity and the Aix-Marseille University charter on the fight against plagiarism.

This work has not been submitted previously either in this country or in another country in the same or in a similar version to any other examination body.

Marseille, on 16 January 2024





The content of "Concept of solar restaurants optimised for solar cooking" © 2024 by Gabriel GUILLET is licensed under Creative Commons Attribution 4.0 International (CC BY 4.0) unless otherwise stated.

Scientific communications and participation in scientific events

Publications produced as part of the doctoral project

- G. Guillet, J. Gaspar, S. Barbosa, T. Fasquelle, and B. Kadoch, 'Experimental evaluation of the concentrated solar heat flux distribution provided by an 8 m2 Scheffler reflector', Renewable Energy, p. 119958, Jan. 2024, doi: 10.1016/j.renene.2024.119958.
- T. Fasquelle, B. Kadoch, G. Guillet, and S. Barbosa, 'Open-Source Monte-Carlo Ray-Tracing Model of realistic Scheffler reflectors' (submitted)

Conference papers with full-text refereed proceedings

- G. Guillet, J. Gaspar, T. Fasquelle, S. Barbosa, B. Kadoch, Y. Pizzo, F. Rigollet, C. Le Niliot, and J.-L. Gardarein, 'Estimation par méthode inverse du flux absorbé par une plaque en fonte destinée à la cuisson solaire', in Actes du congrès annuel de la Société Française de Thermique 2021, Belfort, France, Jun. 2021, pp. 269–276. doi: 10.25855/SFT2021-059.
- G. Guillet, S. Barbosa, T. Fasquelle, and B. Kadoch, 'Towards Professional Kitchen with Scheffler Reflectors', in CONSOLFOOD 2022 - Conference Proceedings, Faro, Portugal, Jan. 2022, pp. 99–106.
- G. Guillet, J. Gaspar, T. Fasquelle, S. Barbosa, and B. Kadoch, 'Comment mesurer les caractéristiques d'un flux de rayonnement solaire concentré délivré par un réflecteur de Scheffler ?', in Actes du congrès annuel de la Société Française de Thermique 2023, Reims, France, May 2023, pp. 433–440. doi: 10.25855/SFT2023-066.

Conference presentations

- G. Guillet, 'Estimation par méthode inverse du flux absorbé par une plaque en fonte destinée à la cuisson solaire', presented at Congrès français de thermique 2021 - Thermique et mix énergétique, Belfort, France, 2 Jun. 2021.
- G. Guillet, 'Towards Professional Kitchen with Scheffler Reflectors', presented at CONSOLFOOD 2022 - Fourth International Conference on Advances in Solar Thermal Food Processing, Faro, Portugal, 24 Jan. 2022.

- G. Guillet, 'Towards Restaurants Powered by Scheffler Reflectors - Standard Performance Test of a Basic Solution', presented at Journée des doctorants de l'Ecole Doctorale 353, Marseille, France, 2 Jun. 2022.
- G. Guillet, 'Performance Evaluation of a Professional Cooktop Powered by a Scheffler Reflector', presented at CONSOLFOOD 2023 - Fifth International Conference on Advances in Solar Thermal Food Processing, A Coruna, Spain, 12 Jul. 2023.

Conference posters

- G. Guillet, 'Estimation par méthode inverse du flux absorbé par une plaque en fonte destinée à la cuisson solaire', presented at Congrès français de thermique 2021 - Thermique et mix énergétique, Belfort, France, 2 Jun. 2021.
- G. Guillet, 'Towards Restaurants Powered by Scheffler Reflectors - Standard Performance Test of a Basic Solution', presented at Journée des doctorants de l'Ecole Doctorale 353, Marseille, France, 2 Jun. 2022.
- G. Guillet, 'Comment mesurer les caractéristiques d'un flux de rayonnement solaire concentré délivré par un réflecteur de Scheffler ?', presented at Congrès français de thermique 2023 - Thermique et agroressources, Reims, France, 1 Jun. 2023.

Participation in scientific events during the doctoral project

- 4Sun - Scientific Solar Summer School, 19 - 23 Oct. 2020, Le Bourget-du-Lac, France (online)
- Congrès français de thermique 2021 - Thermique et mix énergétique, 1 - 3 Jun. 2021, Belfort, France (online)
- Thermique atmosphérique et adaptation au changement climatique - Journée thématique de la Société Française de Thermique, 18 Nov. 2021, Villeurbanne, France (online)
- CONSOLFOOD 2022 - Fourth International Conference on Advances in Solar Thermal Food Processing, 24 - 26 Jan. 2022, Faro, Portugal (online)
- Journée des doctorants de l'Ecole Doctorale 353, 2 Jun. 2022, Marseille, France
- Systèmes énergétiques et bâtiment - Journée thématique de la Société Française de Thermique, 6 Oct. 2022, Paris, France (online)
- Congrès français de thermique 2023 - Thermique et agroressources, 30 May - 2 Jun. 2023, Reims, France
- CONSOLFOOD 2023 - Fifth International Conference of Advances in Solar Thermal Food Processing, 12 - 14 Jul. 2023, A Coruna, Spain

Abstract

Le Présage is the first restaurant concept in Europe whose cooking system is powered by solar thermal energy. Having confirmed the feasibility of the concept with its *guinguette solaire*, the company now wants to optimise the cooking system and integrate it into an innovative building with high environmental quality. The cooking system comprises three elements: a Scheffler reflector that collects and concentrates sunlight; a secondary reflector that reflects the concentrated flux upwards; and a cast-iron plate that acts as a solar absorber on the underside and as a cooking plate on the top. The Scheffler reflector is a parabolic dish that is flexible, enabling it to concentrate solar radiation at a fixed point throughout the year, without requiring the reflector to rotate around this point. As a result, the focal point can be positioned inside a building in which a kitchen can be installed. The aim of this doctoral research project is to understand and evaluate the performance of this promising concentrating solar cooker concept.

In the first chapter of this thesis, the overall performance of the solar cooker is evaluated in order to obtain an initial estimate that can serve as a benchmark for comparison with future improvements. First, the different ways of modelling and evaluating solar cooker performance are explored. The specific characteristic time constant, the opto-thermal ratio and the corrected standard power are selected from other performance indicators and expressed using an energy balance based on a lumped-element model. Next, the test bench developed, similar to the cooker used by the Le Présage restaurant, is described. Experiments were carried out using a protocol similar to that used by ASABE, and regression analyses of temperature, efficiency and normalised power are detailed. The opto-thermal ratio of the cooker varies from 0.06 $m^2 \cdot K \cdot W^{-1}$ to 0.22 $m^2 \cdot K \cdot W^{-1}$, while the corrected standard power reaches up to 416 W.

In the second chapter, the Scheffler reflector is studied in more detail. The objectives are to evaluate its energy performance and to obtain information about the shape of the heat flux it delivers. Theoretical and numerical studies in the literature have produced highly variable results, and experimental data is currently lacking. A second test bench and another experimental protocol were therefore developed. Using infrared thermography and inverse techniques, detailed maps of heat flux densities on a vertical absorber were obtained from measurements carried out on different days between March and July. The average energy efficiency is estimated at 68 %. The heat flux distributions provided are then successfully fitted to a two-dimensional Gaussian model. The model parameters are used to calculate, among other things, the mean major and minor diameters of the ellipse containing 99.7 % of the heat flux, i.e. 47 cm and 37 cm respectively. The surface concentration ratio and the heat flux

concentration ratio are evaluated at 36 and 24 respectively. The issue of repeatability of measurements and seasonal/daily variations is also addressed.

Overall, this work provides a detailed data set on the performance of the solar cooker studied using two innovative methodologies. These results provide fundamental information for identifying improvements to the system, for modelling the reflector and for optimising secondary optical systems and the absorber.

Keywords: solar power, solar cooking, Scheffler reflector, heat transfers

Résumé

Le Présage est le premier concept de restaurant en Europe dont le système de cuisson est alimenté à l'énergie solaire thermique. Après avoir confirmé la faisabilité du concept avec sa *guinguette solaire*, l'entreprise souhaite maintenant optimiser le système de cuisson puis l'intégrer dans un bâtiment innovant à haute qualité environnementale. Le système de cuisson est constitué de trois éléments : un réflecteur de Scheffler qui collecte la lumière du soleil et la concentre ; un réflecteur secondaire qui réfléchit le flux concentré vers le haut ; et une plaque en fonte qui fait office d'absorbeur solaire sur sa face inférieure et de plaque de cuisson sur sa face supérieure. Le réflecteur de Scheffler est une parabole qui a la particularité d'être flexible, ce qui lui permet de concentrer le rayonnement solaire en un point fixe tout au long de l'année, sans nécessiter de rotation du réflecteur autour de ce point. Dès lors, le point focal peut être positionné à l'intérieur d'un bâtiment dans lequel une cuisine peut être aménagée. L'objectif de ce projet de recherche doctorale est de comprendre et d'évaluer les performances de ce concept prometteur de cuiseur solaire à concentration.

Dans le premier chapitre de cette thèse, les performances globales du cuiseur solaire sont évaluées afin d'obtenir une première estimation qui pourra servir de référence pour les comparaisons avec les améliorations futures. Premièrement, les différentes manières de modéliser et d'évaluer les performances des cuiseurs solaires sont explorées. La constante de temps caractéristique massique, le rapport opto-thermique et la puissance standard corrigée sont sélectionnés parmi d'autres indicateurs de performance et exprimés à l'aide d'un bilan énergétique basé sur un modèle constitué de blocs fonctionnels. Ensuite, le banc d'essai développé, similaire au cuiseur utilisé par le restaurant Le Présage, est décrit. Des expériences ont été réalisées selon un protocole similaire à celui de l'ASABE et des analyses de régression sur la température, le rendement et la puissance normalisée sont détaillées. Le rapport opto-thermique du cuiseur varie de 0,06 $m^2 \cdot K \cdot W^{-1}$ à 0,22 $m^2 \cdot K \cdot W^{-1}$, tandis que la puissance standard corrigée atteint jusqu'à 416 W. Dans le deuxième chapitre, le réflecteur Scheffler est étudié de manière plus approfondie. Les objectifs sont d'évaluer ses performances énergétiques et d'obtenir des informations sur la forme du flux de chaleur qu'il délivre. Les études théoriques et numériques dans la littérature ont donné des résultats très variables et les données expérimentales manquent actuellement. Un deuxième banc d'essai et un autre protocole expérimental ont donc été mis au point. En utilisant la thermographie infrarouge et des techniques inverses, des cartes détaillées des densités de flux de chaleur sur un absorbeur vertical sont obtenues à partir de mesures réalisées sur des journées différentes entre mars et juillet. L'efficacité énergétique moyenne est estimée à 68 %. Les distributions de flux thermique fournies sont ensuite ajustées avec succès à un modèle gaussien bidimensionnel. Les paramètres du modèle

sont utilisés pour calculer, entre autres, les diamètres majeurs et mineurs moyens de l'ellipse contenant 99,7 % du flux de chaleur, soit 47 cm et 37 cm respectivement. Le rapport de concentration de surface et le rapport de concentration de flux thermique sont évalués respectivement à 36 et 24. La question de la répétabilité des mesures et des variations saisonnières/quotidiennes est également abordée.

Dans l'ensemble, ce travail fourni un jeu de données détaillé sur les performances du cuiseur solaire étudié en utilisant deux méthodologies innovantes. Ces résultats fournissent des informations fondamentales pour l'identification des améliorations à apporter au système, pour la modélisation du réflecteur et pour l'optimisation de systèmes optiques secondaires et de l'absorbeur.

Mots clés : énergie solaire, cuisine solaire, réflecteur de Scheffler, transferts de chaleur

Résumé étendu

En 2020, l'entreprise Le Présage a ouvert sa "Guinguette solaire", le premier concept de restaurant en Europe dont le système de cuisson est alimenté à l'énergie solaire thermique. Aménagée dans un container, la cuisine est en effet alimentée par l'énergie thermique du soleil. Une grande parabole située à l'arrière du container collecte la lumière du soleil et la concentre par une ouverture vers l'intérieur de la cuisine où un réflecteur secondaire la renvoie vers le haut, sous une grande plaque en fonte qui fait office de plaque de cuisson. Une grande fenêtre à l'avant du container permet de servir les clients.

Après avoir confirmé la faisabilité du concept avec sa « guinguette solaire », l'entreprise souhaite maintenant optimiser le système de cuisson puis l'intégrer dans un bâtiment innovant à haute qualité environnementale. Le système de cuisson est constitué de trois éléments : un réflecteur de Scheffler qui collecte la lumière du soleil et la concentre ; un réflecteur secondaire qui réfléchit le flux concentré vers le haut ; et une plaque en fonte qui fait office d'absorbeur solaire sur sa face inférieure et de plaque de cuisson sur sa face supérieure. Le réflecteur de Scheffler à la forme d'une portion excentrée de paraboloïde et a la particularité d'être flexible. Cette particularité lui permet de concentrer le rayonnement solaire en un point fixe tout au long de l'année, sans requérir de rotation du réflecteur autour de ce point. Dès lors, le point focal peut être positionné à l'intérieur d'un bâtiment, dans lequel une cuisine (ou tout autre système nécessitant un apport de chaleur entre 100 °C et 500 °C) peut être installé durablement.

L'objectif de cette thèse est d'évaluer les performances de ce nouveau concept de cuiseur solaire à concentration utilisant un réflecteur Scheffler. Les cuiseurs de type Scheffler sont en effet prometteurs parmi les cuiseurs solaires car ils permettent de maintenir la parabole et le point focal à des positions stationnaires tout au long de l'année. De plus ils sont capable de fournir des puissances et d'assurer des températures suffisantes à la plupart des modes de cuisson et pourraient être adaptés pour de nombreux processus artisanaux et industriels.

Dans le premier chapitre de ce mémoire, les performances globales du cuiseur solaire sont évaluées afin d'obtenir une première estimation à laquelle les améliorations futures pourront être comparées.

Tout d'abord, les manières existantes de modéliser et d'évaluer les performances des cuiseurs solaires sont explorées. Les trois normes historiques (indienne, européenne et américaine) ainsi que des indicateurs variées sont présentés et leur intérêt respectif est discuté. Dans la plupart des cas, la procédure expérimentale consiste à soumettre le cuiseur solaire à un échelon de rayonnement solaire et à enregistrer sa réponse thermique à vide et/ou en charge. En s'appuyant sur ces travaux, un modèle en bloc

fonctionnels suffisamment général pour décrire les différents types de cuiseur solaire est élaboré. Il consiste en un système représentant la charge à réchauffer (*e.g.* de l'eau), imbriqué dans un second système représentant à la fois l'ustensile (*e.g.* la casserole) et le cuiseur solaire. Un bilan énergétique est réalisé sur cet ensemble et un système de deux équations différentielles couplées est obtenu. Bien qu'un peu complexe, ce système d'équations semble pouvoir décrire l'ensemble des cuiseurs solaires. Contrairement à l'expression usuellement utilisée, il permet de prendre en compte l'inertie thermique du cuiseur solaire et ainsi de décrire son comportement dès le début de la phase de chauffe. Néanmoins, ce système d'équations n'est pas facile à manipuler, c'est pourquoi des hypothèses simplificatrices et spécifiques au système étudié sont ensuite ajoutées. Le système d'équation est réduit à une seule équation plus spécifique, de laquelle sont dérivés l'expression de la température de la charge en fonction du temps ainsi que les expressions de l'efficacité énergétique et la puissance normalisée du cuiseur en fonction de la différence de température entre l'eau et l'air rapportée à l'irradiance solaire. Entre autres indicateurs, la constante de temps massique, le rapport opto-thermique et la puissance standard corrigée sont sélectionnés pour décrire les performances du système et identifiés dans ces trois expressions.

Ensuite, la méthodologie expérimentale est présentée. La maquette expérimentale construite pour cette étude comprend notamment une reproduction quasi à l'identique du système de cuisson du Présage. Deux différences importantes sont toutefois à noter. Dans le système du Présage, le réflecteur de Scheffler est couvert par un revêtement réfléchissant continu et le miroir secondaire est incurvé, tandis que dans la configuration étudiée, le réflecteur de Scheffler est couvert de facettes planes et le réflecteur secondaire est plan. La maquette expérimentale comprend également une casserole remplie d'eau et disposée sur la plaque de cuisson. L'irradiance horizontale globale, l'irradiance normale directe, la température de l'eau dans la casserole, celle de l'air et la vitesse du vent sont mesurées. Un protocole expérimentale similaire à celui de l'ASABE est mis au point. Celui-ci consiste à mettre en place la maquette expérimentale à un emplacement ensoleillé, régler la courbure du réflecteur de Scheffler, puis chauffer une masse d'eau donnée de la température ambiante jusqu'à ébullition. La température de l'eau est sur-échantillonnée puis moyennée sur une fenêtre glissante afin d'améliorer la résolution de mesure et réduire le bruit de mesure, tandis que les données environnementales sont traitées conformément aux directives de l'Organisation Mondiale de Météorologie. Les données expérimentales sont ensuite ajustées aux expressions de la température, de l'efficacité énergétique et de la puissance normalisée. Les fonctions de régression obtenues permettent enfin de calculer les indicateurs de performance.

Trois expériences ont été réalisées le 17 décembre 2021, le 18 juillet 2022 et le 22 juillet 2022. Les deux premières expériences ont été réalisées sans préchauffe tandis que la dernière est réalisée avec une préchauffe de 46 min. La qualité de l'ajustement de la température, de l'efficacité énergétique et de la puissance normalisée à leur modèle respectif est jugée bonne suite à une évaluation graphique et statistique. Les indicateurs de performances sont alors calculés à partir des paramètres estimés par

régression.

Le modèle physique accompagné de la procédure expérimentale a permis d'estimer approximativement les indicateurs de performance. Bien que de grandes variations soient observées sur certains indicateurs entre les expériences, elles peuvent être expliquées qualitativement. Avec une efficacité optique totale comprise entre 21 % et 22 % (réflecteur rénové), il existe un grand potentiel d'amélioration sur cet aspect. À basse température, le système est capable de fournir une puissance assez élevée (entre 600 W et 700 W de puissance standardisée) grâce à sa grande ouverture. Cependant, la puissance diminue au fur et à mesure que la température de l'eau augmente, et ce de manière particulièrement brutale s'il y a du vent. Ceci est dû à l'absence d'isolation et à la grande surface de perte liée à l'utilisation d'une plaque de cuisson. En effet, la plaque de cuisson est un système intrinsèquement inefficace du point de vue thermodynamique, mais c'est une interface très appréciée par les chefs de restaurant car elle leur permet de cuisiner avec précision et efficacité pour un grand nombre de clients. La performance thermique a des répercussions directes sur le temps caractéristique spécifique.Associé à la variation saisonnière de l'ouverture, cela fait varier encore plus le rapport opto-thermique (de 0,06 $m^2 \cdot K \cdot W^{-1}$ à 0,22 $m^2 \cdot K \cdot W^{-1}$). La puissance standard reflète également ces faits.

Plus généralement, la méthodologie utilisé dans ce travail a permi de définir des bonnes pratiques. Tout d'abord, plusieurs modèles physiques et méthodes d'évaluation coexistent dans la littérature en raison de la grande variété de conceptions des cuiseurs solaires et de l'équipement de mesure disponible. Néanmoins, l'utilisation de l'analyse de régression est préférable aux méthodes d'estimation basées sur seulement deux points de mesure. En complément de l'irradiance solaire globale horizontale, il semble également nécessaire de mesurer ou au moins d'estimer l'irradiance normale directe pour l'évaluation des performances des cuiseurs à concentration. Deuxièmement, un modèle tel que celui défini par l'ASABE implique des hypothèses importantes. Celles-ci doivent être gardées à l'esprit lors de l'analyse des données expérimentales, en particulier lors de la sélection de l'intervalle sur lequel sont effectuées les analyses de régression. En effet, le début et la fin de la phase de chauffage ne peuvent être décrits par ce type de modèle. Dériver ces indicateurs de performance d'un bilan d'énergie spécifique au système étudié semble être un bon moyen de mettre en évidence les hypothèses et d'obtenir une expression des indicateurs de performance représentative de chaque cuiseur solaire. Troisièmement, le temps caractéristique spécifique et le rapport opto-thermique sont deux indicateurs de performance importants pour le concepteur comme pour l'utilisateur puisqu'ils répondent aux questions :

- Quelle est la température maximale que le cuiseur solaire est capable d'atteindre dans des conditions climatiques données ?
- Combien de temps faut-il pour chauffer une masse d'eau donnée de la température ambiante à cette température maximale ?

Dans le deuxième chapitre, le réflecteur Scheffler est étudié de manière plus approfondie. Les objectifs sont d'évaluer ses performances énergétiques et d'obtenir des

informations sur la forme du flux de chaleur délivré par le réflecteur, afin d'optimiser sa combinaison avec le réflecteur secondaire et l'absorbeur. Dans la littérature, les études théoriques et numériques ont donné des résultats très variables et les données expérimentales manquent. Les évaluations précises sont rares, probablement parce que l'évaluation de la distribution d'un flux solaire concentrée dans la zone focale n'est pas une tâche facile. Elle nécessite un système de détection doté d'un large champ de vision, d'une résolution spatiale élevée et d'une grande résistance au flux de chaleur. Les méthodes couramment utilisées dans le domaine de l'énergie solaire concentrée sont les suivantes.

Un deuxième banc d'essai et un autre protocole expérimental ont donc été mis au point. Pour comprendre le comportement et évaluer les performances d'un réflecteur, il faut connaître les caractéristiques du flux thermique qu'il recueille et délivre. Le flux de chaleur collecté est évalué à l'aide de l'ouverture du réflecteur et de l'irradiance solaire directe normale enregistrée par un pyrhéliomètre. Le calcul prend en compte l'irradiance normale directe et non l'irradiance normale globale car le réflecteur a un angle d'acceptation faible. Le flux de chaleur délivré par le réflecteur est d'abord recueilli par un écran (récepteur) placé verticalement dans le plan focal du réflecteur. Des mesures de la température de l'air et de la vitesse du vent permettent d'évaluer les échanges convectifs et radiatifs entre l'écran et l'environnement. Ensuite, une caméra infrarouge mesure le rayonnement émis par le dos de l'écran et l'émissivité de la surface émettrice permet de déduire le champ de température. A partir de ce champ de température, un modèle thermique de l'écran et des techniques inverses sont utilisés pour estimer le flux de chaleur initialement absorbé par l'écran. L'absorptivité solaire de l'écran est ensuite utilisée pour obtenir le flux de chaleur délivré par le réflecteur. Enfin, une analyse de régression par rapport à un modèle gaussien bidimensionnel est effectuée pour en déduire des informations quantitatives sur la distribution (en particulier sa taille).

Tout d'abord, le système est installé dans un endroit exposé au soleil et sans aucune ombre pouvant interférer avec l'expérience. Pendant toute la durée de l'expérience, la plaque en fonte et les instruments de mesure sont protégés de la lumière directe du soleil afin d'éviter la réflexion de la lumière directe du soleil de la plaque sur la caméra et d'éviter la surchauffe de l'électronique. Ensuite, le réflecteur de Scheffler est brièvement tourné vers le soleil pour établir sa courbure et mesurer son angle par rapport à la verticale. Une fois cette opération effectuée, le vent et la température ambiante commencent à être enregistrés ; l'irradiance directe normale est enregistrée en continu par la station météorologique. Le Scheffler est à nouveau tourné vers le soleil et le système de suivi du soleil est activé. Lorsque l'état d'équilibre est atteint, plusieurs mesures sont effectuées à intervalles réguliers avec la caméra infrarouge autour de midi solaire. Pour chacune de ces mesures, une courte vidéo est enregistrée avec chaque filtre et avec des temps d'intégration multiples. Une image moyenne combinant toutes les images enregistrées est ensuite sauvegardée. Cela permet de réduire le bruit de la mesure et de saisir toute la gamme des températures observées. Enfin, le réflecteur est détourné du soleil et chaque enregistrement est arrêté.

L'utilisation d'une caméra infrarouge et de techniques inverses permet d'obtenir

une carte détaillée des densités de flux de chaleur sans aucun a priori. La densité maximale du flux de chaleur, la puissance totale et l'efficacité énergétique sont données avec une incertitude relativement faible allant de 6 % à 10 % et sont en accord satisfaisant avec la littérature, confirmant la pertinence de la méthode.Bien que la méthode expérimentale ait démontré ses capacités, elle n'a pas permis d'analyser en détail les variations de la forme de la distribution du flux de chaleur en fonction du temps. En effet, en raison de l'inertie thermique de l'écran, de l'hypothèse d'un régime permanent et de la durée de la mesure, les résultats sont sensibles aux variations rapides du vent et de l'irradiance normale directe. Une autre raison est que les résultats semblent être sensibles à la précision avec laquelle le banc d'essai est mis en place avant chaque expérience (orientation nord-sud, inclinaison de l'axe de rotation, courbure, emplacement du récepteur, etc.)

Les distributions expérimentales de flux de chaleur sont comparées avec succès à un modèle basé sur une fonction gaussienne bidimensionnelle. Les paramètres estimés ont permis une analyse plus détaillée des données expérimentales et, en particulier, ont fourni des données quantitatives sur la taille de la distribution du flux de chaleur sans avoir besoin d'un seuil arbitraire. Il s'agit d'un point essentiel pour comparer ce travail avec d'autres, en particulier avec le travail de Dib. L'étude du contour de la distribution du flux de chaleur est intéressante à première vue parce qu'elle peut être faite théoriquement et assez facilement ; elle devient discutable dans les études numériques et encore plus dans les études expérimentales parce que le contour n'a pas d'existence réelle. De plus, la connaissance de la distribution du flux de chaleur permet une optimisation thermique, alors que le contour ne permet qu'une optimisation géométrique. La variation de la taille de la distribution du flux de chaleur en fonction de l'heure du jour ou du jour de l'année ne semble pas suivre de schéma identifié et semble être du même ordre de grandeur que la variabilité observée à travers les différentes expériences. Soit la taille ne dépend pas du temps, soit sa dépendance est très faible et cachée dans la variabilité expérimentale. Cela signifie que le réflecteur ou récepteur secondaire peut être optimisé pour l'ensemble de l'année et pas seulement pour certaines périodes.

En moyenne, 99,7 % du flux thermique fourni par le réflecteur de 8 m^2 est reçu sur l'écran vertical dans une ellipse de diamètres majeur et mineur 47 cm et 37 cm respectivement. Le rapport de concentration de surface et le rapport de concentration de flux de chaleur sont évalués respectivement à 36 et 24. Bien que partiels, ces résultats fournissent déjà des informations fondamentales pour les concepteurs. En fonction des caractéristiques thermiques de l'absorbeur et des caractéristiques de distribution du flux de chaleur, il est déjà possible de déterminer la taille de l'absorbeur qui minimise les pertes de chaleur.

Dans des travaux futurs, l'ensemble des données sur les performances du réflecteur de Scheffler devrait être complété par d'autres expériences réalisées à d'autres moments de la journée et d'autres jours de l'année, notamment de novembre à février (l'ensemble des données expérimentales fournies couvre la période de mars à juin, et donc de juillet à octobre par symétrie). Ceci permettrait de voir plus précisément comment les caractéristiques du flux de chaleur fourni par le réflecteur varient en

fonction du temps. On pourrait même faire des expériences avec différentes tailles de réflecteurs, différentes tailles de facettes, différentes inclinaisons de récepteurs, etc. Dans cette optique, il serait judicieux d'effectuer des travaux expérimentaux et numériques en même temps. Des modèles numériques précis pourraient être construits à partir des données expérimentales et la simulation numérique pourrait alors être utilisée pour suggérer des améliorations à la méthode expérimentale et réduire le nombre d'expériences nécessaires.

To my family and friends for their unwavering support.

Acknowledgements

Walking the doctoral path is like walking through fog: sometimes it is exciting, sometimes it is frightening. Fortunately, I did not walk this long road alone.

First of all, I would like to thank my doctoral supervisor Benjamin Kadoch and my two co-supervisors Thomas Fasquelle and Séverine Barbosa for entrusting me with this project and guiding me throughout. I particularly appreciated their enthusiasm and attention, but also their patience.

I am also grateful to Pierre-André Aubert and Benjamin Leroy, because my doctoral research project would not exist if they had not opened up their own path. More broadly, I would like to thank the whole team of CANOPÉE Le Présage for their warm welcome and for answering my questions about cooking.

I would finally like to thank Benoît Rousseau for agreeing to chair my jury, and Nolwenn Le Pierrès and Yasmine Lalau for agreeing to act as examiners. My special thanks go to Celestino Ruivo and Régis Olivès, who agreed to be reviewers and whose comments helped me to improve the content of this thesis and to prepare the defence.

Along the way, many other people offered me their help and thus contributed to this work.

Among them, Jonathan Gaspar and Nathalie Ehret took part in the experiments and gave me the benefit of their expertise in characterising the thermal properties of materials, infrared thermography and inverse techniques. Christophe Escape carried out complementary measurements. Many thanks to them.

I am grateful to Salmane Zekri for his work on the energy performance of the building of CANOPÉE LE Présage as part of his end-of-master's internship.

I would like to thank Yannick Pizzo who helped me setup the first experiments, and Sady Noël without whom the reflector under study would not be mobile.

I really appreciated the advices of Christophe le Niliot, Fabrice Rigollet and Jean-Laurent Gardarein. I am also thankful to Manuel Collares Perrera and Wolfgang Scheffler for their respective inputs on non-imaging optical systems and Scheffler reflectors.

Finally, I would like to thank all the researchers and doctoral researchers who helped me to improve my work through their advice, questions and comments, in particular Houssine, Yann, Jordan, Alexandre, Arnaud, Alain, Alice, Valentin, Dorian, Nina, Nabila, Enrico, Hamza, San Jeev and Joris.

As the doctorate is not just about research, I would like to thank all the teaching, administrative and technical staff at the IUSTI laboratory, the Polytech Marseille engineering school and Doctoral School 353. In particular, I would like to thank Christian

Mariani and Georges Jourdan, who gave me the benefit of their teaching experience, and Pascal Campion for his attentive ear.

And finally, I would like to thank our funders, i.e. the Région Sud Provence-Alpes-Côte d'Azur and the company CANOPEE Le Présage, who supported this work as part of the Emplois Jeunes Doctorants programme, as well as the Institute of Mechanics and Engineering of Aix-Marseille University.

Table of Contents

Affidavit 2

Scientific communications and participation in scientific events 3

Abstract 5

Résumé 7

Résumé étendu 9

Acknowledgements 16

Table of Contents 18

Symbols 20

1 Introduction 23

2 Overall performance of the solar cooking system 29
- 2.1 Why talking about performance? . . . 30
- 2.2 How is the performance of solar cooking systems assessed? . . . 30
- 2.3 From energy balance to performance indicators . . . 39
- 2.4 Material and methods . . . 49
- 2.5 Data processing . . . 53
- 2.6 Results and discussion . . . 56
- 2.7 Conclusion . . . 62
- 2.8 Perspectives . . . 63

3 Experimental determination of the performance of a Scheffler reflector 65
- 3.1 State of the art . . . 66
- 3.2 Materials and methods . . . 68
- 3.3 Results and Discussion . . . 77
- 3.4 Conclusion . . . 86
- 3.5 Perspectives . . . 87

4 General conclusion and perspectives 89
- 4.1 Summary of the work, findings and their implications . . . 89
- 4.2 Future work . . . 90

5 Appendices **94**
5.1 Heat flux estimation with thermocouples 96
5.2 Paint application, absorptance and emmitance measurements 105
5.3 Example of results without crack in the receiver 109
5.4 Summary of data for each experiment 111
5.5 Influential parameters 115
5.6 Open-Source Monte-Carlo-Ray-Tracing Model of realistic Scheffler Collectors 117
5.7 Dynamic thermal behaviour of a solar restaurant housing two Scheffler parabolas 144

Bibliography **155**

Symbols

A_{1-2}	exchange surface area between S_1 and S_2	m^2
A_{abs}	surface area of the receiving screen plate observed by the infrared camera	m^2
A_{ap}	aperture area	m^2
$A_{ap,r}$	aperture area of the reflector	m^2
$A_{ap,r,max}$	ideal aperture area of the reflector	m^2
$A_{ap,w}$	aperture area of the window	m^2
$A_{ap,w,max}$	ideal aperture area of the window	m^2
A_{ef}	effective reflecting surface area of the Scheffler reflector under study	m^2
A_{im}	focal image surface area	m^2
A_l	heat loss surface area	m^2
A_{th}	theoretical surface area of the Scheffler reflector under study	m^2
B	day angle	rad
C	concentration ratio	1
$\overline{C_a}$	average area concentration ratio	1
$\overline{C_f}$	average heat flux concentration ratio	1
COR	cooker opto-thermal ratio	$m^2 \cdot K \cdot W^{-1}$
C_r	heat capacity ratio between the cooker and its load of water	1
f	focal length	m
f_{lim}	limit sampling frequency	Hz
F'	heat exchange efficiency factor	1
F_1	first performance indicator of Mullick *et al.*	$K \cdot m^2 \cdot W^{-1}$
F_2	second performance indicator of Mullick *et al.*	1
h	convective heat exchange coefficient	$W \cdot K^{-1} \cdot m^{-2}$
I_{DH}	solar diffuse horizontal irradiance	$W \cdot m^{-2}$
I_{DN}	solar direct normal irradiance	$W \cdot m^{-2}$
$\overline{I}_{DN}$	average of I_{DN} over a given period	$W \cdot m^{-2}$
I_{GH}	solar global horizontal irradiance	$W \cdot m^{-2}$
$\overline{I}_{GH}$	average of I_{GH} over a given period	$W \cdot m^{-2}$
I_{ref}	reference value for irradiance	$W \cdot m^{-2}$
J	cost function	
$M(x,y,z)$	point with coordinates (x,y,z)	

$m_1 \cdot c_1$	thermal capacity of S_1	$\mathrm{J \cdot K^{-1}}$
$m_2 \cdot c_2$	thermal capacity of S_2	$\mathrm{J \cdot K^{-1}}$
$m \cdot c$	thermal capacity	$\mathrm{J \cdot K^{-1}}$
$m_c \cdot c_c$	heat capacity of the utensil and interior of a given solar cooker	$\mathrm{J \cdot K^{-1}}$
$m_w \cdot c_w$	heat capacity of a given load of water	$\mathrm{J \cdot K^{-1}}$
n	day number in the year	d
$\vec{n}$	normal to the surface	
$\dot{Q}$	useful power	W
$\dot{Q}_{in}$	power collected by the Scheffler reflector	W
$\dot{Q}_{loss,2}$	power lost by S_2 to its environment	W
$\dot{Q}_{out}$	power delivered by the Scheffler reflector	W
$\dot{Q}_{rad,sun}$	power received by S_2 from the sun	W
$\dot{Q}_s$	standardised useful power	W
$\dot{Q}_{s,50}$	standard power for a temperature difference of 50 °C	W
r	correlation coefficient	1
r^2	determination coefficient of a linear regression	1
S_1	system 1	
S_2	system 2	
t_i	initial instant	s
t_{ref}	characteristic time of S_1	s
$T(x,y,z)$	temperature of the receiving screen	K
T_1	temperature of S_1	K
$T_{1,i}$	temperature at the initial instant t_i	K
$T_{1,max}$	maximum temperature that the system can reach in given conditions	K
T_2	temperature of S_2	K
T_a	air temperature	K
T_d	temperature difference between air and water	K
$T_{d,s}$	standardised temperature difference between air and water	K
T_{env}	environment temperature	K
$\overline{T}_{env}$	average of T_{env} over a given period	K
T_p	plate temperature	K
T_{ps}	plate stagnation temperature	K
T_w	water temperature	K
U_{1-2}	heat exchange coefficient between S_1 and S_2	$\mathrm{W \cdot m^{-2} \cdot K^{-1}}$
U_l	heat exchange coefficient	$\mathrm{W \cdot m^{-2} \cdot K^{-1}}$
V_w	wind velocity	$\mathrm{m \cdot s^{-1}}$
$W_{x_1,99.7\%}$	major width of the ellipse containing 99.7% of the heat flux	m
$W_{y_1,99.7\%}$	minor width of the ellipse containing 99.7% of the heat flux	m

(x_c, y_c)	coordinates of the centre C of the Gaussian curve	
Z	zenith angle of the sun	rad
α	absorptivity	1
α_c	absorptivity of cast-iron	1
β	reflector section plane angle	rad
γ	interception factor	1
Γ_1	boundary of the receiving screen exposed to the solar concentrated heat flux	1
Γ_2	boundary of the receiving screen not exposed to the solar concentrated heat flux	1
δ	declination angle of the sun	rad
ΔT_{max}	difference between T_i and T_{max}	K
ε_c	emissivity of cast-iron	1
ε_p	emissivity of paint	1
η	energy efficiency	1
η_1	energy efficiency of S_1	1
η_{cov}	proportion of the collector theoretical area that is effectively covered with a reflective material (coverage factor)	1
η_o	overall optical performance	1
η_{sch}	Scheffler reflector energy performance	1
$\eta_{tr,DN}$	tracking efficiency for direct normal irradiance	1
$\eta_{tr,GN}$	tracking efficiency for global normal irradiance	1
κ	thermal conductivity	$\mathrm{W \cdot K^{-1} \cdot m^{-1}}$
ρ	reflectivity	1
ρ_{spec}	specular reflectivity	1
σ	albedo of the ground or Stefan-Boltzman constant	1
σ_{x1}	standard deviation of the Gaussian curve along $(C, \mathbf{e}_{x1})$	m
σ_{y1}	standard deviation of the Gaussian curve along $(C, \mathbf{e}_{y1})$	m
τ	optical transmittivity	1
τ_{boil}	time needed to reach boiling point	s
$\varphi(x, y)$	incoming concentrated heat flux on the screen	$\mathrm{W \cdot m^{-2}}$
φ_{max}	maximum value of the Gaussian flux distribution	$\mathrm{W \cdot m^{-2}}$
φ_{offset}	heat flux offset of the Gaussian flux distribution	$\mathrm{W \cdot m^{-2}}$
χ	ratio of the temperature difference to the global normal irradiance	$\mathrm{K \cdot m^2 \cdot W^{-1}}$
Ω	receiving screen	
θ	angle between the reference frame and the frame of the Gaussian curve	rad

1 Introduction

In August 2020, the company Le Présage opened Europe's first solar-powered *guinguette* in Marseille, France [45]. Housed in a container, the kitchen is open to the front to serve customers, and is supplied with heat from behind thanks to a 4-metre-high parabolic dish (Figure 1.1).



Figure 1.1 – Le Presage's *solar guinguette*.

Le Présage was created by a group of people from different backgrounds (engineers, chefs, artists, etc.) who shared the desire to set up an innovative, local, sustainable and inspiring project: building a restaurant equipped with a solar cooking system. The first *solar guinguette* was inaugurated in 2020. This "lighter" version of the solar restaurant confirmed the feasibility of the project, but also, and above all, the interest and support of society for this initiative.

The members of the company have decided to build a high environmental quality building to house their business (Figure 1.2). Moreover, this exemplary building will be surrounded by a permaculture environment and is destined to become a meeting place in the neighbourhood. Finally, the project is already part of a genuine local economic ecosystem.

To understand the originality and the novelty of this project, it is necessary to take a step back. While the world's demand for energy continues to rise, the massive extraction and use of depleting fossil resources to meet this need is responsible for many burdens, including climate change. In this context, solar energy appears to be one of the keys to the problem, along with sobriety. Indeed, though being erratic, it is distributed over the Earth's surface, available for free and will never be depleted on a human timescale.



Figure 1.2 – 3D view of the future building housing the restaurant of Le Presage. By SOLARI et Associés. ©2020 CANOPÉE Le Présage. Cropped.

Solar thermal energy is frequently used for small-scale applications, such as the production of domestic hot water, and large-scale applications, such as the production of electricity using a solar power tower. Medium-scale applications, on the other hand, are rare [55]. However, many processes in this area, such as cooking, baking, drying and distillation, use medium-temperature heat and could be decarbonised using concentrated solar power [56].

Solar energy may be free, but solar collectors and conversion systems are not. They often require substantial investment. It is therefore necessary to develop cost-effective and energy-efficient systems for concentrating solar energy to compete with conventional machines powered by fossil fuels. In addition, the constraints associated with the use of solar energy, particularly its intermittency, are significant. Finally, these constraints are associated with social barriers, as the use of solar systems often involves a change in habits and is sometimes seen as an indicator of low social status or low income [59].

By opening a restaurant equipped with a solar cooking system as its main cooking appliance, Le Présage aims to demonstrate the potential of solar energy for professional applications and to promote solar cooking from the top-down. This means that Le Présage members are already convinced of the benefits of using solar energy and are not particularly subject to the social obstacles.

Although Marseille is a fairly sunny city, they have partially adapted their organisation to the intermittent nature of solar energy. When the weather is cloudy or rainy for a short period, they prepare most of the food in advance and cook the rest using electricity. For longer periods, they simply temporary close the restaurant. While this method of organisation is acceptable for the *guinguette solaire* (snack bar), it is too restrictive for the future restaurant. So, to reduce these constraints and make their business model more reproducible in less sunny areas, they are working on two ideas: heat storage (a few hours) and the production of bio-gas from food waste (several weeks or months).

To tackle the problem of the energy performance of their cooking system, they called on the research laboratory IUSTI. This doctoral project therefore focuses on

enhancing the performance of the solar cooking system.

The solar cooking system designed by Le Présage consists of three components: a Scheffler reflector, a curved secondary mirror and a cast-iron plate. It is illustrated in Figure 1.3. Solar energy is first collected by the parabolic "Scheffler" reflector, then concentrated towards the secondary mirror. This reflects the rays back onto the large cast-iron plate that serves as a cook-top for the cook.

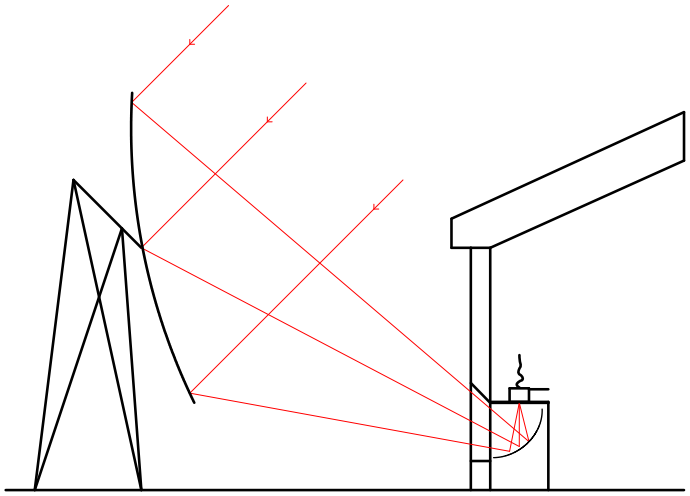

Figure 1.3 – Schematic drawing of Le Présage's solar cooking system.

This configuration is innovative and offers several specific advantages. Firstly, the Scheffler reflector is the only concentrator in existence capable of focusing sunlight on a fixed point all year round with a single reflection and without having to rotate around. Without the Scheffler reflector, concentrating sunlight to a single point throughout the year would require either rotating the reflector in relation to the desired focal point, or using a two-stage concentrator (the first reflector collects the light, the second concentrates it). The Scheffler reflector is unique in that it is a flexible parabola. Unlike a rigid parabola, it can concentrate sunlight into a single point by simply changing its inclination and curvature (see Figure 1.4). Although it is a little more complicated to manufacture, it is very simple to operate and allows indoors cooking (Figure 1.5).

The cook-top is another advantage of the system. As the radiation is concentrated under the middle of the slab, the temperature is higher there and lower on the sides. The cook-top is therefore very similar to a French cook-top (Figure 1.6), which is a well-known cooking appliance appreciated by chefs for its precision, versatility and ergonomics. It allows the cook to use several utensils at the same time and is compatible with most cooking techniques, from simmering (on the sides) to frying (in the centre).

Although the system is already working, it would be interesting to know more about the physical phenomena that take place in it, for the following reasons.

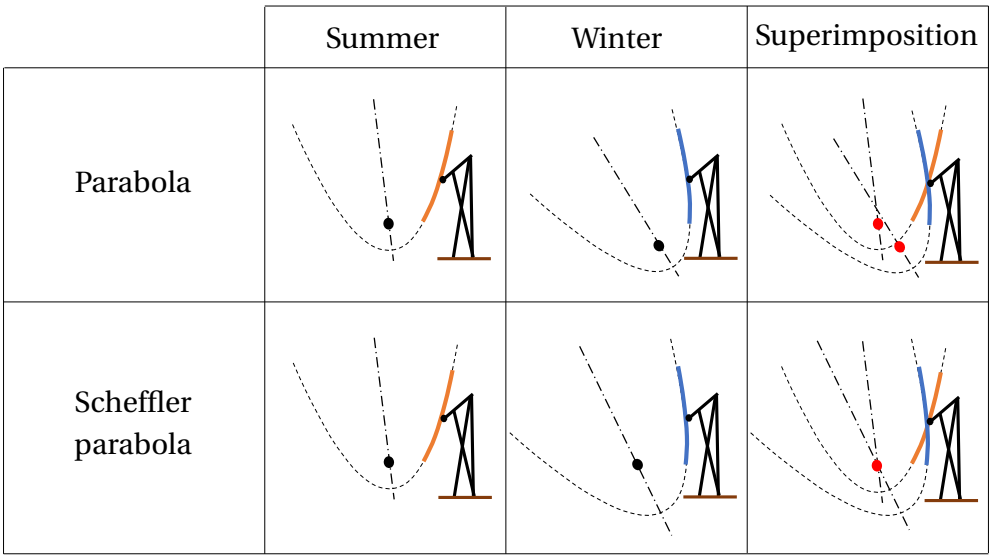

Figure 1.4 – Difference between a rigid parabola and a Scheffler parabola. To concentrate sunlight, the axis of the parabola must be oriented towards the sun. Changing the inclination of a parabola moves the focal point, whereas changing the inclination and curvature of a Scheffler reflector keeps the focal point in the same place.

Firstly, the actual performance of the system is unknown. In fact, this configuration is innovative and unique, and has therefore never been studied. The phenomena are very different from those that occur in a traditional gas french cooktop. They are also different from those that occur in solar cookers which rarely have a cooktop. As a result, there is no mathematical model or detailed experimental data to describe them. It is therefore currently difficult to compare the system with another one, or to say whether the power of the system would meet particular needs. It also makes it difficult to identify opportunities for improvement and thus to optimise the system.

Secondly, the system is made up of complex, hand-crafted components. The Scheffler reflector was invented in the 1980s and spread around the world over the following decades. It has been particularly successful in India; despite this, its manufacture has remained traditional elsewhere and the Scheffler reflector has been little studied, particularly experimentally. Its flexibility can lead to distortions at the focal point, and the secondary reflector cannot be optimised without this knowledge. Moreover, the secondary reflector is also fairly complex to manufacture. Finally, integrating the system into the future Le Présage building requires the system to be adapted to the thickness of the wall (from a few centimetres in the *guinguette* to almost 30 cm in the restaurant), which is not as trivial as it might seem. Identifying the key parameters that make the elements of the system perform, and the precision required to manufacture them, would make it possible to streamline the design and manufacturing processes, improve the fit between its elements and possibly simplify some of them.

Thirdly, detailed knowledge of the system enables results to be predicted under



Figure 1.5 – Egypt's first Scheffler Community Kitchen at El Sherouk Farm near Alexandria [79] by Tom Sponheim CC BY-SA 3.0

given climatic conditions. This is a very important step in adapting the system to the place where it will be used, and in enabling professionals to plan their activity.

This thesis therefore attempts to evaluate the actual energy performance of the system, mainly by experimental means. It focuses on the energy aspect of the problem and does not consider how the system is used.

As Le Présage uses its system for its day-to-day activities, a system similar to that of the *guinguette* was created in the laboratory so that it could be studied independently. Le Présage made things easier by making another Scheffler reflector available to the IUSTI laboratory. However, there are two differences between these systems. In Le Présage's configuration, the Scheffler reflector is covered with a continuous reflective sheet of mirror-polished aluminium and the secondary mirror is curved, whereas in the laboratory's configuration, the Scheffler reflector is covered with small flat glass-coated mirrors and the secondary reflector is flat. This latter difference is a choice justified by the intellectual property covering the curved mirror and the desire to find a simpler technical solution.

Chapter 1: We begin the study by evaluating the overall performance of the system. To do this, we first describe the performance evaluation methods available in the literature. Performance indicators are then derived from an energy balance. An experimental set-up is developed and used in conjunction with a protocol similar to the international standard for testing solar cookers [6]. Finally, the performance values obtained and the limitations of the study are discussed.

Chapter 2: As the Scheffler reflector has not been the subject of many experimental



Figure 1.6 – Gas French cooktop. From [13] ©2021 CBA Advisor. Image taken from the video.

studies, it was the second subject of our attention. Its size, manufacturing quality and flexibility may modify the flux distribution in the focal zone. Knowing the characteristics of this flux distribution is essential for optimising the design of the system's secondary optics and absorber. A test bench and experimental protocol are developed. Thermography and inverse techniques are used to estimate the intensity and distribution of the heat flux delivered by the Scheffler reflector. A regression analysis is also perform to describe the flux distribution with a two-dimensional Gaussian curve. Quantitative criteria are proposed for the design of the secondary optics or absorber.

Conclusion: To end this thesis, a general conclusion is proposed and perspectives of work are given.

Appendices: For ease of reading, some additional information is given in the appendix rather than in the body of the document. Appendix 5.1 presents an experimental method developed prior to that of Chapter 3. Appendices 5.2, 5.3 and 5.5 give details on some aspects of the experimental method, results and discussion in Chapter 3 respectively. Appendix 5.6 presents the ongoing work of my research team on the modelling of Scheffler reflectors, to which I have made a significant contribution. Appendix 5.7 deals with a numerical study on the future building of Le Presage in which the solar cooking system will be included.

2 Overall performance of the solar cooking system

Summary

2.1 Why talking about performance? . . . 30
2.2 How is the performance of solar cooking systems assessed? . . . 30
2.2.1 Talking about performance . . . 30
2.2.2 Mullick's indicators and the Indian standard . . . 31
2.2.3 European Committee for Solar Cooking Research's indicators . . . 35
2.2.4 Funks's indicators and the American standard . . . 35
2.2.5 Other indicators . . . 37
2.3 From energy balance to performance indicators . . . 39
2.3.1 General case . . . 39
2.3.2 Adaptation of the general model for the experimental study of Le Presage's solar cooking system . . . 42
2.3.3 Performance indicators, meaning and limits . . . 46
2.4 Material and methods . . . 49
2.4.1 Test bench . . . 49
2.4.2 Components of the test bench . . . 49
2.4.3 Measuring instruments . . . 51
2.4.4 Experimental protocol . . . 53
2.5 Data processing . . . 53
2.5.1 Measurements averaging . . . 53
2.5.2 Preliminary calculations . . . 54
2.5.3 Temperature regression . . . 55
2.5.4 Efficiency regression . . . 56
2.5.5 Standard power regression . . . 56
2.6 Results and discussion . . . 56
2.6.1 General data . . . 56
2.6.2 Temperature regression analysis . . . 57
2.6.3 Efficiency regression analysis . . . 59
2.6.4 Standard power regression analysis . . . 60
2.6.5 Cooker opto-thermal ratio . . . 61
2.7 Conclusion . . . 62
2.8 Perspectives . . . 63

2.1 Why talking about performance?

The purpose of a solar cooking system is to cook food using solar energy. In the current context of climate change and declining biodiversity, we are seeking to develop the most efficient tools possible. These must meet our needs while consuming as little energy and material resources as possible and having as little impact on our environment as possible. As Duffie wrote: "A good cooker maximises the energy absorbed and minimises heat loss."[22]. In addition, solar cooking systems face strong competition: on the one hand, biomass and fossil fuel cookers are very simple and almost costless (if the resource can be harvested locally), and on the other, gas and electric hobs offer great convenience. Finally, traditional cookers are well known and well integrated into society. Solar cookers, on the other hand, are seen as "new" appliances, requiring people to step out of their comfort zone and accept the risk of change. Nevertheless, comprehensive and reliable information on the use and performance of solar cooking systems can reduce this social barrier. This is why the performance of solar cooking systems needs to be demonstrated and expressed in an understandable way.

This is in this context that we would like to assess the performance of the Le Presage's solar cooking system. Section 2.2 presents the main indicators currently in use and what they represent. In Section 2.3, an energy balance making appear the indicators which will be used in this work is detailed. Sections 2.4, 2.5 and 2.6 detail an experimental evaluation of the performance of a solar cooking system similar to the one of Le Présage, using the indicators previously defined. Finally, Section 2.7 discusses the results and the relevance of the indicators used.

2.2 How is the performance of solar cooking systems assessed?

2.2.1 Talking about performance

Performance is generally expressed using quantitative indicators. But it's not so easy to define good performance indicators. They must accurately represent the specific characteristics of each appliance and enable comparisons to be made between them. To go a step further, a good performance indicator should also be easy to measure, while being able to predict the results of using the appliance in the local conditions of use. Performance definition, assessment and prediction is thus an issue on its own.

The simplest and most basic way of evaluating a cooker is to count the time needed to bring a certain quantity of water contained in a pot from room temperature to boiling point, and then calculate the average power and efficiency [46]. However, the results obtained in this way are performance indicators that are only valid under specific conditions and cannot be compared with those of another system. The results depend not only on uncontrolled weather conditions (*e.g.* solar radiation and air temperature), but also on certain parameters such as the mass of the load, the

number of pots, the frequency of tracking [54], etc. Nor can they be used to predict performance.

This is why, since the 1950s, many researchers have been working on this subject and looking for more advanced performance indicators.

2.2.2 Mullick's indicators and the Indian standard

In 1985, Vaishya *et al.* [83] proposed evaluating box-type solar cookers using an indicator that compares the optical efficiency of the cooker with the quality of its insulation. Two years later, this indicator was taken up by Mullick *et al.* [53]. They called it F_1 and supplemented it with a second indicator called F_2, which represents the quality of heat transfer from the sun to the contents of the cooking pot. Mullick *et al.* proposed to use these two indicators as such, but also to obtain a characteristic curve describing the time required to reach the boiling point as a function of the air temperature and the solar irradiance. The two performance indicators are obtained through "no-load" and "full load" tests respectively.

F_1 is obtained by placing the empty solar cooker under the sun and recording the ambient temperature T_a, the plate temperature T_p (most of the time, there is a black metal plate which ensures radiation absorption at the bottom of solar box cookers) and the global horizontal irradiance I_{GH} until the stagnation temperature T_{ps} is reached. The authors only consider the heat transfer through the window of the box-type solar cooker. At steady state without load, the energy balance of the system is written:

$$\eta_o \cdot I_{GH} = U_l \cdot \left(T_{ps} - T_a\right), \tag{2.1}$$

where η_o represents the overall optical performance and U_l is the overall thermal performance (heat loss factor). Then, the first indicator is defined as:

$$F_1 = \frac{\eta_o}{U_l} = \frac{T_{ps} - T_a}{I_{GH}}. \tag{2.2}$$

A high value of F_1 means a good optical transmission and low overall heat loss factor. According to Mullick' experience, F_1 has a nearly constant value throughout the year.

F_2 is obtained by placing the solar cooker under the sun with a full load of water at room temperature. The ambient temperature T_a, the water temperature T_w and the horizontal irradiance I_{GH} are recorded until the water reached 95 °C. In transient state and with the load, the balance becomes:

$$(m_w \cdot c_w + m_c \cdot c_c) \cdot \frac{dT_w}{dt} = A_{ap} \cdot F' \cdot \left(\eta_o \cdot I_{GH} - U_l \cdot (T_w - T_a)\right), \tag{2.3}$$

where $m_w \cdot c_w$ is the product of the mass of the load of water by its heat capacity, $m_c \cdot c_c$ is the same product for the utensil and interior of the cooker, A_{ap} is the aperture area, and F' is the heat exchange efficiency factor to the content of the vessel. After

integration, the second indicator can be defined as:

$$F_2 = F' \cdot \eta_o \cdot C_r = \frac{F_1 \cdot m_w \cdot c_w}{A \cdot \tau} \cdot \ln\left(\frac{1 - \frac{1}{F_1} \cdot \frac{T_{w1} - T_a}{I_{GH}}}{1 - \frac{1}{F_1} \cdot \frac{T_{w2} - T_a}{I_{GH}}}\right), \tag{2.4}$$

where C_r is the the heat capacity ratio $C_r = \frac{m_w \cdot c_w}{m_w \cdot c_w + m_c \cdot c_c}$, and $\tau = t_2 - t_1$ is the time interval between the measurements of the temperature of the water T_{w1} and T_{w2}.

A high value of F_2 shows a good heat transfer to the content of the vessel (F' is high) and/or a low heat capacity of the interior (C_r is high). This value is independent from the climatic conditions because τ is standardised with the procedure, and all the parameters are known ($m_c \cdot c_c$ is not known, but $m_w \cdot c_w$ is).

Although F_2 should not depend on climatic conditions, it does depend on the pot and the mass of water. This problem is difficult to get round, which is why Mullick *et al.* [53] have proposed to reduce C_r variations by specifying that tests should be carried out with the pot sold with the cooker and "with a 'full load' [of water] as specified (or claimed) by the manufacturer". The authors specified that for the computation of τ, T_{w2} should be taken between 90 and 95 °C to avoid uncertainty due to boiling; and T_{w1} will be taken midway (65 °C) between the ambient temperature and T_{w2} to reduce the range of temperature studied and make true the assumption "heat loss factor is constant". The authors call for a standardising organisation to set these two values.

In the graphical point of view, F_1 and F_2 can be visualised on a graph of the energy efficiency plotted according to the the ratio of the temperature difference to the global horizontal irradiance (Figure 2.1). The efficiency is represented by a linear decreasing function as the thermal losses increase with the temperature difference. On this plot, F_1 is the X-intercept and F_2 is the Y-intercept.

Finally, the characteristic curve of the cooker is plotted as:

$$\tau_{boil} = f\left(\frac{100 - T_a}{I_{GH}}\right) = -\frac{F_1 \cdot m_w \cdot c_w}{F_2 \cdot A_{ap}} \ln\left(1 - \frac{1}{F_1} \cdot \frac{100 - T_a}{I_{GH}}\right). \tag{2.5}$$

The interest of this curve is to allow the cooker user to compute easily the time to boil τ_{boil} according to the local climatic conditions (see Figure 2.2).

The Bureau of Indian Standards has developed a standard based on these indicators, first published in 1992 and revised in 2000 and 2018 [35]. Furthermore, several authors proposed corrections and improvements to the original expression of the equations given above and to the test procedure. None of them have been taken into account in the standard until now.

Originally designed for box-type solar cookers, Mullick *et al.* [52] adapted their own work to concentrating-type solar cookers. In the new procedure, direct normal irradiance is measured instead of global horizontal irradiance, and the "no-load test", which is not feasible in practice with concentrating-type cookers, is replaced by a "cooling test". The latter can be carried out after a "full load test", and involves recording the change in water temperature once the cooker has been turned away

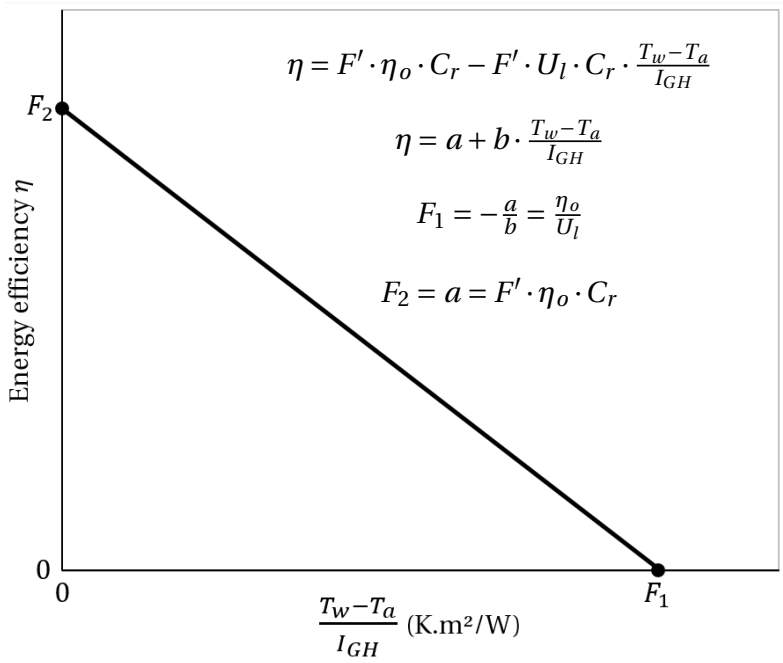

Figure 2.1 – Meaning of the F_1 and F_2 performance indicators of a solar cooker in relation to its energy efficiency. The energy efficiency is plotted according to the ratio of the temperature difference to the global horizontal irradiance.

from the sun (cooling curve). Unlike before, the heat collection surface and the heat loss surface can not be considered to be identical, and their ratio introduces the concentration ratio in the calculations. The indicators $F' \cdot \eta_o$ and $F' \cdot U_l$ (instead of F_1 and F_2) are obtained from the experimental data. These indicators can then be used to calculate the characteristic time of the cooker and to plot its characteristic curve.

De Castell *et al.* [17] proposed several improvements to the procedure of Mullick *et al.* for evaluating box-type solar cookers. Firslty, the latter procedure does not take external reflectors into account. As these mirrors can considerably increase the power of a box-type cooker, De Castell *et al.* fixed this inaccuracy while considering them in the procedure and calculations. Secondly, another test is proposed to assess how long the cooker can be used without being redirected towards the sun. This duration is defined as the time required for the water to fall below 80 °C after the end of the test at full load. Finally, they make a number of improvements to Mullick's work, drawing on Funk's work (see Subsection 2.2.4). In particular, they give values or ranges to the various controlled and uncontrolled parameters in order to standardise the conditions under which solar cookers are tested, and calculate a standard power in addition to F_1 and F_2.

Collares-Pereira *et al.* [14] went one step further in the same direction. They proposed a method to facilitate the measurement of the aperture area inspired from De Castell *et al.* [16]. They also suggested giving standard conditions for constructing a third indicator from the characteristic curve (2.5), which would represent the standard time for bringing water from a reference temperature to the boil.

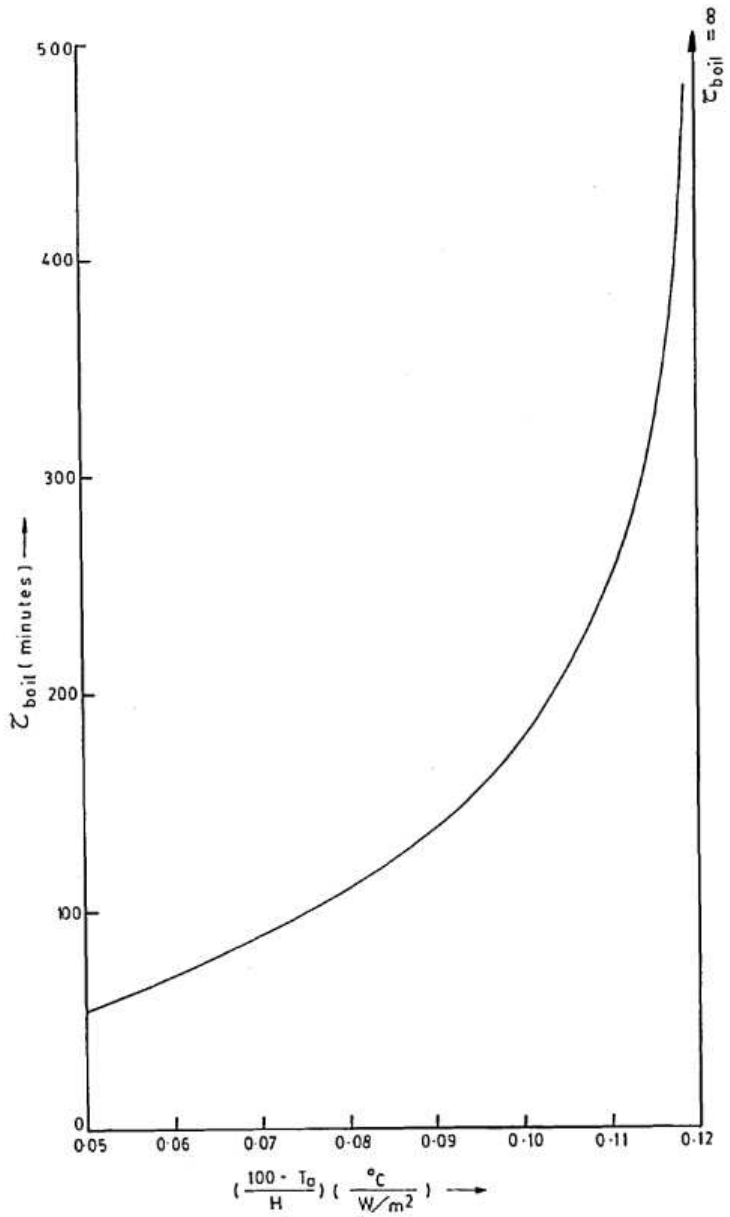

Figure 2.2 – Characteristic curve of a solar cooker. H is the global horizontal irradiance. From [53] by Mullick *et al.* ©1987 Pergamon Journals Ltd.

Lahkar *et al.* [43] took a slightly different approach. They have mathematically derived the expression of a new performance indicator, the "cooker opto-thermal ratio" (COR), from the Hottel-Whillier-Bliss formula. Unlike the F_1 indicator, the COR includes the concentration ratio C: $COR = \frac{\eta_o \cdot C}{U_l}$. The authors chose this indicator because it qualifies the overall performance of the cooker (thermal and optical) and because the maximum temperature achievable in the cooker can easily be calculated from it. Finally, they proposed a procedure for obtaining this indicator, which consists of a single test, identical for box-type and concentrating-type solar cookers.

2.2.3 European Committee for Solar Cooking Research's indicators

The European Committee for Solar Cooking Research (ECSCR) developed its own testing indicators between 1992 and 1994. It adopted a slightly different philosophy than the one of Mullick *et al.*, less technical and rather based on a usage approach [80]. Indeed, the European Committee's standard integrates a comprehensive evaluation of the thermal performance of the cooker with several different tests (with loads of water and oil, with and without tracking, with and without pre-heating, etc.) but only the maximum temperature and the time to reach certain reference temperatures is memorised. Moreover, it gives information on manufacture, safety, ease of use and durability. All information related to one cooker are put together in a single data sheet which can then be provided with the cooker.

Nevertheless, it does not provide any mean to standardise the performance values obtained. The standard is thus useful to compare several cookers which are tested together in the same conditions but of very limited relevance in other cases. Moreover, it seems that the ECSCR stopped its activities at the end of the 1990's without ensuring perennial diffusion of their work. These facts combined may explain why the standard seems having been underused. Indeed, it was used during the test session organised by the ECSCR in 1994 and is mentioned in several reports of the joint project in South Africa of the *Gesellschaft für Technische Zusammenarbeit* (GTZ, Germany) and the Department of Minerals and Energy (DME, South Africa). It is also mentioned in a report of Shaw where he proposes improvements [80]. Despite all of this, Balzar *et al.* [8] and Biermann *et al.* [11] produced the only two scientific papers claiming the use of the standard for the performance assessment of a solar cooker. Other citations of the standard are realised in reviews for bibliographic reference only ([27], [40], [49], [77]).

2.2.4 Funks's indicators and the American standard

Following the work of Funk *et al.* [25], the American Society of Agricultural and Biological Engineers (ASABE) published a standard for testing solar cooker [6] which is used as a reference by the International Organisation for Standardisation (ISO) [36]. This standard contains only one indicator: the standard power $\dot{Q}_{s,50}$. This later is obtained thanks to a "full load test" and corresponds to the power that the cooker

would provide to a given quantity of water under an irradiance of 700 $\mathrm{W \cdot m^{-2}}$ and for a temperature difference of 50 °C between the water and the air.

The American standard is based on a similar energy balance than the second indicator of Mullick *et al.* with the additional assumption that the thermal inertia of the cooker is negligible compared to the one of the load:

$$m_w \cdot c_w \cdot \frac{dT_w}{dt} = A \cdot \left(\eta_o \cdot I_{GH} - U_l \cdot (T_w - T_a)\right). \tag{2.6}$$

The procedure consists of computing the useful power $\dot{Q} = m_w \cdot c_w \cdot \frac{dT_w}{dt}$ regularly during the increase of temperature of the water, standardise it by a global normal solar irradiance of $I_{ref} = 700\ \mathrm{W \cdot m^{-2}}$ as follows:

$$\dot{Q}_s = \dot{Q} \cdot \frac{I_{ref}}{I_{GH}} \tag{2.7}$$

and plot it against the difference of temperature:

$$\dot{Q}_s = f(T_w - T_a). \tag{2.8}$$

Then, a regression analysis with the model:

$$\dot{Q}_s = a + b \cdot (T_w - T_a) \tag{2.9}$$

is performed to estimate the value of the parameters a and b. Finally, the regression function obtained is plotted and its equation is used to calculate the value of the power for a temperature difference of 50 °C:

$$\dot{Q}_{s,50} = \dot{Q}_s(50\ ^\circ\mathrm{C}). \tag{2.10}$$

It is worth noting that Ruivo *et al.* [75] recently pointed out a mistake in this procedure: the regression analysis of the power should be carried out against $T_{d,s} = (T_w - T_a) \cdot \frac{I_{ref}}{I_{GH}}$ instead of $T_d = T_w - T_a$ in order to be mathematically correct. Indeed, the American standard implies:

$$\dot{Q}_s = A \cdot \eta_o \cdot I_{ref} - A \cdot U_l \cdot (T_w - T_a), \tag{2.11}$$

whereas Ruivo *et al.* [75] correct it as:

$$\dot{Q}_s^* = A \cdot \eta_o \cdot I_{ref} - A \cdot U_l \cdot \frac{I_{ref}}{I_{GH}} \cdot (T_w - T_a). \tag{2.12}$$

This mistake particularly affects the estimate of the slope and leads to overestimate the standard power (Figure 2.3).

It is possible to convert the results published before the work of Ruivo *et al.* [75] if I_{GH} variations are small (*i.e.* $I_{GH}(t) \approx \overline{I_{GH}}$). Indeed, a way to get around this mathematical problem is to use the regression function obtained thanks to the procedure of the

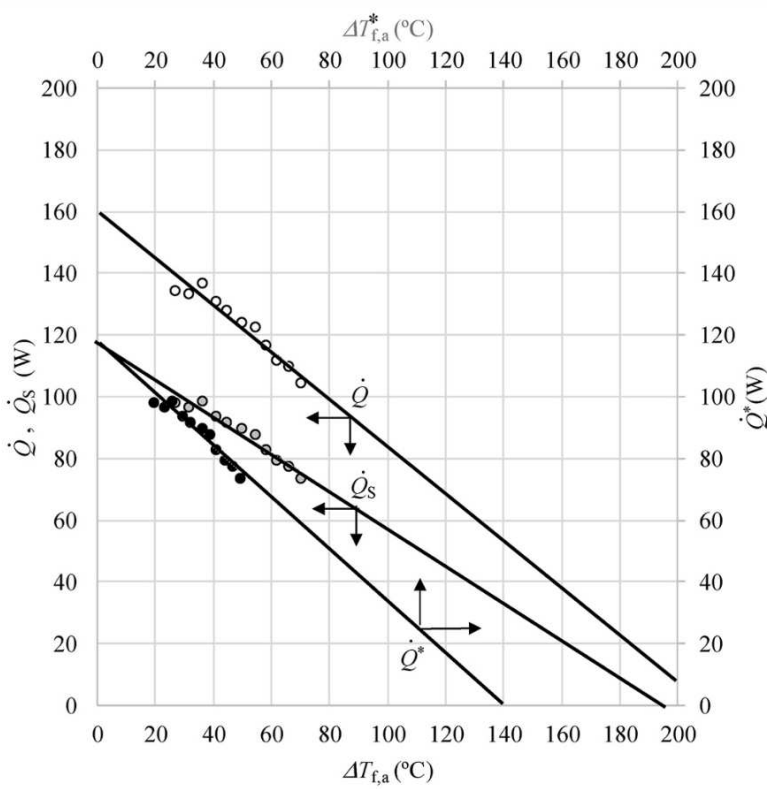

Figure 2.3 – Power $\dot{Q}$, standardised power $\dot{Q}_s$ and Ruivo's corrected standardised power $\dot{Q}^*$. Ruivo's correction has a major impact on the slope obtained by linear regression. From [75] ©2022 Ruivo *et al.* Published by Elsevier Ltd. CC BY 4.0

American standard to calculate the corrected standard power as $\dot{Q}^*_s(50) = \dot{Q}_s(50 \cdot \frac{I_{ref}}{I_{GH}})$. As the standard power is always calculated using the Ruivo correction in what follows, the asterisk will be omitted.

On the one hand, the American standard provides a performance indicator which allows to choose a cooker according to given needs (if utilisation conditions are not far from the standard conditions) and to compare several solar cookers tested in different conditions. On the over hand, this indicator alone is rather meaningless for the characterisation of the energy performance of a cooker: poorer performance can be compensated by a bigger collecting area. For these reasons, authors often show the standard power along with the equation of the regression line or the values of indicators of the Indian standard [35].

2.2.5 Other indicators

Concentrating solar cooking systems use one or several reflectors to collect sun light and reflect it to the absorbing area of the cooker. Reflectors can be characterised by their specular reflectivity, their intercept factor (proportion of the rays reflected

which reach the target) and their concentration ratio. The latter compares the aperture area with the absorption area required by the reflector. This is an important feature, as it may be easier (and more cost-effective) to increase the power of the system by increasing the aperture relative to the absorber area than to reduce the heat loss from the absorber [65].

Rabl [65] has represented indicators for comparing solar concentrators: the concentration ratio, the acceptance angle, the average number of reflections and the ratio of the aperture area to the reflector area. These indicators can be used to qualify any concentrator, but they take on their full meaning when ideal concentrators are studied. The design of ideal reflectors is based on the principles of non-imaging or anidolic optics. While imaging systems attempt to transfer an image from a source to a target, non-imaging systems seek to optimise the transfer of energy only. Non-imaging techniques enable much higher concentration rates and acceptance angles to be achieved. The acceptance angle of a reflector is the maximum angle of incidence of a ray entering the optical system that allows it to reach the target. In other words, any ray arriving within the cone of acceptance reaches the target while the others are rejected (see Figure 2.4). A non-imaging concentrating system can involve multiple reflections. This phenomenon is characterised globally by the average number of reflections. It is preferable to keep this number close to one to limit energy losses due to imperfect reflectivity. A final important performance indicator for non-imaging reflectors is the ratio between the surface area of the aperture and the surface area of the reflector. Non-imaging reflectors often require a large reflector area while the aperture area remains small, which increases the cost of the system. A low ratio is therefore sought. Although Rabl does not talk about solar cooking, his indicators can be applied to the characterisation of solar cooking systems. For instance, a box-type solar cooker without any external reflector will have an acceptance angle close to 90° and will collect all the global horizontal irradiance, whereas a parabolic concentrating-type solar cooker will have an acceptance angle close to 0° and will only collect direct normal irradiance. A solar cooker using a non-imaging reflector will have an intermediate behaviour.

After carrying out an energy analysis, some authors like Ozturk [60] and Petela [62] propose an exergy analysis to find possible losses of energy quality in the whole system. According to Petela, both analyses are complementary as "The energy analysis serves mainly for design purposes, whereas the exergy analysis presents an image of the process quality." [62]. However, this type of analysis is complex and seems difficult to generalise. Furthermore, it goes well beyond the objective of evaluating the overall performance of a solar cooking system, which is why it will not be used in this thesis.

For more information on each indicator or on their evolution and application along the history, see the reviews of Shaw [80], Saxena *et al.* [77] and Gorjian *et al.* [27]. For specific information on exergy analyses, see the work of Kumar [42].

The main performance indicators and assessment methods have been presented with their relative strengths and weaknesses, and a combination of them will be used in the following. Nevertheless, they use different notations and involve different assumptions. For this reason, the following section attempts to sum it all up properly.

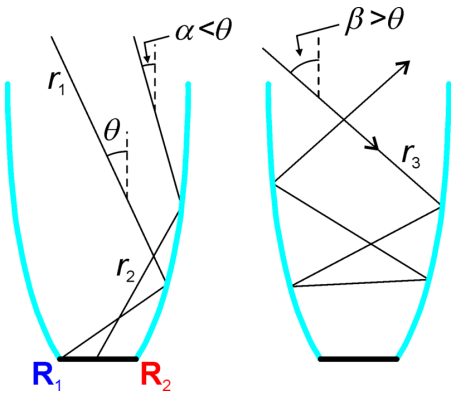

Figure 2.4 – Acceptance angle of a non-imaging concentrator: any ray arriving with an angle of incidence less than the acceptance angle θ is reflected towards the receiver (*e.g.* r_1, r_2), while the others are returned to the ambient after several bounces (*e.g.* r_3). From [57] ©2011 CC BY-SA 3.0

2.3 From energy balance to performance indicators

With today's experimental and numerical resources, it would be possible to describe a given solar cooker and the physical phenomena that take place in it very precisely. However, there is such a wide variety of solar cooker designs that it is not feasible to carry out this type of in-depth study on all of them. This is why the objective of the authors mentioned above and our current objective are different, because we would like to have a model that could approximate the overall performance of all solar cookers, and whose main physical characteristics could be identified using a single, relatively simple experimental procedure. This would make it technically and financially accessible to as many people as possible, and would make it easy to compare solar cookers (even home-made) with each other, whatever the date, location and test conditions.

Starting from an energy balance that is sufficiently general to describe any solar cooking system, and based on the above-mentioned literature, we first aim to define the notations, list and justify all the calculation hypotheses and obtain a general solar cooking system model. This model is then adapted to Le Presage's solar cooking system. Finally, the characteristics are grouped into indicators that can be evaluated experimentally.

2.3.1 General case

Let's model a solar cooking system containing a quantity of food. The cooker and its content are initially at ambient temperature and are exposed to the sun from time t_i. The food is called load and considered as a closed and non-deformable thermodynamic system denoted S_1. Thus, the thermodynamical processes in the system are isochoric. Moreover, we assume that the system is at an homogeneous temperature, and that chemical reactions in the load are neither endothermal nor

exothermal. Then, let's consider that this first system only exchanges heat with a second system S_2 in which it is nested (see Figure 2.5).

During a thermodynamic process, the energy of the system S_1, quantified thanks to its mass m_1, heat capacity c_1 and temperature T_1, varies according to the heat exchanges with the system S_2 at temperature T_2. These heat exchanges are a combination of conductive, convective and radiative heat transfers in series and parallel. Making an energy balance, we obtain:

$$m_1 \cdot c_1 \cdot \frac{dT_1}{dt} = A_{1-2} \cdot U_{1-2} \cdot (T_2 - T_1), \tag{2.13}$$

where U_{1-2} represents the overall heat transfer coefficient (thermal transmittivity) between S_1 and S_2 through the surface A_{1-2}. It approximately corresponds to the heat exchange efficiency factor (F') of Mullick *et al.* [52].

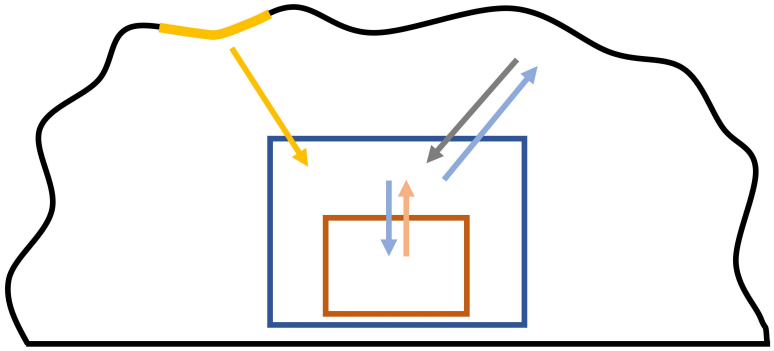

Figure 2.5 – Thermodynamic system. The red square represents the load (water), the blue the cooker, the black line the environment and the yellow the sun.

The second system, S_2, includes the pot and the parts of the cooker which interact with the load. As with the first system, it is described by a mass m_2, heat capacity c_2 and temperature T_2. It is closed too, and exchanges heat with the load and the environment. An energy balance realised on the system S_2 gives:

$$m_2 \cdot c_2 \cdot \frac{dT_2}{dt} = \dot{Q}_{rad,sun} - \dot{Q}_{loss,2} - A_{1-2} \cdot U_{1-2} \cdot (T_2 - T_1). \tag{2.14}$$

Note that unlike the first system, this one is "virtual". It is defined from the point of view of this energy analysis and does not represent exact reality. For example, if considering T_1 as the real temperature of the water is a fairly good approximation (the temperature is approximately homogeneous due to natural convection in the pot), considering the same thing for T_2 is wrong. Instead, the temperature T_2 should be considered as a "representative" temperature of the virtual system S_2, which is used to approximate heat transfers. It is therefore not possible to measure the exact value of T_2. Similarly, the thermal mass of S_2 does not necessarily correspond to the actual thermal mass of the cooker. As the power is stored in the mass of the cooker

by conduction, the smaller are the exchange surface, conductivity, heat capacity and density of the materials, the smaller is the thermal mass of the virtual system S_2.

The system S_2 receives heat from the Sun which is considered as a black body. The radiant flux can be collected directly or after being concentrated by one or several reflectors or both at the same time.

In the first case, the global normal irradiance I_{GN} is collected by the aperture area of the window $A_{ap,w}$. Due to imperfections in the tracking, this aperture may be smaller than the ideal aperture $A_{ap,w,max}$. This phenomenon is modelled by the tracking efficiency $\eta_{tr,GN}$, defined as $A_{ap,w} = \eta_{tr\,GN} \cdot A_{ap,w,max}$ [74]. Then, the collected irradiance goes through the window of optical transmittivity τ and reaches the absorber of absorptivity α. If the system does not include any window, the aperture of the absorber is considered instead, and the transmittivity is omitted.

In the second case, the radiant flux is collected by the aperture area of the reflector $A_{apref} = \eta_{tr,DN} \cdot A_{ap,r,max}$. It is then reflected, process which generally reduces the radiant flux to its direct part I_{DN} due to the low acceptance angle of imaging reflectors. Moreover, due to reflector imperfections, a part of the flux may not reach the target; this is modelled by the interception factor γ. The end of the process is similar to the first case: the radiant flux cross the window (if there is one) and reach the absorber.

In order to keep a general expression, the radiant flux received from the Sun is written as (2.15). The first right term of (2.15) describes the heat flux which crosses the potential window of the cooker and is absorbed. The second right term describes the heat flux which is reflected (ρ) in the right direction (γ) before to cross the window and be absorbed.

$$\dot{Q}_{rad,sun} = A_{ap,w,max} \cdot \eta_{tr,GN} \cdot \tau \cdot \alpha \cdot I_{GN} + A_{ap,r,max} \cdot \eta_{tr,DN} \cdot \rho \cdot \gamma \cdot \tau \cdot \alpha \cdot I_{DN}. \quad (2.15)$$

The system S_2 also exchanges heat with its environment through a combination of conductive, convective and radiative heat transfers in series and parallel. The environment is considered as a black body which temperature T_{env} is homogeneous. We approximate the view factor from the environment to the system to be close to one because the Sun is seen as very small. These heat transfers can be written:

$$\dot{Q}_{loss,2} = A_l \cdot U_l \cdot (T_2 - T_{env}) \quad (2.16)$$

It is worth to specify here that, as the coefficient U_l also represents radiative heat transfers, it depends on T^3. As soon as T_2 is big enough, it can no longer be considered constant and heat transfers between S_2 and the environment can no longer be considered as linear.

The temperatures of S_1 and S_2 are coupled. Combining the equations (2.13), (2.14) ,

(2.15) and (2.16), we can write:

$$\begin{cases} m_1 \cdot c_1 \cdot \frac{dT_1}{dt}(t) = A_{1-2} \cdot U_{1-2} \cdot (T_2(t) - T_1(t)) \\ m_2 \cdot c_2 \cdot \dfrac{dT_2}{dt}(t) = A_{ap,w,max} \cdot \eta_{tr,GN} \cdot \tau \cdot \alpha \cdot I_{GN} \\ \qquad\qquad + A_{ap,ref,max} \cdot \eta_{tr,DN} \cdot \rho \cdot \gamma \cdot \tau \cdot \alpha \cdot I_{DN} \\ \qquad\qquad + A_l \cdot U_l \cdot (T_{env} - T_2(t)) \\ \qquad\qquad + A_{1-2} \cdot U_{1-2} \cdot (T_1(t) - T_2(t)) \\ T_1(t_i) = T_{env} \\ T_2(t_i) = T_{env} \end{cases} \tag{2.17}$$

The time dependence of variables $T_1(t)$ and $T_2(t)$ is shown to emphasise the fact that the other quantities involved can be regarded as (at least approximately) constant during use in good conditions.

This general expression should be valid for most of solar cooking system types and can be easily adapted to take into account the particularity of each of them. As the one of Mullick *et al.* [52], it takes into account the thermal mass of the cooker and the heat exchange coefficient between the cooker and the load. While they can often be neglected, considering them in the energy balance may help to explain and model particular solar cooking systems (*e.g.* indirect solar cookers). It may also help describing the behaviours of certain solar cooking systems at the beginning of the heating phase.

For example, we can confront the model developed above to the experimental data of Ruivo *et al.* [73]. In this article, the authors observed unexpected behaviours when studying a box-type solar cooker and a panel-type solar cooker. On Figure 2.6, both solar cookers have temperature curves with zero slope at the initial instant. This fact is more marked in the data from the box-type solar cooker than in the data from the panel-type solar cooker. Moreover, on Figure 2.7, from $0\,^{\circ}\mathrm{C}\cdot\mathrm{m}^2\cdot\mathrm{W}^{-1}$ to $0.10\,^{\circ}\mathrm{C}\cdot\mathrm{m}^2\cdot\mathrm{W}^{-1}$, the curve of efficiency is far from the linear decreasing trend expected from the model of the ASABE's standard.

The model described by (2.17) is able to explain both of these observations. Indeed, the initial conditions imply that the derivative of the water temperature, the power delivered to the water and the efficiency of the cooker are all zero at the initial instant. Moreover, it is rather intuitive that the more significant is the thermal mass of the cooker compared to the one of the load, and the lower is the thermal transmittivity between S_1 and S_2, the more visible are these effects.

2.3.2 Adaptation of the general model for the experimental study of Le Presage's solar cooking system

A general model describing heat transfers in solar cooking systems has been detailed; we can now adapt it to the specific features of Le Présage's solar cooking system in order to identify the characteristics which can be evaluated experimentally.

In Le Presage's solar cooking system, solar energy is first collected and concentrated

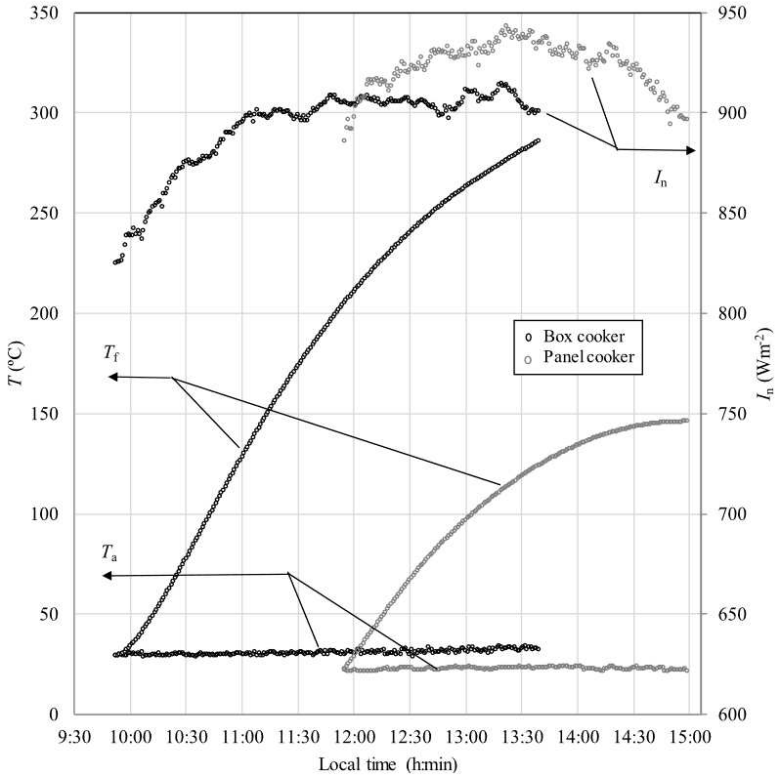

Figure 2.6 – Experimental data from the evaluation of a box-type solar cooker and a panel-type solar cooker. The zero slope of the curve at the initial moment is much more visible in the data from the box-type solar cooker than in the data from the panel-type solar cooker. From [73] ©2022 Ruivo *et al.* Published by Elsevier Ltd. CC BY 4.0

using a Scheffler reflector. This reflector has a small acceptance angle, so only direct normal irradiance is taken into account in the energy balance. The concentrated heat flux is then reflected by a secondary reflector directly to the underside of the cook-top. There are no windows in the actual system. After being absorbed, the heat flux propagates inside the cook-top, towards the pot and finally towards the water. The amount of global normal irradiance received by the pot and the top of the cooking plate is neglected compared to the amount of direct normal irradiance collected by the Scheffler reflector.

By definition, the system S_2 represents the parts of the cooker which interact with the load. In the actual case, it comprises parts of the cook-top and the cooking pot. It is planned to test the cooker with a load of water, which thermal mass is high compared to the assumed thermal mass of the cooker, *i.e.* $m_2 \cdot c_2 << m_1 \cdot c_1$. Moreover, there is a time where the slope of $T_2(t)$ becomes smaller than the slope of $T_1(t)$. From this instant, we can assume that variation of the energy stored in S_2 becomes negligible compared to the variation of the energy stored in S_1 ($m_2 \cdot c_2 \cdot \frac{dT_2}{dt} << m_1 \cdot c_1 \cdot \frac{dT_1}{dt}$).

On the same interval, we may also assume that the temperature of both systems are

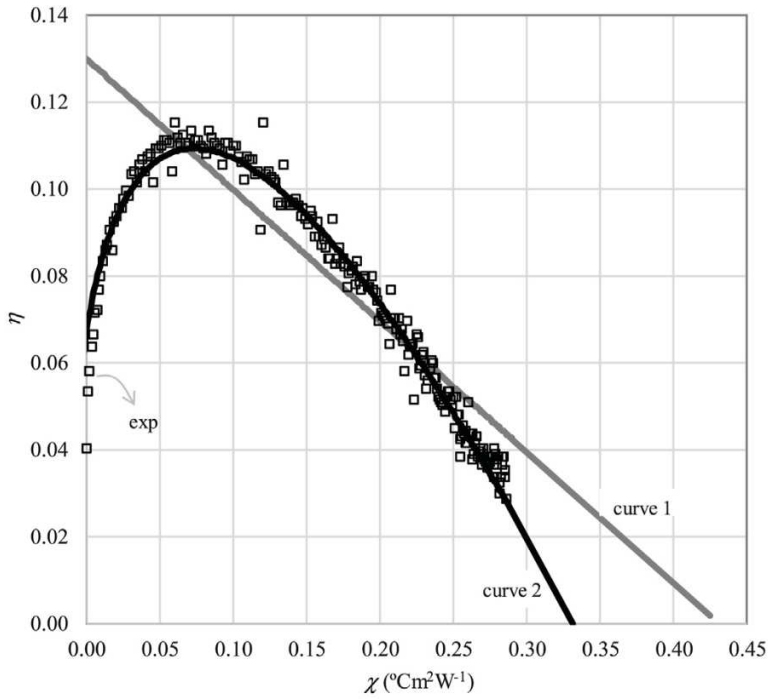

Figure 2.7 – Efficiency curve of a box-type solar cooker and two regression functions. The experimental efficiency of the box-type solar cooker is very low at the initial instant. From [73] ©2022 Ruivo *et al.* Published by Elsevier Ltd. CC BY 4.0

close ($T_2 \approx T_1$). This implies that the heat transfer coefficient between both systems is high (which is a sought-after characteristic). This hypothesis is more uncertain and may lead to overestimate the coefficient of thermal losses. Nevertheless, it enables us to obtain an energy balance similar as in the ASABE standard. The validity of these hypotheses are discussed more in details with the experimental results.

With these hypotheses, if T_1, T_{env} and I_{DN} evolution are recorded according to time and m_1, c_1 and $A_{ap,r,max}$ are known, we can rewrite (2.17) as:

$$m_1 \cdot c_1 \cdot \frac{dT_1}{dt}(t) \approx A_{ap,r,max} \cdot \eta_o \cdot I_{DN} + A_l \cdot U_l \cdot (T_{env} - T_1(t)), \tag{2.18}$$

where η_o is the overall optical efficiency $\eta_o = \eta_{tr,DN} \cdot \rho_r \cdot \gamma_r \cdot \rho_r \cdot \gamma_r \cdot \alpha$. Thus, the overall optical efficiency η_o and the heat loss product $A_l \cdot U_l$ are the unknowns of this equation.

According to Ruivo *et al.* [73], assuming that the direct normal irradiance and the temperature of the environment do not vary much relatively to their mean over the experiment ($I_{DN}(t) \approx \overline{I_{DN}}$ and $T_{env}(t) \approx \overline{T_{env}}$), this equation is a linear ordinary

differential equation of first order and its solution can be written as:

$$T_1(t) = \left(T_{1,max} - T_{1,i}\right) \cdot \left(1 - \exp\left(-\frac{t - t_i}{t_{ref}}\right)\right) + T_{1,i}, \tag{2.19}$$

where:

- $T_{1,max} = \overline{T_{env}} + \frac{A_{ap,r,max} \cdot \eta_o}{A_l \cdot U_l} \cdot \overline{I_{DN}}$ is the maximum temperature that the system can reach in the local conditions,
- $T_{1,i}$ is the initial temperature of the load at the initial instant t_i,
- and $t_{ref} = \frac{m_1 \cdot c_1}{A_l \cdot U_l}$ is the characteristic time of the system.

By examining the expression of the maximum temperature, we can define the quantity $C = \frac{A_{ap,r,max}}{A_l}$ as a sort of concentration ratio which compares the maximum aperture to the total loss area of the cooker. This then allows us to recognise the opto-thermal ratio $COR = \frac{\eta_o \cdot C}{U_l}$ as defined by Lahkar *et al.* [43] (also called F_1 by Mullick *et al.*).

As explained in Section 2.2, whereas Mullick's experimental procedure is based on only two measurements, Funk's one is based on a regression and takes into account all the data. The later would therefore better represent the experimental data and is adopted here. Thus, a regression on the temperature evolution according to time with the function above allows to directly find the values of $T_{1,max}$ and t_{ref}. With this knowledge, it is then possible to find the value of the thermal conductance, the total optical efficiency and the cooker opto-thermal ratio. The fit could also be done on the evolution of the power according to time or the efficiency according to time but there is really no point.

Another way to access the characteristics of the solar cooking system is to write the energy balance (2.18) as an energy efficiency. This method has the advantage of taking into account small variations of irradiance and ambient temperature, but requires the global normal irradiance I_{GN} to be measured. The equation obtained is:

$$\frac{m_1 \cdot c_1 \cdot \frac{dT_1}{dt}(t)}{A_{ap,r,max} \cdot I_{GN}(t)} \approx \eta_o \cdot \frac{I_{DN}(t)}{I_{GN}(t)} + \frac{U_l}{C} \cdot \left(\frac{T_{env}(t) - T_1(t)}{I_{GN}(t)}\right). \tag{2.20}$$

With η_1 the energy efficiency and χ the ratio of the temperature difference to the global normal irradiance, this gives:

$$\eta_1(\chi) \approx \eta_o \cdot \frac{I_{DN}}{I_{GN}} + \frac{U_l}{C} \cdot \chi. \tag{2.21}$$

When performing the fit, the derivative of the temperature $\frac{dT_1}{dt}$ can be either approximated by a finite difference or using the analytical derivative of (2.19) as proposed by Ruivo *et al.* [73]. The first method is good if the data sampling frequency is high compare to the limit sampling frequency ($f_{lim} = 2 \cdot \frac{1}{t_{ref}}$) according to Nyquist-Shannon theorem. If not, the second method should be preferred. In this case, note that only

the central part of the heating phase should be taken into account for the fit. Indeed, some assumptions made to obtain the fit model are not true at the beginning and end of the heating phase.

In order to calculate the standard power (as corrected by Ruivo *et al.*), we can rewrite (2.18) as:

$$m_1 \cdot c_1 \cdot \frac{dT_1}{dt}(t) \cdot \frac{I_{ref}}{I_{GN}(t)} \approx A_{ap,r,max} \cdot \eta_o \cdot \frac{I_{DN}(t)}{I_{GN}(t)} \cdot I_{ref} + A_l \cdot U_l \cdot (T_{env}(t) - T_1(t)) \cdot \frac{I_{ref}}{I_{GN}(t)}, \tag{2.22}$$

or:

$$\dot{Q}_{1,s}(T_{d,s}) \approx A_{ap,r,max} \cdot \eta_o \cdot \frac{I_{DN}}{I_{GN}} \cdot I_{ref} + A_l \cdot U_l \cdot T_{d,s}. \tag{2.23}$$

From here, we have two options. We can proceed in the same way as before with the energy efficiency, *i.e.* use the experimental data to calculate $\dot{Q}_{1,s}$ and $T_{d,s}$, then fit these data to the model to obtain the values of the parameters, and finally calculate the standard power $\dot{Q}_{1,s}(50\,^{\circ}\mathrm{C})$. Alternatively, the values of the aperture, the reference irradiance and the parameters estimated in the previous analysis can be used directly to calculate $\dot{Q}_{1,s}(50\,^{\circ}\mathrm{C})$.

It is interesting to note that the efficiency of concentrating-type solar cookers at ambient temperature is generally limited by more factors than the one of box-type solar cookers (without "booster mirrors"). Indeed, the optical efficiency of concentrating-type solar cookers is limited by the reflectivity and the interception factor of its reflector. This limitation can become particularly strong if there are multiple reflections. But there is also a limitation due to the ratio of direct irradiance to global irradiance $\frac{I_{DN}}{I_{GN}}$. As these limitations are offset by a larger aperture, a compromise has to be found between using high-performance materials, and using a greater quantity of materials to increase the size of the reflectors. At higher temperatures, this handicap can be overcome thanks to the advantages of concentration. Given the same aperture, concentrating-type cookers can have smaller absorption area and thus lower heat losses than box-type cookers.

Another comment can be made on the ratio $\frac{I_{DN}}{I_{GN}}$: while the ASABE standard gives a standardisation value for the global normal irradiance, it does not provide any mean to standardise the direct normal irradiance. This means that the same concentrating solar cooker could be tested under the same global normal irradiance and give different standard powers ratings, since the direct normal irradiance is not the same. The easiest way around this problem is to give an interval for the direct normal irradiance, *e.g.* between 75 % and 95 % of the global normal irradiance.

2.3.3 Performance indicators, meaning and limits

Most of the intrinsic characteristics that could describe a solar cooker have been defined when the energy balance was drawn up. Subsequently, only those modelling Le Presage's solar cooking system have been retained. However, the objective is not to assess the value of each of these characteristics using specific measurements, but

rather to assess the overall performance of the cooker with the simplest possible procedure, similar to that defined by the ASABE.

In the considered procedure, the uncontrolled variables T_1, T_{env}, I_{DN}, I_{GN} and V_w (wind velocity) are recorded according to time, the controlled variable m_1 is chosen arbitrarily (rather high compare to the expected value of m_2), and c_1 and $A_{ap,r,max}$ are known. These measurements give us access to the temperature, power and efficiency. Their graphical representation are only useful to the trained eye of specialists and are difficult to standardise, particularly with respect of the wind velocity and thermal mass of the fluid. Thus, these plots are not convenient for sharing and comparison.

This is why combinations of characteristics that can be assessed using these measurements have been identified. They are summarised in Table 2.1. Those that are more or less independent of local conditions can then be used to identify the qualities and weaknesses of the solar cooker, to compare it with others and to predict its behaviour in given conditions.

The cooker's time constant is the time required to raise the temperature of a given load by 63 % of the maximum difference of temperature ($\Delta T_{1,max} = T_{1\,max} - T_{env}$) reachable by the solar cooker. However, this quantity is not very practical because it is only valid for a given mass. It may be more convenient for the user to have the specific time constant (*i.e.* the time required per kilogram of water), so that it can be compared with other cookers and the heating time can be calculated as a function of the mass of the load (assuming that the load has a heat capacity close to that of water). From the designer point of view, the lower the specific characteristic time, the better insulation of the cooker. From the user point of view, the lower the specific characteristic time, the faster the cooker heats food.

Similarly, the maximum temperature that the cooker can reach depends on the temperature of the environment and normal direct irradiation. It is therefore more useful to have the cooker's opto-thermal ratio, which can be used to calculate the maximum temperature under local conditions. This presupposes access to local values of environment temperature and direct normal irradiance. In terms of performance, the higher the opto-thermal ratio, the higher the maximum temperature. It is thus a good indicator for the designer as for the user and a particular attention will be put on this indicator in the following. While the opto-thermal ratio provides information on the relative value of two quantities, the thermal conductance and the total optical efficiency provide information on the absolute value of insulation quality and the optical efficiency respectively. As such, they are good indicators for the designer, but rather meaningless for the user. It should be noted that the higher is the value of U_l, the more sensitive it is to wind velocity.

Finally, the standard power gives the user a reference for the power supplied by the system. However, this value is given under arbitrary environmental conditions and with an arbitrary mass of fluid. It can therefore be used as one of several comparison criteria, but not as an absolute selection criterion.

Note that the value of the concentration ratio can not be determined through this procedure since the value of A_l is not known independently from U_l.

Also note that, according to the hypotheses made to derive indicators from the

Table 2.1 – List of indicators.

Name	Expression
Temperature regression model	$T_1(t) = \left(T_{1,max} - T_{1,i}\right) \cdot \left(1 - \exp(-\frac{t-t_i}{t_{ref}})\right) + T_{1,i}$
Temperature regression parameters	
Characteristic time constant, t_{ref} (s)	$t_{ref} = \frac{m_1 \cdot c_1}{A_l \cdot U_l}$
Maximum temperature, $T_{1,max}$ (K)	$T_{1,max} = \overline{T_{env}} + \frac{\eta_o \cdot C}{U_l} \cdot \overline{I_{DN}}$
Derived from the regression parameters	
Specific time constant, $t_{ref,m}$ ($\mathrm{s \cdot kg^{-1}}$)	$t_{ref,m} = \frac{t_{ref}}{m_1}$
Thermal conductance, $A_l \cdot U_l$ ($\mathrm{W \cdot K^{-1}}$)	$A_l \cdot U_l = \frac{m_1 \cdot c_1}{t_{ref}}$
Total optical efficiency, η_o	$\eta_o = COR \cdot \frac{A_l \cdot U_l}{A_{ap,r,max}}$
Opto-thermal ratio, COR ($\mathrm{m^2 \cdot K \cdot W^{-1}}$)	$COR = \frac{T_{1,max} - \overline{T_{env}}}{\overline{I_{DN}}}$
Efficiency regression model	$\eta_1(\chi) \approx a + b \cdot \chi$
Efficiency regression parameters	
Y-intercept, a	$a = \eta_o \cdot \frac{I_{DN}}{I_{GN}}$
Slope, b ($\mathrm{W \cdot m^{-2} \cdot K^{-1}}$)	$b = \frac{U_l}{C}$
Derived from the regression parameters	
Specific time constant, $t_{ref,m}$ ($\mathrm{s \cdot kg^{-1}}$)	$t_{ref,m} = \frac{c_1}{A_l \cdot U_l}$
Thermal conductance, $A_l \cdot U_l$ ($\mathrm{W \cdot K^{-1}}$)	$A_l \cdot U_l = b \cdot A_{ap,r,max}$
Total optical efficiency, η_o	$\eta_o = a \cdot \frac{I_{GN}}{I_{DN}}$
Opto-thermal ratio, COR ($\mathrm{m^2 \cdot K \cdot W^{-1}}$)	$COR = \frac{a}{b} \cdot \frac{I_{GN}}{I_{DN}}$
Standardised power regression model (according to Ruivo *et al.*)	$\dot{Q}_{1,s}(T_{d,s}) \approx a' + b' \cdot T_{d,s}$
Standardised power regression parameters	
Y-intercept, a' (W)	$a' = A_{ap,r,max} \cdot \eta_o \cdot \frac{I_{DN}}{I_{GN}} \cdot I_{ref}$
Slope, b' ($\mathrm{W^2 \cdot K^{-1} \cdot m^{-2}}$)	$b' = A_l \cdot U_l$
Derived from the regression parameters	
Standard power, $\dot{Q}_{1,s,50}$ (W)	$\dot{Q}_{1,s,50} = a' + b' \cdot 50$

The Y-intercept of the efficiency curve a is similar to F_2 in the formulation of Mullick *et al.* [53]. The cooker opto-thermal ratio COR is similar to F_1 in the formulation of Mullick *et al.* [53].

energy balance (2.17), their expression can vary. For example, according to the mass of the load, the mass of the cooker may not be negligible. One could assume that $\frac{dT_1}{dt} \approx \frac{dT_2}{dt}$ and $T_1 \approx T_2$, then the efficiency expression would be:

$$\eta_1(\chi) \approx C_r \cdot \eta_o \cdot \frac{I_{DN}}{I_{GN}} + C_r \cdot \frac{U_l}{C} \cdot \chi. \tag{2.24}$$

The heat capacity ratio C_r is defined in the same way as by Mullick *et al.* [53], as follows: $C_r = \frac{m_1 \cdot c_1}{m_1 \cdot c_1 + m_2 \cdot c_2}$. As the virtual thermal mass of the cooker would not be known, the

thermal conductance and the total optical efficiency could not be estimated; only the opto-thermal ratio could be derived. It is thus important to estimate the thermal mass of the cooker.

More generally, a great number of hypotheses were formulated and a deeper work could be realised on the behaviours of the solar cooker outside of the validity range of these hypotheses, notably at the beginning and at the end of the heating phase (which would require to evaluate the thermal mass of the cooker). The steady state phase and the cooling phase were not raised here but they could be used to check the results obtained during the heating phase. Also, a "full load test with a preheated cooker" and a "nearly non load test" could be carried out to assess the thermal mass of the cooker. Nevertheless, this is let outside of the scope of this thesis.

The performance indicators being defined, they can now be used for the performance assessment of a reproduction of Le Presage's cooker.

2.4 Material and methods

The aim of this section is to evaluate the overall performance of the cooking system, while providing an initial estimate of its characteristics using the procedures and indicators given previously. An earlier version of this work was the subject of a communication at the international conference for solar cooking and food processing CONSOLFOOD [28]. With a little hindsight, this estimate can be seen as a benchmark against which potential improvements can be identified, and to which the performance of future prototypes can be compared.

2.4.1 Test bench

In the context of this study, an experimental bench similar to Le Présage's cooker has been built. It is shown on Figure 2.8. It consists of a Scheffler reflector equipped with an automatic sun-tracking system, a flat secondary reflector, a cast-iron slab and a cooking pot.

2.4.2 Components of the test bench

The Scheffler reflector used has a focal length f of about 1.47 m and a theoretical surface area A_{th} of 8 m^2 (same characteristics as the one described by Munir [55]). It is mounted on a trailer to ease its displacement. The surface area is composed of hundreds of flat mirrors of 8 cm x 10 cm and 2.5 cm x 15 cm, made of a thin reflective sheet covered by a layer of glass. As the reflector under study was built in 1999, it has been renovated several times. After our first measurement (17/12/2021), we renovated it ourselves, replacing the damaged mirrors with new ones.

The mirrors do not cover the complete surface of the reflector due to missing ones, spacing between themselves, the elliptical shape of the reflector and the small photovoltaic module used to power the sun tracking system. Thus, the effective

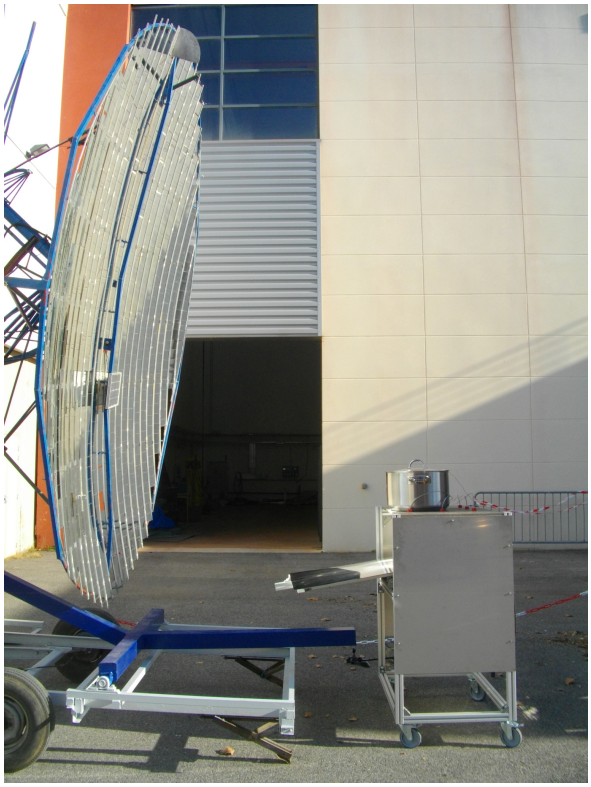

Figure 2.8 – Picture of the test bench. It consists of an 8 m^2 Scheffler reflector equipped with an automatic sun-tracking system, a flat secondary reflector, a cast-iron slab, and a 30 L cooking pot.

reflecting surface area A_{ef} was estimated to 5.9 $m^2 \pm 0.3$ m^2 before renovation and is estimated to 7.5 $m^2 \pm 0.3$ m^2 after renovation. The area loss between theoretical and effective reflective area can be expressed as a coverage factor η_{cov}, whose value is 74 % and 94 % respectively, and which specifies the proportion of the collector theoretical area that is effectively covered with a reflective material.

Another consequence of the successive partial renovations is that the mirrors covering the reflector are not all of the same quality. Thanks to measurements, the global reflectivity ρ of the reflector has been estimated to 80 % ± 5 %.

The reflector is also equipped with an electronic sun tracking device. It consists of two photodiodes separated by a wall and connected to an electronic board (Arduino Uno) that controls a small motor. The device ensures the sun tracking by rotating the reflector until both photodiodes receive a similar amount of sunlight.

The system was tested with a flat secondary mirror, rather than a curved reflector as in Le Presage's cooker, because it is easier to manufacture and theoretically performs just as well. It is also closer to a "low-tech" approach. This mirror is 0.85 m long and 0.70 m wide, and is made from mirror-polished aluminium.

Two cast iron cooking plates were used successively in the test bench because a crack appeared on the first during an experiment and led to its replacement. Both

slabs are made of lamellar graphite cast-iron (JL200), and are 1 m long and 0.6 m high. However, the first was 13 mm thick whereas the second one is 15 mm thick. The secondary mirror and the cooking plate are mounted on a trolley to ease their displacement.

The cooking pot has a diameter of 40.0 cm, a height of 24.5 cm and a volume capacity of 30.7 L. Its bottom is 10 mm thick. The pot and its lid are made of stainless steel 18/10 and weighs 7.33 kg and 0.82 kg respectively.

2.4.3 Measuring instruments

Assessing the performance of the system requires to monitor the heat flux it collects, the heat flux it delivers and the environmental conditions. In order to situate this system in relation to the literature, the main guidelines of the test protocol defined by the ASABE standard [6] are followed.

The heat flux collected by the system is the product of the aperture A_{ap} by the global normal irradiance I_{GN}. The latter can be calculated from the global horizontal irradiance I_{GH} and the direct normal irradiance I_{DN}. The solar global horizontal irradiance is measured using a Kipp & Zonen SMP10-A pyranometer and the the direct normal irradiance is measured using a Kipp & Zonen SHP1-A pyrheliometer. The two measuring devices are mounted on the same RaZON+ base from Kipp & Zonen (see Figure 2.9) and their measurements are recorded every minutes by a common data logger. Their response time is less than 2 s and the measurement uncertainty is estimated at 2 %.



Figure 2.9 – Pyrheliometer and pyranometer mounted on their base.

The calculation of the heat flux delivered by the system (to the water in the pot) requires measuring the mass of water put into the cooking pot and the change in water temperature as a function of time.

According to the standard, 7 kg of water per m^2 of aperture are required. In our case, it means using from 30 kg to 50 kg of water according to the aperture! However, the studied system is not as energy-efficient as a solar box cooker and such a mass of water would require more time than is available. That is why a lower mass has been arbitrarily chosen. The mass of water is measured with an electronic scale Soehnle Professional 7755.

The temperature is measured with ungrounded type K thermocouples with a 1.5 mm diameter 310 stainless steel sheath. According to the manufacturer, the sensor response time (63.2 %) is 0.3 s. As seen previously, in the case studied, the cook-top acts as an internal heat storage: a part of the power captured by the system can be absorbed by the plate and released later. For this reason, several supplementary sensors are placed on the cook-top to measure its surface temperature (Figure 2.10). This makes it possible to consider qualitatively the energy stored or released by the cast iron slab. Ideally, the cook-top should have a constant temperature throughout the experiment: this would mean that all the power is transferred to the water. The sensors used are grounded type K thermocouples spring-loaded with a magnet. According to the manufacturer, the response time (63.2 %) of these sensors is 30 s. The temperature are recorded thanks to the multichannel Lutron BTM4208sd data logger at a frequency of 1 Hz. This data logger is placed in an insulated box to protect it from direct sunlight and air temperature change.



Figure 2.10 – Locations of temperature sensors on a picture (left) and on a top view diagram (right).

Air temperature measurement uses the same type of sensor and data logger as water temperature measurement. The sensor is placed in an open but shaded area, as air must circulate freely around the sensor, but the sensor must not be exposed to sunlight.

The horizontal wind speed is measured near the test bench at a frequency of 1 Hz with a Davis 7911 cup anemometer (Figure 2.11) connected to an electronic board (Arduino Uno). The board itself is connected to a computer on which the data is recorded using a small programme written in Python.



Figure 2.11 – Davis 7911 cup anemometer.

2.4.4 Experimental protocol

The experimental protocol begins with setting up the system in a place exposed to the sun and without any shadows to interfere with the experiment. Then the Scheffler reflector is briefly turned towards the sun to establish its curvature. It is eased by a flat black vertical target placed at the focal point. Once this is done, the trolley supporting the secondary reflector and the cook-top is set up and all measuring devices are started. There are then two possibilities: either the pot is immediately placed on the cook-top, or the pot is placed on the cook-top after preheating. In both cases, the Scheffler reflector is turned again towards the sun and the sun tracking system is activated. When the water temperature reaches 95 °C or stabilises at a lower temperature, the reflector is turned away from the sun. Finally, every recording is stopped after a few minutes.

2.5 Data processing

2.5.1 Measurements averaging

The temperature of the water in the pan is an analogical continuous-time signal whose recording involves sampling and quantification. According to Nyquist-Shannon theorem, the sampling frequency must be at least twice as high as the highest frequency in the signal being sampled to avoid aliasing. Oversampling consists of choosing a sampling frequency much higher than this limit. This technique makes possible to improve the resolution and to reduce the noise on the signal by averaging it. This preliminary step is particularly useful when the signal needs to be amplified and/or derived. In preliminary experiments, we estimated the characteristic time of the sys-

tem to be several hours, when tested with 20 kg to 25 kg of water. This means that if environmental conditions remain stable, no rapid change in system temperature is expected. In the most restrictive case, the characteristic time would be around one hour, and the data logger sampling frequency (1 Hz) would then be 1800 times greater than the sampling limit frequency ($2 \cdot 1/3600$). There is therefore a significant margin for applying a moving average to the signal.

As the standard recommends taking a measurement at least every ten minutes, we positioned ourselves at the limit by calculating a moving average over a centred window of 10 min. As the results were good, the processing method was applied to water temperature signal for all the experiments. In this way, the resolution of the data logger is artificially improved from 0.1 °C to 0.000 17 °C ($0.1/600$), which is useful for the power calculation.

According to the World Meteorological Organization [1], air temperature, wind velocity and solar irradiance must also be averaged, each according to its physical characteristics. Air temperature is averaged over a centred window of 1 min. Wind is averaged over a centred window of 3 s (characteristic time of a wind gust). Average values of direct normal irradiance and global horizontal irradiance are recorded every minutes by the data logger. To obtain values for each instant (as for the other signals), the signals are interpolated using the "next" method, then averaged over a centred window of 1 min.

The averages and standard deviations on the studied periods are calculated from the smoothed signals.

2.5.2 Preliminary calculations

While the temperature is already known, the energy efficiency and the standardised power must be calculated in order to carry out the regression analyses. The global normal irradiance I_{GN} is required to calculate both of them.

The global normal irradiance I_{GN} is the sum of the direct normal irradiance (first term in Equation (2.25)), the diffuse normal irradiance (second term) and the reflected normal irradiance due to the ground (third term):

$$I_{GN} = I_{DN} + \left(\frac{1}{2} + \frac{1}{2} \cdot \cos Z\right) \cdot I_{DH} + \left(\frac{1}{2} - \frac{1}{2} \cdot \cos Z\right) \cdot \sigma \cdot I_{GH}. \tag{2.25}$$

The first term is directly obtained from measurement. The second can be calculated from the sun's zenith angle Z and the diffuse horizontal irradiance I_{DH}; the diffuse horizontal irradiance being itself calculated from the global horizontal irradiance I_{GH}, the direct normal irradiance I_{DN} and the azimuth angle Z as:

$$I_{DH} = I_{GH} - I_{DN} \cdot \cos Z. \tag{2.26}$$

The third term is obtained from the sun's zenith angle Z, the global horizontal irradiance I_{GH} and the albedo of the ground σ. As the ground is covered with asphalt, its albedo is assumed to be 0.1.

The efficiency of the solar cooking system is calculated as described by (2.20). With the derivative approximated by a finite difference, this gives:

$$\eta(t) = \frac{m_1 \cdot c_1 \cdot \frac{T(t+\delta t)-T(t)}{\delta t}}{A_{ap,r,max} \cdot I_{GN}(t)}, \tag{2.27}$$

where the period δt is equal to 1 s as the acquisition frequency of the temperature is 1 Hz, and the heat capacity of water is taken as 4186 $\mathrm{J \cdot kg^{-1} \cdot K^{-1}}$. The ideal aperture $A_{ap,max}$ is calculated from the theoretical area of the reflector A_{th}, its coverage factor η_{cov}, the angle of the parabola section plane β [55], and the declination angle δ:

$$A_{ap,max} = A_{th} \cdot \eta_{cov} \cdot \cos(\beta + \frac{\delta}{2}). \tag{2.28}$$

The declination angle and the section plane angle are expressed in rad. The declination is calculated as indicated by Spencer (1971) in the form adapted by Kalogirou [38]:

$$\begin{aligned} \delta = {} & 0.006918 \\ & - 0.399912 \cdot cos(B) + 0.070257 \cdot sin(B) \\ & - 0.006758 \cdot cos(2 \cdot B) + 0.000907 \cdot sin(2 \cdot B) \\ & - 0.002697 \cdot cos(3 \cdot B) + 0.00148 \cdot sin(3 \cdot B) \end{aligned} \tag{2.29}$$

where the "day angle" B on day number n is $B = \frac{2 \cdot \pi \cdot (n-1)}{365}$.

The standard power is calculated according to the standard [6]:

$$\dot{Q}_s(t) = m \cdot c \cdot \frac{T(t+\delta t) - T(t)}{\delta t} \cdot \frac{I_{ref}}{I_{GN}(t)}, \tag{2.30}$$

with a reference irradiance I_{ref} of 700 $\mathrm{W \cdot m^{-2}}$.

2.5.3 Temperature regression

The temperature evolution of the system can be described as the one of a first order system, except at the beginning of the heating phase and at its end, as it has been mentioned in Section 2.3. For the beginning, this is because the cooker's own thermal inertia is neglected. For the end, water evaporation is neglected and radiation emitted from the system to the environment is linearised. For these reasons, the analysis is realised for all measurements from 40 min after the pot began to be heated, to the time where the temperature reaches 80 °C. On this range, a regression analysis can be realised against the regression model:

$$T(t) = \Delta T_{max} \cdot \left(1 - \exp\left(-\frac{t - t_i}{t_{ref}}\right)\right) + T_i, \tag{2.31}$$

where ΔT_{max}, t_i and t_{ref} are the unknown parameters, t is the independent variable, $T(t)$ is the dependent variable and T_i is a problem parameter which value corresponds to the initial temperature of the water. The initial instant t_i is given in relation to the start of the analysis range. As a consequence, it is a negative number. The regression analysis is carried out on the software MATLAB thanks to the non linear least squares method. The same "options" (start point, upper and lower bounds, maximum evaluation number, etc.) are used for all analyses.

2.5.4 Efficiency regression

The energy efficiency regression analysis is carried out against the following regression model:

$$\eta(\chi) = a + b \cdot \chi, \tag{2.32}$$

where a and b are the unknown parameters, χ is the independent variable and $\eta(\chi)$ is the dependent variable. The linear regression analysis is carried out on the software MATLAB.

The determination coefficient, noted as r^2, is obtained with the linear regression. Here, this coefficient qualifies the proportion of the variation of the standard power predictable from the temperature difference. The determination coefficient tends towards 1 if the prediction is perfect, and towards 0 if the prediction is not possible at all.

2.5.5 Standard power regression

The standard power regression analysis is carried out while following the recommendation of Ruivo *et al.* [75], *i.e.* against the regression model:

$$\dot{Q}_s\left(T_{d,s}\right) = a + b \cdot T_{d,s}, \tag{2.33}$$

where a and b are the unknown parameters, $T_{d,s}$ is the independent variable and $\dot{Q}_s\left(T_{d,s}\right)$ is the dependent variable. The linear regression analysis is carried out on the software MATLAB.

2.6 Results and discussion

2.6.1 General data

Three experiments were carried out in Marseille, France (lon. 5.4374° E, lat. 43.3449° N, alt. 120 m), on 17 December 2021, 18 July 2022 and 22 July 2022. The characteristics of these three tests are given in Table 2.2 and their environmental conditions are presented in Table 2.3. Although the aperture variation between winter and summer is usually close to 50 %, it is lower here because the parabola was renovated and the reflective area increased between the first and the two following measurements. In

order to assess the system in "usage" conditions, the last test was carried out after preheating. In each section, the results of the first experiment are described in details, then the results of all experiments are compared.

Table 2.2 – Information on the experiments.

Exp.	Date	Day n	Declination δ (°)	Aperture A_{ap} (m^2)	Load m (kg)	Preheating (min)
1	17/12/2021	351	−22.79	5.0	22.0	0
2	18/07/2022	199	21.43	4.4	25.0	0
3	22/07/2022	203	20.70	4.5	25.0	46

Table 2.3 – Mean and standard deviation ($k = 1$) of the environmental variables during the selected period.

Date	Air temp. T_a (°C)	Wind velocity V_w ($m \cdot s^{-1}$)	GNI[a] I_{GN} ($W \cdot m^{-2}$)	DNI[b] I_{DN} ($W \cdot m^{-2}$)
17/12/2021	16.3 (0.6)	very low	1074 (17)	785 (17)
18/07/2022	34.2 (0.7)	0.6 (0.6)	903 (9)	734 (9)
22/07/2022	34.7 (0.7)	0.8 (0.6)	969 (6)	822 (6)

[a] GNI is the abbreviation for global normal irradiance
[b] DNI is the abbreviation for direct normal irradiance

2.6.2 Temperature regression analysis

Figure 2.12 shows the temperature evolution observed and its regression function for the first experiment. On the range studied, we observe that the latter fits the first very well. The residuals are signed but their value is negligible compared to the variations observed. An unexpected failure in the tracking system happened: it stopped from 12:10 to 12:20 approximately. But its seems that the system was not much affected by this failure since no temperature fall is observed in the water. This shows that the method can work even with imperfect experiments. Finally, the coefficient of determination is very close to one, showing a statistical validation of the regression model. Nevertheless, the regression function does not stick to the experimental data outside of the range studied (extrapolation). It highlights the fact that the regression model is not valid outside the validity range of its assumptions. Thus, despite the very good suitability between the experimental data and the estimated function, the values of the estimated parameters must be taken with care.

Indeed, the confrontation of the results of the three experiments evidences great variations (Table 2.4). The second experiment was carried out with a lower aperture, a slightly thicker cooking top, a higher mass of water, at a higher air temperature and

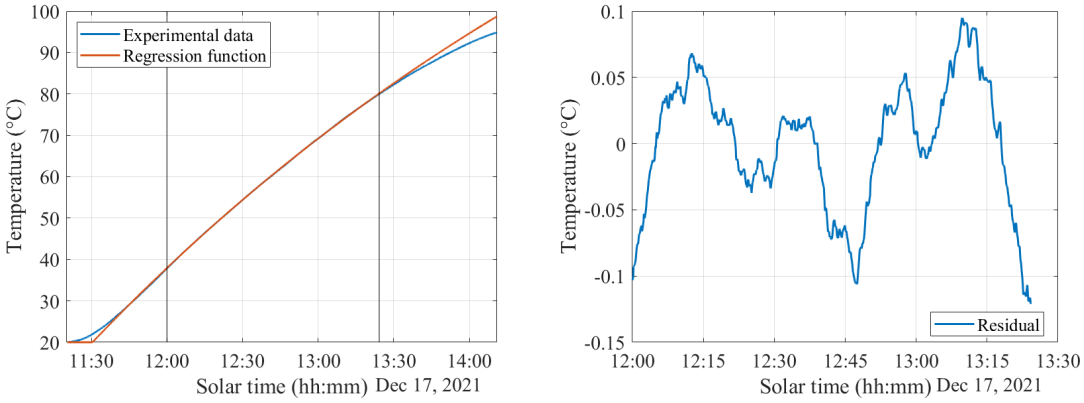

(a) (b)

Figure 2.12 – Regression analysis of the temperature for the experiment on 17 December 2021. Temperature evolution and its regression function (a), and the residual (b). The model is fitted to the experimental data between the two vertical lines visible on (a).

with a higher wind velocity (qualitative estimate made by the experimenter) than the first. Experiments 2 and 3 were carried out in very similar conditions but differ with preheating.

Table 2.4 – Estimated parameters of the regression function for temperature.

Date	ΔT_{max} (°C)	t_i (s)	t_{ref} (s)	T_i[a] (°C)	Correlation coef. r
17/12/2021	185	-1.7725e+3	1.7396e+4	20	1.000
18/07/2022	56	-1.5786e+3	5.6912e+3	29	0.999
22/07/2022	75	-2.1386e+3	8.4015e+3	31	0.999

[a] The initial temperature is a problem parameter of the regression, it is not estimated but rather fixed according to the experimental data of each experiment.

The values of the maximum temperature difference and the characteristic time are not compared here because they are compared later, using the values of the opto-thermal ratio and the specific characteristic time respectively.

Nevertheless, we can note from a user point of view that the system offers very variable characteristics. The value of the maximum temperature difference of the first experiment is high enough to enable grilling food, whereas cooking is at the limit to be possible with the maximum temperature difference of the second experiment.

Moreover, we can see in experiments 1 and 2 that the initial instant is predicted with a delay of 10 min and 14 min respectively compared to the experiment start. This delay is reduced to 4 min for Experiment 3 thanks to preheating.

2.6.3 Efficiency regression analysis

Figure 2.13 shows the efficiency as a function of $\chi = (T_w - T_a)/I_{GN}$, its regression function and the residuals, through the selected range for the first experiment. The experimental points clearly show a trend but with a significant dispersion around it. As the residuals are randomly distributed around the x-axis, they are probably due to measurement noise, which is amplified by the calculation of the power despite the averaging described in Section 2.5.4. On closer inspection, we observe a small drop from 0.025 °C·m^2·W^{-1} to 0.035 °C·m^2·W^{-1} approximately. It could be due to the failure of the sun-tracking system, in spite of its short duration. The noise and this failure explain the rather low determination coefficient of the linear regression (see Table 2.5), although there is a good match between the experimental data and the regression function.

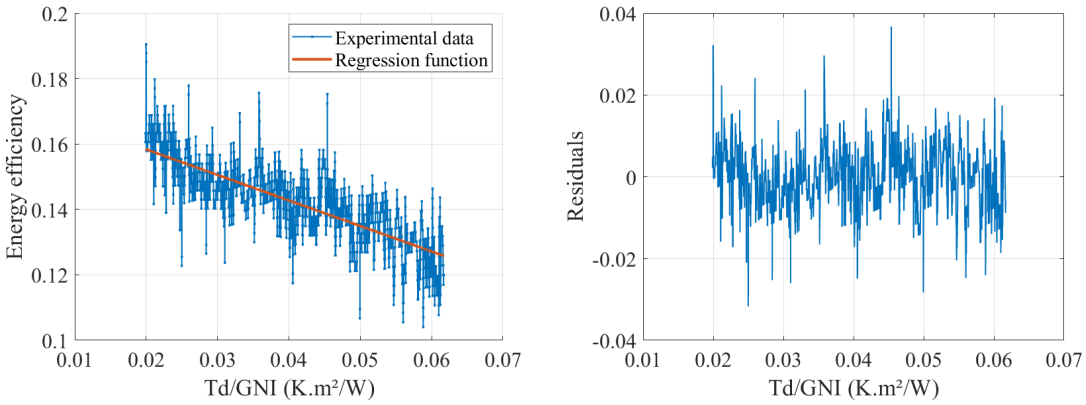

Figure 2.13 – Regression analysis of the efficiency for the experiment on 17 December 2021. Efficiency evolution and its regression function (a), and the residual (b).

The comparison between the different experiments shows similar values for the intercept and great variations for the slope. The intercept of Experiment 2 is 29 % greater than the one of Experiment 1. It can be explained qualitatively. Indeed, we know that between experiments 1 and 2:

- the Scheffler reflector has been cleaned,
- and the ratio of direct normal irradiance over global normal irradiance has increased (11 %).

These two facts would respectively increase the coefficients η_o and I_{DN}/I_{GN} in Equation 2.21 and may explain the global increase between experiments 1 and 2.

The estimated y-intercepts of experiments 2 and 3 are closer: the second is only 5 % lower than the first. This is a good point, as they were carried out in very similar conditions. In addition, it would reinforce the hypothesis that the effect of the preheating occurs mainly in the first tens of minutes, which are excluded from the studied period.

Indeed, a heat transfer supplied from the cook-top to the water would rather imply an increase of the y-intercept of Experiment 3 compared with Experiment 2.

Table 2.5 – Estimated parameters for the regression of the efficiency according to χ

Date	Y-intercept	Slope	Determination coef. r^2
17/12/2021	0.17	-0.8	0.60
18/07/2022	0.22	-3.8	0.94
22/07/2022	0.21	-2.8	0.85

In the same way as for the intercept, we can carry out a qualitative analysis for the slope. The wind velocity would be greater for experiments 2 and 3 than for Experiment 1, involving a higher value of transmittance U_l. Assuming to have the same heat loss surface for all experiments, the aperture reduction (−12 %) would decrease the concentration ratio C. As a global result, the slope coefficient would increase in absolute value.

While the difference between experiments 1 and 2 can be qualitatively explained thanks to identified physical phenomena, it is more difficult for the difference between experiments 2 and 3. In the same way than the previous analysis, the preheating does not seem to impact Experiment 3 inside the selected period. As the concentration ratio vary only a little, the quantity which should be the main responsible for this difference is the thermal transmittivity U_l. It would be risky to go any further without additional information, but it can be concluded that, due to the lack of insulation, the U_l is very sensitive to the environment conditions.

2.6.4 Standard power regression analysis

As the mathematical expressions of the standard power and the efficiency are close, their results are visually similar. Thus, the evaluation of the goodness of fit of the standard power for Experiment 1 (Figure 2.14) repeats elements mentioned for the efficiency. Indeed, the experimental points also clearly show a trend with a significant dispersion around the trend line. This is quantified by the determination coefficient r^2, whose value is at the limit defined by the standard ($r^2_{min} = 0.75$). We can also see the small drop due to the sun-tracking system failure.

The effect of the standardisation following the ASABE standard or Ruivo *et al.* recommendation are shown on Figure 2.14b with the experimental data of the Experiment 1. Whereas the ASABE standardisation greatly affects the slope, the Ruivo standardisation tends to keep the slope of the original curve. In the present case, the solar irradiance slowly decreases throughout the experiment, but if it would not, the original and the Ruivo curves would have exactly the same slope.

The results of the regression analyses and the standard power for the three experiments are shown in Table 2.6. We can see that the standard power for a temperature difference of 50 °C varies greatly according to the experiment. While the system

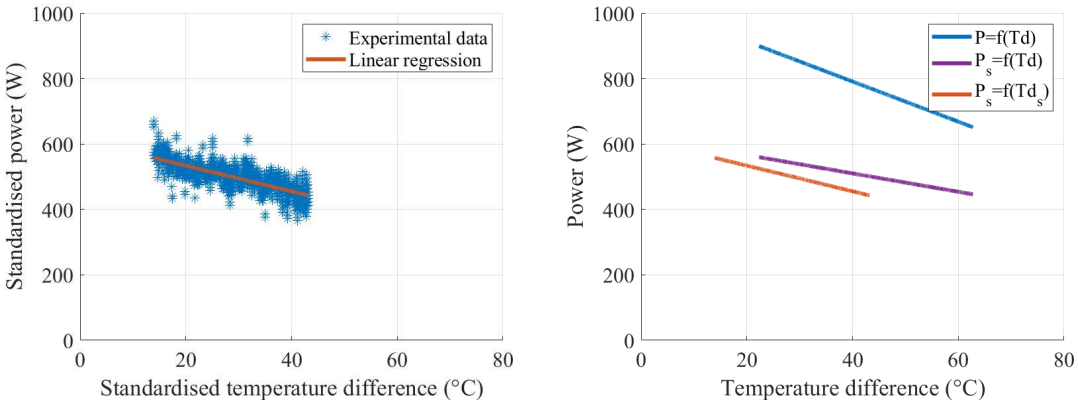

(a) (b)

Figure 2.14 – Regression analysis on the standardised power for the experiment on 17 December 2021. Power evolution and its regression function (a), and power, standardised power, Ruivo's corrected standardised power (b).

provided a power of 416 W in the first experiment, it is close to zero for the third experiment, meaning that the solar cooking system manages to heat the water 50 °C higher than the ambient temperature, but hardly more. The solar power collected by the system is just enough to compensate the heat losses. It is even negative for the second experiment, meaning that the cooker cannot reach this temperature difference under an irradiance of 700 $W \cdot m^{-2}$. A supplementary power of 169 W would be required to reach it.

Table 2.6 – Estimated parameters for the regression of the standard power and standard power for 50 °C difference.

Date	Y-intercept	Slope	Determination coef. r^2	$\dot{Q}_{s,50}$
17/12/2021	612	-3.9	0.75	416
18/07/2022	671	-16.8	0.93	-169
22/07/2022	643	-12.7	0.85	10

2.6.5 Cooker opto-thermal ratio

As explained in Section 2.3, the cooker opto-thermal ratio is a performance indicator that can be calculated from experimental data, either from the temperature or the efficiency regression analysis. The results are shown in Table 2.7.

In the case of each experiment, we can see that the calculation based on the efficiency regression gives a close but systematically smaller result than the one of the temperature regression, *i.e.* −8 %, −25 % and −22 % respectively. We can also note that the opto-thermal ratio of Experiment 1 is approximately three times greater than

Table 2.7 – Cooker opto-thermal ratio (COR) obtained from regression analyses on the temperature and energy efficiency.

Date	COR	
	Regression on temperature	Regression on efficiency
	$(m^2 \cdot K \cdot W^{-1})$	
17/12/2021	0.24	0.22
18/07/2022	0.08	0.06
22/07/2022	0.09	0.07

the two other experiments. To justify it, we can put forward the same explanations as for the efficiency.

2.7 Conclusion

In this work, a cooker similar to the one used by the restaurant Le Présage and consisting of a Scheffler-type reflector, a flat secondary reflector and a cast-iron cooking top, is studied.

First, the different existing ways to model and assess the performance of solar cookers are explored. A summary of these approaches is produced and applied to the cooker studied, while mentioning all the underlying assumptions. Performance indicators are identified and their usefulness is discussed. Then, a test bench is designed and experimental methods are described. Finally, three experiments are carried out and their results are detailed.

Several important conclusions can be drawn from this work. Firstly, several physical models and assessment methods co-exist in the literature due to the great variety of solar cooker designs and to available measurement equipment. Nevertheless, the use of regression analysis is preferred compared to methods based on only two data points. It also appears necessary to measure or at least estimate the direct normal irradiance for the performance evaluation of concentrating cookers.

Secondly, a model such as the one defined by the ASABE implies important assumptions. These later must be kept in mind during the analysis of the experimental data, especially when selecting the interval on which is carried out the regression analyses. Indeed, the beginning and the end of the heating phase can not be described by this kind of model. Deriving the performance indicators from a personalised energy balance would be a good way to highlight these hypotheses and to obtain a representative expression of the performance indicators for each cooker.

Thirdly, the specific characteristic time and the opto-thermal ratio are two important performance indicators for the designer as for the user as they answer to the questions:

- What is the maximum temperature that the cooker is able to reach in given climatic conditions?

- How long does it take to heat a given mass of water from the ambient temperature to this maximum temperature?

The optical efficiency and thermal conductance are useful for in-depth performance analysis. The corrected standard power can be calculated as an additional data.

Fourthly, the main guidelines of the experimental procedure of the ASABE's standard are respected. Nevertheless, the mass of water is smaller than recommended due to practical reasons. Regression analyses are carried out on the temperature of water, on the energy efficiency and on the standardised power. The two first allow a double check of the parameters estimated. The thermal mass and the concentration ratio can not be evaluated with this procedure.

Finally, the physical model accompanied with the experimental procedure allowed to approximately estimate the performance indicators. Despite great variations are observed on some indicators between experiments, they can be explained qualitatively. With a total optical efficiency between 21 % and 22 % (renovated reflector), there is a large potential for improvement on this aspect. At low temperature, the system is able to deliver a rather high power anyway (between 600 W and 700 W of standardised power) thanks to its great aperture. However, the power falls as the temperature of water increases, especially abruptly if it is windy. This is due to the absence of any insulation and the wide loss area linked to the usage of a cook-top. Indeed, the cook-top is an intrinsically inefficient system on the point of view from the thermodynamic, but it is an interface which is really appreciated by restaurant chefs because it allows them to cook precisely and for a lot of customers. Associated with seasonal variation of aperture, this makes the opto-thermal ratio vary even more (from 0.06 $m^2 \cdot K \cdot W^{-1}$ to 0.22 $m^2 \cdot K \cdot W^{-1}$). The standard power also reflects these facts.

2.8 Perspectives

In this section, prospects for the future are outlined.

While Mullick's experimental procedure is outdated, its performance indicators are still actual. The heat transfer efficiency F' (which approximately correspond to $A_{12} \cdot U_{12}$) and the heat mass C_r can not be estimated properly with the current model and experimental procedure. They are although important since the characteristic time of the cooker and the heat losses depend on it. The general model developed in this thesis is an attempt to make appear these indicators (which are usually neglected) and to better describe the time where their influence is not negligible, *i.e.* at the beginning of the heating phase.

On the topic of the performance indicators, the concentration ratio could not be identified. The others have been roughly estimated, although they showed a variability according to the climatic conditions. Note however that the optical efficiency of concentrating-type solar cookers depends on the ratio $\frac{I_{DN}}{I_{GN}}$, which is not standardised. Moreover, several indicators depend on the aperture which varies throughout the year. Finally, some other important indicators have not been evaluated at all, as the required tracking frequency for example.

The fluid, its mass, the number of containers, their thermal characteristics, geometry and filling rate: all these parameters play a role in the performance of solar cookers. And no perfect solution has been found until now. The ASABE's standard recommends to use an arbitrary mass of 7 kg of water per square metre of aperture, evenly distributed between the cooking vessels supplied with the cooker. Moreover, the cooker should be tested under conditions close to the conditions of use.

Firstly, using water has a lot of advantages, but it does not allow to test correctly concentrating-type solar cooker which can reach higher temperatures than the boil. Secondly, the mass is not adapted since concentrating-type cookers often have a large aperture but also a generally lower efficiency than box-type solar cookers. This leads to very long experiments, when they are possible. Finally, the standard states that the cooker should be tested under conditions close to the conditions of use. But the way to use a French cook-top varies from one restaurant to another, thus the "normal conditions of use" give only a few information on the utensils to use. By covering the whole cooking top with several pots instead of only one, the performance would be better.

In the same way, the recommended measurement frequency is not adapted to all solar cookers. The mass of water and the measurement frequency could maybe be set from the experiment duration (two hours from 11:00 to 13:00) using the specific characteristic time of the cooker studied. This however implies to carry out preliminary measurements.

Finally, the question of the preheating is not treated: should the test start with a receiver at the ambient temperature, or should the slab be in a steady-state regime before putting the pot on the top of it?

Thus, there is no doubt that the current standards need to be revised, but many questions remain to be answered before a new standard can be published.

In real conditions, the performance of Le Presage's solar cooking system are expected to be higher, as the cook-top is used inside a building and the system would be thus less sensible to wind. Nevertheless, optical losses have to be reduced and the problem of combining the flat secondary reflector with the Scheffler reflector must be resolved. To this end, non-imaging optics could be useful. It also means that thermal losses should be reduced. Some ideas like adding a window, using selective paint, or focusing the light on a smaller area, would reduce losses on the underside. For the top, it is more complicated since we need to keep an interface compatible with the kitchen but using a low-emissivity finish could reduce radiation losses.

In order to provide more detail on the performance of the system, its components can be studied separately. While the heating plate and the mirror are simple elements, the Scheffler reflector is rather complex and deserves a closer look.

3 Experimental determination of the performance of a Scheffler reflector

Summary

3.1 State of the art . . . 66
3.1.1 Theoretical and numerical studies . . . 66
3.1.2 Experimental studies on systems including a Scheffler reflector 66
3.1.3 Experimental studies on the heat flux distribution . . . 67
3.1.4 Novelty of this work . . . 68
3.2 Materials and methods . . . 68
3.2.1 Main principles . . . 68
3.2.2 Object under study and measuring instruments . . . 69
3.2.3 Experimental protocol . . . 69
3.2.4 Heat flux collected . . . 72
3.2.5 Heat flux delivered estimated by inverse method . . . 72
3.2.6 Heat flux distribution . . . 75
3.2.7 Variables of interest . . . 76
3.3 Results and Discussion . . . 77
3.3.1 First results and observations . . . 77
3.3.2 Experimental temperature field . . . 78
3.3.3 Experimental heat flux intensity and distribution . . . 78
3.3.4 Heat flux distribution . . . 81
3.3.5 Measurement repeatability and evolution with time . . . 84
3.4 Conclusion . . . 86
3.5 Perspectives . . . 87

As explained in the introduction, the curvature of Scheffler reflectors needs to be regularly adjusted to take advantage of its great benefit: concentrating sunlight to the same location throughout the year. However, mechanical stresses and manual adjustments could prevent the reflectors from achieving an exact parabolic shape and lead to distortions in the heat flux delivered. As a result, these distortions could affect the performance of absorbers and any secondary optical systems. Recent work has explored theoretically and numerically the heat flux intensity and distribution provided by Scheffler reflectors, however the characteristics of this heat flux have been little investigated experimentally. This chapter therefore proposes to explore this subject in greater depth. It consists in an extended and improved version the work published by Gabriel *et al.* [29].

3.1 State of the art

3.1.1 Theoretical and numerical studies

Since Scheffler reflectors have been introduced in the scientific literature [58], their geometric characteristics have been studied [55], and more recently, charts have been realised to facilitate their fabrication [68].

Most studies on the Scheffler reflector are theoretical and numerical works that derive from geometry. Often, they assume that the contour of the heat flux distribution has an elliptical shape. For example, Dib and Fiorelli [19] studied the theoretical size of the area receiving heat flux at the focus of a standing reflector having an aperture area of 1 m^2 at equinox. They showed that this ellipse area is larger in summer than in winter due to optical imperfections, the tilt of the reflector and the declination of the sun. Reddy and Khan obtained more accurate information on the heat flux distribution thanks to ray-tracing simulations. They were thus able to study the effect of some adjusting parameters, *i.e.* the mirrors' size and the tracking delay [67]. Fontani *et al.* [24] also brought information on dispersion caused when bending the reflector, combining mechanical simulation and ray-tracing analysis.

Nevertheless, theoretical and numerical studies have produced highly variable results, as little is known about the actual characteristics of Scheffler reflectors (which are closely related to the hand-crafted manufacturing process).

3.1.2 Experimental studies on systems including a Scheffler reflector

Oelher and Scheffler [58] reported that their 8 m^2 reflector, having an aperture of 4.7 m^2 at the date of the measurement, could deliver 2.1 kW at the focus on a 0.6 m diameter area. This leads to an energy efficiency of 60 % and a concentration ratio of 16.6. This is an important first data set, however it does not give details on the heat flux distribution on the absorber.

Other studies have given the overall energy efficiency of a Scheffler reflector combined with an absorber, often referred to as "optical efficiency". One can cite Ayub *et al* [7] and Kanyowa *et al* [39], who measured respectively optical efficiencies of 37 % to 65 %, and 70 % to 80 %. However, this does not give any information about the Scheffler reflector alone, nor about the heat flux distribution at the focus.

Ayub *et al.* [7] measured energy and exergy efficiencies on an experimental baking oven powered by a 10 m^2 Scheffler reflector. They studied the global system, the reflector and absorber together, and the oven, using calorimetric techniques while baking cakes at 180 °C (transient state). Kanyowa *et al.* [39] studied a bigger system constituted of 14 pairs of 10 m^2 Scheffler reflectors which provides steam to feed a kitchen serving 2000 to 6000 meals per day. Calorimetric measurements were carried out on one pair of reflectors and its absorber while assuming steady-state. The authors mentioned the reflectivity of the mirrors but the overall efficiency of the reflector cannot be deduced from this.

3.1.3 Experimental studies on the heat flux distribution

Alberti [2] further investigated the intensity and distribution of heat flux in the focal zone. He observed that the light focused by a 2 m^2 reflector was contained in a 15 cm square and stated that most of the energy would certainly be contained in a 5 cm square. An image of the heat flux distribution at the focus is provided (using moonlight instead of sunlight), but not enough methodology is presented to conclude quantitatively on the performance of the reflector used. Finally, in their description of a marmalade factory, Pulfer *et al.* [64] mentioned that the diameter of the "focus area" generated by the 4.5 m^2 Scheffler collector is approximately 0.4 m which is again only an order of magnitude.

Sasidharan and Dutta [76] attempted to bring more details. They measured the heat flux in the focal area of a 32 m^2 reflector with 5 fluxmeters. Then, they built a 3D numerical model of the Scheffler reflector and refined the experimental data by ray-tracing. As a result, a random heat flux distribution was obtained on the focal plane and the total heat flux hitting the target was estimated to 860 W. According to them, the difference between the theory and their results can be explained by the integration of ray spillage and reflector surface characteristics in the simulation.

Accurate evaluations are rare, probably because evaluating the distribution of concentrated sunlight in the focal area is not a trivial task. It requires a detection system with a wide field of view, high spatial resolution and high heat flux resistance. The methods that are commonly used in the concentrated solar power field [69] require cooled Lambertian screens (*i.e.* with an assumed total diffusive reflection), a Charged-Coupled Device (CCD) camera and a cooled flux sensor. The procedure is as follows; For calibration, the flux sensor is positioned at a given point of the focal plane and measures a reference solar heat flux concentrated at this precise location; The Lambertian screen is then placed in the focal plane while the CCD camera records the brightness distribution at its surface; the heat flux is estimated from the reference flux and the comparison of the grey shades of the pixels.

Several variants of this technique have been proposed and compared, all showing relatively low uncertainty on estimates, and with different complexities [69], *e.g.* i) a system with moving parts can be used to avoid cooling, ii) a large amount of heat flux sensors can be applied to obtain a large heat flux map from their interpolation, iii) a coupling between optical modelling and measurements can be considered, iv) the actual absorber can be acted as the measurement surface with calorimetry, v) the flux distribution can be estimated from the total heat flux, the mirror's reflectivity and the grey levels obtained with a non-calibrated CCD camera.

With this last method, Dib [18] assessed the heat flux distribution on a receiving screen in the focal area of a Scheffler collector, which is located in São Paulo, Brazil (lat. -23.65°) and which has an aperture area of 2 m^2 (2.7 m^2 collector area). The authors used a CMOS (Complementary Metal-Oxide-Semiconductor) camera instead of CCD and found heat flux densities up to 377 $kW \cdot m^{-2}$ distributed in an ellipsoidal shape. Depending on the day of the year, the major axis (major diameter) of the latter was ranging from 0.252 m to 0.348 m and the minor axis (minor diameter) from 0.284 m to 0.293 m.

3.1.4 Novelty of this work

The objective of this work is to provide the heat flux distribution characteristics of an 8 m^2 Scheffler collector. The method is based on measurements on a screen with a high resolution infrared camera, coupled with a heat transfer model and inverse techniques. This method has already been developed in previous works, notably for nuclear energy research [26], and can also be applied to concentrating solar systems. It can be used to evaluate the heat flux distribution directly on an interface, with or without complex secondary optics that would make the use of conventional techniques more complicated. The novelty of this work is therefore twofold: the originality of the technique for concentrated solar power application and the supply of currently lacking detailed experimental data on 8 m^2 Scheffler collectors.

For this purpose, Section 3.2 gives the description of the experimental test-bench and procedure. Then, Section 3.3 details the results and compares the heat flux distribution with the curve of a two-dimensional Gaussian function. Finally, conclusions and perspectives are given in Section 3.4.

3.2 Materials and methods

3.2.1 Main principles

Understanding the behaviour and assessing the performance of a reflector requires to know the characteristics of the heat flux it collects $\dot{Q}_{in}$ (input) and delivers $\dot{Q}_{out}$ (output). The heat flux collected is assessed using the aperture of the reflector and the solar direct normal irradiance recorded by a pyrheliometer. The heat flux delivered by the reflector is first collected by a screen (receiver) positioned vertically in the reflector

focal plane. Measurements of air temperature and wind velocity are used to evaluate convective and radiative exchanges between the screen and the environment. Then, an infrared camera measures the radiation emitted by the back of the screen, and the emissivity of the emitting surface is used to deduce the temperature field. From this temperature field, a thermal model of the screen and inverse techniques are used to estimate the heat flux initially absorbed by the screen. The solar absorptivity of the screen is then used to obtain the heat flux delivered by the reflector. Finally, a regression analysis against a two-dimensional Gaussian model is performed to deduce quantitative information about the distribution (especially its size). The test bench obtained is shown in Figure 3.1 and the main steps of the method are summarised in Figure 3.2.

3.2.2 Object under study and measuring instruments

For the present work, the Scheffler reflector of the cooker presented in Chapter 2 is isolated in order to study its performance and the characteristics of the heat flux in its focal area.

Direct normal irradiance, air temperature and wind velocity are measured the same way as in Chapter 2.

The infrared camera used for the measurements is of reference Telops FAST M3K. This camera works in the infrared range from 3.0 µm to 5.5 µm. It is equipped with a filter wheel containing one empty slot and three neutral-density filters (therefore four positions in total) and is able to realise multi integration times acquisitions. Thus, it is calibrated over a wide temperature range going from 0 °C to 1500 °C. To obtain accurate measurements over the temperature range expected here, 50 °C to 500 °C, the three first filter wheel positions and four integration times per position are used. The camera provides an image of 320 x 256 pixels. In the test-bench configuration, it is used with a 13 mm lens and provides a pixel size projected on the cast-iron plate of about 3.5 x 3.5 mm^2.

As mentioned earlier, a screen is used as interface between the reflector and the infrared camera. This screen must be flat, dimensionally stable, a good conductor of heat and large enough to receive the entire heat flux distribution. As the cast-iron plate used as a cooktop in Chapter 2 meets these requirements, it is reused as the receiver in this test bench. When using an infrared camera without additional direct temperature measurement, it is necessary to know the emissivity of the observed surface. In addition, measurements are made easier if this emissivity is stable over time and homogeneous over the surface. For this reason, the surface of the plate observed by the infrared camera was painted with the special high-temperature paint Pyromark 2500 from LA-CO Industries. The application process is described in Appendix 5.2.1.

3.2.3 Experimental protocol

To begin with, the system is set up in a place exposed to the sun and without any shadows to interfere with the experiment. During the entire experiment, the cast

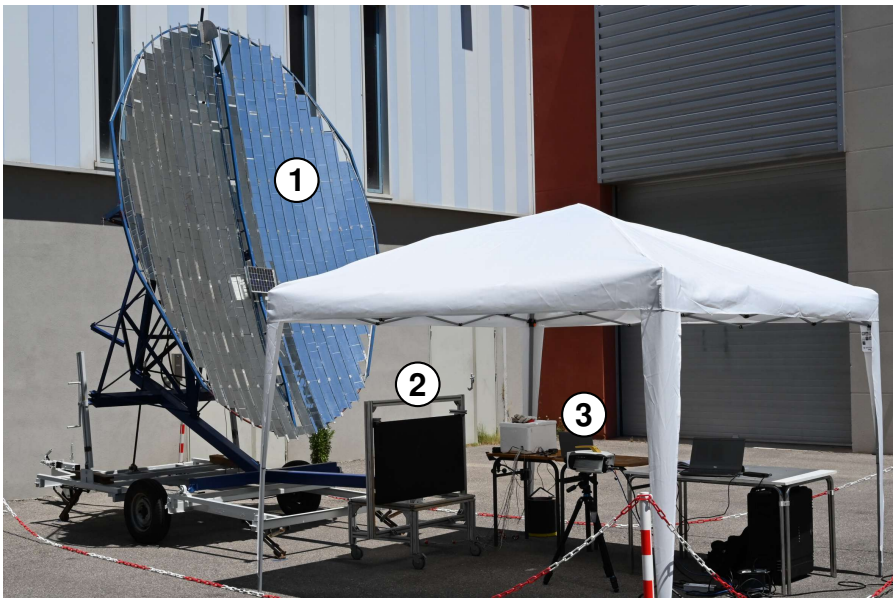

(a)

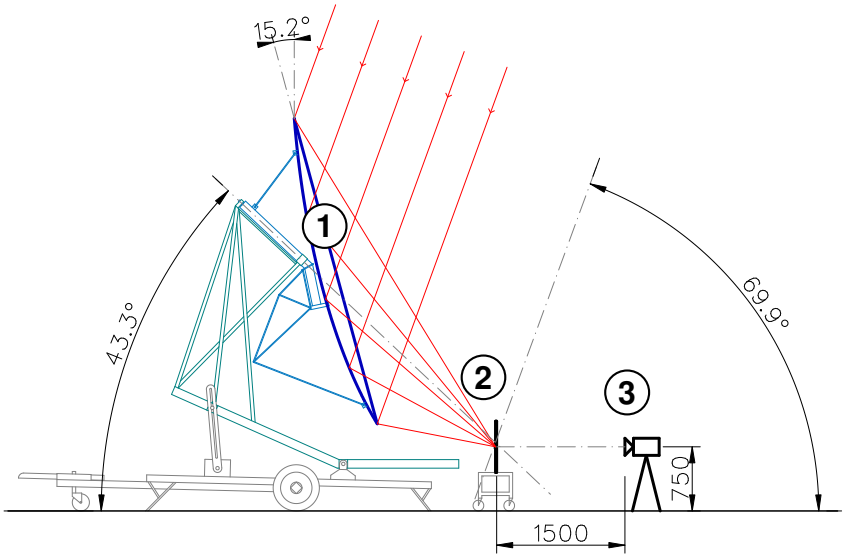

(b)

Figure 3.1 – Picture (a) and schematic diagram (b) of the test bench on 14/06/2022. The Scheffler reflector (1) focuses the sun light directly on the cast-iron slab (2). This last one is vertical and painted in black at the face observed by the infrared camera (3). Distances are given in millimetres and angles in degrees.

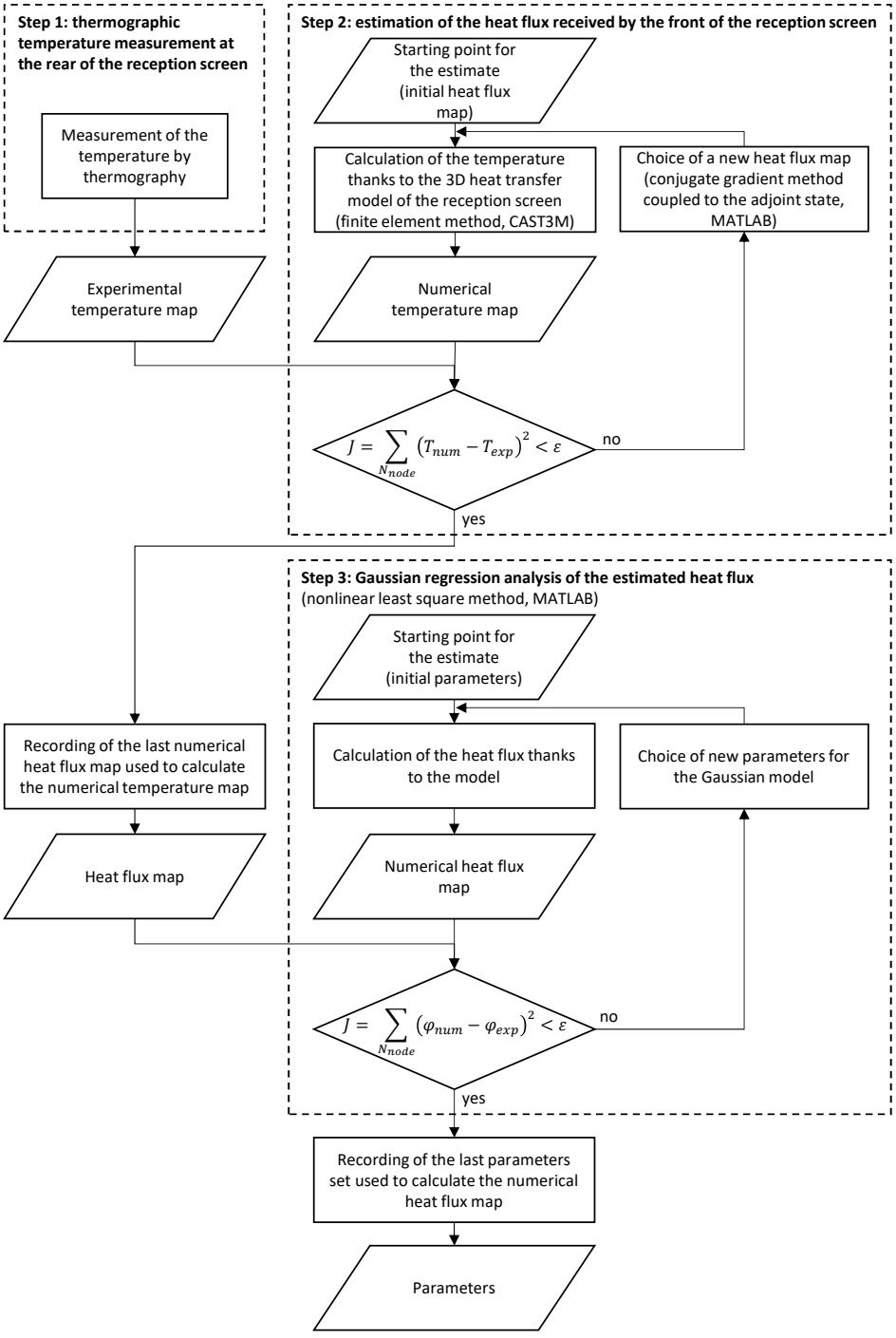

Figure 3.2 – Flowchart describing the methodology.

iron plate and the measuring instruments are protected from direct sunlight in order to avoid reflection of direct sunlight from the plate onto the camera and to avoid overheating of the electronics.

Then the Scheffler reflector is briefly turned towards the sun to establish its curvature and measure its angle to the vertical. Once this is done, the wind and ambient temperature start to be recorded; the normal direct irradiance is continuously recorded by the weather station. The Scheffler is turned again towards the sun and the sun tracking system is activated.

When steady state is reached, several measurements are taken with the infrared camera around solar noon at regular intervals. For each one of these measurements, a short video (approximately 400 frames at 20 Hz) is recorded with each filter and with multi-integration times. The conditions are assumed to remain stable during the recording period, *i.e.* a bit less than 10 min. Then an average image combining all those recorded is saved. This allows reducing the measurement noise and catching the full range of temperatures observed.

Finally, the reflector is turned away from the sun and every recording is stopped.

3.2.4 Heat flux collected

The total intensity of the heat flux collected by a Scheffler reflector [33] depends on its aperture area, denoted $A_{ap,n}$, and on the direct normal irradiance (DNI), denoted I_{DN}. This gives:

$$\dot{Q}_{in} = A_{ap,n} \cdot I_{DN}. \tag{3.1}$$

Assuming that the tracking is perfect, $A_{ap,n}$ can be calculated with (2.28) and (2.29). In Chapter 2, the calculation of the heat flux collected takes into account the global normal irradiance because the objective is to compare box-type cookers and concentrating cookers on an equal footing. In the present case, we are interested in the intrinsic performance of the reflector and we know that it has a low acceptance angle, so we use the direct normal irradiance.

3.2.5 Heat flux delivered estimated by inverse method

In order to estimate the heat flux delivered by the Scheffler reflector, the cast-iron plate is represented by a three-dimensional thermal model whose conductivity depends on temperature. This non-linear model is studied in steady state with radiative and convective exchanges at its boundaries (Figure 3.3a). The main properties taken into account in the model are given in Table 3.1. Heat transfer inside the cast-iron slab is described thanks to the thermal conductivity.

To determine the heat exchange by radiation, the cast iron plate is assumed to be a grey body in a black body environment. The proportion of the incident concentrated solar heat flux that is absorbed by the cast iron plate is quantified by the solar absorptivity of cast-iron α_c. Heat exchanges between the plate and its environment are quantified by two emissivities, that of the cast iron ε_c and that of the of the paint

ε_p. Several measurements were carried out to determine the absorptivity and the emissivities, and are described in Appendix 5.2. It should be noted that because of the tent on one side and the reflector on the other, the cast iron plate can hardly "see" the sky. It therefore exchanges radiation with its immediate surroundings, which are considered to be at air temperature.

Estimating the solar heat flux density also necessitates estimating the heat exchange by convection. Open convection on a vertical plate with inhomogeneous temperature can be particularly complex. For this reason, there is no simple correlation appropriate to the experimental set-up. Another method was therefore used. It is assumed that convective heat exchange can be represented by a single coefficient h that is estimated for each measurement. It is obtained by iteration, adjusting it in the numerical model until the flux estimated by inverse techniques at the edges of the plate is equal to the vertical global irradiance.

With this model and knowing the incoming heat flux $\varphi(x,y)$, it is possible to determine the temperature $T(x,y,z)$ in any point $M(x,y,z)$ of the plate Ω: this is the direct problem described by the following equations. One notes Γ_1 the boundary of the plate exposed to the solar concentrated heat flux and Γ_2 the boundary of the other side of the plate and the sides. Moreover, the vector $\vec{n}$ is defined as the normal to the surface a the point $M(x,y,z)$. Finally, to ease the comprehension, one notes the temperature $T(x,y,z) = T$, the thermal conductivity $\kappa(T) = \kappa$ and the heat flux density at the boundary exposed to concentrated heat flux $\varphi(x,y) = \varphi$.
Thus, for any M in Ω, there is:

$$\nabla \cdot (\kappa \cdot \nabla T) = 0. \tag{3.2}$$

For all M on Γ_1, the condition at this boundary is written:

$$-\kappa \cdot \frac{\partial T}{\partial n} = -\alpha_c \cdot \varphi + \varepsilon_c \cdot \sigma \cdot \left(T^4 - T_{env}^4\right) + h \cdot (T - T_{env}). \tag{3.3}$$

For all M on Γ_2, the condition at this boundary is written:

$$-\kappa \cdot \frac{\partial T}{\partial n} = \varepsilon_p \cdot \sigma \cdot \left(T^4 - T_{env}^4\right) + h \cdot (T - T_{env}). \tag{3.4}$$

The direct problem is solved with the CAST3M software using the finite element method. The mesh consists of 24 000 cubic quadratic elements with 8 nodes: 100 in the length of the cast-iron slab (x-axis), 60 in its height (y-axis) and 4 in its thickness (z-axis).

The inverse problem is to determine the intensity and distribution of the concentrated heat flux absorbed on the reflector-side of the plate that causes the temperature measured on the camera-side of the plate. It is solved thanks to a minimisation based on the conjugate gradient method coupled with the adjoint state [26]. In other words, we estimate the heat flux density $\varphi(x,y)$ that minimises the cost function J, which is the sum of the squares of the differences between the experimental temperature and

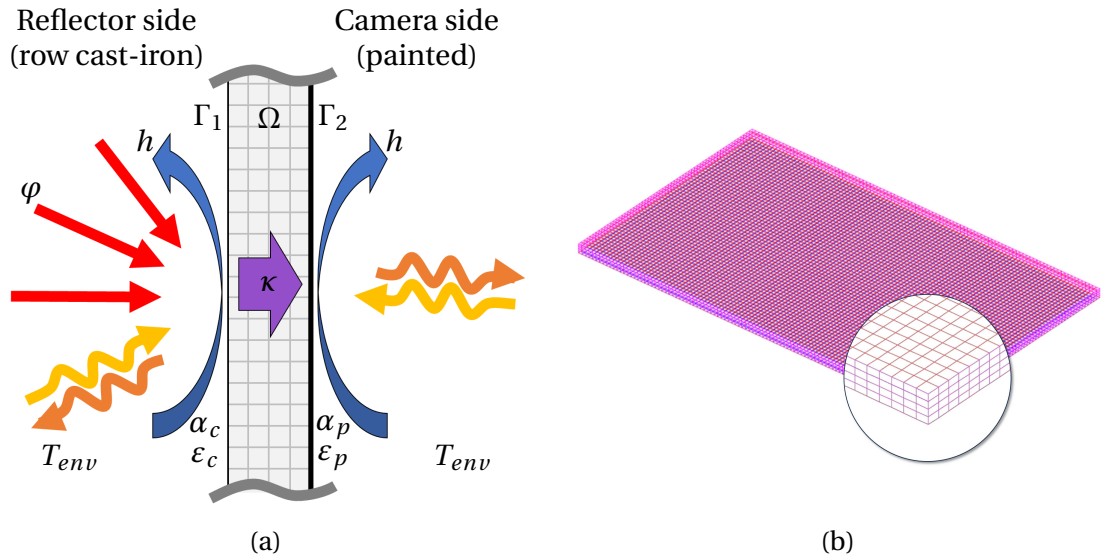

Figure 3.3 – Side view of the receiver with the heat transfers (a) and mesh of the 3D model (b). The mesh consists of 24 000 cubic quadratic elements with 8 nodes: 100 in the length of the cast-iron slab (x-axis), 60 in its height (y-axis) and 4 in its thickness (z-axis).

the numerical temperature:

$$J = \sum_{N_{node}} \left(T_{num} - T_{exp}\right)^2. \tag{3.5}$$

In addition to the heat flux density map obtained, the total intensity of the heat flux delivered by the reflector $\dot{Q}_{out}$ can be calculated as:

$$\dot{Q}_{out} = \int_{A_{abs}} \varphi(x,y)\, dA_{abs}, \tag{3.6}$$

with A_{abs} the surface area of the cast iron plate observed by the infrared camera.

The total intensity of the heat flux delivered can be compared with the theoretical one. Indeed, (3.7) shows that the theoretical total intensity of the heat flux delivered $Q_{out,th}$ can be estimated from the heat flux collected $\dot{Q}_{in}$, the specular reflectivity of the mirrors ρ_{spec} and the proportion of the rays collected by the reflector which reach the target γ, *i.e.* the intercept factor of the screen.

$$\dot{Q}_{out,th} = \rho_{spec} \cdot \gamma \cdot \dot{Q}_{in}. \tag{3.7}$$

The specular reflectivity of the mirrors is assumed to be close to the global reflectivity of the mirrors. And as the measurement interface is big and should thus collect most of the concentrated heat flux, the value of the intercept factor γ is expected to be close to 100 %.

Before continuing, it should be noted that a crack appeared in the cast-iron slab

Table 3.1 – Material properties taken into account in the thermal model of cast iron. The solar absorptivity is the average of the monochromatic absorptivities between 0.25 µm and 2.5 µm weighted by the standard solar spectrum. Similarly, the spectral emissivity is the average of the monochromatic emissivities between 2.5 µm and 25 µm weighted by the emission spectrum of a black body of given temperature between the same wavelengths. The average spectral emissivity is then the average of the spectral emissivities obtained for blackbody temperatures between 50 °C and 500 °C. For more details, see Appendix 5.2.

Property	Value
Thermal conductivity, κ ($W \cdot m^{-1} \cdot K^{-1}$)	$\kappa = 49.85 - 0.0106 \cdot T$ [32] (T expressed in °C)
Solar absorptivity of cast-iron, α	0.88
Mean spectral emissivity of cast-iron, ε_c	0.77
Mean spectral emissivity of the paint, ε_p	0.77
Convective exchange coefficient, h ($W \cdot m^{-2} \cdot K^{-1}$)	7

before the measurements on 14 June 2022. This crack, visible on Figure 3.4, is probably due to the high temperature gradient in the plate. Its effect on heat conduction is not taken into account in the numerical thermal model and will be discussed in Sections 3.3.2 and 3.3.3. Another cast-iron plate without crack is used for the other experiments.

3.2.6 Heat flux distribution

Using inverse techniques, the heat flux delivered by the Scheffler reflector is estimated without any preconceived ideas about the shape of the distribution. This allows us to avoid introducing bias into the estimation. However, once the estimate has been made, it is interesting to find a model that fits the data because it can help to describe it.

Preliminary experiments have shown that the heat flux distribution appears to behave like a two-dimensional Gaussian curve. A regression analysis is therefore carried out to test this hypothesis. If the fit is good, the model is validated and its estimated parameters can be used to describe the heat flux distribution quantitatively and objectively. The chosen regression function model is:

$$\varphi(x,y) = \varphi_{max} \cdot \exp\left(-a \cdot (x-x_c)^2 - 2 \cdot b \cdot (x-x_c) \cdot (y-y_c) - c \cdot (y-y_c)^2\right) + \varphi_{offset} \tag{3.8}$$

with $a = \frac{\cos^2(\theta)}{2 \cdot \sigma_{x1}^2} + \frac{\sin^2(\theta)}{2 \cdot \sigma_{y1}^2}$, $b = +\frac{\sin(2 \cdot \theta)}{4 \cdot \sigma_{x1}^2} - \frac{\sin(2 \cdot \theta)}{4 \cdot \sigma_{y1}^2}$, and $c = \frac{\sin^2(\theta)}{2 \cdot \sigma_{x1}^2} + \frac{\cos^2(\theta)}{2 \cdot \sigma_{y1}^2}$.

The maximum of the Gaussian curve is denoted φ_{max}. It can also be written as the product of the the direct normal irradiance and the maximum local flux concentration

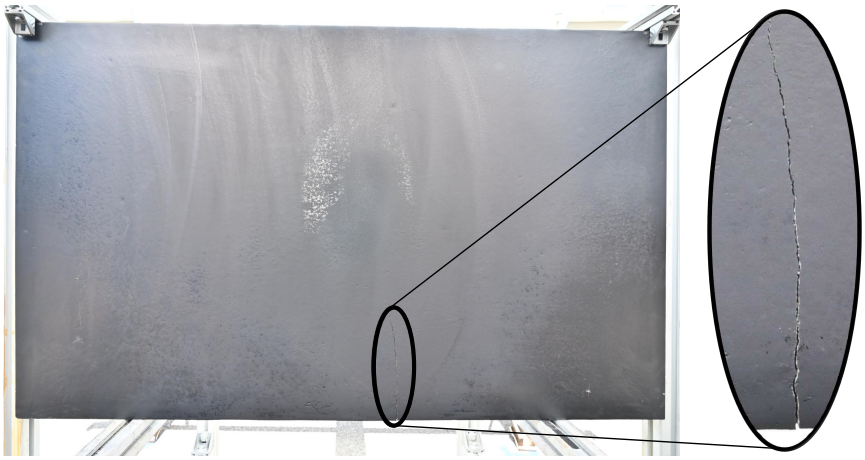

Figure 3.4 – Visual aspect of the painted face of the first cast-iron slab. A crack appeared before the measurements.

ratio. The two-dimension curve is centred on the position (x_c, y_c) and spreads along its two axes according to the standard deviation σ_{x1} and σ_{y1}. The angle θ describes the angle between the reference frame $(O, \mathbf{e}_x, \mathbf{e}_y, \mathbf{e}_\varphi)$ and the frame of the Gaussian curve $(C, \mathbf{e}_{x1}, \mathbf{e}_{y1}, \mathbf{e}_\varphi)$. It rotates the Gaussian curve in the trigonometric direction as it increases. And the last parameter φ_{offset} is the heat flux offset due to the solar vertical global irradiance received by the cast-iron plate from the environment by diffusion and reflection.

The estimation of the parameters is realised with a non linear least square minimisation on MATLAB. The minimisation converges rapidly and is robust against the start point and bounds. The goodness of fit is assessed graphically, by studying the experimental data, the regression function obtained and the residuals.

3.2.7 Variables of interest

The key quantities in this work are the density and total intensity of the heat flux supplied and the shape and size of the heat flux distribution. To enable the results to be compared with other work, they are accompanied by dimensionless quantities.

As first dimensionless performance indicator, the total heat flux delivered by the Scheffler reflector $\dot{Q}_{out}$ can be compared with the heat flux collected $\dot{Q}_{in}$, as shows (3.9), to obtain the experimental energy efficiency η_{sch} of the Scheffler reflector.

$$\eta_{sch} = \frac{\dot{Q}_{out}}{\dot{Q}_{in}}. \tag{3.9}$$

It should be noted that the term "optical efficiency", often denoted η_o, usually refers to the efficiency of the optical part of a system (such as a solar cooker) and therefore includes the reflectivity of a possible secondary mirror, the transmissivity of a possible

transparent cover on the absorber and the absorptivity of the absorber (definition adopted in Chapter 2). As this work intends to go into more detail in the performance analysis of the Scheffler reflector, the latter is studied without any secondary optics and the output power is defined as the power received, and not absorbed, by the flat vertical screen located in the focal area. In this way, the calculated energy efficiency gives information about the reflector only, and thus allows comparison between different reflectors independently from the absorber and any intermediate optical object.

Another important characteristic of a reflector is its concentration ratio. The concentration ratio has several definitions, all of which have their advantages and disadvantages [10], [21]. In the present case, the characteristics of the reflector are studied without any *a priori* on the absorber size. That is why the area concentration ratio $\overline{C_a}$ is defined by:

$$\overline{C_a} = \frac{A_{ap,n}}{A_{im,n}}. \tag{3.10}$$

This ratio compares the aperture area of the reflector $A_{ap,n}$ with the area of the image $A_{im,n}$ produced in the focal zone of the reflector (*e.g.* on a measurement screen). Note that, as $A_{ap,n}$ varies through the year, $\overline{C_a}$ is also expected to vary. Knowing the value of the area concentration ratio throughout the year enables the absorber to be designed accordingly and a detailed performance analysis to be carried out. In addition, this concentration ratio can be measured regularly over the lifetime of the reflector and used to assess the loss of concentration due to reflector ageing.

Energy efficiency is an energy indicator and the surface concentration ratio is a geometric indicator. It is also interesting to have other quantities which combine these to aspects. The average heat flux density concentration ratio $\overline{C_f}$ is defined by (3.11).

$$\overline{C_f} = \frac{\dot{Q}_{out}}{A_{im,n} \cdot I_{DN}}. \tag{3.11}$$

This latter indicator gives a measure of the reflector's performance in simultaneously transmitting and concentrating solar energy.

Now that the performance indicators are defined, the results can be presented.

3.3 Results and Discussion

3.3.1 First results and observations

The experiments took place in Marseille, France (lon. 5.4374° E, lat. 43.3449° N, alt. 120 m), on 14 June 2022, 22 March 2023, 20 April 2023, 26 May 2023, 19 June 2023 and 28 June 2023. As the analysis procedure is the same for all the measurements, one measurement is first described in detail, then the results of the other measurements are briefly presented and compared.

Thus, this section mainly describes the measurement 3 on 14 June 2022. It was realised close to solar noon (11:57), a few days before the June solstice (northern

hemisphere). That day, the intercept area of the reflector $A_{ap,165}$ was 4.3 $m^2 \pm 0.2$ m^2. The average direct normal irradiance during this measurement was 904 $W \cdot m^{-2}$ with a standard deviation of 0.7 $W \cdot m^{-2}$ (k = 1).

The following graphs are drawn from the point of view of the infrared camera, the x-axis being horizontal (length of the cast-iron slab), the y-axis being vertical (height) and the z-axis coming from the cast-iron slab to the camera (thickness).

3.3.2 Experimental temperature field

Figure 3.5 shows the temperature measurement at the camera-side of the cast-iron slab. As the emissivity of the surface has been taken into account, these temperatures are expressed as "true temperatures", by opposition to "black body temperatures".

From a qualitative point of view, one can see a hot spot at the middle and a temperature gradient from this point to the edges of the plate. The isothermal lines appear almost circular. On the picture, a small defect is visible at the bottom of the plate: this is a temperature discontinuity due to the narrow crack which appeared before our measurement. Its influence on the heat flux estimate is discussed in Section 3.3.3. In addition, the fact that there is no other temperature discontinuity confirms the hypothesis of a homogeneous emissivity despite the visual aspect of the screen (3.4). From a quantitative point of view, the temperature varies from 45 °C at the edges, to 486 °C ± 5 °C in the middle.

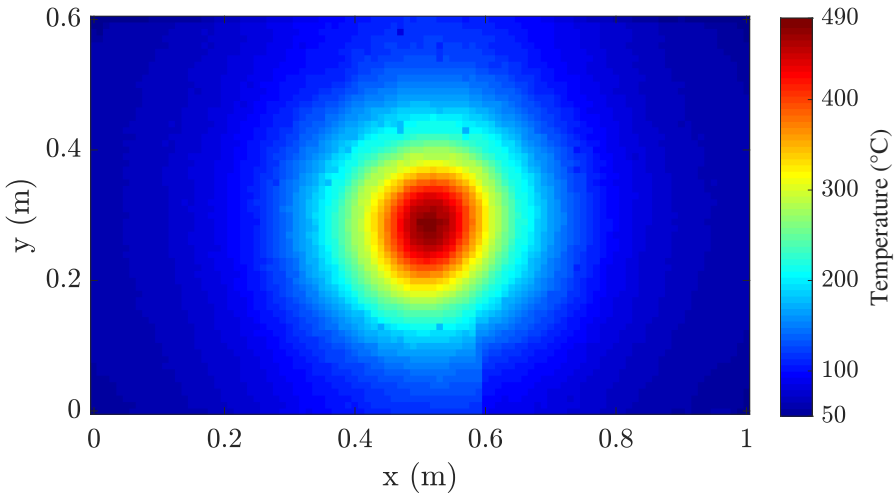

Figure 3.5 – Experimental temperature field obtained with the infrared camera and after treatment with emissivity.

3.3.3 Experimental heat flux intensity and distribution

As explained in Section 3.2, the received heat flux is estimated from the temperature measurements using inverse techniques. Figure 3.6 represents the heat flux density received by the cast-iron slab. This figure shows that the use of an infrared camera in

combination with the inverse techniques represents a relevant solution to access the whole heat flux distribution with a good resolution.

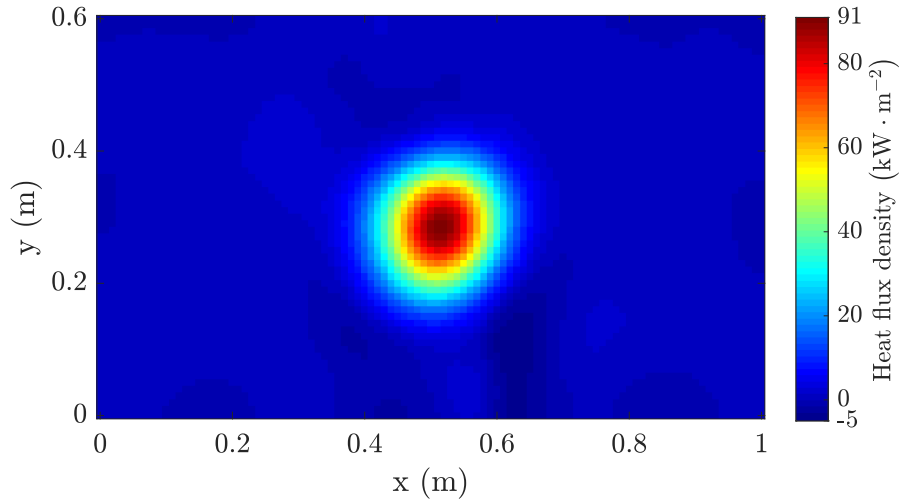

(a)

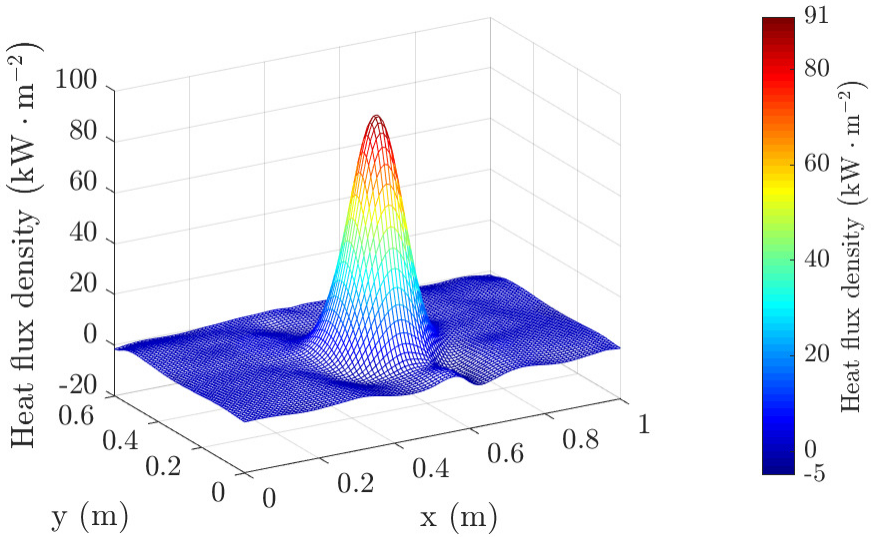

(b)

Figure 3.6 – Experimental heat flux map in a 2D representation (a) and in a 3D representation (b). The heat flux density varies from -5 kW$\cdot$m^{-2} (numerical artefact) to 91 kW$\cdot$m^{-2} and gives a total heat flux received by the cast-iron plate equal to 2.5 kW.

The heat flux distribution shape is similar but narrower than the temperature one. The estimation of the heat flux density generated a small "wave" near the location of the crack. This non-physical phenomenon is partly due to our model and to inverse techniques, which do not take the crack into consideration. But this is only a local issue and global results are visually not much affected. This demonstrates the robustness of

the method, even in an unfavourable case. Another measurement carried out using a screen without crack is showed in Appendix 5.3.

The heat flux density reaches a maximum of 91 $kW \cdot m^{-2} \pm 9\ kW \cdot m^{-2}$ and the total intensity of the heat flux received by the cast-iron plate is $2.5\ kW \pm 0.2\ kW$.

The surface of the cast iron plate exposed to the concentrated solar heat flux also receives a diffuse solar heat flux, either directly or indirectly after reflection in the environment. As it represents around 4 % of the total heat flux, it is smaller than the uncertainty and is neglected in this work.

As the direct normal irradiance was $904\ W \cdot m^{-2} \pm 9\ W \cdot m^{-2}$ and the aperture of the Scheffler reflector was $4.3\ m^2 \pm 0.2\ m^2$, the power received by the Scheffler reflector was $3.9\ kW \pm 0.2\ kW$. Thus, the efficiency of the Scheffler reflector to concentrate and transmit the solar radiation to the plate was $63\ \% \pm 6\ \%$.

The efficiency is a bit low compare to our expectations and measurement uncertainties do not explain the difference. Indeed, (3.7) and (3.9) give rise to (3.12).

$$\eta_{sch} = \rho_{spec} \cdot \gamma \tag{3.12}$$

Thus, either the specular reflectivity is below 80 % (i.e., below the value of the global reflectivity), or the intercept factor is below 100 %, or both. Given the large size of the receiving screen and the fact that there is no visible "sunlight leakage", the first explanation is privileged: the mirrors are not perfectly specular and scatter the sunlight.

Despite this last point, these results are in good agreement with those of Oelher and Scheffler [58]. The latter carried out measurements in April using an $8\ m^2$ reflector. With an aperture of $4.7\ m^2$ (8 % bigger) and a direct normal irradiance of $730\ W \cdot m^{-2}$ (19 % smaller), they obtained a total heat flux of 2.1 kW (15 % smaller), giving an efficiency of 61 % (only 2 % smaller than ours).

However, the results are significantly different from those of Sasidharan and Dutta [76]. They studied a reflector four times bigger (area of $32.0\ m^2$ and aperture estimated to $27.1\ m^2$) and with a direct normal irradiance of $651\ W \cdot m^{-2}$ (28 % smaller), they obtained a total heat flux of only 860 W (65 % smaller). Moreover, the maximum heat flux density is $45\ kW \cdot m^{-2}$ (two times smaller), and they have a nearly random heat-flux distribution whereas Figure 3.6 shows a very typical distribution. There are several possible explanations for this. Firstly, a $32\ m^2$ Scheffler reflector is further away from the focal point and more difficult to build than an $8\ m^2$ reflector, therefore the heat flux may be more distributed due to shape defects. Secondly, as the curvature of the reflector is adjusted manually, this could be due to inaccurate adjustment. Finally, as they used only 5 heat flux sensors, they needed a hybrid experimental-numerical technique to reconstruct the heat flux distribution, which led to significant assumptions, especially in the ray-tracing model. In contrast, the measurement technique described in Section 3.2 uses an infrared camera to provide a spatially resolved measurement over the entire surface of the receiving screen. It therefore requires very few assumptions to give a detailed description of the phenomenon. For the above reasons, the experimental results of Sasidharan and Dutta cannot therefore be used to validate

or invalidate the present results.

On the other hand, our results are fairly consistent with those of Dib [18]. He carried out a measurement with a 2.7 m^2 Scheffler reflector on 8 December in the southern hemisphere, a date roughly comparable to the June solstice in the northern hemisphere. With an aperture of 1.3 m^2 (71 % smaller) and under a direct normal irradiance of 996 $W \cdot m^{-2}$ (10 % bigger), he measured a total heat flux of 1.3 kW (49 % smaller) and heat flux densities up to 299 $kW \cdot m^{-2}$ (229 % bigger). It should be noted that the latter two results could be overestimated. Indeed, the total heat flux seem to be calculated from the aperture and the direct normal irradiance neglecting the reflectivity of the mirrors (about 90 %); the heat flux densities are estimated on the basis of this total flux and the grey scale map obtained with a CMOS camera. Nevertheless, once again, a bigger reflector generally implies a more distributed heat flux. Moreover, Dib's reflector is covered by an aluminium reflective film which stick to the parabolic structure, whereas the present reflector is covered with flat glass mirrors; the concentration and the heat flux densities are thus more limited in the present case than in Dib's case (see the work of Reddy and Khan [67]).

Dib also gave information on the size of the heat flux distribution. Nevertheless, it appears that determining the contour of the distribution is not an easy task and may be subjective because the boundaries are not clear. Instead of arbitrarily setting a heat flux threshold that would define the distribution boundary, we decided to choose a model and fit it to the experimental data in order to provide more objective and quantitative information on the heat flux distribution.

3.3.4 Heat flux distribution

The estimated parameters of the model for the measurement 3 on 14 June 2022 are presented in Table 3.2.

Table 3.2 – Parameters of the Gaussian function model estimated for the measurement 3 of the experiment carried out on 14 June 2022. Parameters are: the maximum heat flux density (φ_{max}), the heat flux density offset due to global vertical irradiance (φ_{offset}), the position of the centre (x_c, y_c), two standard deviations (σ_x, σ_y) and the rotation angle (θ).

Parameter	Value
φ_{max} ($kW \cdot m^{-2}$)	93.5
φ_{offset} ($kW \cdot m^{-2}$)	0.3
x_c (mm)	514
y_c (mm)	284
σ_{x1} (mm)	66
σ_{y1} (mm)	60
θ (°)	60

A comparison between the experimental heat flux measurement and the Gaussian

model is given on Figure 3.7 (Gaussian curve with 2 axes), Figure 3.8a (axis (Cx_1)) and Figure 3.8b (axis (Cy_1)). A good match can be observed on all figures and the residuals are signed but remain small compare to the heat flux received in the middle of the cast-iron plate. It can be noted that the peak of the experimental heat flux distribution is slightly flattened compared to the model. This could be partly due to the flat facets of the reflector. Indeed, a reflector with smaller facets should theoretically achieve higher heat flux densities, and would fit the model better. Nevertheless, the model gives an estimated maximum density only 3 % greater. If the experimental distribution is not exactly a Gaussian curve, it is still a very good approximation. Moreover, as the value of the first deviation (σ_x) remains 10 % lower than that of the second (σ_y), the experimental distribution is closer to a two-dimensional Gaussian curve than to a one-dimensional Gaussian curve. Finally, the centre of the Gaussian curve is close to the middle of the cast iron plate, *i.e.* where the focal point is supposed to be (with an accuracy estimated to ±5 cm in each direction).

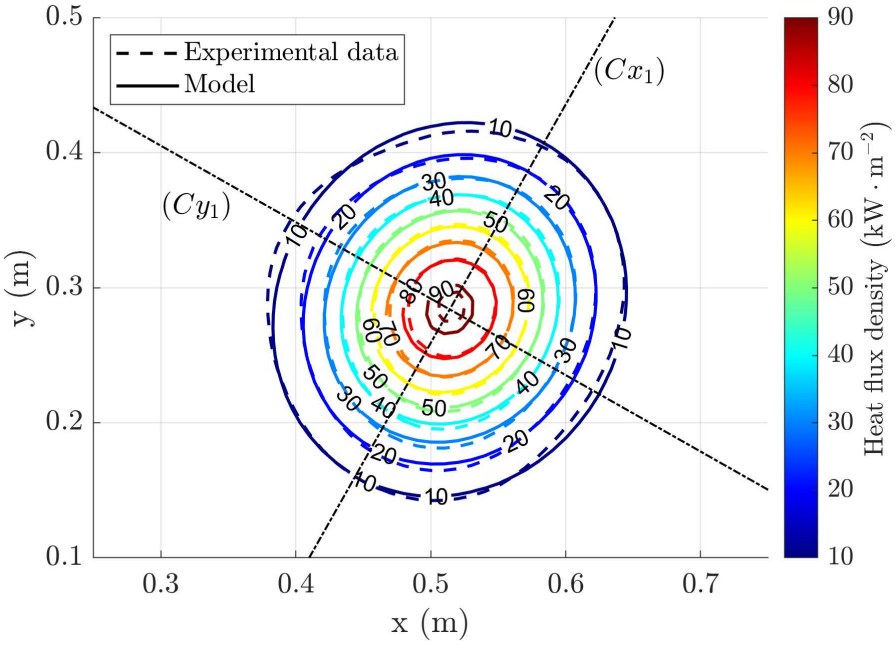

Figure 3.7 – Experimental heat flux distribution versus fitted function. The two dotted lines represent the axes (Cx_1) and (Cy_1) of the Gaussian regression function.

The model fits the experimental data very well, so it is reasonable to use it to describe the heat flux distribution quantitatively. In order to compare the present results with other works, in which authors often consider the contour containing about 100 % of the heat flux, a coverage factor k of 3 was chosen, thus defining an ellipse containing 99.7 % of the heat flux. Thus, the major and minor axes (or major and minor widths) of this ellipse are calculated with:

$$W_{x_1,99.7\%} = 2 \cdot k_{99.7\%} \cdot \sigma_{x1} \quad \text{and} \quad W_{y_1,99.7\%} = 2 \cdot k_{99.7\%} \cdot \sigma_{y1}. \tag{3.13}$$

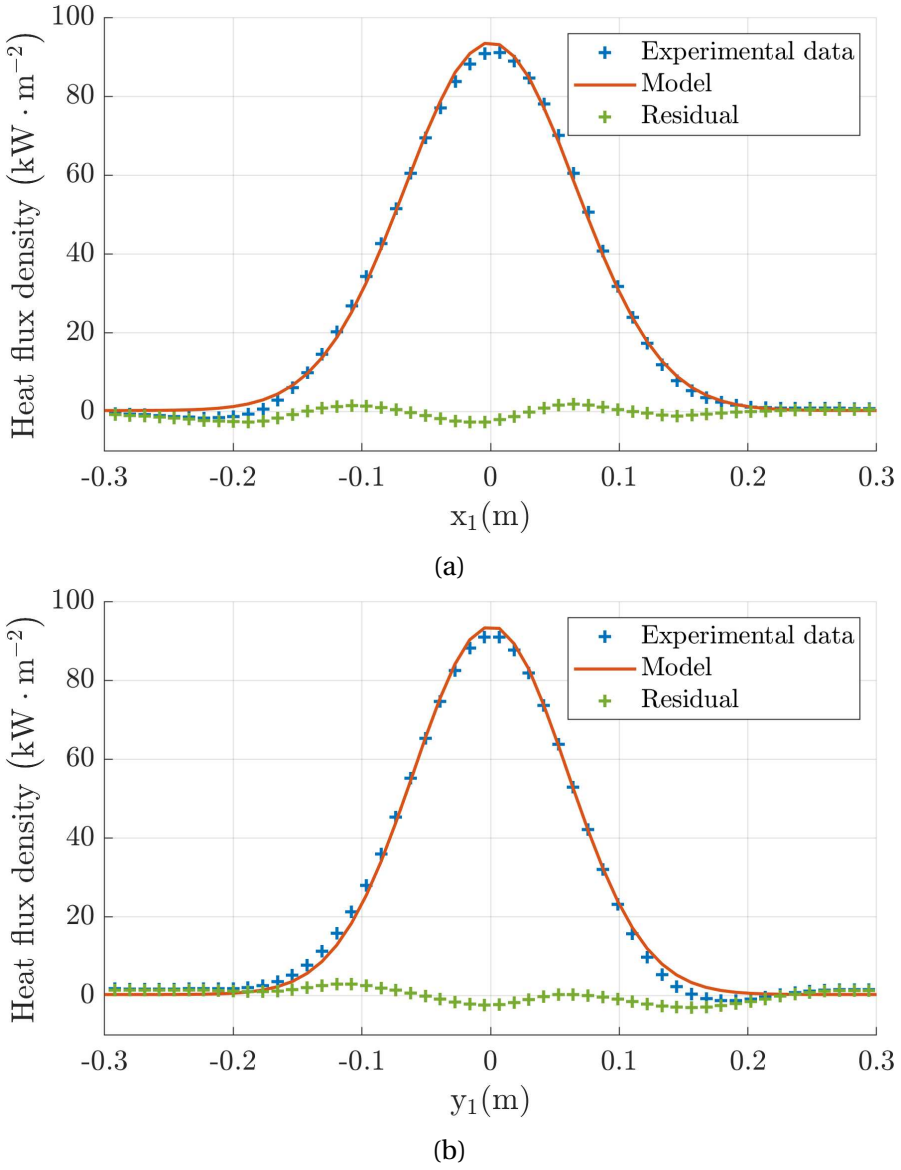

Figure 3.8 – Experimental data versus model data according to (Cx_1) axis (a) and (Cy_1) axis (b)

This gives respectively 0.399 m and 0.358 m, and the surface area covered by the heat flux distribution, called image area, is thus 0.112 m^2. As a direct consequence, the area concentration ratio of the reflector is 39 and the average flux concentration ratio is 24. Firstly, it can be seen that the surface is consistent with the idea that the spot can never be smaller than the size of a mirror of the parabola. Secondly, it can be assumed that misalignment and scattering are responsible for the larger size of the spot.

These experimental results can now be compared with those of Dib [18]. He also assumed the heat flux distribution to be elliptical and found major and minor axes of 0.347 m and 0.286 m respectively. This results in an image area of 0.078 m^2, *i.e.*

30 % smaller. This comparison corroborates the results, as it is consistent with the explanations given in Section 3.3.3: Dib's reflector has a shorter focal length and provides higher heat flux densities than ours due to a narrower heat flux distribution, even though the total heat flux is lower.

In summary, the comparison between the current results and the literature shows a satisfactory agreement, thus validating the method and the results.

3.3.5 Measurement repeatability and evolution with time

Now that a measurement has been analysed in detail, the results of the measurements can be studied more globally. All the information, measurements and results of the experiments are summarised in Appendix 5.4.

Among the performance indicators calculated, energy efficiency is an indicator that should not change depending on the time of day or the day of the year. The average energy efficiency of all the data is 68 %, with a standard deviation of 6 % and a range of 8.5 %, while the uncertainty is estimated at ±6 %. Variability in energy efficiency is therefore relatively low and could be attributed mainly to the uncertainty of the measurements. So far, the measurements appear to be fairly repeatable.

Note that although the method has acceptable repeatability (variations slightly less than the uncertainties), it may not be easily reproducible due to its complexity. Potentially influential parameters are discussed in the Appendix 5.5. In addition, the performance characteristics of Scheffler reflectors may also vary considerably due to the lack of standardisation in their design and use. Thus, other methods such as the use of a cooled Lambertian screen and flow sensors would suffer from similar limitations.

Unlike the energy efficiency, the area concentration ratio and the average flux concentration ratio should vary from one day to the next, as they depend on the aperture area and the image area. The aperture area varies according to the day of the year, but what about the image area? Using the same definition as in the previous section, the image area corresponds to the area of the ellipse containing 99.7 % of the heat flux received. According to Figure 3.9, no trend towards daily or seasonal variation can be identified for the major and minor diameters of the heat flux distribution. The average appears to be a good way of giving orders of magnitude for the variables of interest.

The mean image area over all measurements is 0.135 m^2 with a standard deviation of 0.028 m^2. Its major and minor diameters are 0.46 m and 0.36 m respectively. Thus, the average area concentration ratio is 36, and the average heat flux concentration ratio is 24.

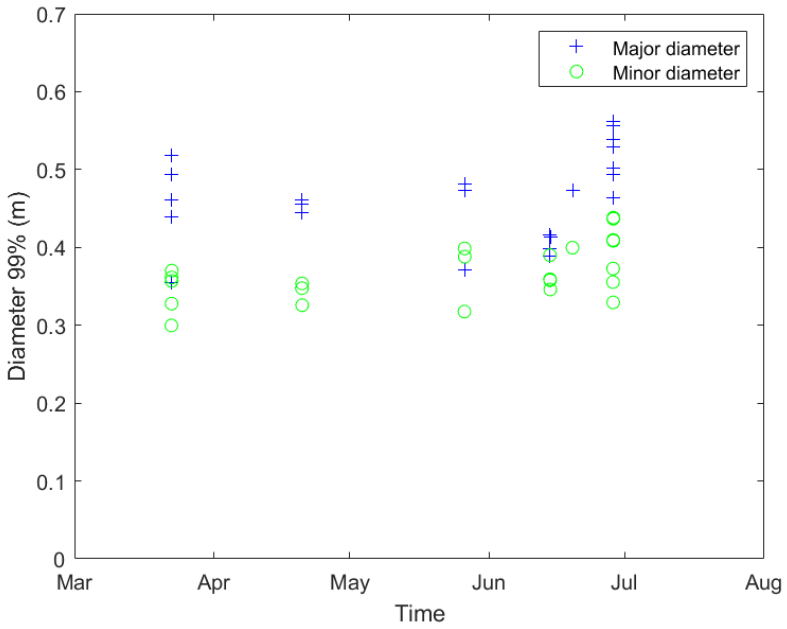

Figure 3.9 – Major and minor diameters of all measurements.

3.4 Conclusion

In this work, the distribution of the concentrated heat flux delivered by an 8 m^2 Scheffler reflector similar to the one used by the restaurant Le Présage but with facets is studied. Firstly, a review of the scientific literature shows that, although the scientific community's interest in the reflector is growing, it has not been much studied, particularly experimentally. Furthermore, theoretical and numerical work has produced highly variable results, demonstrating the need for detailed experimental data.

Secondly, using an infrared camera and inverse techniques, a detailed map of heat flux densities is obtained without any preconceptions. The maximum heat flux density, total power and energy efficiency are given with a relatively low uncertainty ranging from 6 % to 10 % and are in satisfactory agreement with the literature, confirming the relevance of the method. Although the experimental method demonstrated its capabilities, it did not allow detailed analysis of variations in the shape of the heat flux distribution as a function of time. Indeed, due to the thermal inertia of the screen, the assumption of a steady state and the duration of the measurement, the results are sensitive to rapid variations in wind and direct normal irradiance. Another reason is that the results appear to be sensitive to the precision with which the test bench is set up before each experiment (North-South orientation, rotation axis inclination, bending, location of the receiver, etc.).

Thirdly, the experimental heat flux distributions are successfully compared with a model based on a two-dimensional Gaussian function. The estimated parameters allowed a more detailed analysis of the experimental data and, in particular, provided quantitative data on the size of the heat flux distribution without the need for an arbitrary threshold. This is an essential point for comparing this work with others, in particular with the work of Dib. The study of the contour of the heat flux distribution is interesting at first sight because it can be done theoretically and quite easily; it becomes questionable in numerical studies and even more so in experimental studies because the contour has no real existence. In addition, knowledge of the heat flux distribution enables thermal optimisation, whereas the contour only enables geometric optimisation.

Fourthly, the variation in the size of the heat flux distribution as a function of time of day or day of year does not seem to follow any identified pattern and appears to be of the same order of magnitude as the variability observed across the different experiments. Either the size does not depend on time, or its dependence is very weak and hidden in the experimental variability. This means that the secondary reflector or receiver can be optimised for the whole year and not just for certain periods.

Finally, in average, 99.7 % of the heat flux provided by the 8 m^2 reflector is received on the vertical screen in an ellipse of major and minor diameters 46 cm and 37 cm respectively. And the area concentration ratio and heat flux concentration ratio are evaluated respectively to 39 and 25. Although only partial, these results already provide fundamental information for designers. Depending on the thermal characteristics of the absorber and the heat flow distribution characteristics, it is already possible to determine the absorber size that minimises heat loss.

3.5 Perspectives

In the present work, the test bench was set up and dismantled for each experiment for practical reasons. Variations in settings could be considerably reduced if a permanent experimental space were available. In addition, the accuracy of the settings could be improved if the remaining key parameters of the setting were identified and the required accuracy assessed.

Carrying out experiments under real conditions has a number of advantages: it avoids the need to use heavy instruments such as a solar simulator and brings the experiments closer to real conditions. There are also disadvantages. The climatic conditions are not controlled and make the experiments difficult. For example, around 50 measurements were taken on 15 different days and only 23 were successful. Nothing can be done about unexpectedly overcast weather. However, a windscreen could be used to reduce forced convection on the receiver; a more detailed natural convection model could then be used, which would improve the accuracy of the results.

The experimental method would also benefit from being faster on different aspects. On a first aspect, the use of an infrared camera with a filter wheel whose rotation speed is synchronised with the acquisition frequency of the detector would enable continuous measurements to be taken, thereby reducing acquisition time. Combined with a screen with lower thermal inertia, this would enable the experimental method to take better account of variations in environmental conditions. On a second aspect, another method could be developed to provide real-time heat flux estimations. This would make it possible to observe in real time the impact of a parameter or variable, such as the curvature of the reflector. The current method uses a detailed heat transfer model taking into account the non-linearity of the direct problem (due to temperature-dependent material properties and radiative heat exchange). This implies to use an iterative method to solve the inverse problem. As a result, estimating the heat flux takes several days (for a computer with 2 CPUs). There are several ways of reducing the calculation time. If accuracy is not a key issue for the user, a linear model could be used instead of the non-linear model. Using a reduction in the order of the model could lead to better accuracy. Coupling the non-linear model with artificial intelligence could also yield good results, once it has been trained. Finally, speeding up the method would also require interfacing the infrared camera and the various software packages involved in the estimation process.

Once the distribution shape of the heat flux identified, it can be estimated using less-resolved measurement devices, such as thermocouples, combined with a shape *a priori*. From an industrial point of view, it could be interesting to have a turnkey solution for estimating radiative heat flux that combines simple measurement devices and a rapid estimation method. This would enable the quality of the manufacture or installation of a Scheffler reflector, for example, to be assessed quickly and easily.

In future work, the set of data on the performance of the Scheffler reflector should be supplemented by other experiments carried out at other times of day and on other days of the year, in particular from November to February (the set of experimental data provided covers the period from March to June, and therefore from July to October by

symmetry). This would enable us to see more precisely how the characteristics of the heat flux supplied by the reflector vary as a function of time.

Experiments could even be carried out with different reflector sizes, different facet sizes, different reflective materials, different receiver inclinations, etc. With this in mind, it would make sense to carry out experimental and numerical work at the same time. Accurate numerical models could be built from the experimental data and the numerical simulation could then be used to suggest improvements to the experimental method and reduce the number of experiments needed.

At first sight, someone wishing to improve the performance of a Scheffler reflector would certainly concentrate on the shape and reflectivity of the reflector. The above comments on the precision of installation are also true outside the context of research and show that the installation stage of a system such as Le Presage's cooker should not be neglected. More generally, many parameters can play a non-negligible role in the shape and intensity of the heat flux distribution (see Appendix 5.5), particularly when high performance is required.

The Scheffler reflector of the Le Presage solar cooker is covered with a continuous sheet of reflective aluminium. Its greater reflectivity would mean greater energy efficiency and would stretch the distribution of the heat flux upwards. The maximum heat flux density would increase, while the other characteristics of the Gaussian curve would remain identical to those of the reflector studied. The total heat flux would also be higher.

By eliminating the limitation of facet size, the continuity of the reflective coating would push the maximum area concentration ratio higher. The peak of the heat flux distribution should therefore be sharper. Nevertheless, the shape of the distribution is not expected to change much elsewhere. The major and minor diameters obtained in this work should therefore be of a good order of magnitude compared with those of the Presage reflector and could be used as design parameters for a new secondary reflector.

The next step would be to use the experimental method to evaluate the heat flux provided by the Scheffler reflector with the current secondary reflector, and then with prototypes. To do this, a number of technical challenges still need to be overcome. For example, the infrared camera will have to be held vertically at 3 m above the ground in order to film the receiving screen. Nevertheless, this would enable us to assess the performance of the combination of the two reflectors and would be useful for optimising the absorber. This would complete the analysis of the system's internal performance.

4 General conclusion and perspectives

4.1 Summary of the work, findings and their implications

The company Le Présage has developed an innovative and unique solar cooker using a Scheffler reflector. In order to better understand and optimise the heat transfer phenomena that take place in this solar cooker, we carried out an experimental study on a reproduction of it.

In the first chapter of this thesis, the overall performance of the system has been assessed. The idea was to obtain an initial estimate of the system's performance against which future improvements can be compared. A literature review was first carried out to recap the various commonly used methods and performance indicators. Secondly, starting from an energy balance on a lumped-element model, several performance indicators were expressed: the specific time constant, thermal conductance, optical efficiency and opto-thermal ratio. Thirdly, a test bench was elaborated and three experiments were carried out using a protocol similar to the one of the ASABE, which consists in heating a load of water from room temperature to the boil. Finally, regression analyses were performed on the temperature, efficiency and standardised power, and the performance indicators were calculated.

In the second chapter, the Scheffler reflector was studied more in-depth. The objectives were to assess its energy performance and to get information on the shape of the heat flux delivered by the reflector in order to allow the optimisation of its association with the secondary reflector and the absorber. A second test bench and another experimental protocol were developed for this purpose. The temperature at the rear face of a receiver placed in the focal zone of the Scheffler reflector was measured with an infrared camera. Using inverse techniques coupled to a three dimensional model of the receiver, a map of the heat flux delivered by the reflector has been obtained for each measurement. The heat flux distribution has been successfully compared to a two-dimensional Gaussian curve. The results of 23 measurements on 6 different days from March to July have been analysed and overall energy efficiency, area concentration ratio, flux concentration ratio and diameters of the heat flux distribution were calculated.

The findings of this work are of two kinds: methodological and data-related. With regard to methodology, Chapter 2 proposes recommendations for improving the assessment of solar cookers: use of the characteristic time, the opto-thermal ratio and

the standard power as performance indicators; derivation of the expression of these indicators from a customised energy balance; measurement of the direct normal irradiation; elimination of the start and end of the acquisition before analysis; use of regression analysis; and double-checking of the estimated indicators. The experimental method adapted in Chapter 3 allows to obtain a detailed map of heat flux densities delivered by the Scheffler reflector without any preconceptions. Moreover, fitting the experimental data with a two-dimensional Gaussian function makes possible to describe quantitatively the shape and size of the heat flux without arbitrary threshold.

With regard to data, the results of both chapters can be combined on a diagram (Figure 4.1). It illustrates graphically the potential for improvement and the limits of the system. As the Scheffler reflector has a low acceptance angle, the amount of solar energy collected is limited to the direct part. Moreover, its aperture varies from 57 % to 85 % relatively to its reflective surface, limiting the collecting area. In Chapter 3, the efficiency of the Scheffler reflector has been determined. Combined with the optical efficiency of the system, determined in Chapter 2, the efficiency of the secondary reflector and the absorber can be deduced. In Chapter 2, the thermal efficiency of the cook-top and the cooking pot in transmitting the power to the water for a temperature difference of 50 °C has also been evaluated.

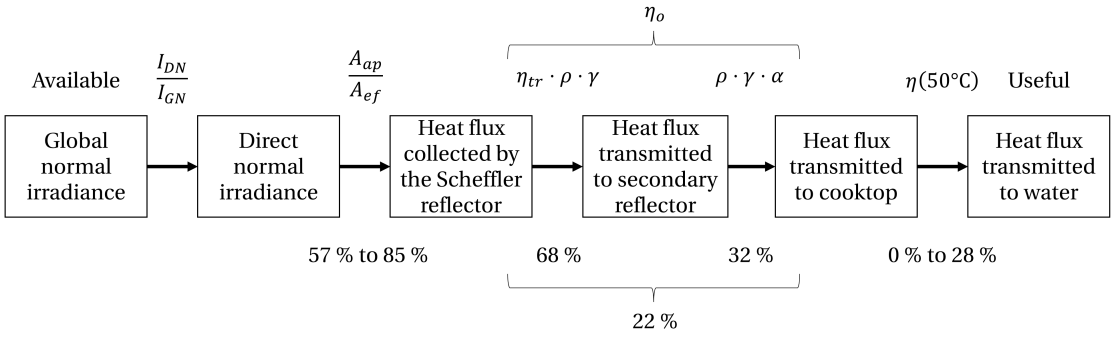

Figure 4.1 – Diagram of the power in the solar cooker studied.

In addition to the energy efficiency of the Scheffler reflector (68 %), Chapter 3 also brought information about the size of the heat flux distribution delivered by the reflector. Its major and minor diameters are 0.465 m and 0.367 m respectively. This data has then be used to calculate the average area concentration ratio (36), and the average heat flux concentration ratio (24). Although it is not directly visible on the diagram, the shape of the heat flux distribution contributes in the value of the interception factor of each reflector and in the thermal efficiency.

4.2 Future work

This doctoral thesis highlights a number of research prospects. Chapter 2 illustrated that some behaviours of solar cookers can not be described by actual physical models, especially at the beginning and end of their heating phase. These behaviours seem

to be due to the cooker thermal inertia and to the radiative exchange linearisation respectively. The general model developed in Chapter 2 attempts to propose a solution to the first problem. Although it has not been used in the present work due to its complexity, it seems promising and could be the object of further research.

Moreover practical problems remain in experimental assessment procedures. A large number of issues had already been identified, notably: mass and type of fluid; container geometry, thermal characteristics and filling rate; cold/hot start; measurement frequency; etc. This work adds some more ones. A first one is linked to the work presented above on the modelisation of solar cooker: how to experimentally estimate the thermal mass/inertia of a cooker and the heat transfer efficiency between its different parts?
Another issue is raised on the topic of the acceptance angle of a solar cooker (closely related to the required tracking frequency): how to take it into account in the efficiency formulation to compare all cooker types on the same basis? A box-type solar cooker without external reflectors has an acceptance angle close to 90° (it can collect all the global normal irradiance), an imaging concentrating-type solar cooker has an acceptance angle close to 0° (it can only collect the direct normal irradiance), a non-imaging concentrating-type solar cooker has an acceptance angle in between those latter. If non-imaging concentrators were not existing, it would have been sufficient to give a standard value to the ratio I_{DN}/I_{GN}.
As last issue, how to give the performance of cooker which aperture area changes throughout the year?
A particular attention should be put on modelling and experimental aspects, in order to allow fine characterisation of the very wide varieties of solar cookers with simple procedure.

Chapter 3 mentions the limits of the method used to measure the concentrated heat flux delivered by a Scheffler reflector. Observations of the heat flux distribution of Scheffler reflector should be multiplied in order to complete the dataset and allow to understand the importance of each parameter on the results. To do so, a very accurate experimental method still need to be developed.
The Scheffler reflector is a very ingenious and useful device. Nevertheless, it is not widespread around the world except in India. Its fabrication process remains complex and its bending adjustment remains manual. Studying the mechanical structure may lead to simplify the fabrication and to automate its bending. As bending is the characteristic of Scheffler reflectors which makes all their added value, one could try to associate other geometries with bending. Finally, associating Scheffler reflectors with secondary optics appears as a good way to reach high temperature and ease building integration.

For Le Presage's cooker, several areas for improvement have been highlighted. The secondary optics remains to optimise but it is the next step after the development of a model for the Scheffler reflector. Indeed, a numerical model is currently developed on the Soltrace open-source software. Based on the experimental data presented in this thesis, it has been used to carry out a sensitivity analysis of the Scheffler reflector to various parameters. I have made a significant contribution to the work that my



Figure 4.2 – Prototype of cooker without secondary reflector.

research team is carrying out on this topic and a part of the work realised is added in Appendix 5.6.

In addition, prototypes have already been developed to give greater flexibility in the location of the cooktop in relation to the Scheffler reflector. For example, a system without secondary optics (Figure 4.2) has been produced. Its circular target was intended to absorb the concentrated heat flux and transmit it by conduction to the top of the cook-top. However, the moderate conductivity of cast-iron combined with manufacturing constraints and high heat losses have rendered this prototype ineffective.

Several non-imaging secondary reflectors (Figure 4.3) have also been fabricated and are currently tested.

Finally, a numerical energy analysis of the future building of Le Presage has been carried out on Pleiades software (see Appendix 5.7) and sensors will enable an experimental assessment of the performance of the building as well as of the impact of the cooking system on the comfort in the building.

With its content, this doctoral thesis attempts to improving our knowledge of the Scheffler reflector, a technology that could see significant development in the years to come.

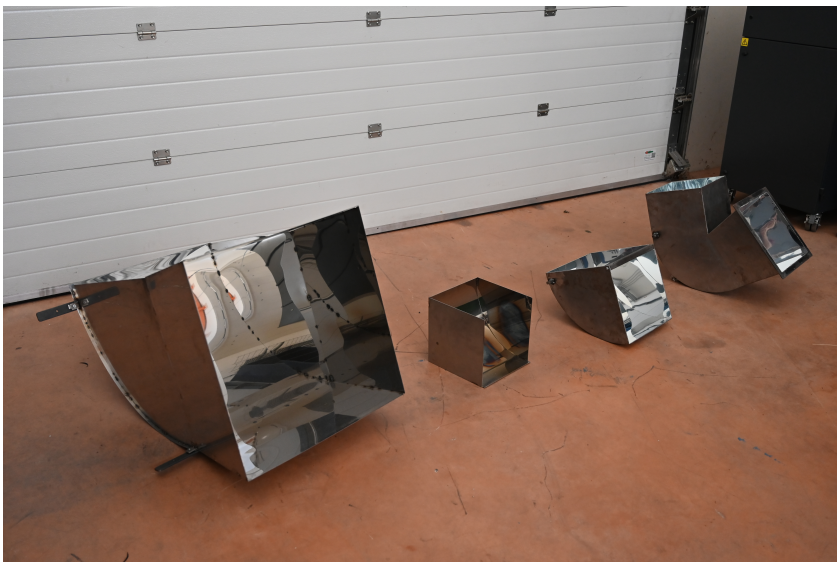

Figure 4.3 – Prototypes of non-imaging reflectors.

5 Appendices

Summary

5.1 Heat flux estimation with thermocouples . . . 96
5.2 Paint application, absorptance and emmitance measurements . . . 105
5.2.1 Paint application . . . 105
5.2.2 Spectral emissivity and solar absorptivity estimation method . . . 105
5.2.2.1 Monochromatic emissivity measurement method . . . 105
5.2.2.2 Spectral emissivity . . . 106
5.2.2.3 Solar absorptivity: spectral emissivity for the range 250 nm - 2500 nm . . . 107
5.2.2.4 Uncertainties . . . 107
5.2.2.5 Results . . . 108
5.3 Example of results without crack in the receiver . . . 109
5.4 Summary of data for each experiment . . . 111
5.5 Influential parameters . . . 115
5.6 Open-Source Monte-Carlo-Ray-Tracing Model of realistic Scheffler Collectors . . . 117
5.6.1 Introduction . . . 117
5.6.2 Methodology . . . 118
5.6.2.1 Equations giving the position of the paraboloid's facet and the receiver . . . 120
5.6.2.2 General input parameters . . . 122
5.6.2.3 Optical input parameters . . . 122
5.6.2.4 Processing of results . . . 123
5.6.2.5 Definitions . . . 123
5.6.3 Results and Discussion . . . 124
5.6.3.1 Model of an 8 m^2 Scheffler reflector with facets and no further optical errors . . . 124
5.6.3.2 Model of an 8 m^2 Scheffler reflector with facets and optical errors so as to obtain "experimental-like" results . . . 124
5.6.3.3 Variations of the focal image with day and time . . . 127
5.6.3.4 Sensibility analysis to set-up defaults and implications for the model . . . 127
5.6.4 Conclusion . . . 136
5.6.5 Appendix 1 : continuous parabola . . . 137
5.6.5.1 Ideal focal image . . . 137

5.6.5.2 Estimate of optical errors . . . 138
5.6.6 Appendix 2 : Results with other k_{sun} . . . 138
5.6.6.1 Results for $k_{sun} = 1$ . . . 138
5.6.6.2 Results for $k_{sun} = 3$ . . . 139
5.6.6.3 Results for $k_{sun} = 5$ . . . 140
5.6.6.4 Results for $k_{sun} = 9$ . . . 140
5.7 Dynamic thermal behaviour of a solar restaurant housing two Scheffler parabolas . . . 144
5.7.1 Foreword . . . 144
5.7.2 Short description of the restaurant building . . . 144
5.7.3 Expected Building thermal performances . . . 146
5.7.4 Reference study of the building's thermal dynamic behaviour . . . 146
5.7.4.1 Reference Dynamic Thermal Simulation (DTS) parameters 146
5.7.4.2 Results of the reference Dynamic Thermal simulation . 149
5.7.4.3 Conclusions on the reference DTS . . . 149
5.7.5 Effects of a few parameters on the dynamic thermal behavior of the restaurant . . . 150
5.7.5.1 Effects of the solar caps . . . 150
5.7.5.2 Effects of the nigth-time over-ventilation . . . 151
5.7.5.3 Effects of the heat release by customers . . . 152
5.7.6 Conclusions & perspectives . . . 153

5.1 Heat flux estimation with thermocouples

This appendix consists of a conference paper presenting an experimental method developed prior to the one presented in Chapter 3. The test benches are similar, but the measurements are made in transient mode, thermocouples are used to measure the temperature at the receiver, and the inverse techniques use an *a priori* form for the heat flux distribution (two-dimensional Gaussian).

Estimation par méthode inverse du flux absorbé par une plaque en fonte destinée à la cuisson solaire

Estimation of the flux absorbed by a cast iron slab for solar cooking purpose

Gabriel GUILLET, Jonathan GASPAR, Thomas FASQUELLE, Séverine BARBOSA, Benjamin KADOCH, Yannick PIZZO, Fabrice RIGOLLET, Christophe LE NILIOT, Jean-Laurent GARDAREIN

Aix Marseille Univ, CNRS, IUSTI, Marseille, France

Résumé - Dans le cadre de l'étude d'un cuiseur solaire de Scheffler, une estimation du flux de rayonnement absorbé par sa plaque de cuisson en fonte est recherchée. Un banc d'expérimentation constitué d'un panneau rayonnant et d'une plaque en fonte équipée de thermocouples est développé. Une méthode d'inversion utilisant la méthode des gradients conjugués couplée à l'état adjoint est aussi présentée. Elle est vérifiée sur un cas numérique puis appliquée sur les mesures de température du banc d'essai. Bien que des écarts soient constatés, les résultats sont encourageants et quelques améliorations permettront l'utilisation de cette méthode pour caractériser les performances des cuiseurs solaires.

Mots-clés : technique inverse ; estimation de flux ; cuiseur solaire ; métrologie ; expérience.

Abstract - In the context of a study about Scheffler solar cooker, we investigate a method to estimate the absorbed thermal radiation by the cooking slab. An experimental bench consisting of a radiant panel facing a cast iron plate provided with thermocouples was set up. An inversion method using the conjugate gradient method and the adjoint state is presented. This method is verified on a numerical case and then applied to the temperature measurements of the test bench. Although some discrepancies are noted, the results are encouraging and some improvements could allow using this method to characterize the performance of solar cookers.

Keywords: inverse method; flux estimation; solar cooker; metrology; experiment.

Nomenclature

c_p	capacité thermique massique, $\mathrm{W.K^{-1}.kg^{-1}}$
e	épaisseur, m
$F_{\Gamma_1 \to amb}$	facteur de forme de Γ_1 vers amb
l	longueur, m
h	coefficient de convection, $\mathrm{W.K^{-1}.m^{-2}}$
L	largeur, m
n	normale extérieure à la surface
t	temps, s
T	température, K
(x, y, z)	coordonnées spatiales, m
(x_c, y_c)	centre de la fonction gaussienne, m
α	absorptivité
Γ_1	limite exposée au flux
Γ_2	limite non exposée au flux
∇	opérateur nabla
ε	émissivité totale
θ	inclinaison de la fonctions gaussienne, rad
λ	conductivité thermique, $\mathrm{W.K^{-1}.m^{-1}}$
ρ	masse volumique, $\mathrm{kg.m^{-3}}$
σ	constante de Stefan-Boltzmann, $\mathrm{W.m^{-2}.K^{-4}}$
σ_x	écart-type selon x de la gaussienne, m
σ_y	écart-type selon y de la gaussienne, m
$\sigma_{0,01}$	écart-type d'un bruit de mesure, $^\circ\mathrm{C}$
φ	flux surfacique, $\mathrm{W.m^{-2}}$
abs	absorbé
amb	ambiant
inc	incident, reçu

https://doi.org/10.25855/SFT2021-059

1. Introduction

L'invention du "four boîte" date du XVIIIe siècle [1]; ce qui n'était à ce moment qu'une curiosité scientifique s'est vu peu à peu améliorée et déclinée en plusieurs versions. Au cours de l'histoire, l'intérêt pour les cuiseurs solaires s'est justifié de deux façons. D'une part, ils restent généralement peu coûteux, simples à fabriquer, à utiliser et à entretenir; ils sont utilisables en toute place recevant le rayonnement direct du soleil et peuvent être transportables. D'autre part, les cuiseurs solaires peuvent engendrer d'importantes économies de ressources (temps, argent, matières premières, ressources énergétiques). Pour ces raisons, il existe aujourd'hui des applications dans les domaines de la restauration, de l'agroalimentaire et de l'industrie [2, 3].

Alors que les cuiseurs solaires à concentration paraboliques atteignaient une plus grande puissance de cuisson que les autres types de cuiseur [4], ils présentaient jusque là l'inconvénient d'avoir un foyer optique mobile selon la saison. Le réflecteur de Scheffler est venu pallier ce défaut en compensant la variation saisonnière de la hauteur du soleil par une déformation du réflecteur primaire [5]. Il est alors devenu possible d'alimenter la cuisine d'un bâtiment en énergie solaire.

Dans le cadre du projet "Conception de restaurants optimisés pour la cuisine solaire" (CROCS) et en collaboration avec la Société Le Présage [6], un cuiseur de ce type et son intégration dans un restaurant à haute qualité environnementale sont étudiés. Une méthode de caractérisation des performances énergétiques du système est notamment en cours de développement.

Dans ce contexte, une étude de l'efficacité de la partie optique du cuiseur solaire est actuellement en cours, un intérêt particulier étant porté au flux solaire reçu, φ_{inc}, par la plaque en fonte. Mesurer un flux radiatif incident sans le perturber peut être complexe, d'autant plus lorsqu'il est inhomogène et que son intensité est relativement importante. Une solution est donc d'utiliser des techniques inverses pour estimer le flux absorbé par la plaque $\varphi_{abs} = \varepsilon\varphi_{inc}$ à l'aide d'une instrumentation simple, peu coûteuse et peu intrusive. Dans cet article, nous présenterons la méthode inverse utilisée, sa validation numérique ainsi qu'une application sur un banc d'expérimentation.

2. Cuiseur, banc d'essai et métrologie

Le cuiseur solaire évoqué précédemment est constitué d'un réflecteur primaire de Scheffler, d'un réflecteur secondaire et d'une plaque en fonte. La plaque en fonte joue le rôle d'absorbeur sur sa face inférieure et le rôle de plaque de cuisson sur sa face supérieure. Une fois le flux de rayonnement absorbé, le transfert thermique a lieu par conduction de sa face inférieure vers sa face supérieure, mais aussi de son milieu vers sa périphérie. Le cuisinier peut ainsi utiliser le centre de la plaque très chaud pour saisir ses aliments et les bords tièdes pour les laisser mijoter.

Afin de valider la méthode proposée, un banc de mesure simplifié a été élaboré. Il est constitué d'un panneau rayonnant placé face à la plaque en fonte positionnée verticalement. Des thermocouples mesurent la température sur la face de la plaque non exposée au flux.

Le panneau rayonnant, alimenté au propane, a une surface émettrice carrée de $0{,}50\ \mathrm{m}$ de côté. La plaque de cuisson, en fonte, a été meulée sur la face destinée à être utilisée par le cuisinier. C'est un parallélépipède de $1{,}00\ \mathrm{m}$ de long, $0{,}60\ \mathrm{m}$ de large et de $13 \pm 1\ \mathrm{mm}$ d'épaisseur. Ses propriétés thermophysiques sont récapitulées dans le tableau 1 . La face exposée au flux Γ_1 sera appelée "face avant", et la face non exposée et les bords Γ_2 seront nommés "face arrière".

Les capteurs de température sont des thermocouples chemisés de type K de $1{,}5\ \mathrm{mm}$ de diamètre. Le système d'acquisition a une résolution de $0{,}1\ ^{\circ}\mathrm{C}$ et une fréquence de mesure de

Propriétés de la fonte (supposée former un corps gris)	(T exprimée en °C)
Masse volumique	$\rho = 7194 - 0,0199 \cdot T$
Capacité thermique massique	$c_p = 450,5 + 0,4714 \cdot T$
Conductivité thermique	$\lambda = 49,85 - 0,0106 \cdot T$
Emissivité (= absorptivité) totale	$\varepsilon = 0,65$

Tableau 1 : *Propriétés thermophysiques supposées de la plaque en fonte [7, 8, 9].*

1 Hz. Il est caractérisé par une incertitude type égale à $\pm(\frac{0,4}{100} \cdot T + 0,5)$ °C. Les thermocouples sont fixés en dix emplacements sur la surface de la plaque à l'aide de bandes adhésives en aluminium. Un thermocouple supplémentaire est fixé sur un bord de la plaque de manière à être directement exposé au flux, donnant ainsi les instants exacts d'allumage et d'extinction du panneau rayonnant. Par soucis de commodité, on écrira aussi bien "thermocouple 10" ou "Th10" et "courbe 10" pour désigner respectivement le thermocouple fixé au point 10 et la courbe de température obtenue grâce à ce thermocouple.

Un fluxmètre commercial CAPTEC de type Captherm "flux total" est utilisé pour réaliser des mesures ponctuelles. L'incertitude type qui lui est associée est ± 3 %.

Pour l'expérience, la distance entre le panneau rayonnant et la plaque en fonte est fixée à $0{,}460 \pm 0{,}005$ m. Au préalable, le flux reçu par la plaque est mesuré à l'aide du fluxmètre placé successivement à la position de chaque thermocouple. Ensuite, un créneau de puissance radiative est appliqué sur la plaque de t_a (allumage du panneau rayonnant) à t_b (extinction et éloignement) et sa réponse thermique est enregistrée. Une attention particulière est portée sur l'atteinte du régime quasi-permanent pendant et après le créneau.

3. Modèle direct

Connaissant le flux incident $\varphi_{inc}(x, y, t)$ et les propriétés thermophysiques de la plaque (tableau 1), il est possible de déterminer la température $T(x, y, z, t)$ en tout point $M(x, y, z)$ de la plaque Ω : il s'agit du problème direct décrit par les équations ci-dessous.

On note $\boldsymbol{n}$ la normale à la surface au point $M(x, y, z)$, et pour une meilleure compréhension on note aussi : $T(x, y, z, t) = T,\ \rho(T) = \rho,\ c_p(T) = c_p,\ \lambda(T) = \lambda,\ \varphi_{inc}(x, y, t) = \varphi_{inc}$.

Pour tout $M \in \Omega$, on a :

$$\rho c_p \frac{\partial T}{\partial t} - \nabla \cdot (\lambda \nabla T) = 0. \tag{1}$$

Dans les mêmes dispositions et à $t = 0$, la condition initiale s'écrit :

$$T = T_{amb}. \tag{2}$$

Pour tout $M \in \Gamma_1$ et pour $t_a < t < t_b$, la condition à cette limite s'écrit :

$$-\lambda \frac{\partial T}{\partial n} = -\varepsilon \varphi_{inc} + \varepsilon \sigma T^4 - F_{\Gamma_1 \to amb}\, \varepsilon \sigma T_{amb}^4 + h(T - T_{amb}). \tag{3}$$

Pour tout $M \in \Gamma_1$ et pour $t > t_b$, de même que pour tout $M \in \Gamma_2$ et quel que soit t, la condition à ces limites s'écrit :

$$-\lambda \frac{\partial T}{\partial n} = \varepsilon \sigma (T^4 - T_{amb}^4) + h(T - T_{amb}). \tag{4}$$

On suppose que l'environnement radiatif est assimilable à un corps noir de température constante, uniforme et égale à la température ambiante. De même, on présume que le coefficient de convection est constant et uniforme sur toute la surface de la plaque.

On admettra enfin que le flux absorbé par la surface de la plaque $\varphi_{abs} = \varepsilon\varphi_{inc}$ peut être décrit par une fonction gaussienne à deux écarts types pouvant pivoter sur son axe et définie par :

$$\varphi_{abs}(x,y) = \varphi_{abs,max} \exp\left(-(a(x-xc)^2 + 2b(x-x_c)(y-y_c) + c(y-yc)^2)\right) \qquad (5)$$

avec : $a = \frac{\cos^2(\theta)}{2\sigma_x^2} + \frac{\sin^2(\theta)}{2\sigma_y^2}$ $\quad b = \frac{\sin(2\theta)}{4\sigma_x^2} + \frac{\sin(2\theta)}{4\sigma_y^2}$ $\quad c = \frac{\sin^2(\theta)}{2\sigma_x^2} + \frac{\cos^2(\theta)}{2\sigma_y^2}$.

Le problème direct est résolu par le programme CAST3M [10] à l'aide de la méthode des éléments finis. Le maillage est formé de $1\ 440$ éléments quadratiques cubiques à 8 noeuds, mesurant chacun $5\ \mathrm{cm}$ de côté dans le plan (xy), et il y a 6 couches d'éléments dans l'épaisseur de la plaque.

4. Problème inverse, méthode d'inversion et validation sur un cas numérique

Le problème direct étant défini, il reste maintenant à estimer le flux absorbé $\varphi_{abs} = \varepsilon\varphi_{inc}$ en fonction des températures mesurées sur la face arrière de la plaque. Résoudre ce problème inverse revient à minimiser l'écart au sens des moindres carrés (fonction coût) entre l'effet simulé par le modèle direct et l'effet mesuré expérimentalement. Pour résoudre ce problème mal posé et non linéaire, nous avons opté pour la méthode des gradients conjugués couplée à l'état adjoint [11]. La résolution du problème par itération nécessite de connaître, à chaque itération, la profondeur et la direction de descente. Ces dernières sont respectivement obtenues grâce au problème de sensibilité et au problème adjoint non présentés ici [11]. L'utilisation d'une méthode de résolution par itération implique aussi de définir un critère d'arrêt. Dans notre cas, le calcul s'arrête dès que la valeur de la fonction coût est inférieure à un seuil correspondant au niveau de bruit ou bien lorsque l'algorithme a convergé vers une solution stable.

Comme nous ne disposons que de dix mesures ponctuelles, l'*a priori* sur la distribution du flux défini précédemment est nécessaire. Ainsi, la résolution du problème inverse revient à estimer l'évolution temporelle du maximum de cette fonction ainsi que des paramètres décrivant sa forme.

Avant de pouvoir traiter des données expérimentales, il est nécessaire de réaliser une validation numérique de la méthode d'inversion. Une sollicitation est entrée dans le modèle direct et un bruit de mesure est ajouté aux températures obtenues. La méthode d'inversion est ensuite appliquée sur ces mesures simulées. Afin d'éviter l'*inverse crime*, l'expérience numérique est réalisée à l'aide d'un modèle numérique différent (maillage, méthode de résolution, logiciel...) de celui sur lequel repose le problème inverse (Matlab ®). Ici, la sollicitation originale est un créneau de flux absorbé de $15\ \mathrm{kW.m^{-2}}$ et d'une durée de $450\ \mathrm{s}$. A partir de celle-ci, une réponse thermique sans bruit est simulée et trois réponses thermiques supplémentaires sont créées en y ajoutant un bruit de mesure d'écart-type 0,05 ; 0,1 et 1 °C respectivement.

L'évolution des fonctions coût des cas numériques a été tracée dans la figure 1 . On observe que les fonctions coûts diminuent avec les itérations et se rapprochent de leurs critères d'arrêt (lignes pointillés). Néanmoins seul le cas avec un bruit d'écart type de 1 °C atteint son seuil, tandis que les autres cas présentent plus de difficultés pour atteindre le leur. Le cas sans bruit de mesure reste même à un niveau équivalent aux cas avec un faible bruit de mesure. Ce comportement s'explique en observant les résidus du cas sans bruit de mesure sur la figure 2 . On constate que les principaux écarts entre les courbes du modèle et de l'expérience numérique se situent principalement au début et à la fin du créneau : ce phénomène est dû aux limites de la modélisation numérique. A l'exception de ces instants les résidus sont faibles et inférieurs à $0{,}2$ °C. Ceci est à comparer à la température de la plaque qui varie entre 20 °C et 300 °C.

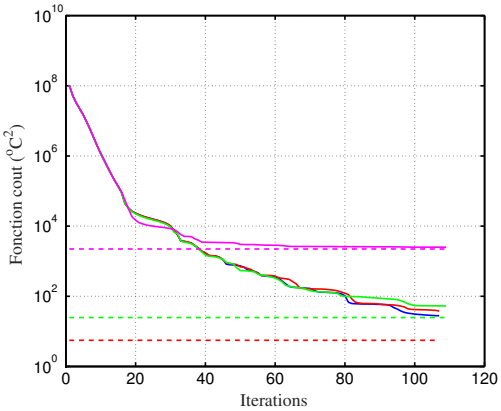

Figure 1 : *Fonctions coût des quatre cas numériques.*

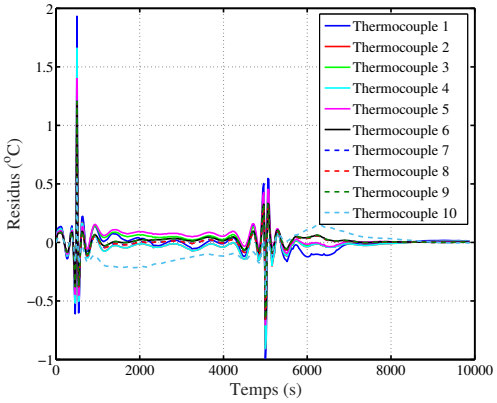

Figure 2 : *Résidus pour le cas numérique sans bruit.*

La figure 3 présente l'évolution temporelle du flux maximum absorbé estimé pour chacun des cas numériques ainsi que l'évolution du flux exact en noir. On observe que les courbes se superposent et que les instants de montée et descente sont bien retrouvés. Les oscillations dues aux bruits de mesure sont également faibles et seulement visibles pour le cas présentant un important bruit de mesure (20 fois supérieur au bruit expérimental). Les paramètres estimés qui caractérisent la forme gaussienne du flux, récapitulés dans le tableau 2 , sont quasi égaux entre eux et avec les valeurs exactes quel que soit le bruit de mesure. Tout ceci valide la méthode d'inversion, démontre sa robustesse vis à vis du bruit de mesure et justifie son utilisation quant au cas expérimental.

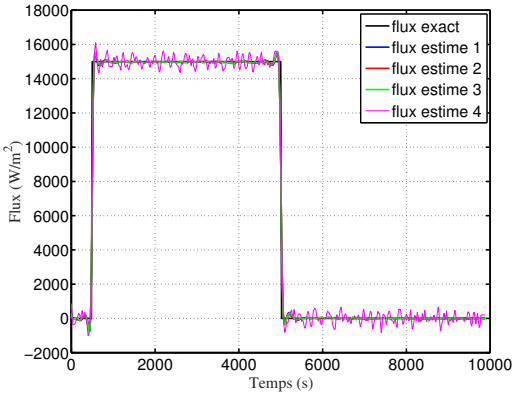

Figure 3 : *Flux absorbés estimés sans bruit (1), avec écart-type de 0,05 °C (2), avec écart-type de 0,1 °C (3) et avec écart-type de 1 °C (4), superposés sur la sollicitation originale (noté "flux exact").*

Paramètres	Unités	σ_{exact}	σ_0	$\sigma_{0,05}$	$\sigma_{0,1}$	σ_1
$\varphi_{abs,max}$	$\mathrm{kW.m^{-2}}$	15,00	14,98	14,98	14,97	15,00
x_c	m	0,500	0,500	0,500	0,500	0,500
y_c	m	0,300	0,300	0,300	0,300	0,300
σ_x	m	0,250	0,250	0,250	0,250	0,250
σ_y	m	0,350	0,352	0,352	0,353	0,351
θ	rad	0,000	0,000	0,000	0,000	0,007

Tableau 2 : *Paramètres de la fonction gaussienne estimés pour plusieurs niveau de bruit : flux maximum moyen ($\varphi_{abs,max}$), position du centre (x_c, y_c), écart-types (σ_x, σ_y) et angle de rotation (θ).*

5. Résultats et interprétation

Avant d'inverser nos mesures expérimentales, nous nous sommes intéressés à la validité de l'*a priori* utilisé pour décrire le flux absorbé. Pour cela nous avons tout d'abord réalisé un calcul de facteurs de forme pour déterminer la distribution spatiale du flux incident lorsqu'une plaque rayonnante de température uniforme fait face à notre plaque. L'intensité du rayonnement reçu par la plaque et normalisée par sa valeur maximale est présentée en figure 4 où la forme obtenue correspond bien à une Gaussienne qui, dans ce cas simplifié, est axisymétrique avec un écart-type de $32{,}5$ cm.

En complément, les mesures directes du flux incident présentées sur la figure 5 confirment ce résultat et appuient l'*a priori* de forme énoncé dans le problème inverse. Cette forme semble être centrée un peu plus haut et à gauche du point 1, situé au milieu de la plaque, ce qui est tout à fait cohérent avec le placement du panneau rayonnant par rapport à la plaque.

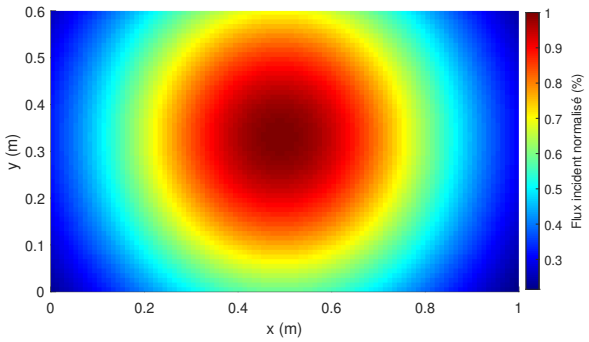

Figure 4 : *Répartition de l'intensité du flux incident normalisé, obtenue par calcul de facteurs de forme.*

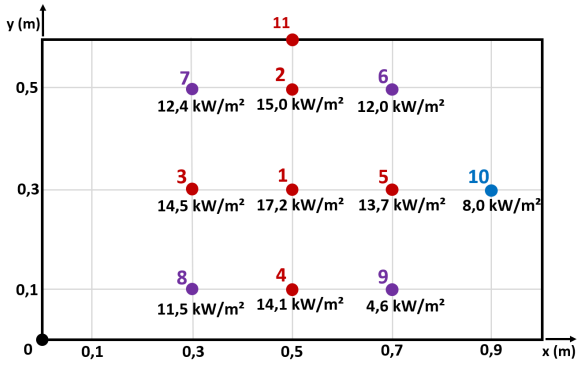

Figure 5 : *Résultats de mesures ponctuelles du flux incident φ_{inc}.*

La figure 6 illustre l'évolution des températures obtenues durant l'expérience. Les courbes de température des points 7 et 8 ont été retirées car les thermocouples se sont décollés de la plaque pendant l'expérience. On retrouve le fait que la tache de rayonnement n'est pas parfaitement centrée sur la plaque. Les valeurs mesurées au point 2 sont supérieures à celles mesurées au point 4 alors qu'ils sont à équidistance du centre de la plaque. De même pour les points 3 et 5.

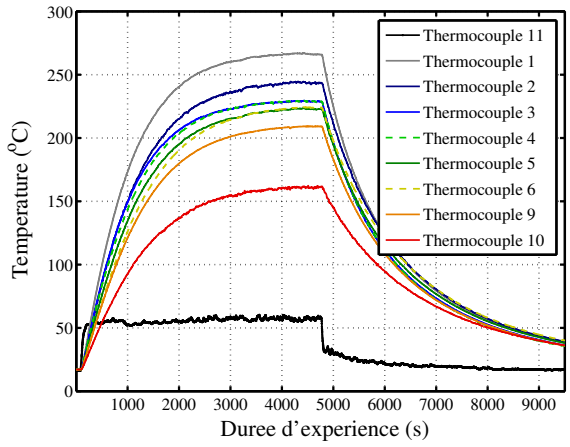

Figure 6 : *Évolution des températures mesurées à la surface de la plaque (face arrière).*

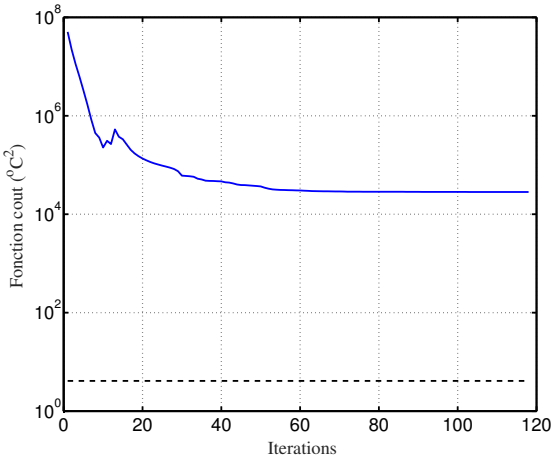

Figure 7 : *Évolution de la fonction coût du cas réel au fur et à mesure des itérations.*

L'évolution de la fonction coût du cas expérimental est tracée sur la figure 7 . Elle converge vers une valeur supérieure d'environ quatre ordres de grandeur au-dessus du niveau de bruit

(droite en pointillés) et les résidus sont plus grands que pour les cas numériques. De plus, ces résidus sont signés, preuve que les mesures et/ou le modèle présentent un biais. Il faut néanmoins modérer ce constat en insistant sur le fait que ces écarts représentent une erreur d'au plus $5\ \%$ sur l'estimation de flux.

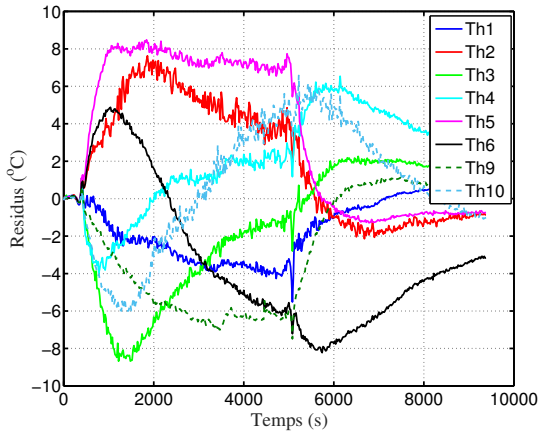

Figure 8 : *Résidus entre les températures estimées et les températures mesurées expérimentalement.*

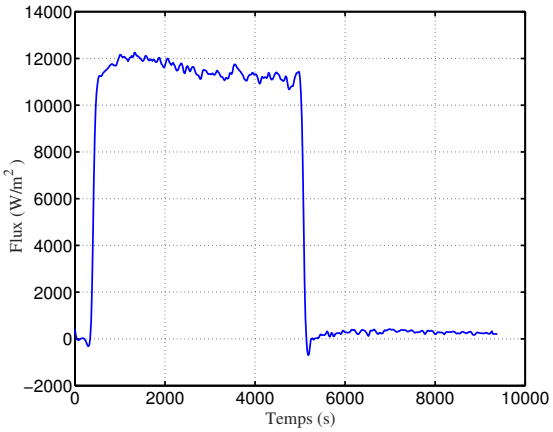

Figure 9 : *Évolution du flux maximal absorbé estimé durant l'expérience réelle.*

La figure 9 représente le flux absorbé estimé au maximum de la fonction gaussienne. On reconnaît les instants d'allumage et d'extinction du panneau rayonnant. On remarque une légère diminution du flux pendant le créneau qui est cohérente avec les observations expérimentales : la détente dans la bouteille de gaz entraîne un refroidissement important ; ceci influe sur le débit de gaz et donc sur le flux de chaleur émis par le panneau rayonnant. La valeur du flux absorbé estimé, environ égale à $11{,}5\ \mathrm{kW.m^{-2}}$, correspond à la valeur du flux incident mesuré avec le fluxmètre à l'absorptivité près (en supposant que $\alpha_{fluxmetre} = 1$ et $\alpha_{plaque} = \varepsilon_{plaque} = 0,65$). Pendant la phase de refroidissement, on observe un flux positif presque nul, ce qui permet de valider l'ordre de grandeur du coefficient d'échange convectif fixé à $7\ \mathrm{W.m^{-2}.K^{-1}}$.

Les paramètres estimés caractérisant la forme du flux absorbé sont récapitulés dans le tableau 5. On obtient finalement des écarts types de $0{,}29\ \mathrm{m}$ et $0{,}28\ \mathrm{m}$ induisant une forme proche d'une courbe gaussienne axisymétrique, comme prévu par le calcul de facteur de forme. On remarque que ces valeurs sont légèrement inférieures aux valeurs calculées. On a en effet supposé que le panneau rayonnant avait une température uniforme, ce qui expérimentalement n'est peut-être pas le cas à cause du système d'injection de gaz localisé au centre du panneau et induisant sans doute une zone centrale plus chaude que les bords. Néanmoins, avec des écarts types expérimentaux environ $10\ \%$ plus faibles que le cas théorique, les écarts restent relativement faibles. Enfin on constate que le flux est positionné près du centre avec un léger décalage vertical.

Paramètres	Unités	Estimations
$\varphi_{abs,max}$	$\mathrm{kW.m^{-2}}$	11,5
x_c	m	0,50
y_c	m	0,33
σ_x	m	0,29
σ_y	m	0,28
θ	rad	1,4

Tableau 3 : *Estimation finale des paramètres caractérisant la tache de flux expérimentale : flux maximum moyen ($\varphi_{abs,max}$), position (x_c, y_c), écarts-types (σ_x, σ_y) et angle de rotation (θ)*

6. Conclusion et perspectives

Dans cet article, nous nous intéressons à une méthode de caractérisation des cuiseurs solaires. Pour cela, nous avons présenté le banc expérimental développé et son instrumentation. Nous avons également décrit les transferts énergétiques qui ont lieu à l'intérieur et aux interfaces de la plaque en fonte du cuiseur solaire étudié via un modèle direct.

Afin de résoudre le problème inverse non linéaire et mal posé associé à ce modèle, nous avons adapté une méthode d'inversion et l'avons testé sur un cas numérique. Sa convergence, sa précision et sa robustesse par rapport au bruit de mesure ont ainsi été démontrées. L'application de cette méthode d'inversion aux mesures de température réalisées sur le banc d'expérimentation a permis d'obtenir une estimation du flux absorbé φ_{abs} par la plaque. Les caractéristiques de ce flux concordent avec les mesures expérimentales du flux incident φ_{inc} réalisées grâce à un fluxmètre commercial et avec le calcul de facteur de forme (à l'émissivité près).

Bien que le résultat obtenu soit encourageant, les résidus montrent qu'il reste des écarts à justifier et à réduire avant de pouvoir prétendre à la caractérisation de performances des cuiseurs solaires. Une meilleure connaissance des caractéristiques thermophysiques de la plaque en fonte et une prise en compte plus fine du coefficient d'échange convectif dans le modèle pourrait réduire ces écarts. De plus, l'utilisation de thermocouples brasés dans la plaque pourraient améliorer la précision des mesures et diminuer leur sensibilité aux perturbations. Une caméra infrarouge pourrait également être utilisée pour doubler les mesures de température et augmenter la fiabilité de l'estimation.

Références

[1] M. Aramesh, A review of recent advances in solar cooking technology, *Renewable Energy*, 140 (2019) 419-435.

[2] http ://www.solare-bruecke.org/index.php/fr/die-scheffler-reflektoren (site consulté le 13/01/2021)

[3] https ://www.solarcookers.org/partners/distribution-solar-cookers (site consulté le 13/01/2021)

[4] N. Kumar, An exergy based unified test protocol for solar cookers of different geometries, *Renewable Energy*, 44 (2012) 457-462.

[5] U. Oelher, The use of indigenous materials for solar conversion, *Solar Energy Materials and Solar Cells*, 33 (1994) 379-387.

[6] https ://lepresage.fr/ (site consulté le 25/01/2021)

[7] H.T. Angus, *Cast Iron : Physical and Engineering Properties (Second Edition)*, Butterworth-Heinemann (1976).

[8] R. L. Hecht, Thermal transport properties of grey cast irons, *SAE Technical Papers*, 10 (1996).

[9] D. Holmgren, Review of thermal conductivity of cast iron, *Journal of Cast Metals Research*, 18 (2005) 331-345.

[10] http ://www-cast3m.cea.fr/ (site consulté le 25/01/2021)

[11] J. Gaspar et al., First heat flux estimation in the lower divertor of WEST with embedded thermal measurements, *Fusion Engineering and Design* 146 (2019) 757-760.

Remerciements

Les auteurs remercient la Région Sud Provence-Alpes-Côtes-d'Azur et la Société Le Présage pour leur intérêt et leur soutien financier à ce projet de recherche dans le cadre du dispositif "Emplois Jeunes Doctorants".

5.2 Paint application, absorptance and emmitance measurements

5.2.1 Paint application

The surface of the plate observed by the infrared camera was painted with the special high-temperature paint Pyromark 2500 from LA-CO Industries.

It was applied to the ground face of the cast iron slab using a short nap paint roller, after cleaning with sandpaper and acetone. It was left to dry for 63 h, and was then heated for an hour using a gaz-fired radiant panel; it reached 300 °C at the middle and 200 °C on the edges. The plate was subjected to three heating cycles prior to this study. The paint flaked slightly near the centre of the plate during the 2nd cycle. However, its condition appears to have remained stable during subsequent cycles.

Concerning the characteristics of the paint, Ho *et al.* [31] have shown that the substrate to which the paint is applied has an impact on its final emissivity. In addition, Coventry and Burge [15] and Caron *et al.* [12] have respectively shown that the final emissivity of the paint also depends on the painting and curing procedures. For these reasons, complementary emissivity measurements were made and taken into account in the temperature calculation. Notably, these measurements showed that the emissivity is homogeneous on the surface of the plate despite the flaking paint.

5.2.2 Spectral emissivity and solar absorptivity estimation method

In order to estimate the solar absorptivity and the infrared emissivity of the cast iron plate, samples have been analysed by PROMES-CNRS laboratory (Odeillo, France), for a measurement of their monochromatic emissivities, then, by applying a weighted-average of the product of the emissivity and the Planck's law (for spectral emissivities) or the Sun's irradiance spectrum (for solar absorptivity), spectral values were obtained for the different bandwidths of interest.

5.2.2.1 Monochromatic emissivity measurement method

Using a variable monochromatic light source, the samples were illuminated with a given angle of incidence θ and a given wavelength λ, then the hemispheric reflectivity was estimated using an integrating sphere and two different spectrophotometers, of which the main information are given in Table 5.1. This was repeated over the entire wavelength range covered by the instruments.

From this reflectivity, considering that the material is opaque and assuming Kirchhoff's law of thermal radiation, the monochromatic directional emissivity $\varepsilon(\lambda,\theta)$ and absorptivity $\alpha(\lambda,\theta)$ can be obtained, *c.f.* equation 5.1

$$\alpha(\lambda,\theta) = \varepsilon(\lambda,\theta) = 1 - \sigma(\lambda,\theta) \tag{5.1}$$

Table 5.1 – Main information about the two spectrophotometers that were used to estimate the monochromatic reflectivities of the cast iron samples

Spectrophotometer	Perkin Elmer Lambda 950	Nicolet FTIR
Wavelength range	0.150 µm - 3.3 µm	1.25 µm – 25 µm
Wavelength step	10 nm	variable (3 nm - 850 nm)
Absolute uncertainty	0.005 (k=2)	0.005 (k=2)

While it is known that absorptivities and emissivities depend on direction angle [82], here they had to be assumed independent of θ.

5.2.2.2 Spectral emissivity

The estimated spectral emissivity is obtained by comparing the flux emitted by the sample, thus weighted by its monochromatic emissivities and a flux emitted by a black body at the same temperature, as illustrated in Figure 5.1, equation 5.2 and equation 5.3.

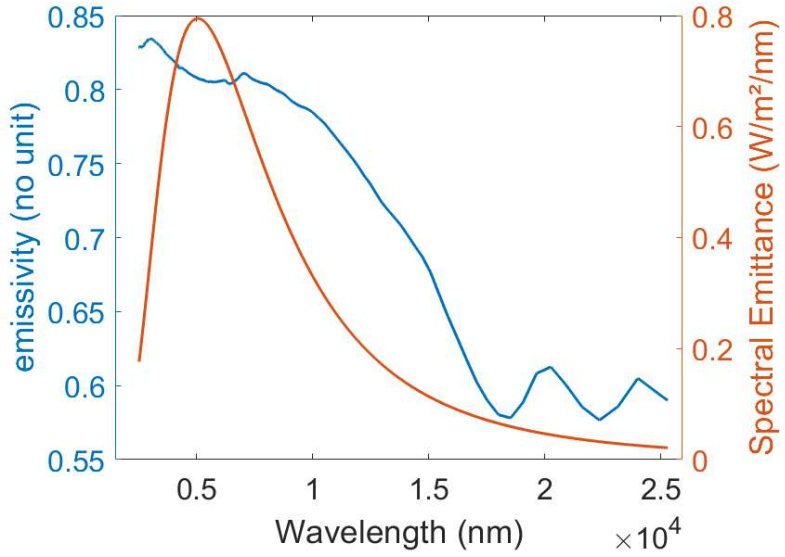

Figure 5.1 – Monochromatic emissivity of cast iron between 2.5 µm and 25 µm, and Planck spectrum of a black-body at 300 °C

$$\varepsilon(\lambda_{min} -> \lambda_{max}) = \frac{\int_{\lambda_{min}}^{\lambda_{max}} \varepsilon(\lambda) \cdot M(\lambda) \cdot d\lambda}{\int_{\lambda_{min}}^{\lambda_{max}} 1 \cdot M(\lambda) \cdot d\lambda} \tag{5.2}$$

$$M(\lambda) = \frac{2 \cdot \pi \cdot h \cdot c^2}{\lambda^5} \cdot \frac{1}{\exp(\frac{h \cdot c}{\lambda \cdot k_B \cdot T}) - 1} \tag{5.3}$$

Note that the limits of the integrals are set by the limitations of the spectrophotometer, *i.e.* $\lambda_{min} = 250\ nm$ and $\lambda_{max} = 25\ \mu m$ and this affects the uncertainties on the

estimate.

5.2.2.3 Solar absorptivity: spectral emissivity for the range 250 nm - 2500 nm

The general equation for solar absorptivity that is estimated from the data is obtained by comparing a non-concentrated incident solar flux absorbed by the sample and the solar flux that would be absorbed by a black body, as shown in equation 5.4 and Figure 5.2.

$$\alpha_{solar} = \frac{\int_{\lambda_{min}}^{\lambda_{max}} I_{sun}(\lambda) \cdot \alpha(\lambda) \cdot d\lambda}{\int_{\lambda_{min}}^{\lambda_{max}} I_{sun}(\lambda) \cdot 1 \cdot d\lambda} \tag{5.4}$$

The solar spectral irradiance $I_{sun}(\lambda)$ are those of ASTM G-173-03, obtained through

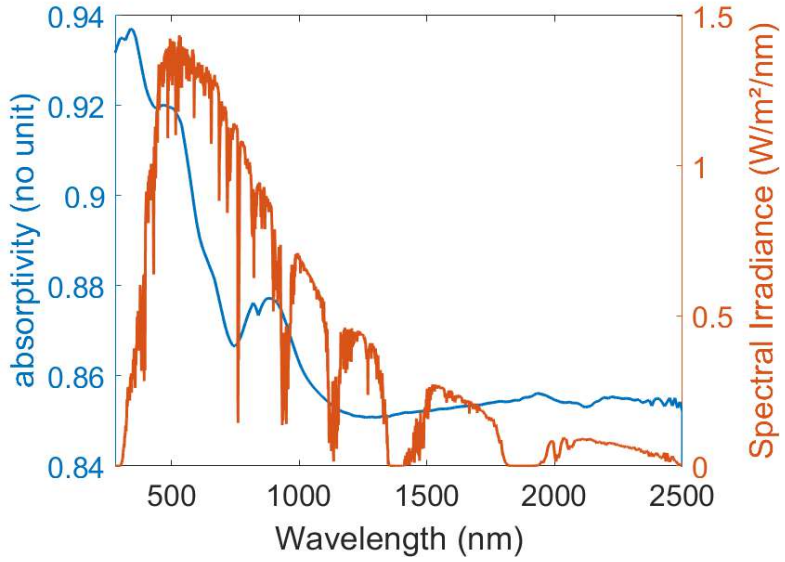

Figure 5.2 – Monochromatic emissivity/absorptivity of cast iron between 0.25 µm an 2.5 µm, ASTM G-173-03 solar spectrum

the NREL website.

5.2.2.4 Uncertainties

To estimate spectral emissivities/absorptivities, the integrations are performed over all the interval of wavelengths that is made possible by the spectrophotometers. However, taking the approximation that about 96 % of the spectrum's energy lays within $\lambda_{min} = \lambda(M_{max})/2$ and $\lambda_{min} = \lambda(M_{max}) \cdot 5$, with $\lambda(M_{max})$ the wavelength for which the emittance M is maximum, which depends on the Wien constant and the temperature of the object, *c.f.* equation 5.5,

$$\lambda(M_{max}) = \frac{\sigma_W}{T} = \frac{2.898 \cdot 10^{-3}}{T} \tag{5.5}$$

one can see that the spectral emissivity estimate for low temperatures will lack a non-negligible amount of data. The related uncertainty has therefore been set as the emittance difference between the black-body spectrum in the range of λ_{min} - λ_{max} and the emittance of the whole black-spectrum. Results vary between +2.7 % (@ 500 °C) and -16 % (@ 20 °C). Propagation from other uncertainties, *i.e.* deviation of the monochromatic emissivity measurements, differences between actual spectrums and reference ones, and directional dependence of emissivity, are difficult to estimate and are considered relatively negligible in comparison to these previous estimates, however, a 2 % relative uncertainty has been added to take them into account.

5.2.2.5 Results

The emissivity estimation has been performed for different blackbody temperatures, and results are gathered in Table 5.2. It should be known that the effect of temperature, varied from ambient to 500 °C, on the monochromatic emissivity spectrums were negligible. Because the cast iron slab is mainly above ambient and since the uncertainties

Table 5.2 – Spectral emissivity and absorptivity results.

T	20 °C	100 °C	200 °C	300 °C	400 °C	500 °C	5777K
$\lambda(M_{max})$ [µm]	9.89	7.77	6.13	5.06	4.31	3.75	0.50
$\lambda(M_{max})/2$ [µm]	4.95	3.89	3.06	2.53	2.15	1.88	0.250
$\lambda(M_{max})\cdot 5$ [µm]	49.5	38.9	30.6	25.3	21.5	18.8	2.50
$\varepsilon(\lambda_{min}-\lambda_{max})$	0.71	0.74	0.76	0.78	0.79	0.80	0.88
$u(\varepsilon)$	-0.16/0.01	-0.10/0.02	-0.06/0.02	-0.04/0.02	-0.03/0.02	-0.03/0.02	-0.02/0.02

on the values at low temperature are high, an average value of 0.77 +0.02/-0.05 has been chosen for the spectral emissivity. Note that his value should slightly vary across the slab but it has been set as constant for convenience.

5.3 Example of results without crack in the receiver

As indicated in Section 3.2.5, the crack in the receiver for the 14 June 2022 experiment is visible on the temperature map and causes a small wave on the heat flux map. A new receiver was used for the other experiments. Taking the data from the first measurement carried out on 22 March 2023, the temperature map shows no discontinuity (Figure 5.3) and the heat flux map shows "smoother" waves which are due to the numerical method (Figure 5.4).

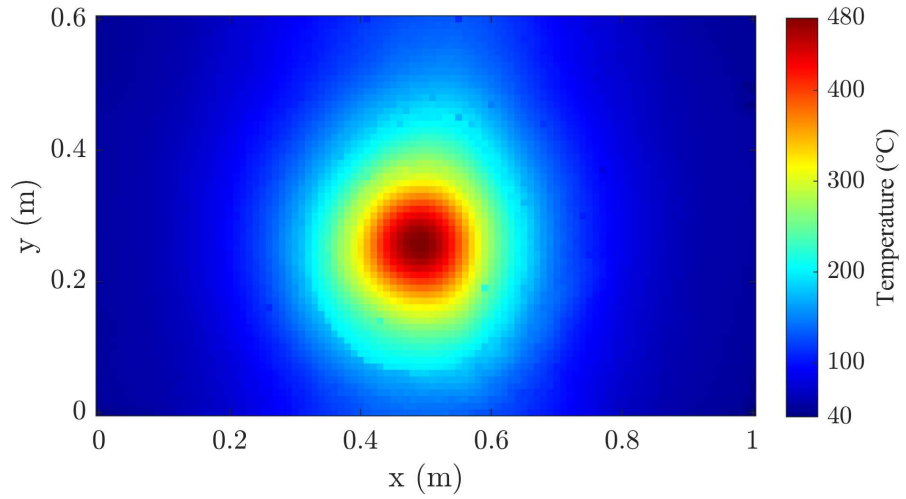

Figure 5.3 – Experimental temperature field obtained with the infrared camera for the first measurement on 22 March 2023.

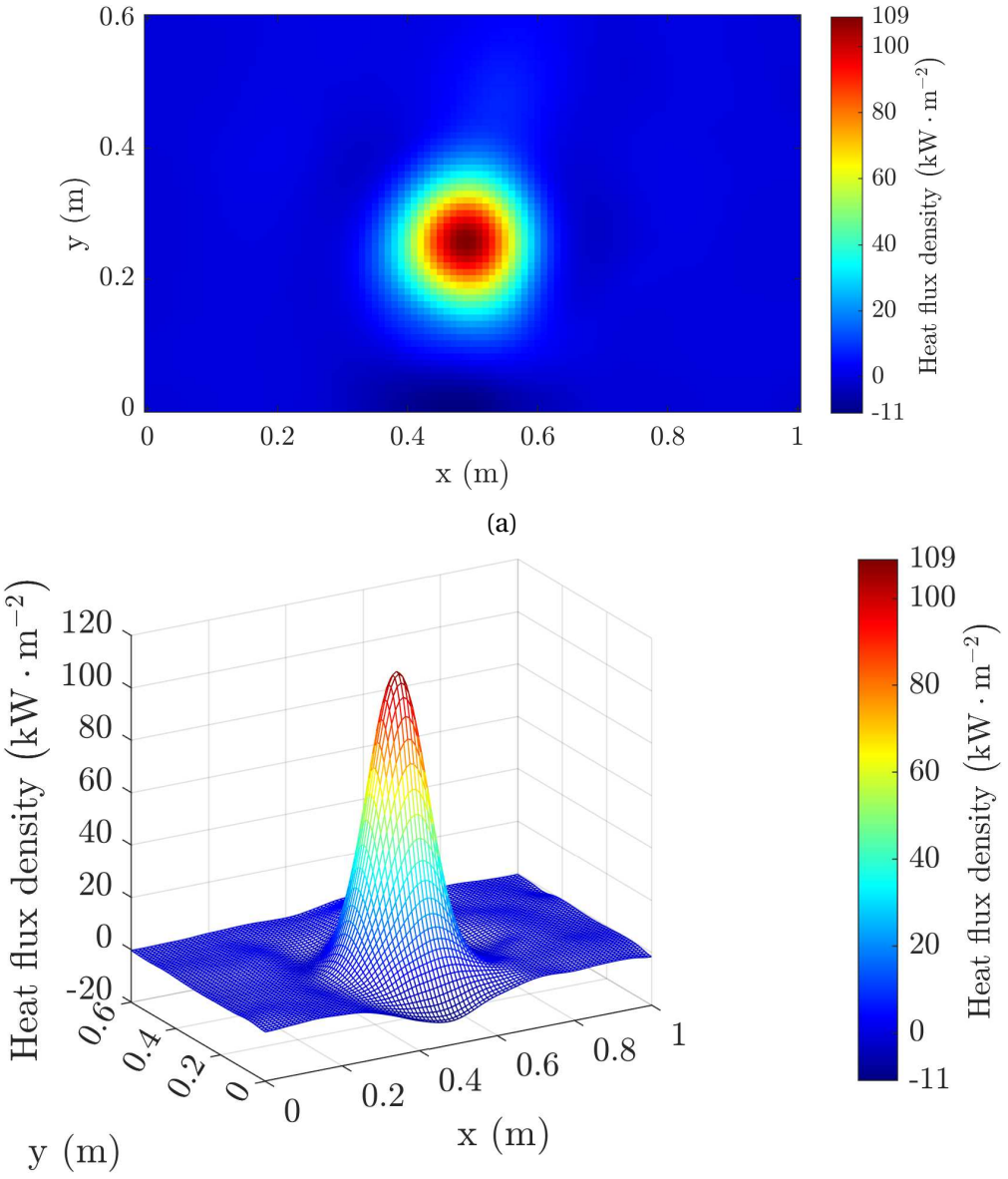

Figure 5.4 – Experimental heat flux map in a 2D representation (a) and in a 3D representation (b) for the first measurement on 22 March 2023.

5.4 Summary of data for each experiment

This appendix summarises all the information, measurements and results of the experiments in Tables 5.3, 5.4, 5.5 and 5.6.

Table 5.3 – Data of the experiment on 14 June 2022.

General information				
Date (dd/mm/yyyy)	14/06/2022			
Solar time (hh:mm)	11:14	11:32	11:57	12:52
Aperture (m^2)	4.3			
Environment data				
DNI ($W \cdot m^{-2}$)	900	902	904	907
Air temperature (°C)	29.5	28.9	30.2	31.2
Wind velocity ($m \cdot s^{-1}$)	0.5	1.0	0.9	0.5
Experimental data (thermography and inverse techniques)				
h ($W \cdot m^{-2} \cdot K^{-1}$)	7	7	7	7
Max. temperature (°C)	474	476	486	485
Max. heat flux ($kW \cdot m^{-2}$)	90.8	81.1	91.1	92.9
Tot. heat flux (kW)	2.4	2.4	2.5	2.5
Efficiency (%)	61	61	63	63
Estimated parameters (two-dimensional Gaussian model)				
φ_{max} ($kW \cdot m^{-2}$)	93.2	82.6	93.5	95.4
φ_{offset} ($kW \cdot m^{-2}$)	0.3	0.1	0.3	0.3
x_c (mm)	517	515	514	508
y_c (mm)	275	278	284	297
σ_{x1} (mm)	65	69	66	69
σ_{y1} (mm)	60	65	60	58
θ (°)	72	64	60	60
Deduced data (ellipse containing 99.7 % **of the heat flux)**				
Major diameter (m)	0.389	0.416	0.398	0.413
Minor diameter (m)	0.359	0.390	0.358	0.346
Image area (m^2)	0.110	0.128	0.112	0.112
Area C.R.	40	34	39	39
Average flux C.R.	24	20	24	24

Table 5.4 – Data of the experiment on 22 March 2023.

General information					
Date (dd/mm/yyyy)	22/03/2023				
Solar time (hh:mm)	12:04	12:43	13:07	13:33	14:02
Aperture (m^2)	5.5				
Environment data					
DNI ($W \cdot m^{-2}$)	876	886	885	873	861
Air temperature (°C)	18.8	19.2	20.1	19.9	19.8
Wind velocity ($m \cdot s^{-1}$)	0.5	0.7	0.3	0.4	0.5
Experimental data (thermography and inverse techniques)					
h ($W \cdot m^{-2} \cdot K^{-1}$)	8	8	8	8	8
Max. temperature (°C)	472	469	471	463	460
Max. heat flux ($kW \cdot m^{-2}$)	111.0	96.2	105.9	98.5	91.2
Tot. heat flux (kW)	3.1	3.2	3.2	3.2	3.2
Efficiency (%)	64	65	65	67	67
Estimated parameters (two-dimensional Gaussian model)					
φ_{max} ($kW \cdot m^{-2}$)	111.2	95.3	105.4	97.0	90.0
φ_{offset} ($kW \cdot m^{-2}$)	0.4	0.3	0.4	0.4	0.3
x_c (mm)	492	499	503	505	502
y_c (mm)	277	286	291	302	310
σ_{x1} (mm)	71	81	78	83	87
σ_{y1} (mm)	59	64	59	60	62
θ (°)	71	73	73	76	80
Deduced data (ellipse containing 99.7 % **of the heat flux)**					
Major diameter (m)	0.424	0.484	0.465	0.498	0.521
Minor diameter (m)	0.354	0.382	0.351	0.361	0.372
Image area (m^2)	0.118	0.145	0.128	0.141	0.152
Area C.R.	46	38	43	39	36
Average flux C.R.	30	25	28	26	24

Table 5.5 – Data of the experiments on 20 April 2023, 26 May 2023 and 19 June 2023.

General information							
Date (dd/mm/yyyy)	20/04/2023			26/05/2023			19/06/2023
Solar time (hh:mm)	11:02	11:33	12:01	12:02	13:00	13:30	11:06
Aperture (m^2)		5.0			4.4		4.3
Environment data							
DNI ($W \cdot m^{-2}$)	911	911	913	818	804	786	622
Air temperature (°C)	19.1	19.7	20.4	25.7	26.2	26.2	32.2
Wind velocity ($m \cdot s^{-1}$)	0.4	0.4	0.5	0.6	0.5	0.5	0.6
Experimental data (thermography and inverse techniques)							
h ($W \cdot m^{-2} \cdot K^{-1}$)	10	10	10	9	9	9	9
Max. temperature (°C)	461	460	460	414	403	393	317
Max. heat flux ($kW \cdot m^{-2}$)	111.1	107.6	115.8	116.9	75.2	74.4	55.7
Tot. heat flux (kW)	3.1	3.1	3.2	2.4	2.3	2.3	1.8
Efficiency (%)	68	70	70	66	66	67	69
Estimated parameters (two-dimensional Gaussian model)							
φ_{max} ($kW \cdot m^{-2}$)	116.7	112.8	121.2	120.2	76.1	75.0	58.2
φ_{offset} ($kW \cdot m^{-2}$)	−0.1	0.0	0.3	0.0	−0.2	−0.1	−0.1
x_c (mm)	492	492	492	497	505	514	491
y_c (mm)	274	273	274	278	262	258	307
σ_{x1} (mm)	76	77	74	62	79	80	79
σ_{y1} (mm)	58	59	54	53	66	65	67
θ (°)	86	86	88	54	62	65	85
Deduced data (ellipse containing 99.7 % **of the heat flux)**							
Major diameter (m)	0.455	0.461	0.445	0.371	0.474	0.481	0.473
Minor diameter (m)	0.348	0.354	0.326	0.318	0.399	0.388	0.400
Image area (m^2)	0.124	0.128	0.114	0.093	0.148	0.147	0.149
Area C.R.	40	39	43	48	30	30	29
Average flux C.R.	27	27	31	32	20	20	20

Table 5.6 – Data of the experiment on 28 June 2023.

General information							
Date (dd/mm/yyyy)	28/06/2023						
Solar time (hh:mm)	11:03	11:32	12:01	12:16	12:30	12:45	13:00
Aperture (m^2)	4.3						
Environment data							
DNI ($W \cdot m^{-2}$)	766	765	762	755	747	737	730
Air temperature (°C)	29.8	29.8	30.4	30.2	30.6	30.8	31.7
Wind velocity ($m \cdot s^{-1}$)	1.0	1.0	0.8	0.9	1.0	0.9	0.8
Experimental data (thermography and inverse techniques)							
h ($W \cdot m^{-2} \cdot K^{-1}$)	10	10	10	10	10	10	10
Max. temperature (°C)	380	377	366	359	354	348	342
Max. heat flux ($kW \cdot m^{-2}$)	81.0	74.6	65.4	81.8	62.5	56.8	55.6
Tot. heat flux (kW)	2.3	2.5	2.5	2.5	2.4	2.4	1.4
Efficiency (%)	71	76	75	76	76	76	77
Estimated parameters (two-dimensional Gaussian model)							
φ_{max} ($kW \cdot m^{-2}$)	87.1	79.4	69.1	84.3	65.3	59.3	57.9
φ_{offset} ($kW \cdot m^{-2}$)	−0.2	0.0	−0.1	0.2	0.0	0.0	0.0
x_c (mm)	501	499	501	504	507	513	524
y_c (mm)	291	280	269	259	259	258	256
σ_{x1} (mm)	77	82	88	84	90	93	94
σ_{y1} (mm)	59	62	68	55	68	73	73
θ (°)	83	86	89	91	93	95	97
Deduced data (ellipse containing 99.7 % **of the heat flux)**							
Major diameter (m)	0.464	0.493	0.529	0.501	0.539	0.556	0.562
Minor diameter (m)	0.356	0.373	0.410	0.329	0.408	0.437	0.438
Image area (m^2)	0.130	0.144	0.170	0.130	0.173	0.191	0.193
Area C.R.	33	30	25	33	25	23	22
Average flux C.R.	24	23	19	25	19	17	17

5.5 Influential parameters

The comparison between the current results and the literature shows that as soon as important parameters change, such as the size of the reflector or the date of the experiment, the experimental results differ considerably. Furthermore, the theoretical and numerical results also vary greatly depending on the assumptions made. This section therefore proposes an attempt to list the parameters influencing the results, to evaluate the limitations of the measurement method.

The size and shape of the heat flux distribution seem to have three main origins: the width of the sun, the intrinsic characteristics (or design features) of the reflector, and the reflection errors due to material manufacturing and installation. Firstly, the width of the sun implies that the sunlight arrives and is reflected in a cone. Secondly, reflector characteristics such as the size of the mirrors, its focal length, and its tilt with respect to the declination of the Sun impact the size of the heat flux distribution (without changing the angle of the cone), as they respectively limit the concentration and modify the distance between the reflector and the focal point. Finally, manufacturing and installation errors lead to an increase in the size of the heat flux distribution or a distortion of its shape. The angle of the cone in which an incident beam is likely to be reflected may increase according to the quality of the reflecting material and its cleanliness, because the reflected radiation may be slightly scattered (imperfect specularity). The shape of the heat flux distribution can be distorted by errors in the shape of the reflector due to its construction and bending; the orientation of the reflection may be deviated by misalignment of the mirrors; and system settings such as sun tracking, orientation of the reflector axis (azimuth and tilt) and the relative position of the reflector and receiving screen may also modify the shape of the heat flux distribution.

Among the latter parameters, the inclination of the receiving screen can be questioned. Indeed, a paraboloid theoretically reflects rays coming parallel to its axis at a point, whereas in reality the rays are concentrated in a zone around this point. So how to define a reception plane, improperly called the focal plane? For example, it can be vertical, normal to the axis of rotation of the reflector or normal to the bisector of the extreme rays. This choice is particularly important because distortions in the shape of the heat flux distribution will be observed depending on this choice. Nevertheless, it should be kept in mind that the characteristics of the heat flux delivered by the reflector are explored in order to improve the design of the absorber or secondary optics of a system incorporating a Scheffler reflector. Therefore, the receiving screen should be roughly representative of an absorber (e.g. it should have a fixed inclination angle). In addition, the experimental data must be comparable to the literature. In the present work, the observation plane was chosen to be vertical to facilitate the measurements.

The measurement itself could also lead to inaccuracies. A lot of work, presented in Section 3.2, has been done to make it reliable and the main parameter that could be discussed would be the convective exchange coefficient; although its order of magnitude is rather certain. Nevertheless, like any measurement method, there are

limitations. In this case, the method leads to an almost negligible spatial smoothing of the heat flow variations, due to lateral conduction in the cast iron slab. Indeed, the phenomenon is taken in consideration in the thermal model of the cast-iron slab. Moreover, this lateral heat transfer is low due to the small thickness of the slab and its conductivity. Finally, it is not expected to observe abrupt heat flux variations given the size of the mirrors of the reflector. There is, however, a temporal smoothing due to diffusion. This implies that the results of the measurement are influenced by the "thermal history" of the cast-iron slab. To give an order of magnitude, the 95 % step response time has been roughly estimated at 40 min. But as the course of the Sun is slow and other parameters are stable, the system is studied in quasi steady state and no quick changes are expected.

5.6 Open-Source Monte-Carlo-Ray-Tracing Model of realistic Scheffler Collectors

The work presented in this appendix is an adapted version of an article that was submitted in January 2024. It uses experimental results from Chapter 3 as a basis for developing a numerical model of the Scheffler reflector and performing a sensitivity analysis of the configuration parameters.

5.6.1 Introduction

The decarbonization of human society requires the use of renewable energies such as wind and solar. In the latter case, a wide range of technologies coexist and can be separated into three families: photovoltaics, non-concentrated solar thermal systems and concentrated solar systems. The latter have the advantage of being able to reach relatively high temperatures (up to thousands of degrees) with a relatively high solar-to-heat efficiency ($40\% - 70\%$), where photovoltaic systems directly produce electricity but at a low efficiency ($\sim 20\%$ for commercial single-junction silicon cells) and non-concentrated solar systems are limited to low temperatures (typically $< 200\ ^{\circ}C$). The disadvantages of concentrating systems are i) cost; ii) the need for direct solar radiation; iii) the need for a complex and accurate tracking system that moves both the reflector and receiver [38]. Scheffler reflectors, which concept is illustrated in figures 5.5 and 5.6, are a special type of concentrators that have the great advantage of a fixed focus while the reflector moves around it during the day or changes shape throughout the year. This concept was created by Wolfgang Scheffler in a "low-tech" spirit, allowing the population to build and maintain it with relatively common materials and skills [58]. Scheffler reflectors are thus positioned and adjusted manually, thanks to simple tools such as levels, compass and integrated extensible arms. Scheffler reflectors can reach up to $800\ ^{\circ}C$ [78] and can be used for a variety of applications [61] such as baking bread, generating steam for cooking [9] or even for cremation of bodies [78]. Since Wolfgang Scheffler's first communications on this technology, his parabola has spread all over the world and especially in India [33], [39]. However, scientific studies dealing with its operating principle, its performance, its modeling and its improvement have been quite rare. In fact, to the best of our knowledge, the first paper dealing with its design was published by Munir *et al.* in 2010 [55]. In 2018, Reddy *et al.* completed the previous work by giving a comprehensive methodology to build a Scheffler reflector [68], and even proposed new designs supported by a simple ray tracing code [67]. The latter uses geometric optics and can estimate the size of the Scheffler's image but it does not give details on heat flux distribution. Actually, efficient and versatile modeling codes are scarce, and they have rarely been validated by experimental results, as the number of complete performance characterization and details on focal images is also limited. For instance, Ruelas *et. al.* [70], [71] developped a ray-tracing code for a Scheffler-type reflector to help design their absorber, however their numerical reflector is non-deformable. Some other

authors developped rather complete models but using proprietary softwares: Sasidharan *et. al.* [76] used a 3D CAD software and the module "Ray Optics" from ComSol Multiphysics to estimate their experimental flux distribution, however the capabilities and limitations of their tool are not clear. The same goes for Fontani *et. al.* [24] who used SolidWorks and Zemax-OpticStudio to understand the effect of the mechanical deformations on the irradiance maps and size their receiver. In a previous paper [29] we tried to partially fill the experimental data gap and qualitatively compared our results with the extensive work of Dib *et al.* [20]. Using this experimental knowledge, the present work provides an opensource code under Soltrace software [85] to allow the scientific community to perform Monte-Carlo-Ray-Tracing (MCRT) simulations of Scheffler reflectors. Soltrace has been developped by the National Renewable Energy Laboratory (NREL) and is one of the most used ray-tracing software for Concentrating Solar Power (CSP) applications, such as central receivers [37], parabolic troughs [48] and Fresnel linear reflectors [41]. It has the advantage of being open-source, free, versatile and allows parametric studies and post-processing with other softwares. It has some drawbacks such as the impossibility to upload CAD models, or the fact that it does not include an attenuation coefficient for central receivers. [37] (though an analog version is used for this purpose in the Solar Pilot open-source software from NREL, that is dedicated to central receivers [84]). Because it uses MCRT, Soltrace is a reliable tool to predict heat flux distribution of solar collectors in a relatively low computing time. This software can therefore help to understand, design and test new ideas about Scheffler technology. The present work gives details on the code that has been developped and shared on a dedicated platform, and shows some of its capabilities. The following sections are structured as follows: i) Methodology with the main equations and the main parameters of interest, ii) Adjustment of the optical parameters to fit our experimental data; iii) Parametric studies to evaluate the margin for errors in the Scheffler reflector positioning and adjustment; iv) Conclusions and perspectives.

5.6.2 Methodology

The Soltrace script that is provided with this article creates a parabola made of mirror facets, in a cartesian coordinate system (x,y,z) and with three main inputs defined as in [68] (see Figure 5.6):

- The focal length of the parabola at the equinox f(m);
- The inclination of the Scheffler reflector aperture plane at design point α, which defines the part of the imaginary parabola that will be approximated by a curved plane, and which should lead to the lowest torque for the metal structure.
- The desired elliptical area $A = \pi \cdot \frac{B_1 \cdot B_2}{4}$ or the desired aperture area $A_{aperture} = \pi \cdot \frac{B_2^2}{4}$ of the reflector (m^2), with B_1 and B_2 the big and small diameters of the ellipse, respectively, and with $B_2 = B_1 \cdot \cos(\alpha)$;

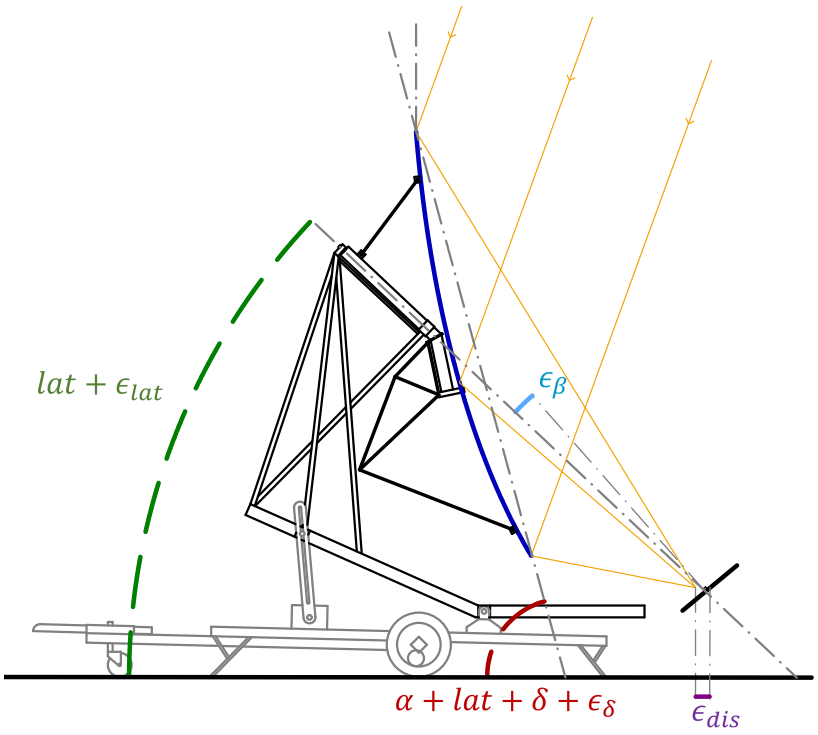

Figure 5.5 – Representation of a Scheffler reflector (in dark blue) with four adjustment errors: ϵ_{lat} for the inclination of the rotation axis, ϵ_δ for the inclination of the reflector (though it is also impacting the curvature of the parabola but this is not pictured here), ϵ_{dist} for the horizontal position of the receiver and ϵ_β for the inclination of the receiver. ϵ_ω and ϵ_{South} are in an orthogonal plane and are therefore not represented. See section 5.6.2 and equations 5.9 to 5.11 for the different definitions.

Then, the parabola is rotated along three different axes to be representative of the right position of the Earth and the right time. To do this, the position of the sun is calculated from the chosen latitude (lat.), day and solar time, using simplified equations. A more complex "true" sun position model could be used, such as the Solar Position Algorithm (SPA) from the NREL [66], but such accuracy is unnecessary for general calculations.

The following subsections deal with the mathematical and numerical particularities of the model, following the theoretical aspects that have been formulated by Reddy *et al.* [68], except that in the present work, the focal point of the parabola is fixed at the coordinate (x=0, y=0, z=0). This choice facilitates the mathematical developments, especially for rotations. It should be noted that the vertex of the imaginary paraboloid that is accommodated by the standing Scheffler reflector is usually located below the ground (*c.f.* Figure 5.6), *i.e.* neither the height position of the receiver nor its distance to the reflector is equal to the focal distance of the parabola (though the

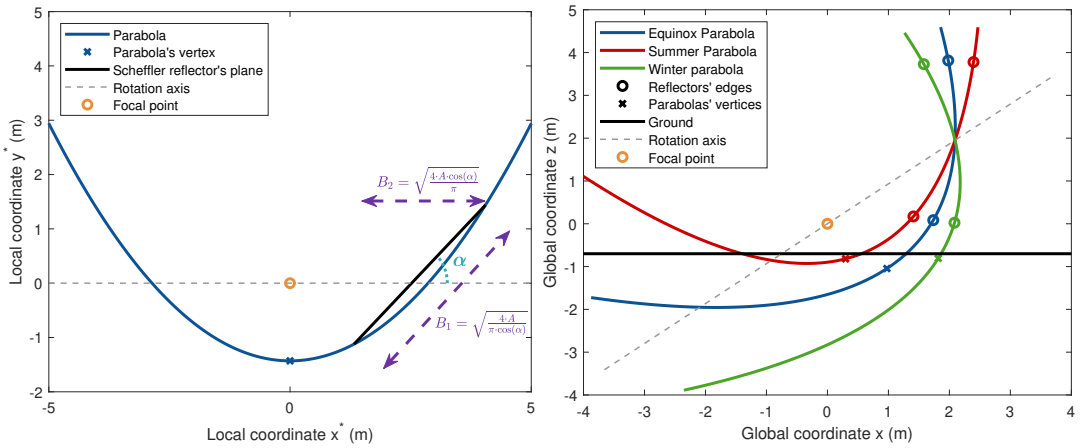

(a) (b)

Figure 5.6 – (a) Construction of a Scheffler reflector: intersection of a parabola and a plane, local coordinate system. (b) Position of a Scheffler reflector located in lat. 43°, with an 8 m^2 aperture and a 1.43 m focal distance, for the equinoxes and the solstices, global coordinate system.

distance between the focal point and the center of the reflector is supposed to be two times the focal distance [68]). Thus, having no tangible meaning, the origin of the coordinate system does not matter.

5.6.2.1 Equations giving the position of the paraboloid's facet and the receiver

The Scheffler reflector is created out of the intersection between a paraboloid and an inclined plane, in a cartesian coordinate system (O, x, y, z) with the focal point as origin. The former is created as if the Sun was exactly on its Zenith (Equator line, Equinox, 12 p.m solar time), then it is rotated several times to match the exact location and time. In this coordinate system, the general equation of a paraboloid oriented towards its zenith, with a focal distance at equinox f is the following:

$$z^*(x,y,z) = \frac{x^2+y^2}{4 \cdot f} - f \tag{5.6}$$

To get a fixed receiver, the paraboloid shape is changed with respect to the chosen day number n (from 1 to 365), parameterized by the declination angle δ_n. Its focal distance is therefore variable and defined by equation 5.7 (*cf.* [68]):

$$f_n = f \cdot (1 - \cos(\pi/2 - \delta_n)) \tag{5.7}$$

To obtain the two edges of the reflector for any day, the following equation is used:

$$(x_{1,2})_n = 2 \cdot f_n \cdot \tan(\alpha + \delta_n/2) \pm \sqrt{\frac{A}{\pi \cdot \cos(\alpha)}} \cdot \cos(\alpha + \delta_n/2) \tag{5.8}$$

In the present work, we assume that the Scheffler reflector is composed of small facets of 0.1 m x 0.1 m whose centres are positioned along the shape of the paraboloid. The mirror's positions and aiming points vectors are obtained by deriving the shape of the parabola. To pass from the general coordinate system "O = focal point", "positive x = toward South", "positive y = toward East" and "positive z = toward Zenith" to the local coordinate system corresponding to a paraboloid with the Sun at its right position and parameterized with $(x^*, y^*, z^*,)$, three successive rotations are performed: one for the declination, then one for the hour angle and finally one for the latitude. When using an actual reflector, these three rotations can be performed with some errors, respectively called ϵ_δ, ϵ_ω and ϵ_{lat}. The two former can be converted in delays of daily adjustment in days and tracking adjustment in minutes; the latter is an error in the inclination of the parabola and can be therefore given in degrees. One final rotation is performed in the global coordinate system to represent a potential error in the adjustment of the North-South alignement of the parabola and is called $\epsilon_{offset_{South}}$ (in degrees). The coordinate of a facet in the main coordinate system with respect to its coordinates in the local system is therefore given by:

$$\begin{pmatrix} x \\ y \\ z \end{pmatrix} = R_z(\epsilon_{South}) \cdot R_y(-lat - \epsilon_{lat}) \cdot R_x(-\omega - \epsilon_\omega) \cdot R_y(\delta + \epsilon_\delta) \cdot \begin{pmatrix} x^* \\ y* \\ z* \end{pmatrix} \tag{5.9}$$

where $R_i(\theta)$ is the rotation matrix around the local axis e_i and with an angle θ.

In a previous paper, we showed some experimental results with a flat receiver which position was vertical for practical reasons. However, the best position of a receiver depends on the latitude, the declination and the chosen slope for the approximated parabola. It is generally stated that an inclination angle β corresponding to the latitude is the best compromise: the receiver is facing toward the rotation line that is almost at the centre of the reflector. Most of the following results will therefore use this orientation. To evaluate the magnitude of the impact of a wrong adjustment of the receiver, errors on its horizontal position, ϵ_{dist}, and on its inclination, ϵ_β, will also be implemented. The receiver's global position and aiming vector are therefore given by:

$$\begin{pmatrix} x_R \\ y_R \\ z_R \end{pmatrix} = \begin{pmatrix} 0 + \epsilon_{dist} \cdot cos(\epsilon_{South}) \\ 0 + \epsilon_{dist} \cdot sin(\epsilon_{South}) \\ 0 \end{pmatrix} \tag{5.10}$$

$$\begin{pmatrix} x_{aim_R} \\ y_{aim_R} \\ z_{aim_R} \end{pmatrix} = \begin{pmatrix} cos(\epsilon_{South}) \cdot cos(\beta + \epsilon_\beta) \\ sin(\beta + \epsilon_\beta) \\ 0 \end{pmatrix} \tag{5.11}$$

To sum up, six different adjustment errors will be evaluated: *i.e.* ϵ_{lat}, ϵ_{South}, ϵ_δ, ϵ_ω, ϵ_{beta} and ϵ_{dist}. Some of these errors are represented on figure 5.5, while the others are in a perpendicular plane and would necessitate a view from above to be pictured.

5.6.2.2 General input parameters

In Soltrace, the modelled reflector is fitted to an experimental set-up in Marseille, France, and has the following features: $f = 1.43$ m, lat. = 43.345°, $A_{ellipse} = 8$ m^2 and $\alpha = 43.23°$. The target is a flat square with an arbitrary surface of 1 m^2, centred at the parabola focal point and more or less inclined towards the reflector. A real receiver would be at the same position and would have a different shape and size, *e.g.* a disk with a 26 cm diameter.

5.6.2.3 Optical input parameters

The concentration factor of the Scheffler reflector first depends on its size and focal distance [68], *i.e.* the highest the view factor of the parabola from the receiver, the highest the possible concentration. These parameters are fixed when designing the system. But it also strongly depends on the optical errors of the whole system. The total optical error σ_{tot} can be estimated with equation 5.12 [47] and depends on five parameters:

- the angular apparent radius of the Sun $\theta_{sun} = 4.65\ mrad$;
- the quality of the specular reflection of the mirrors, quantified in Soltrace by the "specularity error" σ_{spec}. In this case, it depends on the quality of the mirrors, knowing that a glass mirror creates two refractions before and after the reflection on the metal coating, and that a mirror can be dirty and scratched;
- the deviation of the local curvature of the parabola from its theoretical shape, quantified in Soltrace by the "slope error" σ_{slope}. In this case, this error depends directly on the size of the square flat mirrors that is chosen;
- the deviation of the parabola from its theoretical shape, generally quantified by an error σ_{shape} that is independent from σ_{slope}. If the position of the facets is correctly chosen, this error is null in the numerical model. In an actual Scheffler reflector, it can be very important because it represents its ability to reproduce the theoretical shape by bending.
- the deviation between the aiming point of the parabola and the actual position of the Sun, represented by a tracking error $\sigma_{tracking}$.

$$\sigma_{tot}^2 = \sigma_{sun}^2 + \sigma_{spec}^2 + 4 \cdot \sigma_{slope}^2 + 4 \cdot \sigma_{shape}^2 + \sigma_{tracking}^2 \tag{5.12}$$

In Soltrace, the shape errors are implicitly created when designing the different optical stages (position, orientation) and therefore, they cannot be specified by users. The tracking errors can be easily created by users when defining the system. While the angular size of the Sun in the sky is well known, the coupling between the specularity and slope errors is difficult to evaluate without their experimental characterization by photogrammetry [63] or deflectometry [23]. As a consequence, one way to artificially

increase the total error σ_{tot} is to multiply the size of the Sun with an arbitrary factor k_{sun}. This method has no physical significance but leads to similar focal image than using errors while preventing a wrong prediction of their values. In this work, the k_{sun} factor will be varied in order to both fit experimental results and observe its combined influence with other experimental errors (positions and angles).

Hence, apart from the k_{sun} factor that increases the size of the Sun, the general optical parameters are the following:

- The Sun is initially modelled as a pillbox with an angular apparent radius of 4.65 mrad; DNI is 900 $W \cdot m^{-2}$.
- Slope and specularity errors are set to 0.001 mrad and are Gaussian;
- Reflectivity of mirrors is set to 90% while the target's is set to 100%. Transmittivity is always 0%. Absorptivity of the target is set to 100%.

5.6.2.4 Processing of results

Graphs were replotted from Soltrace to Matlab thanks to the tecplot output files. Heat flux maps are given in the local coordinate system of the receiver, parameterized with (x^*, y^*). For heat flux density maps, results highly depends on the pixel sizes that are changing from one result to the other. Therefore, no comparison should be made between two figures, except when it is forced to the same value.

5.6.2.5 Definitions

In this study, several simulations were performed:

- One reference case consisting in a parabola with facets whose positions follow the theoretical shape;
- Parametric studies on the total optical error of this parabola to find a possible configuration for the actual experimental results that are used as tuning reference;
- Parametric study on the tilt of the receiver/target, the accuracy of the Sun's tracking and on the parabola's shape and position in order to understand the possible flexibilities of the Scheffler system.

Results will focus on heat flux distribution and average heat flux density $<\phi>$ onto the target, defined as the ratio between total power P_{tot} in watts (see equation 5.13) and the image total area A_{image}, *c.f.* equation 5.14.

$$P_{tot} = A_{aperture} \cdot DNI \cdot \sigma_{mirrors} \tag{5.13}$$

$$<\phi> = \frac{P_{tot}}{A_{image}} \tag{5.14}$$

A_{image} is defined as the surface circling all the rays that are hitting the target while its centroid is defined as the average position of the rays in the target's local reference frame. When the optical and position errors are not too important, all the rays are hitting the target and both the impacted area and the centroid position can be estimated. For very important errors, some rays miss the target. Concentration ratio can be defined with respect to heat flux density *v.s.* DNI and reflectivity of mirrors $\sigma_{mirrors}$ or with aperture surface of the parabola $A_{aperture}$ *v.s.* the image surface.

$$CR = \frac{A_{aperture}}{A_{image}} = \frac{<\phi>}{DNI \cdot \sigma_{mirrors}} \tag{5.15}$$

It should be noted that since Soltrace is based on statistics, it is likely that a solitary ray deviates significantly from the others and substantially increases the total calculated area. The last indicator will therefore be the power that reaches a hypothetical disk receiver with a 26 cm diameter P_{rec}. In the ideal conditions that represents former experimental results (*vide infra*), this disk receives 95% of the power that is reflected by the parabola. In non-ideal conditions, this power received by this hypothetical receiver will serve as criterion for error quantification.

5.6.3 Results and Discussion

5.6.3.1 Model of an 8 m^2 Scheffler reflector with facets and no further optical errors

A "perfect" Scheffler reflector would use a flexible and continuous mirror with no optical errors and would give the maximum concentration ratio that is possible. Such reflector has been modeled, see Appendix 5.6.5.1, but it is not enough versatile and ergonomic to be used as the main model. Using 0.1 m x 0.1 m flat facets, as illustrated in 5.7-a, inherently creates optical aberrations resulting in heat flux maps that are larger than the ones that could be obtained with continuous parabolas. On figure 5.7-b, it can be observed that because of the facets and with no further optical errors, the size of the focal image is limited by the size of the facets (0.1 m x 0.1 m). The system gives an average flux density of 233.5 kW.m^{-2} for 100% of Φ and 427.1 kW.m^{-2} for 95% of Φ, *i.e.* focal image areas of 0.020 m^2 and 0.011.0 m^2, respectively.

These areas are largely lower than the actual focal images obtained from experimental results with facets, *i.e.* 0.113 m^2 and 0.053 m^2, respectively [29]. Therefore, further optical errors have to be implemented in the simulations.

5.6.3.2 Model of an 8 m^2 Scheffler reflector with facets and optical errors so as to obtain "experimental-like" results

The influence of the multiplicator k_{sun} on the average heat flux density $<\phi>$ and on the centroid position is picutred in Figure 5.8.

The objective was to find the k_{sun} value giving the best fitting. The comparison between the experimental and the numerical Gaussian curves enabled showed that

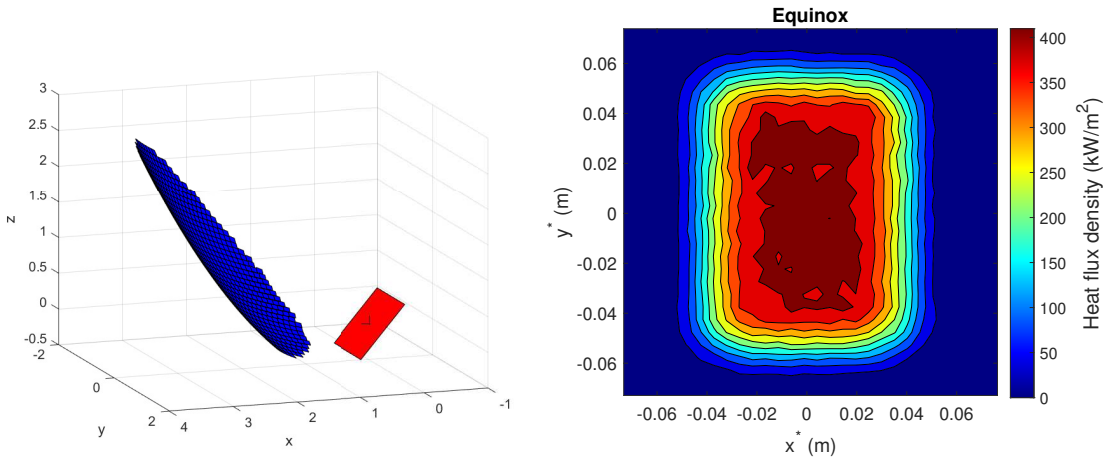

(a) (b)

Figure 5.7 – (a) Reflector's shape (and inclined plane receiver) for the equinox in Marseille (lat. = 43°, long. = 1°) with facets accommodating the parabola's shape (b) Focal image that is obtained from this parabola, with no further optical errors. Aperture area is 5.85 m^2, the transmitted power is 4.74 kW ($\sigma_{mirrors} = 0.9$ and DNI = 900 $W.m^{-2}$), the image area is 203.1 cm^2 (100% of Φ) or 111.0 cm^2 (95% of Φ) and the average power density 233.5 $kW.m^{-2}$ (100% of Φ) or 427.1 $kW.m^{-2}$ (95% of Φ); CR are 288 or 527, respectively.

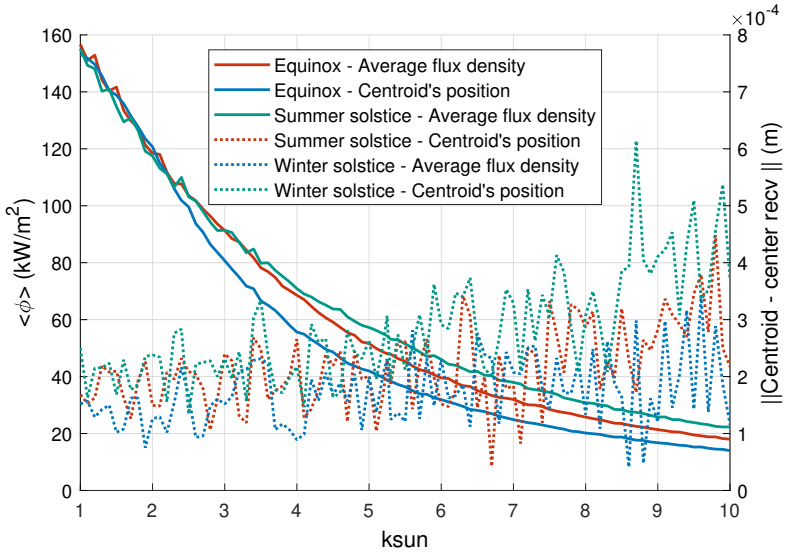

Figure 5.8 – Influence of the Sun multiplicator k_{sun} on the average flux density and the centroid's position.

$k_{sun} = 7.2$ provides the best results. Figure 5.9 shows the comparison between the predicted focal image of the Sun with this best fitting value and the experimental focal image that was presented in [29]. For this comparison, the pixel size is the same for numerical and experimental results, therefore both the heat flux distributions and

absolute values can be compared.

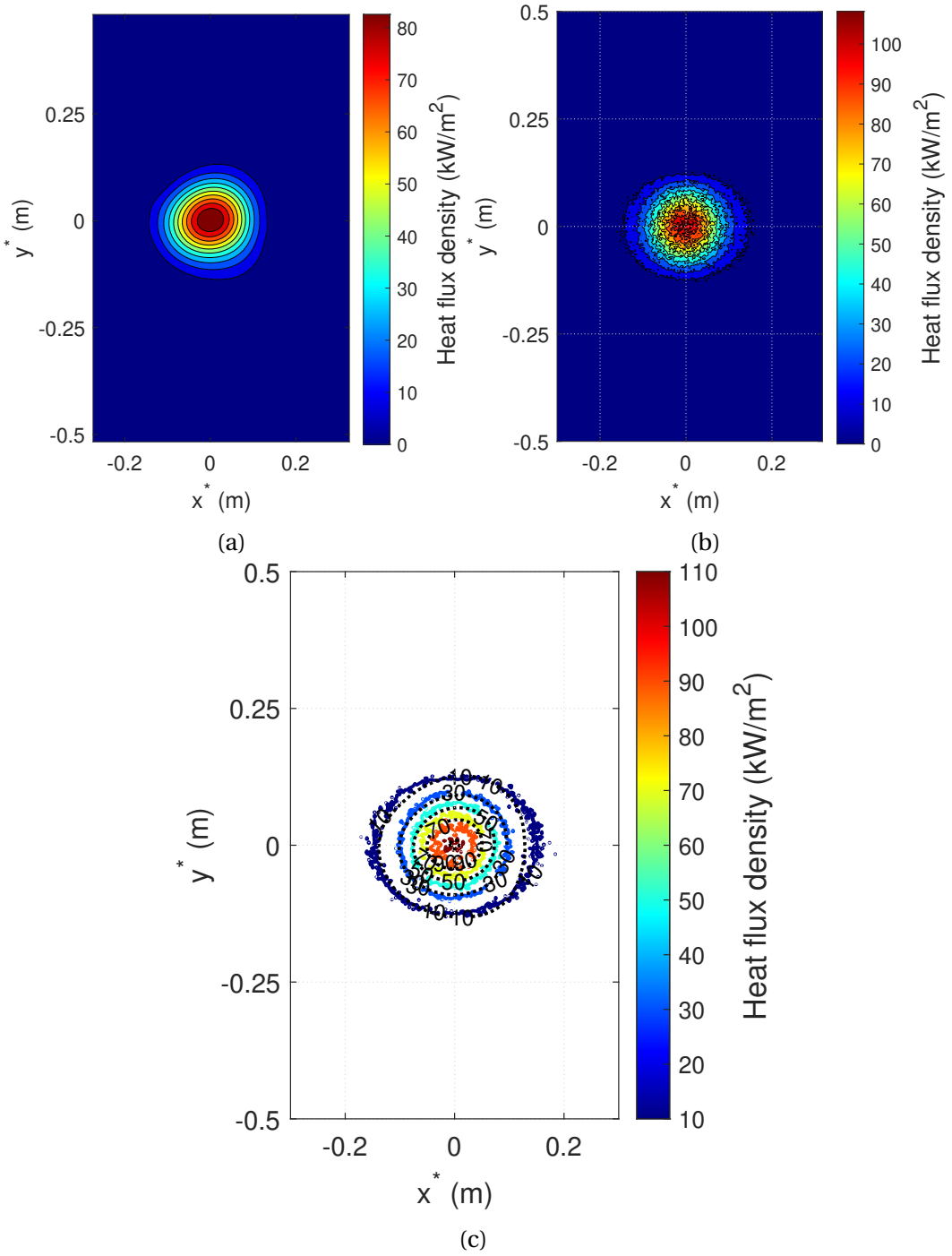

Figure 5.9 – Comparison between (a) the experimental results from a 8 m^2 Scheffler reflector (14 of June 2022, Marseille, 12 p.m solar time, DNI = 900W.m^{-2}) and (b) the numerical results with the best fitting k_{sun} and the same bining (bining = 3.5 x 3.5 mm^2). (c) Comparison of the isoflux lines.

The results are in good agreement, with 95% of the 2.6 kW total power received by a disk with a 26 cm diameter. However, the uncertainty is very large because of all the experimental assumptions that were made here; one can assume that a value of $7 +/- 2$ is a good estimate for this kind of Scheffler reflector; it corresponds to a total error of 20-40 mrad (see 5.6.5 for details).

5.6.3.3 Variations of the focal image with day and time

Because some geometric parameters change with day and time, *e.g.* the theoretical shape of the parabola, the distance and view angles of its edge with respect to the focal point, etc., the theoretical focal image should vary accordingly. Besides, when bending the reflector in the vertical direction with the two integrated extensible arms, a possible horizontal deformation of the reflector can occur, resulting in distortion of the obtained images [24]. Previous studies predicted or found experimental variations of results with respect to the day and time. For instance, Reddy *et al.* [68] found that the focal image should be larger and more elliptical for the summer solstice than for the winter solstice. This result was also confirmed by the experimental work of Dib [20] but not by our previous work (we saw some variations but we did not see any seasonal trend in our experimental results [29]). More experimental results on various Scheffler reflectors are needed to conclude. Meanwhile, numerical studies with possible k_{sun} give an idea of the possible variations that can be expected. For instance, Figure 5.10 shows the flux maps on an inclined receiver that were obtained with $k_{sun} = 7$ for the solar noons of the equinox, the summer solstice and the winter solstice. The only visible difference between the figures is the total flux that is dependent on the daily aperture of the reflector; the apparent sizes are very similar. Different times of the day were also simulated and the results show no difference because it is more or less a 2D-Gaussian function rotating around its centre. Concentration factors are also considerably lower than in [68], *i.e.* in the range of 40-60 for the average against 1000-7000, because actual optical errors are tremendously high.

It can be concluded that, because the optical errors are more important than the theoretical geometric variations, the shape of the focal image is almost always circular and the important variations that could be observed for a perfect shape are totally filtered when a realistic case is used.

The same results for $k_{sun} = 1$ are given in 5.6.6.1 and variations between seasons are more visible.

The importance of the experimental optical errors of actual Scheffler parabolas motivated the parametric studies that will follow. With the developed model and the knowledge from experimental results, it is possible to assess the room for manoeuvre when positioning and using such solar reflectors.

5.6.3.4 Sensibility analysis to set-up defaults and implications for the model

When positioning a Scheffler reflector, the user should (see Figure 5.5):

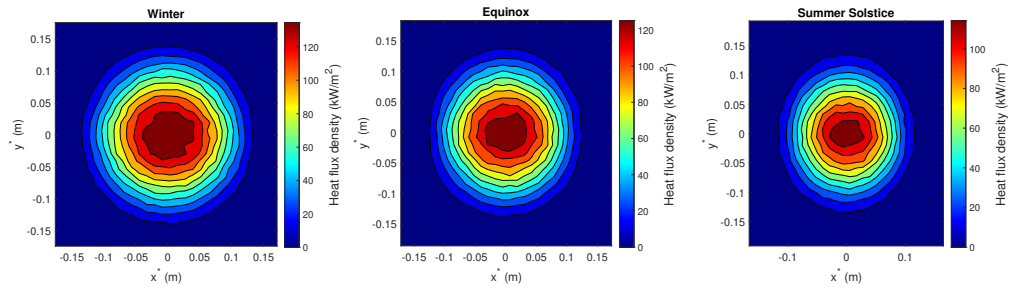

(a) (b) (c)

Figure 5.10 – Variation of the numerical focal image with the declination for k_{sun} = 7: (a) Winter solstice (5.88 kW), (b) Spring equinox (4.94 kW) and (c) Summer solstice (3.87 kW).

- Align the reflector with the North-South axis, towards South in the Northern hemisphere, and towards North in the Southern hemisphere;
- Incline the reflector in order to get the rotation axis parallel to the Earth's rotation axis, i.e. an inclination to the latitude with respect to the ground;
- Position the receiver exactly where the focal point/image should be;
- Incline the receiver to an angle close to the latitude;
- Bend the parabola in order to obtain the right shape for the day of the experiment;
- Turn the parabola's rotating axis in order to track the Sun.

All these steps will be performed with some errors. The following parametric study aims to give the error margin that is acceptable to obtain satisfying results. The chosen criterions can be i) the average solar flux density arriving onto a target (arbritarily defined as a 1 m x 1 m plane inclined to the latitude and centred at the focal point), given by Equation 5.14, ii) the position of the centroid of the focal image in the receiver, iii) the total flux arriving onto a 26 cm diameter disk located in (0,0,0) and representing a potential receiver. These criterions evaluate how the focal image is growing and/or moving, *i.e.* how it can go out of the potential receiver. In the following results, we will consider a single error to be acceptable if it leads to a reduction in the average flux density of the 26 cm disc of less than 10% for the day most sensitive to the chosen parameter. Other parameters will be given as complementary information. Results will be given for a reflector located in Marseille, for the equinox and the two solstices. Because the importance of optical errors plays a role in the dependence of the results to the different design errors, the same parametric study has been performed for k_{sun} of 1, 3, 5, 7 and 9. Results for k_{sun} = 7 will be discussed in the following sections while others are provided in 5.6.6.1, 5.6.6.2, 5.6.6.3 and 5.6.6.4 and obviously show that margin for error is weakened when k_{sun} decreases.

Horizontal alignment of the Scheffler reflector For $k_{sun} = 7$, Figure 5.11-a shows the consequences of an incorrect southward positioning of the reflector on the total power received by the 26 cm diameter virtual receiver P_{rec} . Figure 5.11-b shows the impact of this same parameter on the average flux on the 1m^2 target and on the centroid position. Performance appears to be highly sensitive to this parameter, with a 1° error leading to a 10° reduction in P_c for the winter equinox (the most sensitive day) and an image shift of up to 4.6 cm. The impact on the average flux density of the target is smaller, and its changes in slope for errors of around +/- 5° are due to the fact that the rays start to miss the 1m^2 target. The North-South alignment of the dish is therefore of paramount importance, and must be conscientiously set to an accuracy of 1°; a compass is insufficient due to the Earth's magnetic declination.

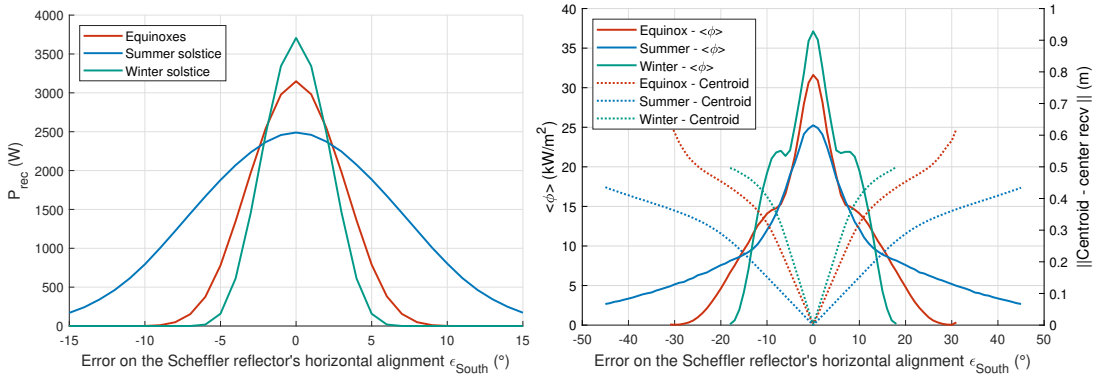

(a) (b)

Figure 5.11 – For $k_{sun} = 7$, theoretical impact of a wrong North-South alignment of a Scheffler reflector on (a) the power received by a hypothetical disk receiver with a diameter of 26 cm (b) the position and heat flux density of the whole focal image (0.1 m x 0.1 m plane target).

Rotation axis' angle with respect to the ground The angle of the axis of rotation in relation to the ground must be set to be equal to the latitude of the location. Depending on the tools used for this adjustment, errors may be created. Figure 5.12-a shows that this error can be as much as 0.8° to accommodate a 10% decrease in P_{rec}, resulting in a focal image shift of around 4.0 cm (for $k_{sun} = 7$). This inclination is therefore also an important parameter, although being easy to adjust using a digital level. Note that the heat flux density behavior of the focal image is not exactly symmetrical with respect to the shift of the line of rotation, due to the change of aperture area of the reflector.

Horizontal position of the receiver Figure 5.13 shows the consequences of incorrect horizontal positioning of the receiver, i.e. placing it too close or too far from the Scheffler reflector, for $k_{sun} = 7$. According to the results, a maximum error of 6 cm is tolerated to avoid a too great reduction in the power received by the virtual disk.

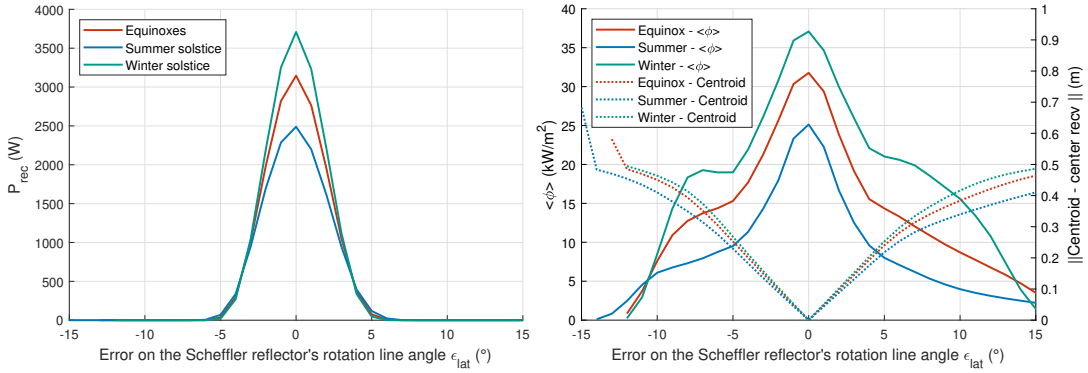

(a) (b)

Figure 5.12 – For $k_{sun} = 7$, theoretical impact of a wrong inclination of the Scheffler reflector's axis of rotation on (a) the power received by a hypothetical disk receiver with a diameter of 26 cm (b) the position and heat flux density of the whole focal image (0.1 m x 0.1 m plane target).

This results in a 3 cm shift in the focal image and a 10% reduction in power for the winter solstice results, which are once again the most affected by this parameter.

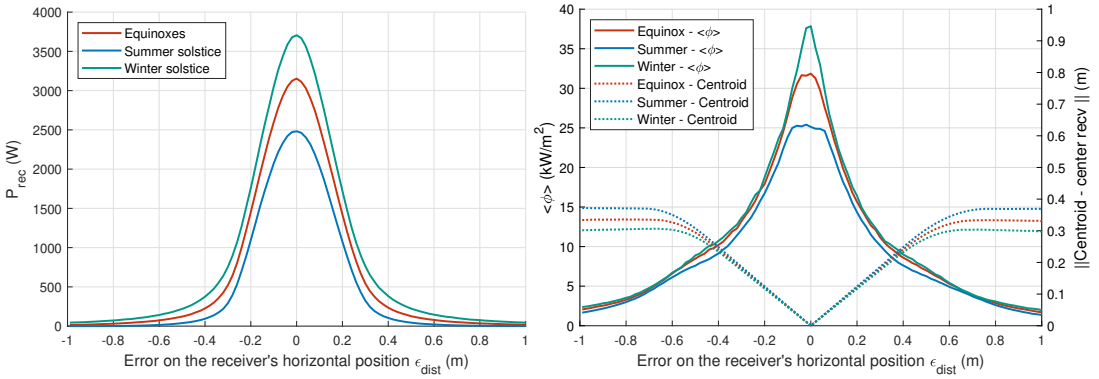

(a) (b)

Figure 5.13 – For $k_{sun} = 7$, theoretical impact of a wrong horizontal position of the Scheffler's receiver (inclined with the latitude to face the center of the parabola) on (a) the power received by a hypothetical disk receiver with a diameter of 26 cm (b) the position and heat flux density of the whole focal image (0.1 m x 0.1 m plane target).

Tilt of the receiver The variation in heat flux density and centroid position as a function of receiver inclination and for $k_{sun} = 7$ is shown in Figure 5.14-b. It can be seen from this figure that placing the receiver vertically does not change the centroid position, but spreads out some of the Sun's rays, resulting in a sharp drop in the average flux density on the target. However, most of the flux still falls onto the hypothetical

receiver (see Figure 5.14-a): a 10% reduction in P_{rec} corresponds to a 31° error in inclination (*i.e.* 74° instead of 43°), whereas positioning the receiver vertically modifies it by only 12%. As a conclusion, while it is advised to tilt the receiver according to latitude, having a vertical receiver such as in our experimental work [29], is not very detrimental to the reflector's performance. Besides, it does not seem that inclining by the latitude angle is exactly the best compromise: the average flux density also depends on the distance between the focal point and the two edges of the reflector that are different from one season to the other.

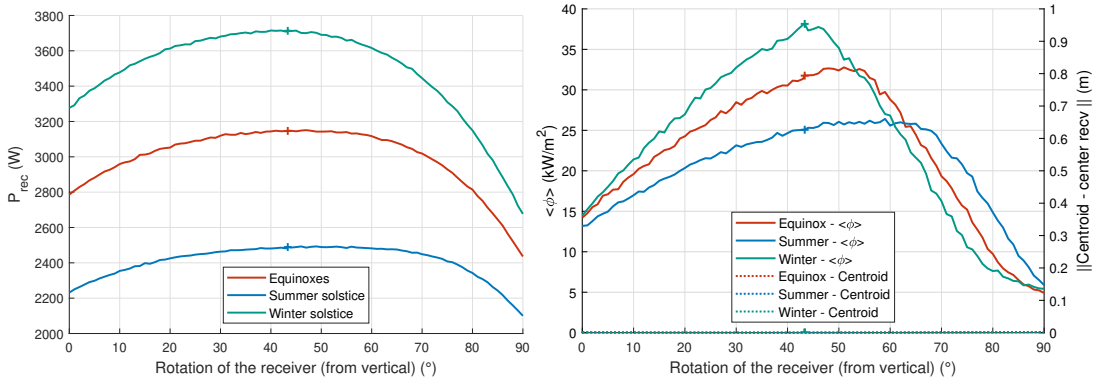

(a) (b)

Figure 5.14 – For $k_{sun} = 7$, theoretical impact of a wrong inclination (from vertical) of the Scheffler's receiver (best position would be an inclination angle equal to the latitude, marked by '+' signs here) on (a) the power received by a hypothetical disk receiver with a diameter of 26 cm (b) the position and heat flux density of the whole focal image (0.1 m x 0.1 m plane target).

Declination adjustment Scheffler reflectors need to be adjusted regularly, using integrated extensible arms that bend the reflector into a given parabolic shape. The question arises as to how often this adjustment is necessary. Figure 5.15 shows that, for $k_{sun} = 7$, it's sufficient to adjust the shape of the parabola every 16 days near the solstices, but only every two days near the equinoxes. This is because the Sun's declination changes much more rapidly for the latter (the derivative of the declination is 0 for the solstices and maximum for the equinoxes). However, when the 10% decrease in P_{rec} is observed, the focal point may have moved 4 cm from its initial point.

Tracking error For $k_{sun} = 7$, Figure 5.16 shows whether the Scheffler parabola should follow the Sun with a very precise tracking system. The criterion is met if the tracking system has a delay of less than 4 minutes, resulting in a reduction in P_{rec} of 10% and a shift of the focal image of 4.6 cm, for the winter solstice. This can easily be achieved using an automatic device or a pendulum.

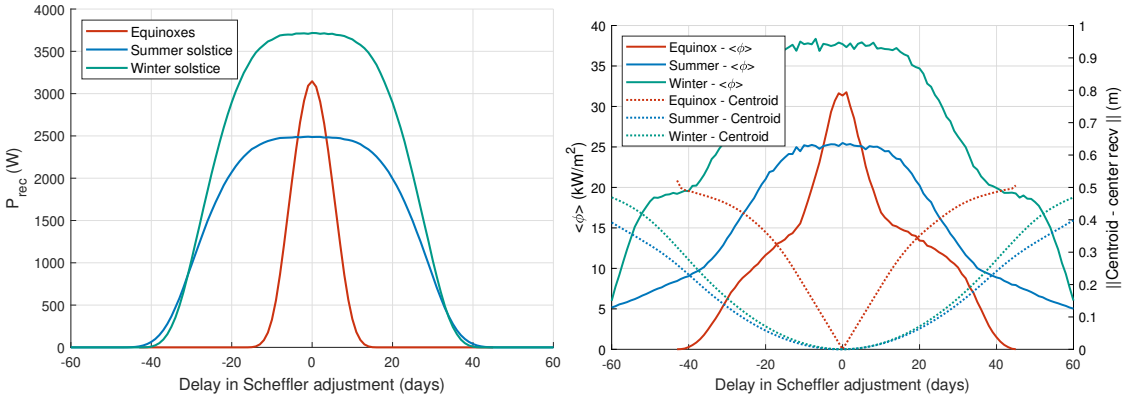

(a) (b)

Figure 5.15 – For $k_{sun} = 7$, theoretical impact of a delay in days in the tuning of the Scheffler reflector's curvature on (a) the power received by a hypothetical disk receiver with a diameter of 26 cm (b) the position and heat flux density of the whole focal image (0.1 m x 0.1cm plane target).

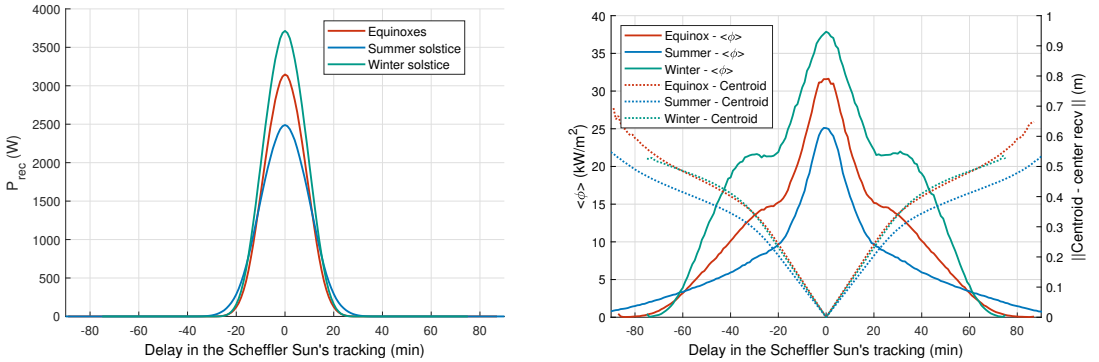

Figure 5.16 – For $k_{sun} = 7$, theoretical impact of a delay in minutes in the tracking system of the Scheffler reflector on: (a) the power received by a hypothetical disk receiver with a diameter of 26 cm (b) the position and heat flux density of the whole focal image (0.1 m x 0.1 m plane target).

Combination of errors and discussions For a real experimental set-up, the adjustment and positioning errors can happen simultaneously. In fact, Scheffler reflectors do not benefit from the same care as regular CSP systems: they are usually positioned and adjusted manually, with simple tools, allowing multiple errors. Figure 5.17 shows the obtained focal images for $A = 8$ m^2, $f = 1.43$ m, $k_{sun} = 7$ and if all the previous errors are set to their maximum value that which have been determined, *i.e.* a North-South alignment error of 1°, a rotation axis error of 0.8°, an error of 6 cm on the horizontal position of the receiver, a declination adjustment error corresponding to 2 days, tracking error corresponding to 4 min, and a receiver with an inclination of 74°. Results can be compared to those shown in Figure 5.10. While the image is a lot distorted, the concentration is still acceptable. However, it is displaced from

the focal point (0, 0) and therefore misses the virtual target. The calculated P_{rec} are 1.82 kW, 1.64 kW and 1.19 kW, for the winter solstice, the summer solstice and the spring equinox, respectively. It corresponds to power reductions of 69%, 67% and 69% when compared to the case with no error. This is not acceptable.

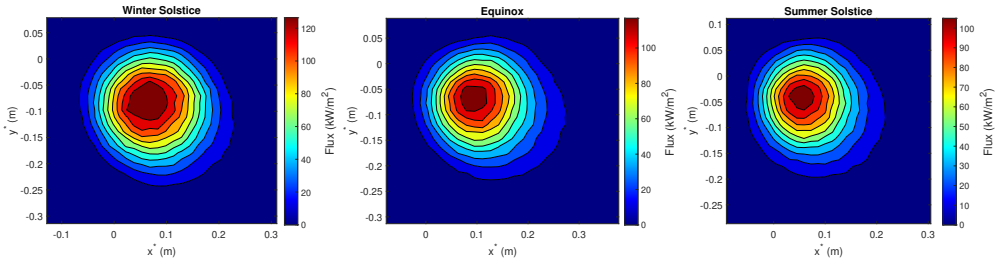

(a) (b) (c)

Figure 5.17 – Obtained focal images with $k_{sun} = 7$ when all the threshold errors are put simultaneously, for Winter Solstice, equinoxes and Summer Solstice.

Sensitivity studies [34], [44] have then been performed for $k_{sun} = 1$ and $k_{sun} = 7$ in order to better assess the parameters and their interaction having the greatest influence on performance. These analyses are conducted using a 2^N factorial plan of experiments [51], where N represents the number of parameters x_i. Each parameter takes two values (minimum and maximum) selected from a reference value ($mean(x_i) = x_{ref}$). This method quantifies the effects of parameters and their interactions on a specific output objective y. The fundamental concept involves approximating the system response as a function of the normalized parameters or input factors X_i :

$$y = \beta_0 + \sum_{i_1=1}^{N} \beta_{i_1} X_{i_1} + \sum_{i_1=1}^{N} \sum_{i_2>i_1}^{N} \beta_{i_1 i_2} X_{i_1} X_{i_2} + \sum_{i_1=1}^{N} \sum_{i_1>i_2}^{N} \sum_{i_3>i_2}^{N} \beta_{i_1 i_2 i_3} X_{i_1} X_{i_2} X_{i_3} + ... + \beta_{i_1 i_2 ... i_N} X_{i_1} X_{i_2} ... X_{i_N} \quad (5.16)$$

$$X_i = \frac{x_i - x_{i_{ref}}}{(max(x_i) - min(x_i))/2} \quad \text{, i=1,N} \quad (5.17)$$

where the subscript $_{ref}$ denotes the reference case. The different effects $\hat{\beta} = \beta_0, \beta_{i_1}, \beta_{i_1 i_2}, ..., \beta_{i_1 i_2 ... i_N}$ are obtained by solving the linear system described in equation 5.16. β_0 can be calculated with the mean value of the output objective y calculated for all parameter sets.

The sum of squares SS for different effects indicates the percentage contribution of each model term relative to the total sum of squares SST:

$$SS_i = 2^N {\beta_i}^2 \qquad , i = 1, 2^N - 1 \tag{5.18}$$

$$SST = \sum_{i=1}^{2^N-1} SS_i = \sum_{i=1}^{2^N} y_i^2 - \frac{(\sum_{i=1}^{2^N} y_i)^2}{2^N} \tag{5.19}$$

where $y_i, i = 1, 2^N$ are the different output quantities from 2^N simulations. The quantity considered in the following is the average heat flux density $< \phi >$.

In our study, $N = 5$ input parameters of the model are considered:
d = ϵ_{dist} (m), d1 = Delay in Scheffler adjustment (days),
d2 = Delay in the Scheffler Sun's tracking (min), S = ϵ_{South}(°) and R = ϵ_{lat}(°).
The table 5.7 summarizes the levels for the parameters considered by the sensitivity study.

x_i	Reference	min	max
d = ϵ_{dist} (m)	0	-0.06	0.06
d1 = Delay in Scheffler adjustment (days)	0	-2	2
d2 = Delay in the Scheffler Sun's tracking (min)	0	-4	4
S = ϵ_{South} (°)	0	-1	1
R = ϵ_{lat} (°)	0	-0.8	0.8

Table 5.7 – Parameter levels for the sensitivity study with $N = 5$ parameters.

Figure 5.18 shows the sensitivity of the average heat flux density $< \phi >$ to both individual parameters and their combinations for the two values of k_{sun}.
The interaction effects (d1d2) of $k_{sun} = 1$ and 7, between the delay in Scheffler adjustment and the delay in the Scheffler Sun's tracking, dominate mainly the process accounting for ~ 87% and ~ 70% of the total variability, respectively. This demonstrates the importance of paying close attention to these two setting parameters, even if their individual contribution is negligible.

The effect due to the combination (dR) for $k_{sun} = 1$ between the error on the receiver's horizontal position and the error on the Scheffler reflector's rotation line angle, is still significant but with much less importance with ~ 7% of the total variability. Whereas for $k_{sun} = 7$, this is the influence of the angle of the line of rotation of the Scheffler reflector (R) which is the second most important factor ~ 12%. This parameter ranks fourth for $k_{sun} = 1$ with ~ 1.5% of the total variability. Moreover, the interaction between the four parameters (dd1d2R) is less significant for $k_{sun} = 7$ than for $k_{sun} = 1$. The sensitivity study shows that the error on the Scheffler reflector's horizontal alignment (S) has no influence on the combined results. The latter results

were to be expected, since the receiver's position is adapted to this alignment, which is not the case for the other parameters. Finally, we note that for $k_{sun} = 7$, the individual distance error parameter (d) has little influence, whereas it has none for $k_{sun} = 1$. Considering the values of SST ($SST(k_{sun} = 1) \sim 2418$ (kW.m^{-2})^2 and $SST(k_{sun} = 7) \sim 69.4$ (kW.m^{-2})^2), the system is less sensitive at stronger optical errors, corresponding to increasing k_{sun}, i.e. optical errors make the system more tolerant of other types of error.

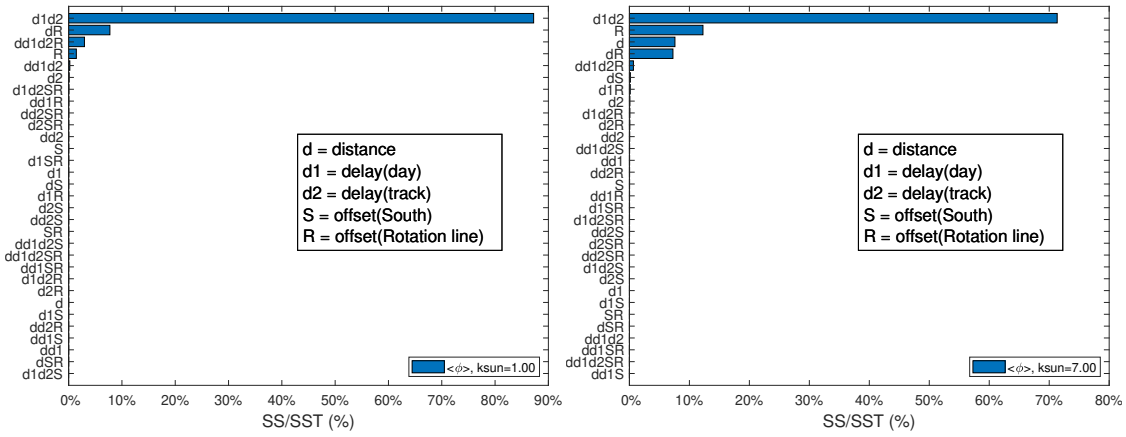

(a) (b)

Figure 5.18 – Normalized sum of squares SS/SST for $k_{sun} = 1$ (a) and $k_{sun} = 7$ (b).

However, the experimental set-up that has been used to calibrate the model with *a priori* no error gave results that were actually dependent on adjustment errors. We estimate that the reflector's south positioning was made with a compass to an accuracy of about 3°; the rotation axis is inclined with a numerical level, to an accuracy of about 2°, the declination is adjusted by hand every day, with an unknown accuracy (~ 7 days), the tracking system is automatic, with an accuracy of 1.25° (5 min) and the receiver is put at the focal point with an horizontal accuracy of ~ 5 cm. If we simulate the parabola with all those errors and with $k_{sun} = 7$, the results are also catastrophic. Several conclusions can be drawn for these previous results: i) The experimental errors that were obtained when manually adjusting the reflector are necessarily lower than both the chosen limits and the estimated accuracies; ii) since the declination adjustment is manual and depends on qualitative results (*i.e.* the reflector is inclined and bent until the focal image is centered on the receiver and small enough to be satisfying), we strongly believe that users compensate part of the errors when they change the curvature of the parabola; iii) since errors are not separable and can compensate each other, assuming reference case with only one parameter (k_{sun}) to represent all the errors can give good order of magnitudes on their relative influences.

5.6.4 Conclusion

The present work shares an open-language and versatile model of a Scheffler reflector enabling Monte-Carlo-Ray-Tracing simulation with the Soltrace software. This model is able to take into account the location, the solar time, the Scheffler reflector's characteristics, the geometry of the receiver, and the tracking and positioning errors. The objective of this model is to help users to understand and build new parabolas, but also to provide a tool simplifying the design of new secondary optical systems that could increase the performance of the solar concentrating system. The main results of this study are:

- Experimental set-up using Scheffler reflectors have huge optical errors that should be lowered. For a Scheffler reflector with an 8 m^2 aperture, a focal distance of 1.43 m and 0.1 m x 0.1 m facets, we roughly estimated them to 20 mrad - 40 mrad. These values include the positioning and adjustment errors;
- The seasonal variations that are predicted by the theory are not visible when considering an actual Scheffler reflector, with real optical errors. The influence of the latter hides the influence of the former;
- While positioning a reflector and tracking the Sun is not easy, we showed that error margins are 1° for the North-South alignment, 0.8° for the rotation axis inclination, 6 cm for the horizontal position of the receiver, 2 days for the declination adjustment and 4 min for the tracking system. All those errors taken independently lead to 10% reduction of the total power received by a hypothetical disk receiver with a diameter of 26 cm. The inclination of the receiver does not influence much the results, with only a 12% decrease of the power when putting vertically instead of following the latitude. The given results are for an 8 m^2 reflector with a focal distance of 1.43 m and located in Marseille (lat. = 43° N), however the model can be used to predict any other configuration.
- When taking all the previous errors together, performance tend to decrease down to...
- In case of Scheffler reflector with better tuning or reflector, results were also given for other optical errors. Obviously, the better the optics, the smaller are the error margins;

Following works should include : i) full optical characterization of Scheffler reflectors in order to quantify the distribution of their optical losses, whether being slope, specularity or shape, to eventually reduce their values; ii) the design of secondary optics for Scheffler reflectors with important optical errors.

5.6.5 Appendix 1 : continuous parabola

5.6.5.1 Ideal focal image

Another code has been developped and creates a continuous Scheffler reflector following the shape of a parabola, with no optical errors and aiming at the Sun that is at the Zenith. Thus, the reference results that are pictured in figure 5.19 show the best image that could be provided with a Scheffler system of this size, with a DNI of 900 W.m^{-2} and with a mirror reflectivity of 0.9. It should be noted that some limitation in the software prevent the user from having a non-zero declination, forbidding the use of this model for the parametric studies that motivated this work.

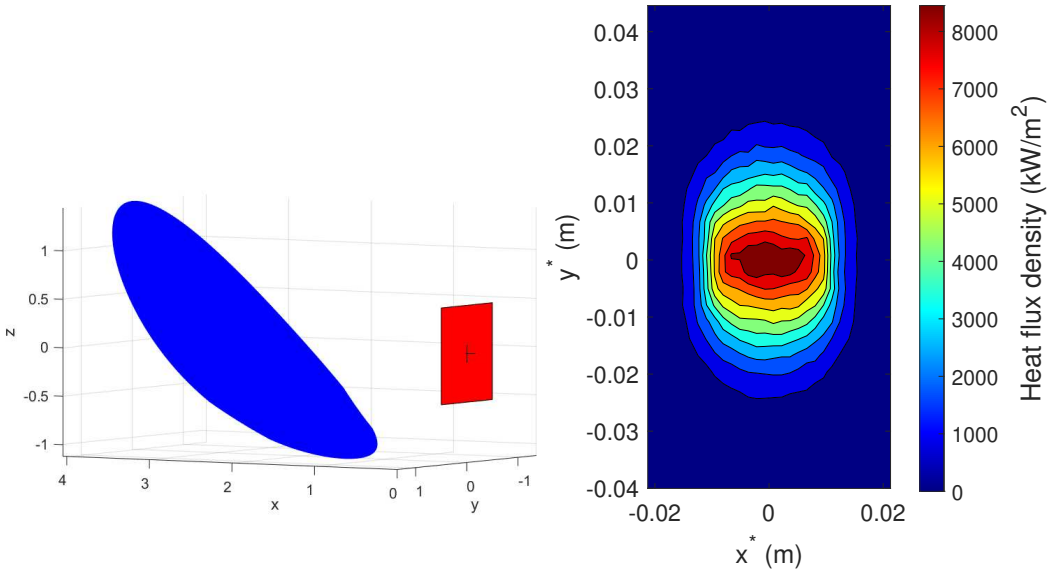

(a) (b)

Figure 5.19 – (a) "Perfect" Scheffler parabola's shape (and inclined plane receiver) for a Sun at Zenith and a day focal distance of 1.43 m; (b) Focal image that is obtained from this parabola at equinox. Aperture area is 5.85 m^2, the transmitted power is 4.74 kW ($\sigma_{mirrors}$ = 0.9 and DNI = 900 W.m^{-2}), the image area is 26.4 cm^2 (100% of Φ) or 14.4 cm^2 (95% of Φ) and the average power density 1975 kW.m^{-2} (100% of Φ) or 3301 kW.m^{-2} (95% of Φ); CR are 2217 and 4076, respectively.

Results show that an 8 m^2 Scheffler reflector with a focal distance of 1.43 m cannot reach more than a CR of about 4076 at the equinox, with the smallest image of the Sun containing 95% of the flux being 14.4 cm^2 (see 5.19-b). These results are in good agreement with those from Reddy *et al.* [68], who developed an analytical model predicting the theoretical ideal shape of the image for different days and found a concentration ratio varying between 1000 (summer solstice) and 7000 (winter solstice) and with a value of $\sim$ 4000 for the equinoxes, for a parabola of 8 m^2 with a focal length of 1.5 m.

The continuous reflector model shows the physical limits of the system. Although not representing the reality, it is a good reference for comparison with other simulations and experiments in order to seek for possible enhancement of the real systems. Thus, when compared to the model with facets, it shows that using flat mirrors strongly limits the possible concentration performance of the Scheffler reflector. Using aluminum thin sheets is a better option to accommodate the shape of the parabola.

5.6.5.2 Estimate of optical errors

Optical errors are the reason why actual reflectors do not reach theoretical focal images. It is therefore important to characterize these errors experimentally. In general, studies on concentrating technologies focus on the slope error, which is generally the most important one and give values $< 4\ mrad$, for parabolic troughs [41], [86], linear Fresnel [30], [41], parabolic dish [3], [81], and central receiver technologies [4], [41], the latter generally showing even lower values. Regarding Scheffler reflectors, thorough optical characterizations are lacking, but some values up to 12.0 mrad or even 26 mrad [76] have been reported [72].

The continuous parabola model has been used to study the influence of the optical errors on the focal image size, and results were compared to experimental ones in order to estimate the magnitude of the errors. Figure X shows the average flux on a vertical 1 m^2 target, as well as the centroid position, with respect to the specularity error, the slope error, and k_{sun}. As it can be seen, the two physical errors have different effects on the focal image size and a simple correspondence cannot be found between k_{sun} and an optical error. The image position is slightly influenced by the slope error only, though it remains negligible. From these results, it is possible to roughly assess the total amount of experimental optical losses: when $k_{sun} = X$, 95% of the theoretical focal image obtained with the continuous reflector is contained in a 26 cm disk, corresponding to a total optical error of 30 mrad. Since this method is not very rigorous, we think that the real value should be included within 20 mrad and 40 mrad.

5.6.6 Appendix 2 : Results with other k_{sun}

One can build or experience a better Scheffler reflector, that is to say one giving smaller focal images. In order to assess the influence of the different parameters that were investigated in this study for different cases, the following subsections give the parametric study results for different values of k_{sun}, *i.e.* 1, 3, 5 and 9.

5.6.6.1 Results for $k_{sun} = 1$

The seasonal variations of the heat flux densities for $k_{sun} = 1$ is given in figure 5.21. Surprisingly, the focal image appears to be larger in winter than in summer, which is the opposite of the result obtained by [68] and [20].

For $k_{sun} = 1$, the average solar flux density on the target $< \phi >$ and the focal image's centroid position *vs.* the different adjustment errors are pictured in 5.22. This repre-

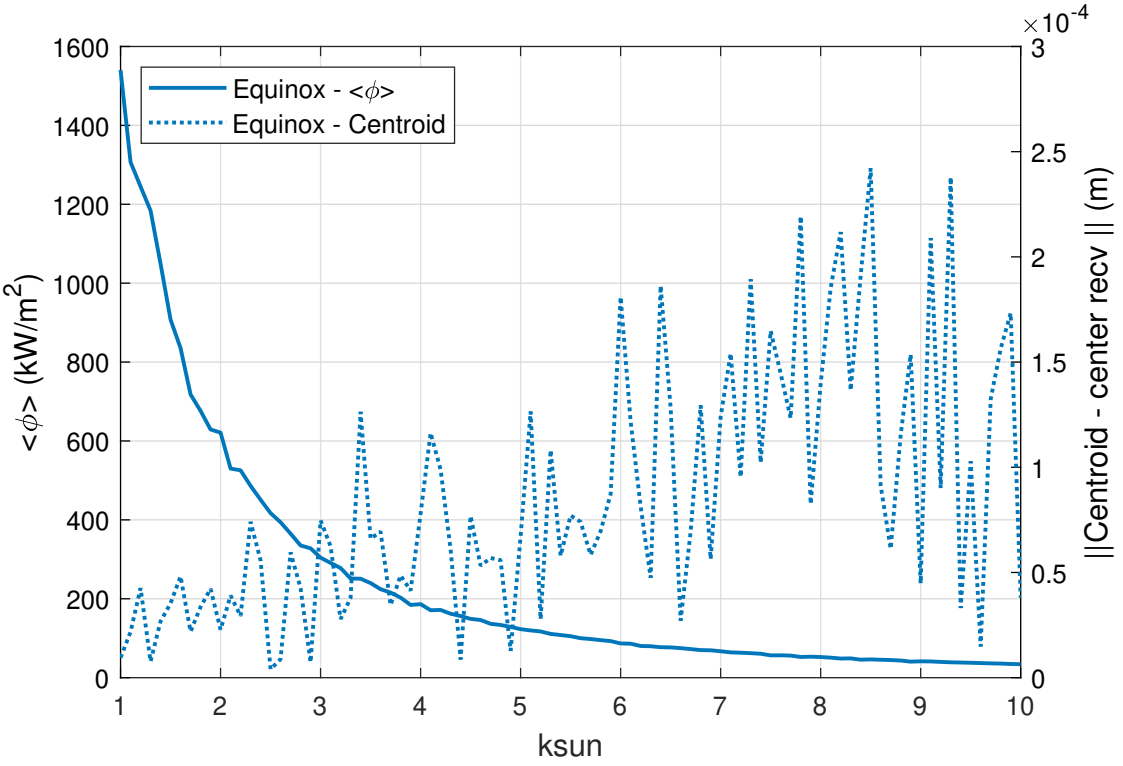

Figure 5.20 – Ideal Scheffler parabola: Influence of k_{sun} on the size of the focal image for the equinoxes

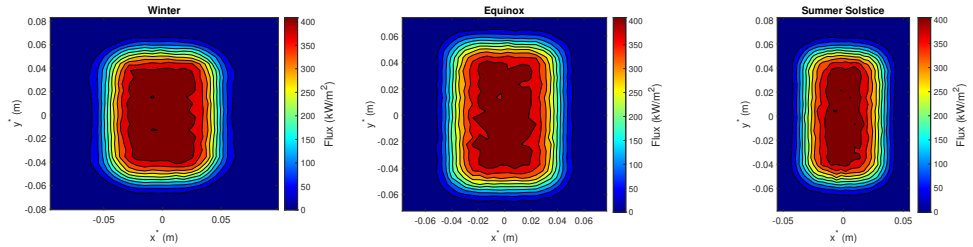

(a) (b) (c)

Figure 5.21 – Variation of the numerical focal image with the declination for $k_{sun} = 1$: (a) Winter solstice; (b) Spring equinox ; (c) Summer solstice

sents a Scheffler parabola with 0.1 m x 0.1 m facets and no slope, specularity or shape errors. An almost perfect system like this one is very sensible to the adjustment errors such as the South offset, the declination adjustment, the tracking, etc.

5.6.6.2 Results for $k_{sun} = 3$

For $k_{sun} = 3$, the average solar flux density on the target $< \phi >$ and the focal image's centroid position *vs.* the different adjustment errors are pictured in 5.23. This corresponds to a Scheffler parabola with 0.1 m x 0.1 m facets and small slope and

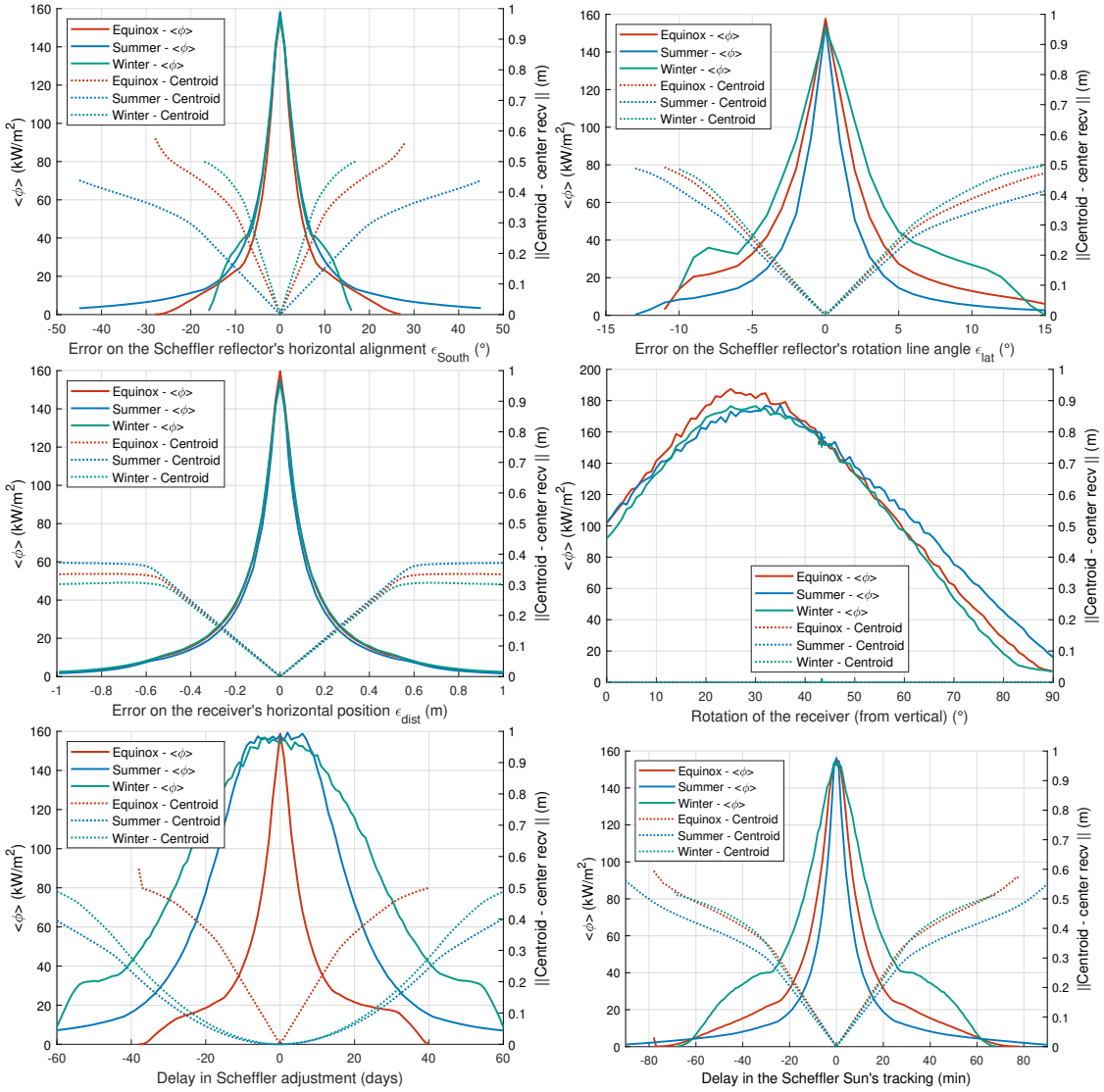

Figure 5.22 – Average solar flux density and centroid position for $k_{sun} = 1$

specularity errors.

5.6.6.3 Results for $k_{sun} = 5$

For $k_{sun} = 5$, the average solar flux density on the target $< \phi >$ and the focal image's centroid position *vs.* the different adjustment errors are pictured in 5.24. This corresponds to a possible Scheffler parabola with 0.1 m x 0.1 m facets and better slope and specularity errors that the one we experimentally observed.

5.6.6.4 Results for $k_{sun} = 9$

For $k_{sun} = 9$, the average solar flux density on the target $< \phi >$ and the focal image's centroid position *vs.* the different adjustment errors are pictured in 5.25. This corre-

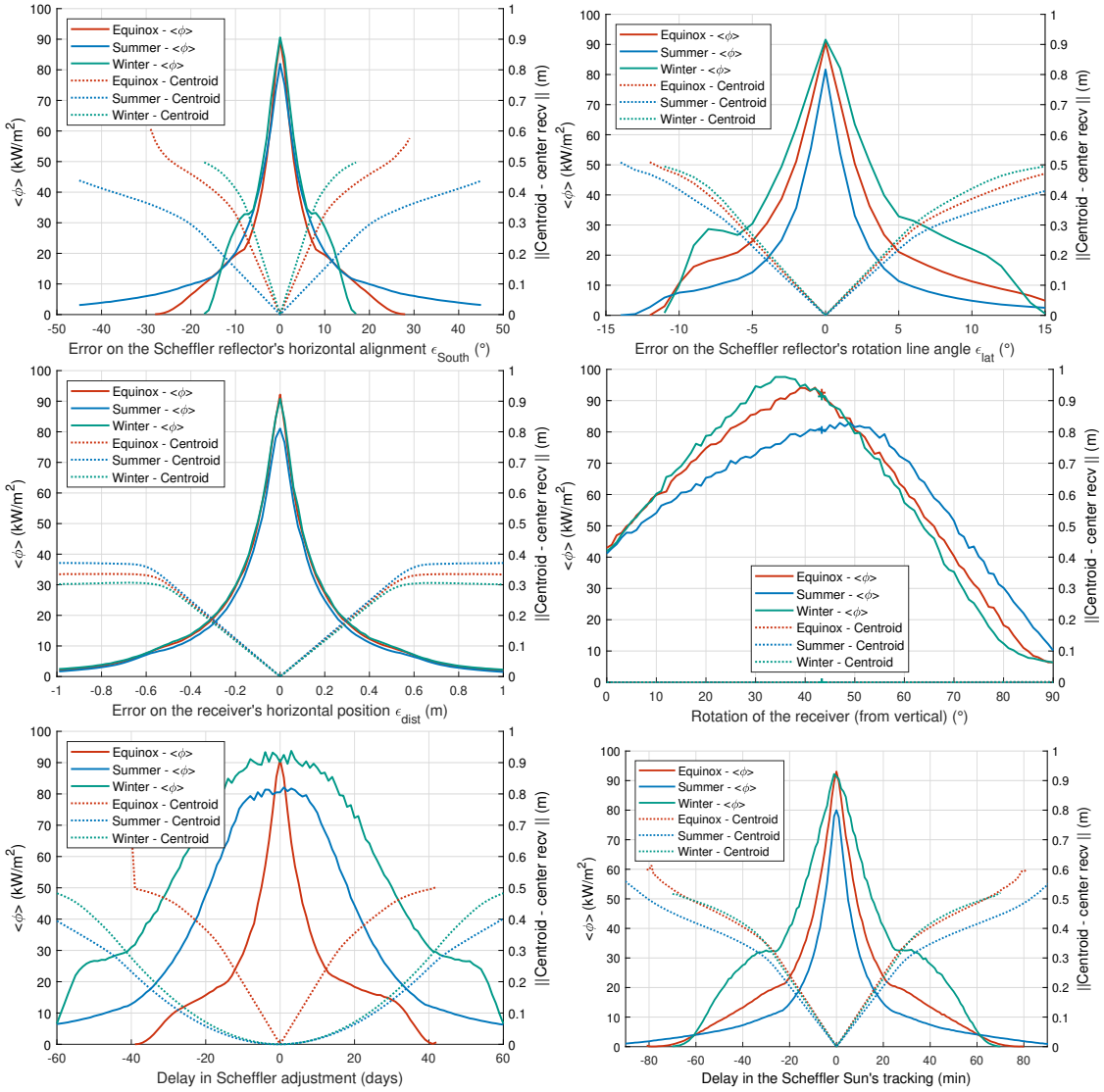

Figure 5.23 – Average solar flux density and centroid position for $k_{sun} = 3$

sponds to a possible Scheffler parabola with 0.1 m x 0.1 m facets and worse slope and specularity errors that the one we experimentally observed. In this case, the system is really resilient to other errors.

.

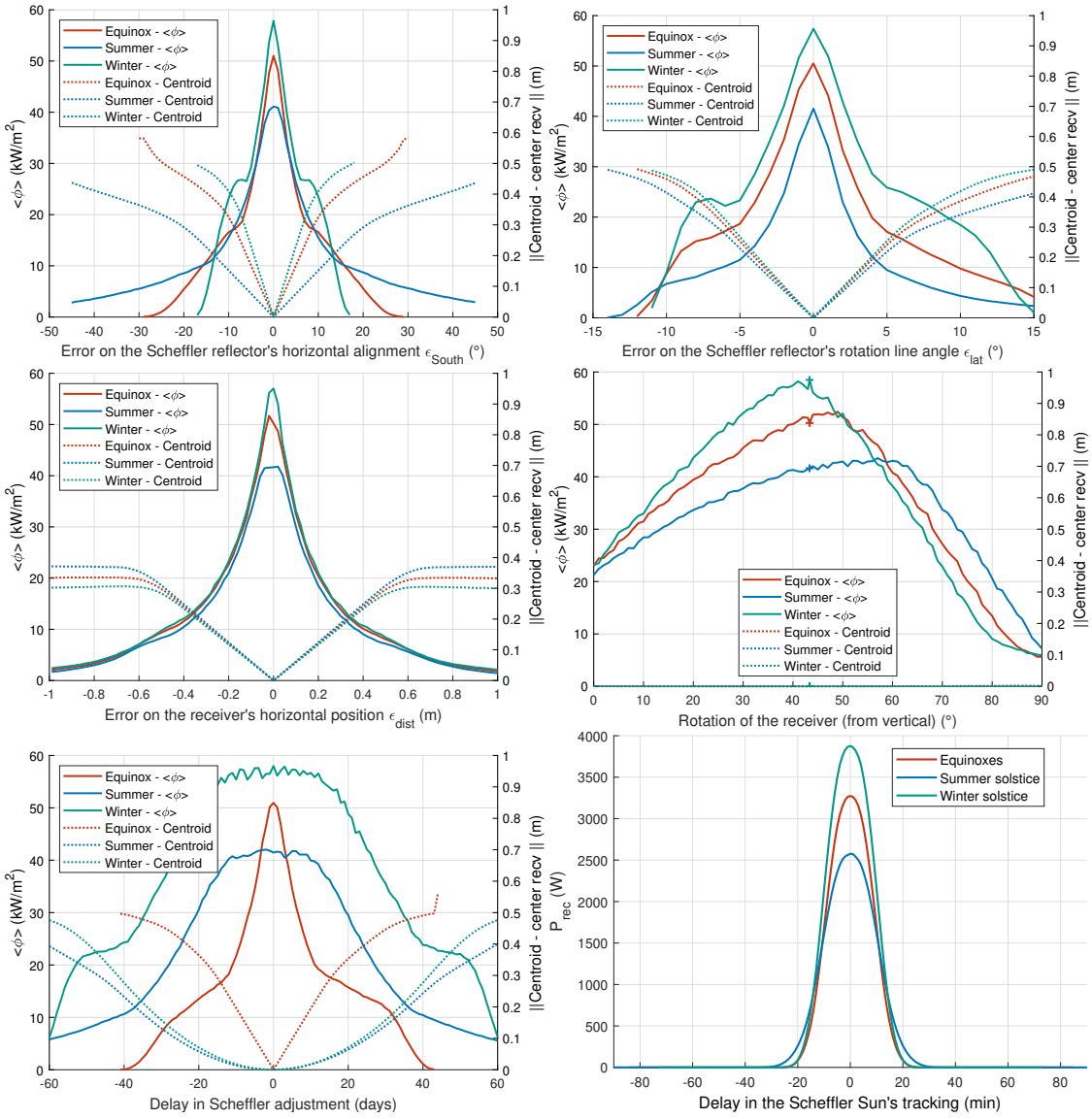

Figure 5.24 – "Average solar flux density and centroid position for $k_{sun} = 5$

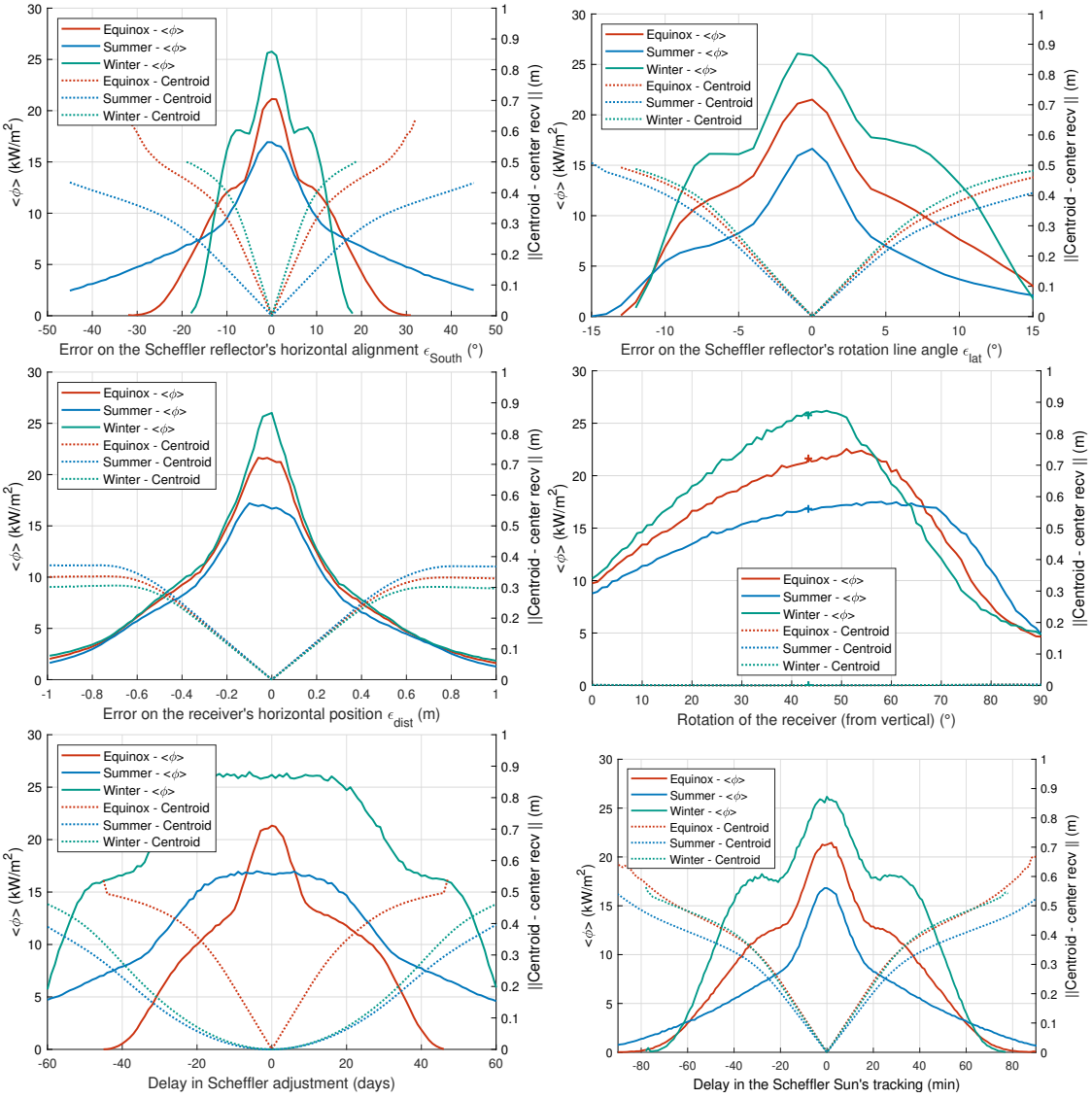

Figure 5.25 – "Average solar flux density and centroid position for $k_{sun} = 9$

5.7 Dynamic thermal behaviour of a solar restaurant housing two Scheffler parabolas

5.7.1 Foreword

An initial thermal study of the restaurant building was carried out in spring 2022 as part of the stage of Master 2 of Salmane Zekri (a student of the Toulouse University III - Paul Sabatier). The construction project was still in design phase, the building plans were not yet definitive and the choice of heating equipments had not yet been finalised. Nevertheless, a summary of the trends in terms of heating requirements and indoor temperatures is presented in the following sections.

5.7.2 Short description of the restaurant building

Due to the concept of their project, the members of the company "Le Présage" have decided to build a high environmental building around their solar cookers. To achieve this, the building is designed in a bio-climatic way and with a reinforced energy efficiency in order to reduce its energy consumption in heating, air conditioning and lighting, while limiting its carbon impact.

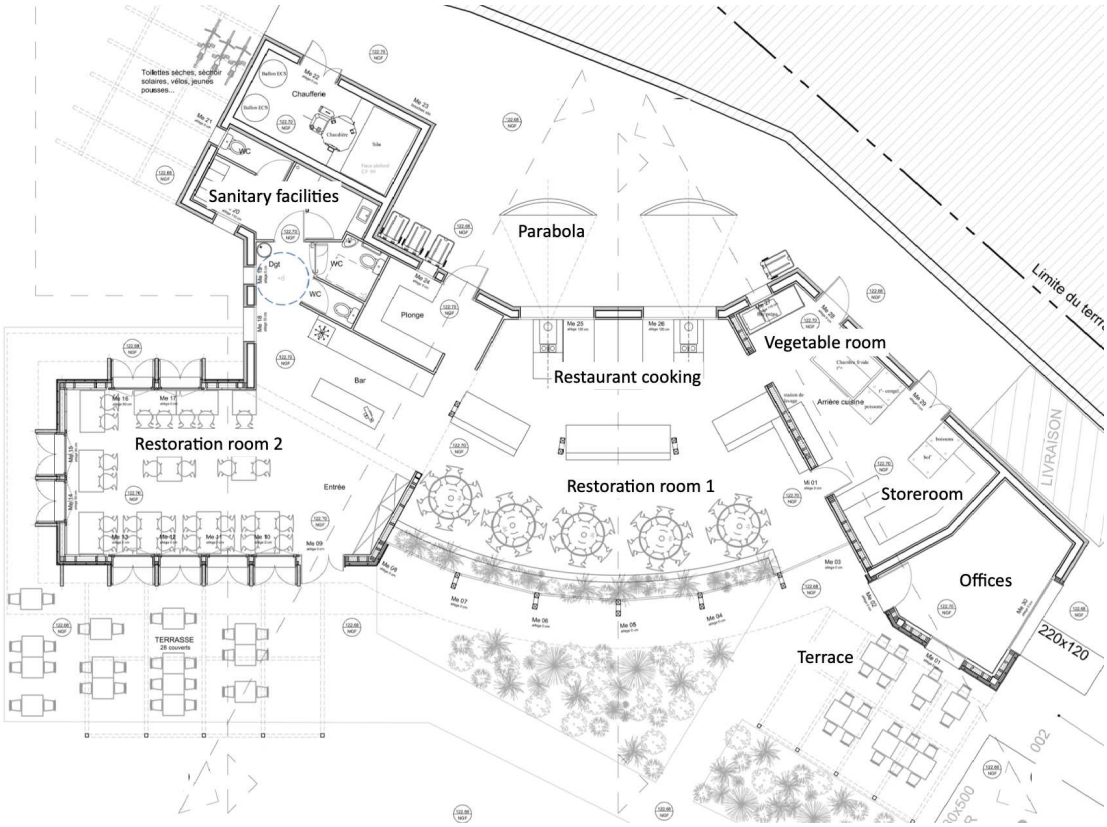

Figure 5.26 – Ground Floor Plan of the restaurant "Le Présage"

The layout of the restaurant's rooms reflects this desire for bio-climatic design: the two restoration rooms equipped of large windows and terrace face south to maximize winter solar gains and take advantage of the view of the garden, while the vegetable store and storeroom face north-east to minimize their inner temperature. On contrary during summer, to reduce solar gains and high inner temperatures in restoration rooms, large solar caps (2.6 m wide above the windows of first level and 1.2 m wide above the windows of ground floor) and trees/vegetation are used to protect windows (see Figure 5.27).

It has to be noted that in addition to the rooms mentioned above, the building

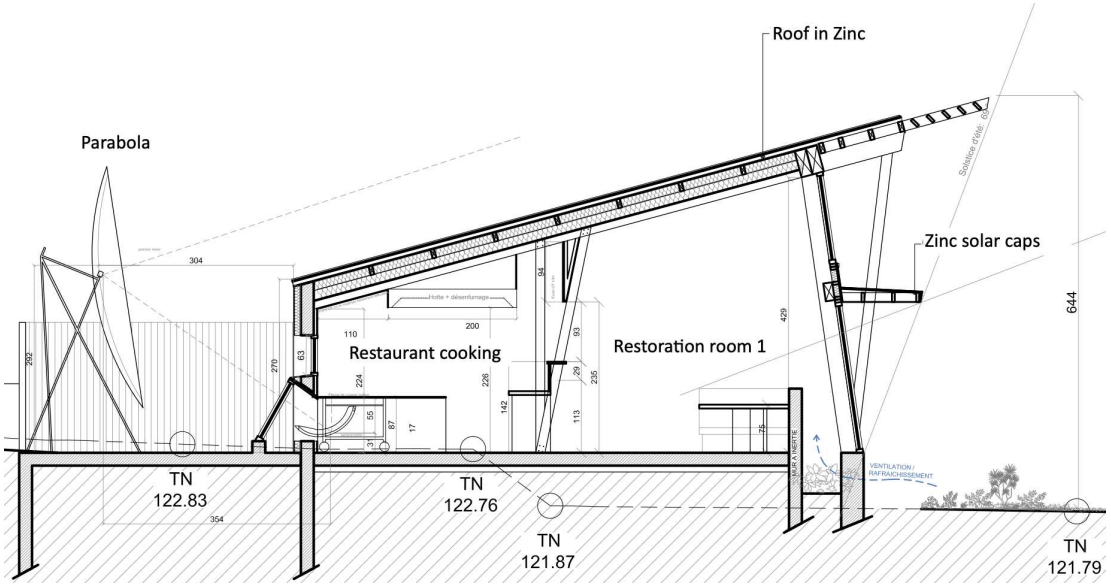

Figure 5.27 – Elevation view of the restaurant "Le Présage"

includes offices, sanitary facilities and employee areas, ..., as shown in Figure 5.26.

The building's high energy efficiency is ensured by the use of external thermal insulation, giving the external walls and low floor thermal resistances of 4.5 to 5 $K.m^2.W^{-1}$, while the roof has a thermal resistance of around 7 $K.m^2.W^{-1}$. Double-glazed windows with a heat loss coefficient of 1.4 $W.K^{-1}.m^{-2}$, a solar factor of 0.5 and a light transmission rate of 0.7 are used. Inertia is provided by concrete partition walls and some concrete external walls.

To limit the building's environmental impact, wood wool is used to insulate the roof, and some external walls are timber-framed and insulated with wood wool. Heating is provided by a wood pellet boiler. To reduce the possibility of high summer temperatures, no active air-conditioning system is planned. Instead, night-time overventilation is envisaged in addition to adiabatic ventilation during the day and natural ventilation, where the air is cooled by the evapotranspiration of the garden plants.

5.7.3 Expected Building thermal performances

In design phase, this construction project has obtained the gold label from the association ENVIROBAT BDM.

In particular, a gain of 22% is announced on the Bbio coefficient defined in the French authority thermal building regulations, RT2012, as [5]:

$$\text{Bbio} = 2 \times \text{Bh} + 2 \times \text{Ba} + 5 \times \text{Bl}, \tag{5.20}$$

where Bh, Ba and Bl are annual heating needs, annual air conditioning needs and annual artificial lighting needs respectively, expressed in kWh.m^{-2}.

In accordance with the RT2012 regulations and assuming a conventional use 17.27 for this building (restaurant serving two meals a day, six days a week) [50] built in the climatic zone H3 at an altitude of 140m, the maximum value of the Bbio coefficient [5] is found to be: Bbiomax =75 points (equivalent to kWh.m^{-2}).

5.7.4 Reference study of the building's thermal dynamic behaviour

Ultimately, the idea is to instrument the restaurant building to measure certain parameters (temperatures, humidity, air speed in particular) to describe the thermal comfort achieved inside. These measured temperatures will be then compared with those obtained in design phase by dynamic thermal simulations using the PLEIADES software distributed by IZUBA.

These are their annual evolutions that are presented and discussed in the following paragraphs.

5.7.4.1 Reference Dynamic Thermal Simulation (DTS) parameters

A digital model of the building is constructed in 2D/3D using *PLEIADES MODELEUR*, while the walls and the windows were defined using *PLEIADES BIBLIOTHEQUE*.
This building digital model is divided into 8 thermal zones (Figure 5.28) in which are applied different scenarios modeling the occupant number, the heat released by equipments, the ventilation, ...

In each thermal zone, the occupant's number and the occupancy periods are based either on the conventional scenarios associated with the above-mentioned conventional use (offices, for example) either on information provided by the managers of "Le Présage". In both restoration rooms, service is from 12 pm to 2 pm, with a maximum of 30 covers simultaneously. A second service is envisaged in restoration room 2 from 7 pm to 9 pm with a maximum of 30 covers simultaneously. 4 people are spread throughout the building, except the office, from 8 am to 11 pm, depending on the use of the different rooms (thermal zones) during meal preparation and cleaning. The office is occupied by one person from 8 am to 8 pm, 5 days a week (see RT2012 regulations [50]. In other thermal zones, such as the toilets and the boiler room, no

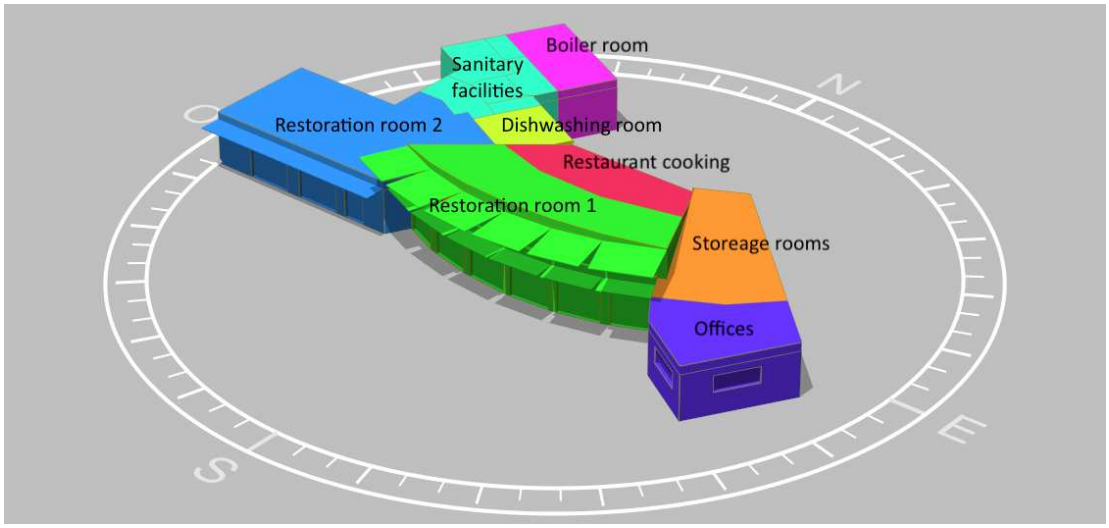

Figure 5.28 – Visualization of the 8 thermal zones of the digital building

occupancy is defined, as it is temporary and of short duration.
At last, DTSs are carried out assuming that each occupant dissipates an instantaneous power of 80 W.

Since DTSs performed for this study are based on simplified aeraulic calculations, different ventilation scenarios are defined for each thermal zone. In both restoration rooms, the French Labour Code requires a ventilation rate of 30 $m^3.h^{-1}$ per person, i.e. a total rate of 900 $m^3.h^{-1}$ for a 100% occupancy. This ventilation rate is modulated by the occupancy rate, while it begins and ends outside service periods at a reduced rate. In the restaurant cooking, the air flowrate that has to be extracted via cooker hoods is 25 $m^3.h^{-1}$ per meal and 30 $m^3.h^{-1}$ per cook. An occupancy flow-rate of 18 $m^3.h^{-1}$ is maintained in the offices and 30 $m^3.h^{-1}$ in other high humidity rooms such as the dish-washing area, the storage room (vegetable room).

The convective and radiative powers of the cookers and the plancha are estimated by assuming that they have respective temperatures and emissivities of 373 K , 473 K, 0.7 and 0.5. Their environment is assumed to have a temperature of 303 K. The location, number and characteristics of other restaurant equipment's were provided by the members of "Le Présage" and taken into account to create suitable power dissipation scenarios.

All these parameters / assumptions are summarized in Figure 5.29.

Finally, the meteorological data used are those from the "Marseille Moyen" station of the Météornom pack distributed by IZUBA.

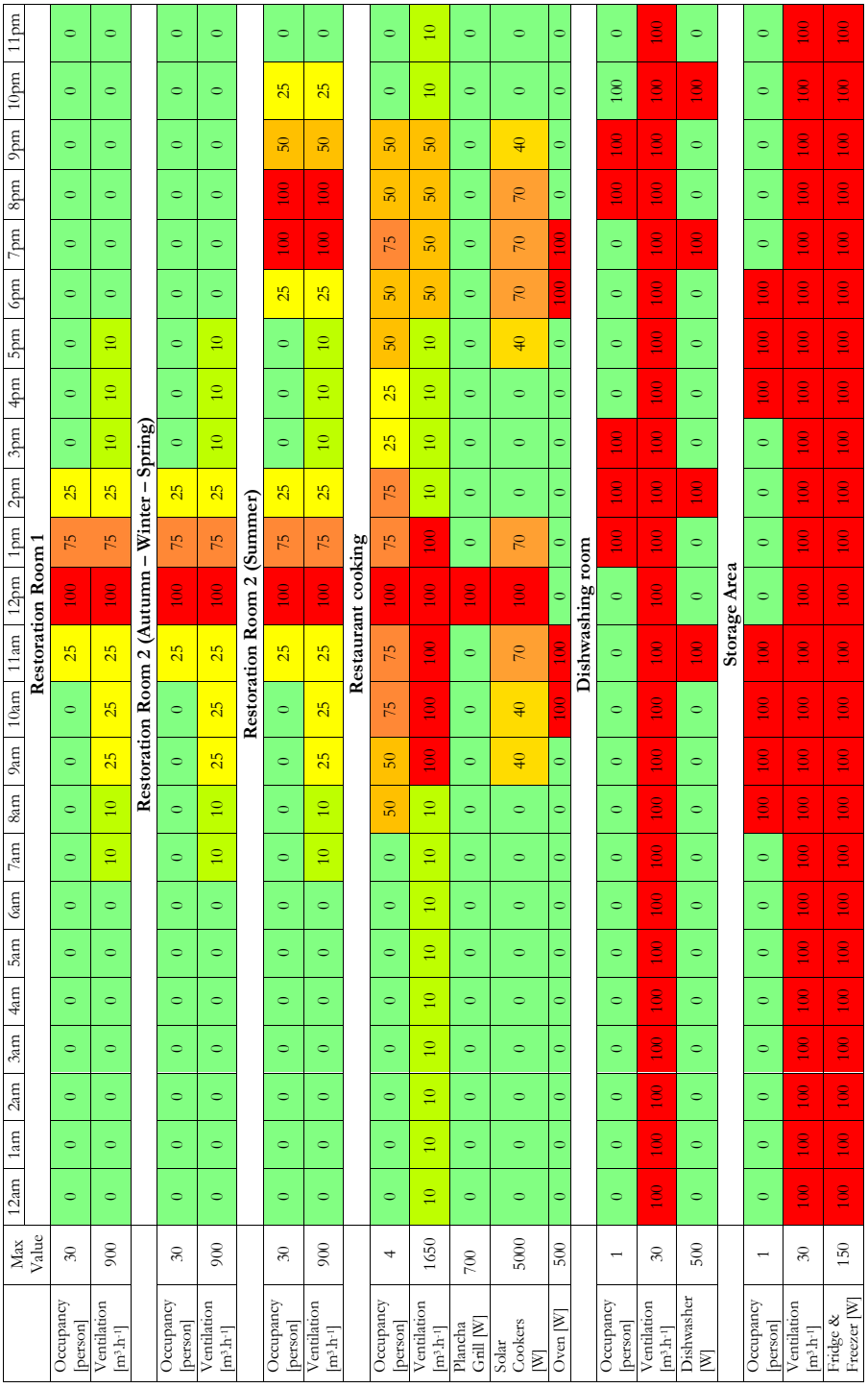

	Max Value	12am	1am	2am	3am	4am	5am	6am	7am	8am	9am	10am	11am	12pm	1pm	2pm	3pm	4pm	5pm	6pm	7pm	8pm	9pm	10pm	11pm
Restoration Room 1																									
Occupancy [person]	30	0	0	0	0	0	0	0	0	0	0	0	25	100	75	25	0	0	0	0	0	0	0	0	0
Ventilation [m³·h⁻¹]	900	0	0	0	0	0	0	0	10	10	25	25	25	100	75	25	10	10	10	0	0	0	0	0	0
Restoration Room 2 (Autumn – Winter – Spring)																									
Occupancy [person]	30	0	0	0	0	0	0	0	0	0	0	0	25	100	75	25	0	0	0	0	0	0	0	0	0
Ventilation [m³·h⁻¹]	900	0	0	0	0	0	0	0	10	10	25	25	25	100	75	25	10	10	10	0	0	0	0	0	0
Restoration Room 2 (Summer)																									
Occupancy [person]	30	0	0	0	0	0	0	0	0	0	0	0	25	100	75	25	0	0	0	25	100	100	50	25	0
Ventilation [m³·h⁻¹]	900	0	0	0	0	0	0	0	10	10	25	25	25	100	75	25	10	10	10	25	100	100	50	25	0
Restaurant cooking																									
Occupancy [person]	4	0	0	0	0	0	0	0	0	50	50	75	75	100	75	75	25	25	50	50	75	50	50	0	0
Ventilation [m³·h⁻¹]	1650	10	10	10	10	10	10	10	10	10	100	100	100	100	100	10	10	10	10	50	50	50	50	10	10
Plancha Grill [W]	700	0	0	0	0	0	0	0	0	0	0	0	0	100	0	0	0	0	0	0	0	0	0	0	0
Solar Cookers [W]	5000	0	0	0	0	0	0	0	0	0	40	40	70	100	70	0	0	0	40	70	70	70	40	0	0
Oven [W]	500	0	0	0	0	0	0	0	0	0	0	100	100	0	0	0	0	0	0	100	100	0	0	0	0
Dishwashing room																									
Occupancy [person]	1	0	0	0	0	0	0	0	0	0	0	0	0	0	100	100	100	0	0	0	0	100	100	100	0
Ventilation [m³·h⁻¹]	30	100	100	100	100	100	100	100	100	100	100	100	100	100	100	100	100	100	100	100	100	100	100	100	100
Dishwasher [W]	500	0	0	0	0	0	0	0	0	0	0	0	100	0	0	100	0	0	0	0	100	0	0	100	0
Storage Area																									
Occupancy [person]	1	0	0	0	0	0	0	0	0	100	100	100	100	0	0	0	0	100	100	100	0	0	0	0	0
Ventilation [m³·h⁻¹]	30	100	100	100	100	100	100	100	100	100	100	100	100	100	100	100	100	100	100	100	100	100	100	100	100
Fridge & Freezer [W]	150	100	100	100	100	100	100	100	100	100	100	100	100	100	100	100	100	100	100	100	100	100	100	100	100

Figure 5.29 – Summary of different dynamic thermal simulation parameters: number of occupants, ventilation and internal heat releases. Percentages in relation with the maximal values are reported inside the table.

Table 5.8 – Estimated Heating needs and power, estimated minimal and maximal temperatures in each thermal zone.

Thermal Zones	Heating Needs kWh.m^{-2}	Heating Power W	Min. Temperature °C	Max. Temperature °C
Rest. room 1	25.81	9,000.00	9.68	35.90
Rest. room 2	9.78	5,955.53	13.27	35.20
Rest. cooking	60.83	11,194.36	10.49	42.04
Office	11.87	2,974.96	12.34	37.42
Storeage rooms	0	0	12.58	34.48
Dishwashing room	0	0	9.57	36.59
Sanitary	0	0	6.86	35.89
Boiler room	0	0	7.24	33.41
Total	24.04	23,257	6.86	42.04

5.7.4.2 Results of the reference Dynamic Thermal simulation

Overall results of the reference DTS are shown in Table 5.8. Annual heating needs are limited: their value is around 3 times lower than that of Bbiomax. However, maximum temperatures reached in all the thermal zones are very high.

Figure 5.30(a) shows the annual evolutions of the outside temperature and the restoration room 1 temperature. The latter is always superior to the outside one due to solar gains through the large windows oriented south and heat release of customers. However, as expected, thanks to the large solar caps, solar gains entering in the restoration room 1 are reduced by a factor of around 3 in summer, as shown in Figure 5.30(b).

Comparisons reported on Figure 5.31 indicate that maximum temperatures are reached in the restoration room 1 during winter and in the restaurant cooking in summer. During winter, restoration room 2 heating is necessary when outside temperature is lower than 10°C or when days are not sunny. During summer, the temperature in restoration room 2 varies between 28°C and 35°C. During winter, heating the restaurant cooking is also necessary because of the high air exchange rate, despite the heat release by the cooking equipment's (slightly visible). In summer, however, the latter lead to temperature peaks in the restaurant cooking each time a meal is prepared. For example, there are two peaks from Wednesday to Saturday when two meals per day are served, a single peak on Mondays and Tuesdays when only one meal is served and no peak on Sundays. However, temperature in restoration room 1 remains high on Sundays because of high solar gains within the large windows oriented south.

5.7.4.3 Conclusions on the reference DTS

In conclusion, reference DTS shows that, as expected, heating needs are limited while inner temperatures are very high because of cooking equipment's, heat releases

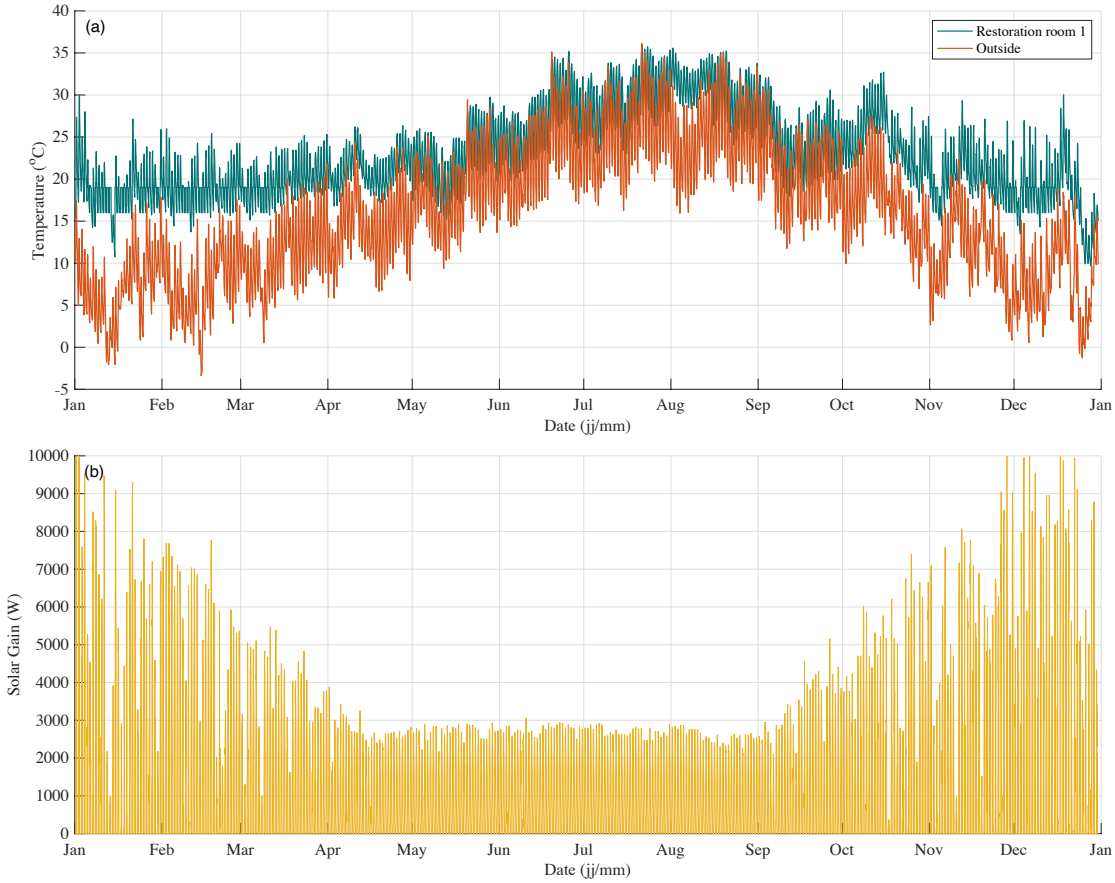

Figure 5.30 – (a) Annual temperature trends outside and in the restoration room 1. (b) Solar gains within the restoration room 1.

due to customers and solar gains in the restoration room 1. Very high temperatures can be observed in the room 1 : almost 25°C in February and 35°C in July. These very high temperatures are the main source of discomfort in this restaurant and are the main area for optimisation.

5.7.5 Effects of a few parameters on the dynamic thermal behavior of the restaurant

5.7.5.1 Effects of the solar caps

Figure 5.32 shows the annual evolution's of the temperature (a) and the solar gains (b) in the restoration room 1 with or without solar caps above the ground floor windows and above those on the first level (visible on Figure 5.28).

The two graphs indicate that these two solar caps help to reduce the inner temperature in the restoration room 1 by preventing direct sun ray from entering through the window. Without solar caps, solar gains in room 1 are about 7 kW during summer and about 18 kW during winter. This can be explained by the fact that in the south,

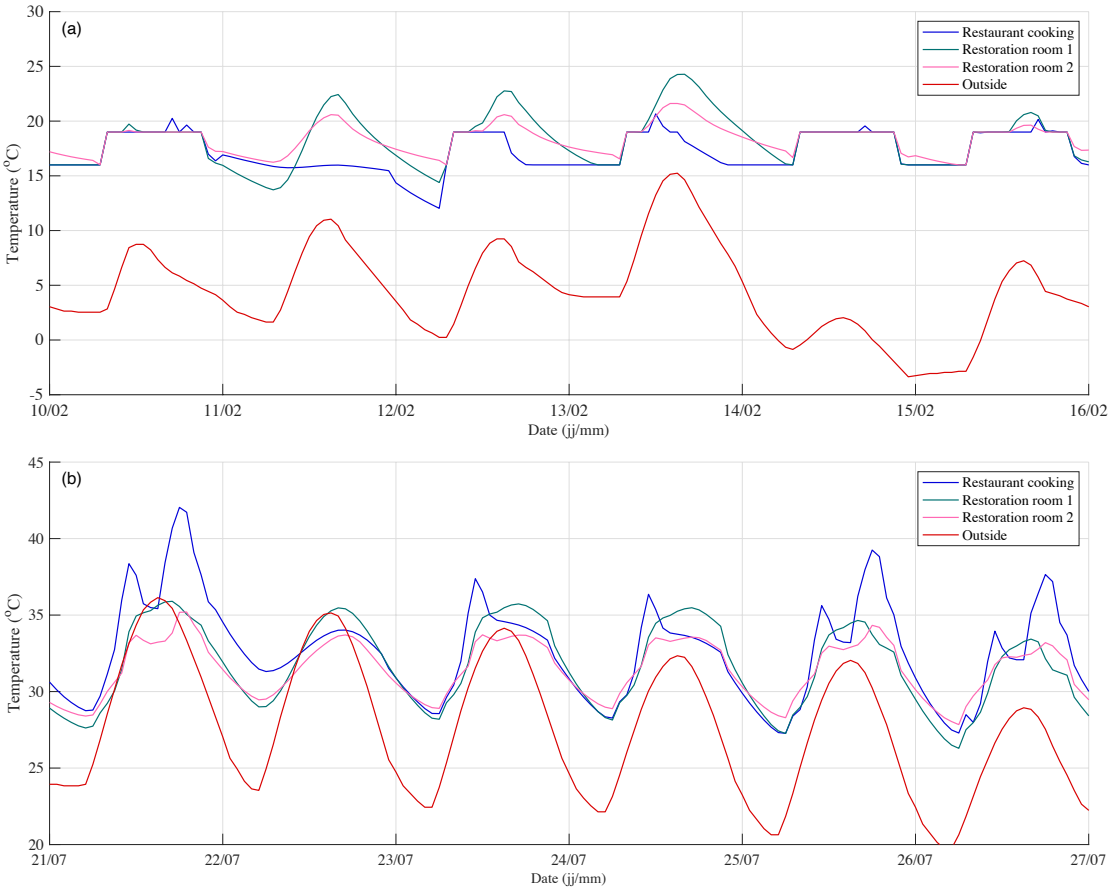

Figure 5.31 – (a) Temperature trends during one week of February. (b) Temperature trends during one week of July.

the Sun is much higher in the sky in summer than in winter. The incident energy for a vertical surface is therefore relatively low, whereas it is very high for a horizontal surface. In winter, the Sun is low in the sky and its path is limited from south-east to south-west: the almost horizontal rays bring more energy to a vertical surface in the south. In addition, Figure 5.32 shows that in summer even with solar shading, it is not possible to reduce solar gain below around 2.5 kW (i.e. 25 W per m^2 of window). This is because a solar cap, however long it may be, cannot block out the diffuse part of the sun's rays. At last, Figure 5.32 indicates that even in winter, the absence of solar protection can lead to a situation of discomfort ($T \approx 30$°C in restoration room 1).

5.7.5.2 Effects of the nigth-time over-ventilation

In order to reduce temperatures in the restoration rooms, it is planned to use night-time over-ventilation (with a flow-rate of 3 vol.h^{-1}) from May to October. The effects of this over-ventilation on the temperature of the restoration rooms are reported on Figures 5.33 which present comparisons between temperatures obtained without and with over-ventilation. The use of this over-ventilation permits to reduce the

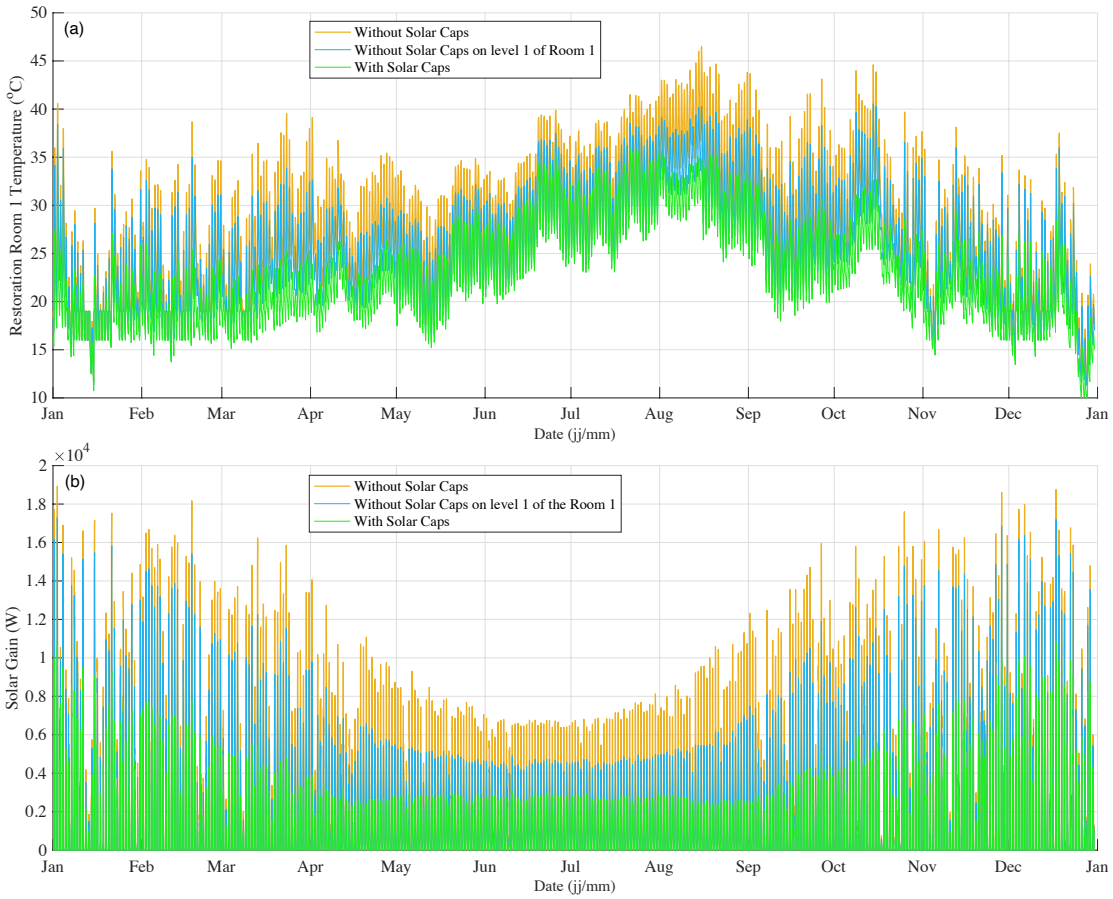

Figure 5.32 – (a) Annual evolution of the temperature in the restoration room 1. (b) Annual evolution of the solar gain in the restoration room 1.

temperatures in these rooms of 2.5 - 3°C.

5.7.5.3 Effects of the heat release by customers

Figure 5.33 also shows the evolution of the temperature in the restoration rooms when no customer is present during summer. The temperature in restoration room 1 is only slightly affected, but it drops by 1.5 to 2.5°C in restoration room 2. In particular, the temperature peaks associated with occupancy are eliminated.



Figure 5.33 – (a) Annual evolution of the temperature in the restoration room 1. (b) Annual evolution of the temperature in the restoration room 2.

5.7.6 Conclusions & perspectives

In 2022, an initial digital model of the restaurant building was realized, enabling first dynamic thermal simulations to be carried out. They show that high inner temperatures may be achieved if no air conditionning is used.

No Dynamic Energy Simulation (DES) was carried out during this initial study because the heating, ventilation and other equipments had not yet been fully selected. In addition, for financial reasons and due to the availability of construction materials, the plans and final choices of the restaurant and its construction materials were reworked in 2023 before construction works began in autumn 2023.

The study therefore needs to be updated. This involves updating the 3D model, making a definitive choice of construction elements, and adapting the various scenarios if necessary, before carrying out new DTS and DES. In addition, the choice of a simplified or detailed aeraulic calculation could also be evaluated.

At last, these updated dynamic thermal and energy simulations will be compared with in-situ measurements taken in the future building, in order to study its energy

efficiency and thermal comfort achieved in it.

Bibliography

[1] "Volume I - Measurement of Meteorological Variables", en, in *Guide to Instruments and Methods of Observation*, ser. WMO 8, W. M. O. (WMO), Ed., 2021st ed., vol. 1, Geneva: World Meteorological Organization (WMO), 2021, p. 558, ISBN: 978-92-63-10008-5 (cit. on p. 54).

[2] S. Alberti, "Analysis and Optimization of the Scheffler Solar Concentrator", en, M.S. thesis, California Polytechnic State University, San Luis Obispo, California, Dec. 2014. DOI: 10.15368/theses.2014.183. [Online]. Available: http://digitalcommons.calpoly.edu/theses/1335 (visited on 06/16/2021) (cit. on p. 67).

[3] C. E. Andraka, "Cost/performance tradeoffs for reflectors used in solar concentrating dish systems", in *Energy Sustainability*, vol. 43208, 2008, pp. 505–513 (cit. on p. 138).

[4] F. Arqueros, A. Jiménez, and A. Valverde, "A novel procedure for the optical characterization of solar concentrators", *Solar energy*, vol. 75, no. 2, pp. 135–142, 2003 (cit. on p. 138).

[5] *Arrete du 28 Decembre 2012*, fr, Dec. 2012. [Online]. Available: https://www.legifrance.gouv.fr/jorf/id/JORFTEXT000026871753 (visited on 12/28/2012) (cit. on p. 146).

[6] *ASAE S580.1 NOV2013 - Testing and Reporting Solar Cooker Performance*, en-US, Nov. 2013 (cit. on pp. 27, 35, 51, 55).

[7] I. Ayub, A. Munir, W. Amjad, *et al.*, "Energy- and exergy-based thermal analyses of a solar bakery unit", en-GB, *Journal of Thermal Analysis and Calorimetry*, vol. 133, no. 2, pp. 1001–1013, Aug. 2018, ISSN: 1588-2926. DOI: 10.1007/s10973-018-7165-3. [Online]. Available: https://doi.org/10.1007/s10973-018-7165-3 (visited on 06/16/2021) (cit. on p. 67).

[8] A. Balzar, P. Stumpf, S. Eckhoff, *et al.*, "A solar cooker using vacuum-tube collectors with integrated heat pipes", en, *Solar Energy*, Selected Proceedings of ISES 1995: Solar World Congress. Part I, vol. 58, no. 1, pp. 63–68, Jul. 1996, ISSN: 0038-092X. DOI: 10.1016/0038-092X(96)00024-2. [Online]. Available: https://www.sciencedirect.com/science/article/pii/0038092X96000242 (visited on 08/28/2023) (cit. on p. 35).

[9] F. J. Barba, M. Gavahian, I. Es, *et al.*, "Solar radiation as a prospective energy source for green and economic processes in the food industry: from waste biomass valorization to dehydration, cooking, and baking", *Journal of cleaner production*, vol. 220, pp. 1121–1130, 2019 (cit. on p. 117).

[10] P. S. Bhambare and S. C. Vishweshwara, "Design aspects of a fixed focus type Scheffler concentrator and its receiver for its utilization in thermal processing units", en-GB, *Energy Nexus*, vol. 7, p. 100 103, Sep. 2022, ISSN: 2772-4271. DOI: 10.1016/j.nexus.2022.100103. [Online]. Available: https://www.sciencedirect.com/science/article/pii/S2772427122000651 (visited on 11/23/2022) (cit. on p. 77).

[11] E. Biermann, M. Grupp, and R. Palmer, "Solar cooker acceptance in South Africa: results of a comparative field-test", en, *Solar Energy*, vol. 66, no. 6, pp. 401–407, Sep. 1999, ISSN: 0038-092X. DOI: 10.1016/S0038-092X(99)00039-0. [Online]. Available: https://www.sciencedirect.com/science/article/pii/S0038092X99000390 (visited on 08/31/2023) (cit. on p. 35).

[12] S. Caron, J. Garrido, E. Setien, *et al.*, "Forty Shades of Black: A Benchmark of High Temperature Sprayable Black Coatings Applied on Haynes 230", en-GB, in *AIP Conference Proceedings*, vol. 2303, Daegu, South Korea: AIP Publishing, Dec. 2020, p. 150 007, ISBN: 978-0-7354-4037-1. DOI: 10.1063/5.0028773. [Online]. Available: https://aip.scitation.org/doi/abs/10.1063/5.0028773 (visited on 03/14/2022) (cit. on p. 105).

[13] CBA Advisor, *Plaque coup de feu gaz*, fr-FR, 2021. [Online]. Available: https://www.youtube.com/watch?v=FSXAjMgDNC0 (visited on 11/05/2021) (cit. on p. 28).

[14] M. Collares-Pereira, A. Cavaco, and A. Tavares, "Figures of Merit and Their Relevance in the Context of a Standard Testing and Performance Comparison Methods for Solar Box – Cookers", en, *Solar Energy*, vol. 166, pp. 21–27, May 2018, ISSN: 0038-092X. DOI: 10.1016/j.solener.2018.03.040. [Online]. Available: https://www.sciencedirect.com/science/article/pii/S0038092X18302731 (visited on 03/01/2021) (cit. on p. 33).

[15] J. Coventry and P. Burge, "Optical properties of Pyromark 2500 coatings of variable thicknesses on a range of materials for concentrating solar thermal applications", en-GB, in *AIP Conference Proceedings*, vol. 1850, American Institute of Physics, Jun. 2017, p. 030 012. DOI: 10.1063/1.4984355. [Online]. Available: https://aip.scitation.org/doi/abs/10.1063/1.4984355 (visited on 03/16/2022) (cit. on p. 105).

[16] M. E. De Castel, A. Finck Pastrana, M. Collares Pereira, *et al.*, "Protocolo de cocción solar de RICSA. Apreciaciones respecto de la determinación de la energía y la carga para determinar la potencia efectiva de cocción", es, *Avances en Energías Renovables y Medio Ambiente*, vol. 4, pp. 77–80, 2000, ISSN: 0329-5184 2796-8111 2314-1433. [Online]. Available: http://sedici.unlp.edu.ar/handle/10915/79080 (visited on 09/11/2023) (cit. on p. 33).

[17] M. E. De Castel, A. Fink Pastrana, M. Collares-Pereira, *et al.*, "Propuestas de procedimiento para la evaluacion del comportamiento termico de cocinas y hornos solares", es, *Avances en Energías Renovables y Medio Ambiente*, vol. 3, no. 2, pp. 133–136, 1999, ISSN: 0329-5184 2796-8111 2314-1433 (cit. on p. 33).

[18] E. A. Dib, "Análise da formação de imagem focal do concentrador solar paraboloidal tipo scheffler", pt-BR, Ph.D. thesis, University of São Paulo, São Paulo, Brazil, 2021 (cit. on pp. 68, 81, 83).

[19] E. A. Dib and F. A. S. Fiorelli, "Scheffler Paraboloidal Concentrator Image Analysis", en, in *Proceedings of the 23rd ABCM International Congress of Mechanical Engineering*, Rio de Janeiro, Brazil, Dec. 2015, p. 8. DOI: 10.20906/CPS/COB-2015-0893. [Online]. Available: http://www.swge.inf.br/proceedings/paper/?P=COB-2015-0893 (visited on 05/23/2022) (cit. on p. 66).

[20] E. A. Dib and F. A. S. Fiorelli, "Análise da formação de imagem focal do concentrador solar paraboloidal tipo scheffler", 2021 (cit. on pp. 118, 127, 138).

[21] J. A. Duffie and W. A. Beckman, *Solar Engineering of Thermal Processes*, en-US, 3rd ed. Hoboken, USA: Wiley, Aug. 2006, Google-Books-ID: tPayQgAACAAJ, ISBN: 978-0-471-69867-8 (cit. on p. 77).

[22] J. A. Duffie, G. O. G. Löf, and B. Beck, "Laboratory and field studies of plastic reflector solar cookers [1st ed]", en, *Solar Energy*, vol. 6, no. 3, pp. 94–98, Jul. 1962, ISSN: 0038-092X. DOI: 10.1016/0038-092X(62)90034-8. [Online]. Available: https://www.sciencedirect.com/science/article/pii/0038092X62900348 (visited on 05/28/2021) (cit. on p. 30).

[23] M. El Ydrissi, H. Ghennioui, A. Farid, *et al.*, "A review of optical errors and available applications of deflectometry technique in solar thermal power applications", *Renewable and Sustainable Energy Reviews*, vol. 116, p. 109 438, 2019 (cit. on p. 122).

[24] D. Fontani, P. Sansoni, F. Francini, *et al.*, "Optical Raytracing Analysis of a Scheffler Type Concentrator", en-GB, *Energies*, vol. 15, no. 1, p. 260, Jan. 2022, Number: 1 Publisher: Multidisciplinary Digital Publishing Institute, ISSN: 1996-1073. DOI: 10.3390/en15010260. [Online]. Available: https://www.mdpi.com/1996-1073/15/1/260 (visited on 11/23/2022) (cit. on pp. 66, 118, 127).

[25] P. A. Funk, "Evaluating the international standard procedure for testing solar cookers and reporting performance", en-US, *Solar Energy*, vol. 68, no. 1, pp. 1–7, Jan. 2000, ISSN: 0038-092X. DOI: 10.1016/S0038-092X(99)00059-6. [Online]. Available: https://www.sciencedirect.com/science/article/pii/S0038092X99000596 (visited on 02/27/2021) (cit. on p. 35).

[26] J. Gaspar, Y. Corre, M. Firdaouss, *et al.*, "First heat flux estimation in the lower divertor of WEST with embedded thermal measurements", en-GB, *Fusion Engineering and Design*, SI:SOFT-30, vol. 146, pp. 757–760, Sep. 2019, ISSN: 0920-3796. DOI: 10.1016/j.fusengdes.2019.01.074. [Online]. Available: https://www.sciencedirect.com/science/article/pii/S0920379619300821 (visited on 06/25/2021) (cit. on pp. 68, 73).

[27] A. Gorjian, E. Rahmati, S. Gorjian, *et al.*, "A comprehensive study of research and development in concentrating solar cookers (CSCs): Design considerations, recent advancements, and economics", *Solar Energy*, vol. 245, pp. 80–107, Oct. 2022, ISSN: 0038-092X. DOI: 10.1016/j.solener.2022.08.066. [Online]. Available: https://www.sciencedirect.com/science/article/pii/S0038092X22006545 (visited on 08/31/2023) (cit. on pp. 35, 38).

[28] G. Guillet, S. Barbosa, T. Fasquelle, *et al.*, "Towards Professional Kitchen with Scheffler Reflectors", en-GB, in *CONSOLFOOD 2022 - Conference Proceedings*, Faro, Portugal, Jan. 2022, pp. 99–106 (cit. on p. 49).

[29] G. Guillet, J. Gaspar, S. Barbosa, *et al.*, "Experimental evaluation of the concentrated solar heat flux distribution provided by an 8 m^2 scheffler reflector", *Renewable Energy*, p. 119 958, 2024, ISSN: 0960-1481. DOI: https://doi.org/10.1016/j.renene.2024.119958. [Online]. Available: https://www.sciencedirect.com/science/article/pii/S0960148124000235 (cit. on pp. 66, 118, 124, 125, 127, 131).

[30] M. Hack, G. Zhu, and T. Wendelin, "Evaluation and comparison of an adaptive method technique for improved performance of linear fresnel secondary designs", *Applied Energy*, vol. 208, pp. 1441–1451, 2017 (cit. on p. 138).

[31] C. K. Ho, A. R. Mahoney, A. Ambrosini, *et al.*, "Characterization of Pyromark 2500 Paint for High-Temperature Solar Receivers", *Journal of Solar Energy Engineering*, vol. 136, no. 1, Jul. 2013, ISSN: 0199-6231. DOI: 10.1115/1.4024031. [Online]. Available: https://doi.org/10.1115/1.4024031 (visited on 03/14/2022) (cit. on p. 105).

[32] D. Holmgren, "Review of thermal conductivity of cast iron", en-US, *International Journal of Cast Metals Research*, vol. 18, no. 6, pp. 331–345, Dec. 2005, Publisher: Taylor & Francis _eprint: https://doi.org/10.1179/136404605225023153, ISSN: 1364-0461. DOI: 10.1179/136404605225023153. [Online]. Available: https://doi.org/10.1179/136404605225023153 (visited on 03/07/2023) (cit. on p. 75).

[33] S. Indora and T. C. Kandpal, "Institutional cooking with solar energy: A review", en-GB, *Renewable and Sustainable Energy Reviews*, vol. 84, pp. 131–154, Mar. 2018, ISSN: 1364-0321. DOI: 10.1016/j.rser.2017.12.001. [Online]. Available: https://www.sciencedirect.com/science/article/pii/S1364032117315320 (visited on 05/21/2021) (cit. on pp. 72, 117).

[34] B. Iooss and P. Lemaître, "A review on global sensitivity analysis methods", in *Uncertainty Management in Simulation-Optimization of Complex Systems: Algorithms and Applications*, G. Dellino and C. Meloni, Eds. Boston, MA: Springer US, 2015, pp. 101–122, ISBN: 978-1-4899-7547-8. DOI: 10.1007/978-1-4899-7547-8_5. [Online]. Available: http://dx.doi.org/10.1007/978-1-4899-7547-8_5 (cit. on p. 133).

[35] *IS 13429 - Part 3 - 2018 - Solar Cooker - Box type - Specification - Part 3 : Test method (second revision)*, en, 2018 (cit. on pp. 32, 37).

[36] *ISO 19867-1:2018 - Clean cookstoves and clean cooking solutions - Harmonized laboratory test protocols - Part 1: Standard test sequence for emissions and performance, safety and durability*, en, Jun. 2018. [Online]. Available: https://www.iso.org/standard/66519.html (visited on 09/08/2023) (cit. on p. 35).

[37] D. Jafrancesco, J. P. Cardoso, A. Mutuberria, *et al.*, "Optical simulation of a central receiver system: comparison of different software tools", *Renewable and Sustainable Energy Reviews*, vol. 94, pp. 792–803, 2018 (cit. on p. 118).

[38] S. Kalogirou, *Solar energy engineering: processes and systems*, en, 2nd ed. Amsterdam: Academic Press Elsevier, 2014, ISBN: 978-0-12-397270-5 (cit. on pp. 55, 117).

[39] T. Kanyowa, G. V. Nyakujara, E. Ndala, *et al.*, "Performance Analysis of Scheffler Dish Type Solar Thermal Cooking System Cooking 6000 Meals Per Day", en-GB, *Solar Energy*, vol. 218, pp. 563–570, Apr. 2021, ISSN: 0038-092X. DOI: 10.1016/j.solener.2021.03.019. [Online]. Available: https://www.sciencedirect.com/science/article/pii/S0038092X2100205X (visited on 06/16/2021) (cit. on pp. 67, 117).

[40] C. Kimambo, "Development and performance testing of solar cookers", en, *Journal of Energy in Southern Africa*, vol. 18, no. 3, pp. 41–51, Aug. 2007, ISSN: 2413-3051, 1021-447X. DOI: 10.17159/2413-3051/2007/v18i3a3384. [Online]. Available: http://192.168.0.120/index.php/jesa/article/view (visited on 09/01/2023) (cit. on p. 35).

[41] N. Kincaid, G. Mungas, N. Kramer, *et al.*, "An optical performance comparison of three concentrating solar power collector designs in linear fresnel, parabolic trough, and central receiver", *Applied energy*, vol. 231, pp. 1109–1121, 2018 (cit. on pp. 118, 138).

[42] A. Kumar, M. Sharma, P. Thakur, *et al.*, "A review on exergy analysis of solar parabolic collectors", en, *Solar Energy*, vol. 197, pp. 411–432, Feb. 2020, ISSN: 0038-092X. DOI: 10.1016/j.solener.2020.01.025. [Online]. Available: https://www.sciencedirect.com/science/article/pii/S0038092X20300323 (visited on 06/18/2021) (cit. on p. 38).

[43] P. J. Lahkar, R. K. Bhamu, and S. K. Samdarshi, "Enabling inter-cooker thermal performance comparison based on cooker opto-thermal ratio (COR)", en, *Applied Energy*, vol. 99, pp. 491–495, Nov. 2012, ISSN: 0306-2619. DOI: 10.1016/j.apenergy.2012.05.034. [Online]. Available: https://www.sciencedirect.com/science/article/pii/S0306261912004072 (visited on 03/01/2021) (cit. on pp. 35, 45).

[44] S. Launay, B. Kadoch, O. L. Métayer, *et al.*, "Analysis strategy for multi-criteria optimization: application to inter-seasonal solar heat storage for residential building needs", *Energy*, vol. 171, pp. 419–434, 2019, ISSN: 0360-5442. DOI: 10.1016/j.energy.2018.12.181. [Online]. Available: http://www.sciencedirect.com/science/article/pii/S0360544218325556 (cit. on p. 133).

[45] *Le projet*, fr-FR. [Online]. Available: https://lepresage.fr/blog/le-projet/ (visited on 11/24/2022) (cit. on p. 23).

[46] G. O. G. Löf, "Recent investigations in the use of solar energy for cooking", en-US, *Solar Energy*, vol. 7, no. 3, pp. 125–133, Jul. 1963, ISSN: 0038-092X. DOI: 10.1016/0038-092X(63)90038-0. [Online]. Available: https://www.sciencedirect.com/science/article/pii/0038092X63900380 (visited on 05/19/2021) (cit. on p. 30).

[47] K. Lovegrove and W. Stein, "Concentrating solar power technology: principles, developments and applications", 2012 (cit. on p. 122).

[48] A. Malan and K. R. Kumar, "A comprehensive review on optical analysis of parabolic trough solar collector", *Sustainable Energy Technologies and Assessments*, vol. 46, p. 101 305, 2021 (cit. on p. 118).

[49] N. Mbodji and A. Hajji, "Performance Testing of a Parabolic Solar Concentrator for Solar Cooking", *Journal of Solar Energy Engineering*, vol. 138, no. 041009, May 2016, ISSN: 0199-6231. DOI: 10.1115/1.4033501. [Online]. Available: https://doi.org/10.1115/1.4033501 (visited on 09/07/2023) (cit. on p. 35).

[50] *Methode de calcul Th-BCE 2012*, fr, 2010 (cit. on p. 146).

[51] D. Montgomery, *Design and analysis of experiments*, 8th. John Wiley & Sons, 2013, ISBN: 978-1-118-14692-7. [Online]. Available: https://www.wiley.com/en-us/Design+and+Analysis+of+Experiments%5C%2C+10th+Edition-p-9781119492443 (cit. on p. 133).

[52] S. C. Mullick, T. C. Kandpal, and S. Kumar, "Thermal test procedure for a paraboloid concentrator solar cooker", en, *Solar Energy*, vol. 46, no. 3, pp. 139–144, Jan. 1991, ISSN: 0038-092X. DOI: 10.1016/0038-092X(91)90087-D. [Online]. Available: https://www.sciencedirect.com/science/article/pii/0038092X9190087D (visited on 03/03/2021) (cit. on pp. 32, 40, 42).

[53] S. C. Mullick, T. C. Kandpal, and A. K. Saxena, "Thermal test procedure for box-type solar cookers", en, *Solar Energy*, vol. 39, no. 4, pp. 353–360, Jan. 1987, ISSN: 0038-092X. DOI: 10.1016/S0038-092X(87)80021-X. [Online]. Available: https://www.sciencedirect.com/science/article/pii/S0038092X8780021X (visited on 02/27/2021) (cit. on pp. 31, 32, 34, 48).

[54] S. C. Mullick, T. C. Kandpal, and S. Kumar, "Testing of Box-Type Solar Cooker: Second Figure of Merit F2 and Its Variation with Load and Number of Pots", en, *Solar Energy*, vol. 57, no. 5, pp. 409–413, Nov. 1996, ISSN: 0038-092X. DOI: 10.1016/S0038-092X(96)00116-8. [Online]. Available: https://www.sciencedirect.com/science/article/pii/S0038092X96001168 (visited on 03/03/2021) (cit. on p. 31).

[55] A. Munir, O. Hensel, and W. Scheffler, "Design principle and calculations of a Scheffler fixed focus concentrator for medium temperature applications", en, *Solar Energy*, vol. 84, no. 8, pp. 1490–1502, Aug. 2010, ISSN: 0038-092X. DOI: 10.1016/j.solener.2010.05.011. [Online]. Available: https://www.sciencedirect.com/science/article/pii/S0038092X10002021 (visited on 03/01/2021) (cit. on pp. 24, 49, 55, 66, 117).

[56] H. Naik, P. Baredar, and A. Kumar, "Medium temperature application of concentrated solar thermal technology: Indian perspective", en-GB, *Renewable and Sustainable Energy Reviews*, vol. 76, pp. 369–378, Sep. 2017, ISSN: 1364-0321. DOI: 10.1016/j.rser.2017.03.014. [Online]. Available: https://www.sciencedirect.com/science/article/pii/S1364032117303313 (visited on 05/21/2021) (cit. on p. 24).

[57] *Nonimaging optics*, en, Page Version ID: 1177861469, Sep. 2023. [Online]. Available: https://en.wikipedia.org/w/index.php?title=Nonimaging_optics&oldid=1177861469 (visited on 01/23/2024) (cit. on p. 39).

[58] U. Oelher and W. Scheffler, "The Use of Indigenous Materials for Solar Conversion", en, *Solar Energy Materials and Solar Cells*, vol. 33, no. 3, pp. 379–387, Jul. 1994, ISSN: 0927-0248. DOI: 10.1016/0927-0248(94)90239-9. [Online]. Available: https://www.sciencedirect.com/science/article/pii/0927024894902399 (visited on 02/08/2021) (cit. on pp. 66, 80, 117).

[59] P. P. Otte, "Solar cookers in developing countries—What is their key to success?", en, *Energy Policy*, vol. 63, pp. 375–381, Dec. 2013, ISSN: 0301-4215. DOI: 10.1016/j.enpol.2013.08.075. [Online]. Available: https://www.sciencedirect.com/science/article/pii/S0301421513008793 (visited on 05/21/2021) (cit. on p. 24).

[60] H. H. Öztürk, "Experimental determination of energy and exergy efficiency of the solar parabolic-cooker", en, *Solar Energy*, vol. 77, no. 1, pp. 67–71, Jan. 2004, ISSN: 0038-092X. DOI: 10.1016/j.solener.2004.03.006. [Online]. Available: https://www.sciencedirect.com/science/article/pii/S0038092X04000556 (visited on 03/01/2021) (cit. on p. 38).

[61] H. Panchal, J. Patel, K. Parmar, *et al.*, "Different applications of scheffler reflector for renewable energy: a comprehensive review", *International Journal of Ambient Energy*, vol. 41, no. 6, pp. 716–728, 2020 (cit. on p. 117).

[62] R. Petela, "Exergy analysis of the solar cylindrical-parabolic cooker", en, *Solar Energy*, vol. 79, no. 3, pp. 221–233, Sep. 2005, ISSN: 0038-092X. DOI: 10.1016/j.solener.2004.12.001. [Online]. Available: https://www.sciencedirect.com/science/article/pii/S0038092X04003482 (visited on 06/15/2021) (cit. on p. 38).

[63] K. Pottler, E. Lu¨pfert, G. H. Johnston, *et al.*, "Photogrammetry: a powerful tool for geometric analysis of solar concentrators and their components", *J. Sol. Energy Eng.*, vol. 127, no. 1, pp. 94–101, 2005 (cit. on p. 122).

[64] J.-C. Pulfer, C. Ingeniería, and R. M. López, "Small marmalade factory in Argentina working with Scheffler type industrial cooker", en, in *Proceedings of Solar Cookers and Food Processing International Conference*, Granada, Spain, Jul. 2006, p. 4 (cit. on p. 67).

[65] A. Rabl, "Comparison of solar concentrators", en-US, *Solar Energy*, vol. 18, no. 2, pp. 93–111, Jan. 1976, ISSN: 0038-092X. DOI: 10.1016/0038-092X(76)90043-8. [Online]. Available: https://www.sciencedirect.com/science/article/pii/0038092X76900438 (visited on 02/22/2021) (cit. on p. 38).

[66] I. Reda and A. Andreas, "Solar position algorithm for solar radiation applications", *Solar energy*, vol. 76, no. 5, pp. 577–589, 2004 (cit. on p. 119).

[67] D. S. Reddy and M. K. Khan, "Design and ray tracing of multifaceted Scheffler reflector with novel crossbars", en-GB, *Solar Energy*, vol. 185, pp. 363–373, Jun. 2019, ISSN: 0038-092X. DOI: 10.1016/j.solener.2019.04.083. [Online]. Available: https://www.sciencedirect.com/science/article/pii/S0038092X1930430X (visited on 03/01/2021) (cit. on pp. 66, 81, 117).

[68] D. S. Reddy, M. K. Khan, M. Z. Alam, *et al.*, "Design charts for Scheffler reflector", en-GB, *Solar Energy*, vol. 163, pp. 104–112, Mar. 2018, ISSN: 0038-092X. DOI: 10.1016/j.solener.2018.01.081. [Online]. Available: https://www.sciencedirect.com/science/article/pii/S0038092X18301026 (visited on 03/01/2021) (cit. on pp. 66, 117–120, 122, 127, 137, 138).

[69] M. Röger, P. Herrmann, S. Ulmer, *et al.*, "Techniques to Measure Solar Flux Density Distribution on Large-Scale Receivers", *Journal of Solar Energy Engineering*, vol. 136, no. 3, p. 031 013, May 2014, ISSN: 0199-6231. DOI: 10.1115/1.4027261. [Online]. Available: https://doi.org/10.1115/1.4027261 (visited on 12/02/2022) (cit. on pp. 67, 68).

[70] J. Ruelas, J. Palomares, and G. Pando, "Absorber design for a scheffler-type solar concentrator", *Applied Energy*, vol. 154, pp. 35–39, 2015 (cit. on p. 117).

[71] J. Ruelas, G. Pando, B. Lucero, *et al.*, "Ray tracing study to determine the characteristics of the solar image in the receiver for a scheffler-type solar concentrator coupled with a stirling engine", *Energy Procedia*, vol. 57, pp. 2858–2866, 2014 (cit. on p. 117).

[72] J. Ruelas, N. Velázquez, and J. Cerezo, "A mathematical model to develop a scheffler-type solar concentrator coupled with a stirling engine", *Applied energy*, vol. 101, pp. 253–260, 2013 (cit. on p. 138).

[73] C. R. Ruivo, X. Apaolaza-Pagoaga, G. Coccia, *et al.*, "Proposal of a non-linear curve for reporting the performance of solar cookers", en, *Renewable Energy*, vol. 191, pp. 110–121, May 2022, ISSN: 0960-1481. DOI: 10.1016/j.renene.2022.04.026. [Online]. Available: https://www.sciencedirect.com/science/article/pii/S0960148122004876 (visited on 07/05/2023) (cit. on pp. 42–45).

[74] C. R. Ruivo, A. Carrillo-Andrés, and X. Apaolaza-Pagoaga, "Experimental determination of the standardised power of a solar funnel cooker for low sun elevations", en, *Renewable Energy*, vol. 170, pp. 364–374, Jun. 2021, ISSN: 0960-1481. DOI: 10.1016/j.renene.2021.01.146. [Online]. Available: https://www.sciencedirect.com/science/article/pii/S0960148121001592 (visited on 06/17/2021) (cit. on p. 41).

[75] C. R. Ruivo, G. Coccia, G. Di Nicola, *et al.*, "Standardised power of solar cookers with a linear performance curve following the Hottel-Whillier-Bliss formulation", en, *Renewable Energy*, vol. 200, pp. 1202–1210, Nov. 2022, ISSN: 0960-1481. DOI: 10.1016/j.renene.2022.10.041. [Online]. Available: https://www.sciencedirect.com/science/article/pii/S0960148122015348 (visited on 07/03/2023) (cit. on pp. 36, 37, 56).

[76] S. Sasidharan and P. Dutta, "Optical characterization of a fixed focus Scheffler reflector for pressurized solar receiver testing", en-GB, *Solar Energy*, vol. 227, pp. 89–100, Oct. 2021, ISSN: 0038-092X. DOI: 10.1016/j.solener.2021.08.078. [Online]. Available: https://www.sciencedirect.com/science/article/pii/S0038092X21007428 (visited on 11/23/2022) (cit. on pp. 67, 80, 118, 138).

[77] A. Saxena, Varun, S. P. Pandey, *et al.*, "A thermodynamic review on solar box type cookers", en, *Renewable and Sustainable Energy Reviews*, vol. 15, no. 6, pp. 3301–3318, Aug. 2011, ISSN: 1364-0321. DOI: 10.1016/j.rser.2011.04.017. [Online]. Available: https://www.sciencedirect.com/science/article/pii/S1364032111001547 (visited on 05/21/2021) (cit. on pp. 35, 38).

[78] W. Scheffler, S. Bruecke, and G. von Werdenbergstr, "Development of a solar crematorium", in *6th International Conference on Solar Cooker, Granada, Spain*, 2006 (cit. on p. 117).

[79] *Scheffler Community Kitchen*, en. [Online]. Available: https://solarcooking.fandom.com/wiki/Scheffler_Community_Kitchen (visited on 01/22/2024) (cit. on p. 27).

[80] S. Shaw, "Development of a Comparative Framework for Evaluating the Performance of Solar Cooking Devices: Combining Ergonomic, Thermal, and Qualitative Data into an Understandable, Reproducible, and Rigorous Testing Method", en, 2002 (cit. on pp. 35, 38).

[81] M. Shortis and G. Johnston, "Photogrammetry: an available surface characterization tool for solar concentrators, part ii: assessment of surfaces", *Journal of Solar Energy Engineering*, vol. 118, no. 3, 1997 (cit. on p. 138).

[82] Y. S. Touloukian, R. W. Powell, C. Y. Ho, *et al.*, "Thermophysical properties of matter - the TPRC data series. Volume 2. Thermal conductivity - nonmetallic solids. (Reannouncement). Data book", en, Purdue Univ., Lafayette, IN (United States). Thermophysical and Electronic Properties Information Center, Tech. Rep. AD-A-951936/4/XAB, Jan. 1971. [Online]. Available: https://www.osti.gov/biblio/5303523 (visited on 03/09/2023) (cit. on p. 106).

[83] J. S. Vaishya, T. C. Tripathi, D. Singh, *et al.*, "A hot box solar cooker: Performance analysis and testing", en, *Energy Conversion and Management*, vol. 25, no. 3, pp. 373–379, Jan. 1985, ISSN: 0196-8904. DOI: 10.1016/0196-8904(85)90057-3. [Online]. Available: https://www.sciencedirect.com/science/article/pii/0196890485900573 (visited on 09/01/2023) (cit. on p. 31).

[84] M. J. Wagner and T. Wendelin, "Solarpilot: a power tower solar field layout and characterization tool", *Solar Energy*, vol. 171, pp. 185–196, 2018 (cit. on p. 118).

[85] T. Wendelin, "Soltrace: a new optical modeling tool for concentrating solar optics", in *International solar energy conference*, vol. 36762, 2003, pp. 253–260 (cit. on p. 118).

[86] T. Wendelin, "Parabolic trough vshot optical characterization in 2005-2006 (presentation)", National Renewable Energy Lab.(NREL), Golden, CO (United States), Tech. Rep., 2006 (cit. on p. 138).